Proceedings

16th International Workshop on Water Waves and Floating Bodies

22-25 April, 2001
Hiroshima, Japan

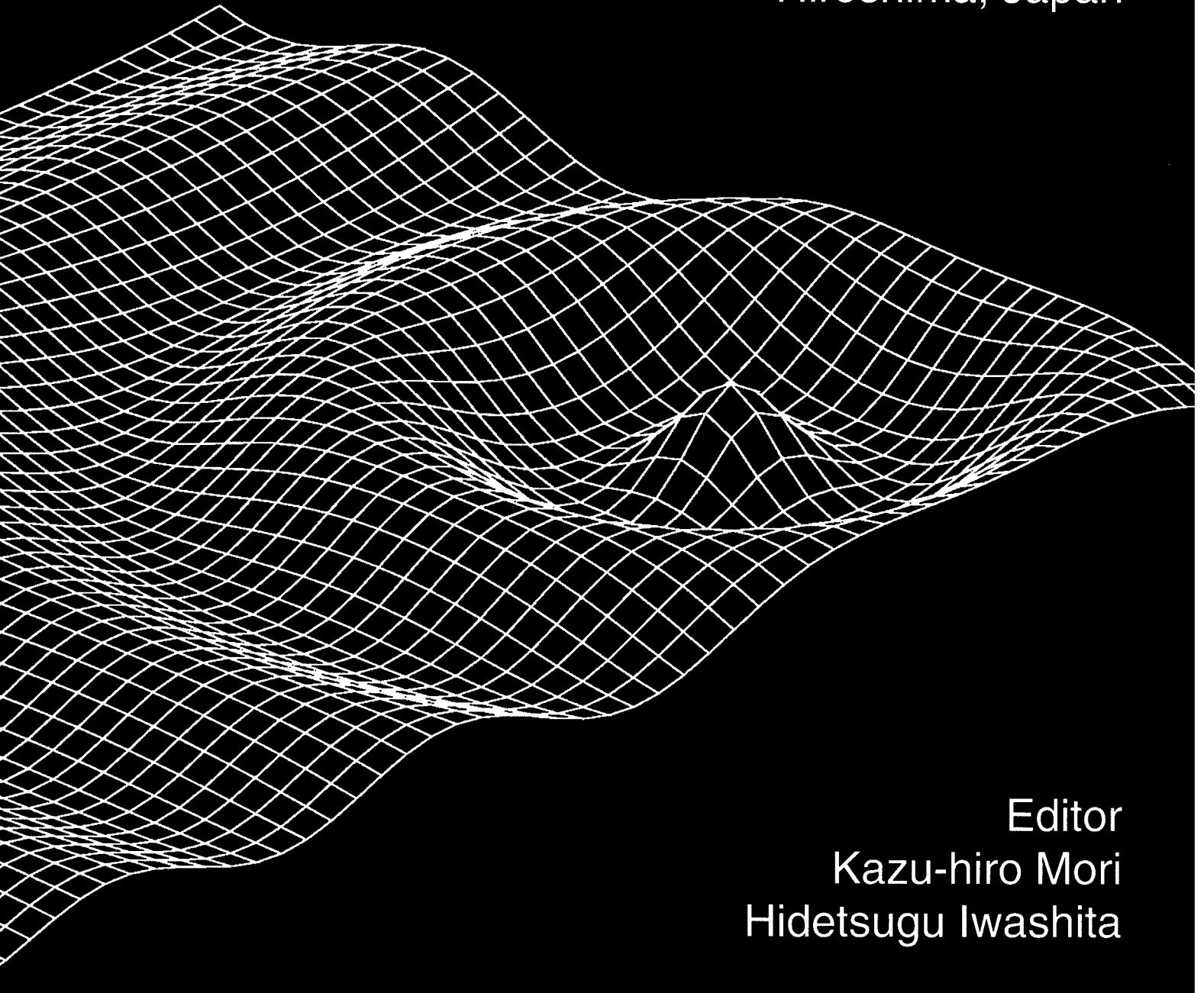

Editor
Kazu-hiro Mori
Hidetsugu Iwashita

REPORT DOCUMENTATION PAGE

Form Approved OMB No. 0704-0188

1. AGENCY USE ONLY (Leave blank)	2. REPORT DATE	3. REPORT TYPE AND DATES COVERED
	April 2001	22-25 April 2001 Conference Proceedings - Final Report

4. TITLE AND SUBTITLE

International Workshop on Water Waves and Floating Bodies (16th) Held in Hiroshima, Japan on 22-25 April 2001

5. FUNDING NUMBERS

N000-

6. AUTHOR(S)

Kaxu-hiro Mori and Hidetgsugu Iwashita, Editors

7. PERFORMING ORGANIZATION NAME(S) AND ADDRESS(ES)

Hiroshima Univeristy
Department of Engineering Systems
Hirshoma, Japan

8. PERFORMING ORGANIZATION REPORT NUMBER

ISBN 4-9900892-0

9. SPONSORING/MONITORING AGENCY NAME(S) AND ADDRESS(ES)

Office of Naval Research,
European Office
PSC 802 Box 39
FPO AE 09499-0039

10. SPONSORING/MONITORING AGENCY REPORT NUMBER

11. SUPPLEMENTARY NOTES

This work relates to Department of the Navy Grant issued by the Office of Naval Research International Field Office. The United States has a royalty free license throughout the world in all copyrightable material contained herein.

12a. DISTRIBUTION/AVAILABILITY STATEMENT

Approved for Public Release; Distribution Unlimited.

12b. DISTRIBUTION CODE

A

12. ABSTRACT (Maximum 200 words)

The International Workshop on Water Waves and Floating Bodies has been held annually since 1986. It brings together specialists who study water waves, hydrodynamic behavior of ocean structures and their interactions. The topics discussed this year include: ship motions in waves; breaking waves by ships; waves generated by ships in restricted waterways; trapped mode by multi-columns; hydroelasticity of BLFS; and nonlinear simulation of motions floating bodies.

13. SUBJECT TERMS

ONRIFO, Foreign reports, Conference Proceedings, Water Waves

15. NUMBER OF PAGES

16. PRICE CODE

17. SECURITY CLASSIFICATION OF REPORT	18. SECURITY CLASSIFICATION OF THIS PAGE	19, SECURITY CLASSIFICATION OF ABSTRACT	20. LIMITATION OF ABSTRACT
UNCLASSIFIED	UNCLASSIFIED	UNCLASSIFIED	UL

Proceedings

16th International Workshop on Water Waves and Floating Bodies

22 – 25 April, 2001

Aki Grand Hotel, Hiroshima
JAPAN

Edited by

Kazu-hiro Mori and Hidetsugu Iwashita

Department of Engineering Systems
Faculty of Engineering, Hiroshima University

Organization:
The 16th International Workshop on Water Waves and Floating Bodies was organized by the Department of Engineering Systems, Faculty of Engineering, Hiroshima University. The workshop was held at Aki Grand Hotel, Hiroshima, JAPAN from the 22nd to the 25th April, 2001.

Sponsors:
The 16th International Workshop on Water Waves and Floating Bodies was sponsored by The Office of Naval Research International Field Office and Electric Technology Research Foundation of Chugoku. The organizing committee cordially appreciate their financial supports.

ISBN 4-9900892-0-0

CONTENTS

Wave-Drift Added Mass of Bodies with Slow Drift Motions

Weiguang BAO and Takeshi KINOSHITA

Institute of Industrial Science, University of Tokyo
4-6-1 Komaba, Meguro-Ku, Tokyo 153-8505 Japan
Tel. & Fax: +81-3-5452-6169 E-Mail: kinoshit@iis.u-tokyo.ac.jp

1.INTRODUCTION

Ocean structures are usually constrained by mooring or tether systems, which supply relatively weak restoring forces in the horizontal plane. Under the slowly varying drift forces exerted by ocean waves, these structures may undergo low-frequency resonant oscillations in the horizontal motion modes, i.e. surge, sway and yaw. The nonlinear wave loads are proportional to the square of the wave amplitude in magnitude and occur at a frequency σ that is the difference between each pair of frequencies, say ω_i and ω_j, in the components of ocean wave spectrum, i.e. $\sigma = |\omega_i - \omega_j|$. Conventional added mass and damping can be obtained by solving a linear radiation problem in which the body of the structures is forced to oscillate in the calm water. In the case when the frequency σ of the oscillation is very small, the wave-radiating damping vanishes with an order of $O(\sigma^7)$ in the horizontal motion modes while the added mass tends to the same order of the displaced water mass. However, with the presence of the incident waves, there exists another kind of added mass and damping that is caused by the nonlinear interaction between waves and slow oscillations. As part of the nonlinear wave loads, their magnitude is proportional to the square of the wave amplitude, which is different from the conventional added mass and damping, and they are called wave drift added mass and wave drift damping respectively. Recently, many studies have been made to evaluate and measure the wave drift damping which is more significant compared with the conventional wave-radiation damping and plays a key role in the simulation of slow drift motions, especially in estimating the resonant response. On the other hand, wave drift added mass is considered less important and relatively less attention has been paid to it. Nevertheless, it has been reported that the added mass increases significantly when measured in waves [1]. Therefore, to simulate slow drift motions accurately and to determine the resonant frequency, it is worth investigating the magnitude of the wave drift added mass and how much it would affect the slow drift motions.

In the present work, the problem of interaction between slow horizontal oscillations of a body and ambient waves is considered. The approach used by Newman [2] to investigate wave drift damping is adopted. The feature of this method is that perturbation expansion based on two time scales is used to simplify nonlinear boundary conditions. The wave forces acting on the body are evaluated by integration of hydrodynamic pressure along the instantaneous wetted body surface. From the quadratic nonlinear forces in terms of the wave amplitude, the wave drift added mass is picked out

by the component in contract phase to the acceleration of the slow oscillations. These results will be compared with the conventional linear added mass to examine their significance.

2.PERTURBATION EXPANSION OF THE POTENTIAL

We are going to consider the problem of a body slowly oscillating in a train of regular waves with a wave number k_0 and incident angle β. The nonlinear interaction among slow oscillation modes is not considered so that each mode can be studied separately. The body is restrained from the linear responses to the incident waves. The frequency of the slow oscillations is assumed to be σ, which is much smaller than the incident wave frequency ω. The oscillatory displacement and velocity are assumed to be $\mathrm{Re}\{i\xi_j e^{-i\sigma t}\}$ and $\mathrm{Re}\{\sigma\xi_j e^{-i\sigma t}\}$ respectively, where the subscript j= 1, 2 and 6 denoting surge, sway and yaw respectively. Following the approach of Newman's [2], the total velocity potential can be expressed by the following perturbation expansion up to the quadratic order in wave amplitude A:

$$\Phi(\boldsymbol{x},t)=\mathrm{Re}\left\{\phi_1 e^{-i\omega t}+\phi_2^{(0)}+\ldots+\xi_j\left[\phi_{0j}e^{-i\sigma t}+\phi_{1j}^{(+)}e^{-i(\omega+\sigma)t}+\phi_{1j}^{(-)}e^{-i(\omega-\sigma)t}+\phi_{2j}^{(0)}e^{-i\sigma t}+\ldots\right]\right\} \quad (1)$$

The potentials on the right-hand side of eqn. (1) depends only on the space position $\boldsymbol{x}$. The number in the subscript indicates the order in wave amplitude while the letter j is related to the corresponding slow motion modes. Superscripts are used if necessary to denote harmonic time dependence in the respective frequencies. Here, potentials associated with double wave frequency are omitted since they will not contribute to the wave-drift added mass and damping. Substituting the above expansion into the boundary conditions satisfied by the total velocity potential and resorting terms with the same order, the boundary value problem governing each order of potentials can be obtained. Detail deduction is referred to Newman's work [2].

3.CALCULATION OF THE WAVE-DRIFT ADDED MASS

The wave forces are evaluated by the integration of the hydrodynamic pressure along the instantaneous wetted body surface and expanded in the same way as the velocity potential, i.e.

$$F_i(t)=\mathrm{Re}\left\{F_{1i}e^{-i\omega t}+F_{2i}^{(0)}+\ldots+\xi_j\left[F_{0ij}e^{-i\sigma t}+F_{1ij}^{(+)}e^{-i(\omega+\sigma)t}+F_{1ij}^{(-)}e^{-i(\omega-\sigma)t}+F_{2ij}^{(0)}e^{-i\sigma t}+\ldots\right]\right\} \quad (2)$$

Here, the subscript i=1, 2, and 6 denoting the force component in surge, sway and yaw direction respectively. In eqn. (2) F_{0ij} is the linear force in i-th direction per unit motion of ξ_j and is related to the linear added mass A_{0ij} and wave-radiating damping B_{0ij} as follows:

$$F_{0ij}=-\left(-i\sigma^2 A_{0ij}+\sigma B_{0ij}\right)=i\sigma\rho\int_{S_0}\phi_{0j}n_i ds \quad (3)$$

where S_0 is the mean wetted body surface. In the limiting case that σ tends to zero, the radiation potential ϕ_{0j} of the slow oscillation tends to satisfy a rigid wall condition on the free surface. It is further normalized as $\phi_{0j}=\sigma\varphi_j$ where φ_j is a real function. Hence, as σ tends to zero, the linear

wave- radiating damping B_{0ij} vanishes while the added mass tends to

$$A_{0ij} = \rho \int_{S_0} \varphi_j n_i ds \tag{4}$$

On the other hand, $F_{2ij}^{(0)}$ is a force component in quadratic order of wave amplitude, which can also be separated into two parts that is in phase with the acceleration and the velocity of the slow oscillation respectively, i.e.

$$F_{2ij}^{(0)} = -\left(-i\sigma^2 A_{2ij} + \sigma B_{2ij}\right) \tag{5}$$

The formula to evaluate the wave-drift added mass is given by

$$\begin{aligned} A_{2ij} = \mathrm{Im}\Big\{ & -\rho \int_{C_0} \left[-i\sigma\phi_{2j}^{(0)} + \tfrac{1}{2}\nabla\left(\phi_{1j}^{(+)} - \phi_{1j}^{(-)}\right)\cdot\nabla\phi_1^* + \nabla\phi_{0j}\cdot\nabla\phi_2^{(0)} + \tfrac{1}{2}i\nabla\phi_1\cdot D_j\left(\nabla\phi_1^*\right)\right] n_i ds \\ & + \frac{\rho}{2g}\int_{C_0}\left[\omega^2\left(\phi_{1j}^{(+)} - \phi_{1j}^{(-)}\right)\phi_1^* + \sigma\omega\left(\phi_{1j}^{(+)} + \phi_{1j}^{(-)}\right)\phi_1^* - \tfrac{1}{2}i\sigma\phi_{0j}\nabla\phi_1\cdot\nabla\phi_1^* + i\omega^2\phi_1 D_j\left(\phi_1^*\right)\right. \\ & \left. -\tfrac{1}{2}i\omega\phi_1\nabla\left(\phi_{0j} - \phi_{0j}^*\right)\cdot\nabla\phi_1^* + i\sigma\omega^2\left(\tfrac{1}{2}\phi_{0jz} + \nu\phi_{0j}\right)\phi_1\phi_1^*\right] n_i dl\Big\} \end{aligned} \tag{6}$$

where C_0 is the mean water line of the body and D_j is a derivative operator which is defined as $D_1 = \partial/\partial x$, $D_2 = \partial/\partial y$ and $D_6 = x\partial/\partial y - y\partial/\partial x = \partial/\partial\theta$. The asterisk * in the superscript denotes the complex conjugate. The letter z in the subscript means the derivative with respect to it.

When σ tends to zero, we define $\phi_{1j}^{(+)} - \phi_{1j}^{(-)} = P_j$ and $\phi_{1j}^{(+)} - \phi_{1j}^{(-)} = \sigma Q_j$ where P_j is related to the linear wave potential ϕ_1 as $P_j = -iD_j(\phi_1) - \kappa_j$ with $\kappa_1 = k_0\cos\beta$, $\kappa_1 = k_0\sin\beta$ and $\kappa_6 = i\partial/\partial\beta$.

Then, in this limiting case the wave drift added mass A_{2ij} can be evaluated simply by an integral along the mean water line of the body:

$$A_{2ij} = \mathrm{Im}\left\{\frac{\rho}{2g}\int_{C_0}\left[\omega Q_j\phi_1^* + i\nu^2\varphi_j\phi_1\phi_1^* - \tfrac{i}{2}\varphi_j\nabla\phi_1\cdot\nabla\phi_1^*\right] n_i dl\right\} \qquad \text{with } \nu = \omega^2/g \tag{7}$$

4.EXAMPLES AND DISCUSSION

A circular cylinder with radius a is taken as an example to calculate the wave drift added mass when the incident wave angle is 0°. Shown in Fig. 1 are results of the wave-drift added mass A_{211} normalized by $\rho\pi a\zeta^2$ where ζ is the wave amplitude. It can be observed that the wave-drift added mass generally is the same order as the wave drift damping in magnitude. In order to compare with the linear added mass, the possible maximum wave amplitude before breaking, i.e. ζ=0.14π/k_0, is used to renormalize the wave-drift added mass and the ratio of the wave-drift added mass A_{211} to the linear added mass A_{011} is plotted in Fig. 2. It can be seen that the contribution from the wave-drift added mass is not negligible if the wave amplitude is comparable to the dimension of the body.

REFERENCE

1. Kinoshita T. Shoji K. Obama H. (1992) Low frequency added mass of semi-submersible influenced by incident waves. Proc. of OMAE, Vol. III: 504-512

2. Newman J. N. (1993) Wave-drift damping of floating bodies. J. Fluid Mech. Vol.249: 241-259

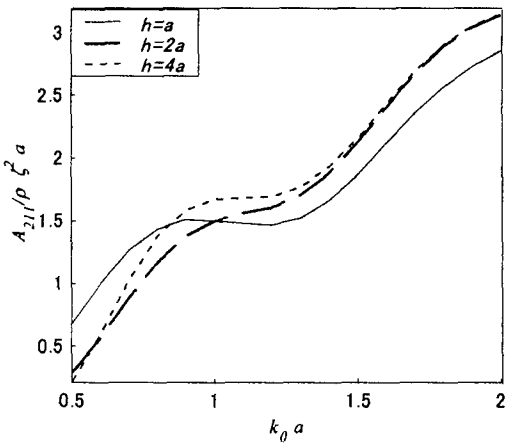

Fig.1a Wave-drift added mass A_{211} for a uniform cylinder in different water depth h.

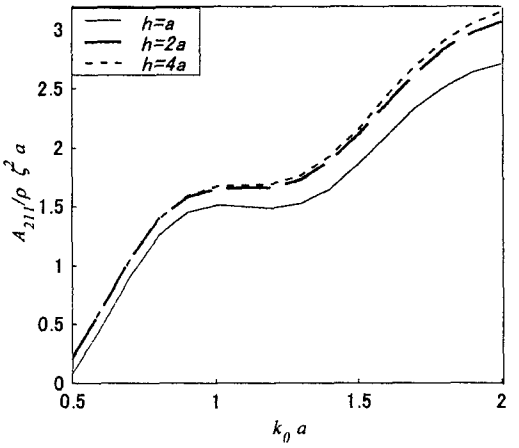

Fig.1b Wave-drift added mass A_{211} for a truncated cylinder with different draught d in a water depth h=4a.

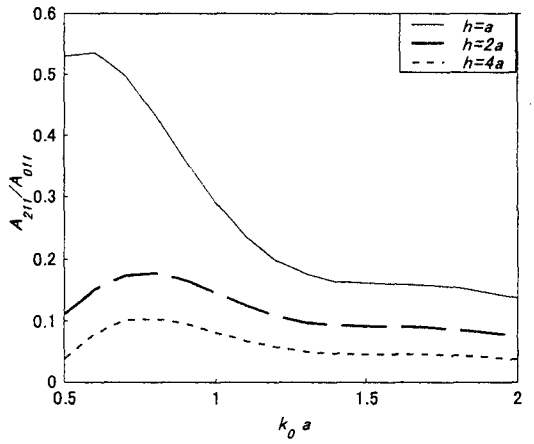

Fig.2a Wave-drift added mass A_{211} compared with linear added mass A_{011} for a uniform cylinder in different water depth h.

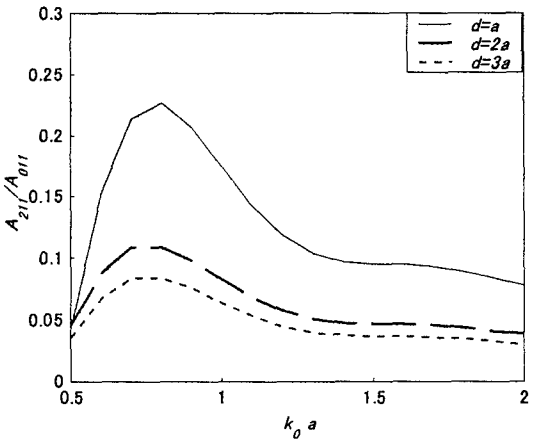

Fig.2b Wave-drift added mass A_{211} compared with linear added mass A_{011} for a truncated cylinder with different draught d in a water depth h=4a.

An Enhanced Nonlinear Strip Method for Seakeeping Analysis

Volker BERTRAM, *HSVA, Hamburg/Germany, bertram@hsva.de*
Ricardo PEREIRA, *MTG, Hamburg/Germany, pereira@mtg-marinetechnik.de*
Maurizio LANDRINI, *INSEAN, Rome/Italy, maulan@waves.insean.it*

Available methods for calculating motions, shear forces and bending moments of a ship in waves are usually based on linear (small wave amplitude) theory. However, for dimensioning ship structures the loads in extreme waves are needed. Also for ship safety in sea waves, we need to consider extreme motions, particularly extreme roll motions up to capsize angles.

The computational effort for a three-dimensional field method or even boundary element method simulating the motions and loads on a ship at each time instant over a long time appears still beyond our current and near future computational capabilities. Thus we try to introduce simplifications that reduce the computational effort drastically without losing too much of the physical significance of the model. The tool of choice appears then to be a nonlinear strip method of some sort. The nonlinear strip method SIMBEL dates back to Söding (1982) and has been extended over the past two decades to include internal forces, propulsion system dynamics and manoeuvring, e.g. Pereira (1988). A long-term goal is to have a tool which can simulate also broaching and capsizing of vessels, i.e. a combination of extreme manoeuvring and seakeeping motions.

The method is a simulation in which large-amplitude rigid-body motions of the ship in 6 degrees of freedom, shear forces and bending moments are determined under the influence of forces and moments due to weight, Froude-Krylov pressure, radiation and diffraction pressure, speed effects (resistance and manoeuvring forces and moments due to oblique forward motion) and propeller and rudder actions. For large amplitude motions, the diffraction and radiation forces cannot be determined independently. But in principle we still couple forces $\underline{F}$ and (derivatives of) motions $\underline{u}$ using basic differential equations.

The forces can be determined by integrating the pressure over the instantaneously wetted surface of the ship. Unfortunately, the pressure distribution does not depend only on instantaneous position, velocity and acceleration of the ship, but also on the history of the motion (memory effects). This affects particularly heave and pitch motions. For linear computations in regular waves, this memory effect results in the frequency dependence of added mass and damping. For nonlinear simulations this is not quite as simple as many frequencies are present at the same time and the superposition principle no longer applies. The memory effects can be expressed in terms of convolution integrals, alternatively one considers 0 to n time derivatives of the force $\underline{F}$ and 1 to $n+1$ time derivatives of the motion $\underline{u}$:

$$B_0\underline{F}(t) + B_1\dot{\underline{F}} + B_2\ddot{\underline{F}} + ... = A_0\dot{\underline{u}}(t) + A_1\ddot{\underline{u}}(t) + ...A_2\,\dddot{\underline{u}}\,(t) + ... \qquad (1)$$

The matrices A_i and B_i are determined in a preprocessing step for various drafts and inclination angles for each section. This procedure is called state space model. It is far more efficient than approaches using convolution integrals. Typical values for n (terms on left and right side) are 2 to 4. We chose 3. With increasing n problems appear with numerically induced oscillations which grow and make the simulation instable.

Now stability and prediction accuracy of SIMBEL shall be improved by using some more advanced numerical methods to derive coefficients in the preprocessing stage. The added mass and damping coefficients for the linear radiation problem are now derived for each section by a three-dimensional Green-function method without forward speed. The forward speed effects are kept as before in the framework of the strip method. The hope is that the three-dimensional

method will improve accuracy nevertheless at the ship ends and may actually also improve the stability of the nonlinear strip method procedures. As a first step a standard Green function method following Landrini (1996) was used to define the hydrodynamic coefficients. This was validated for a Series-60 $C_B = 0.7$ against experiments, Vugts (1971), and a standard close-fit strip method. To the best of our knowledge, this is the first time that such a validation for individually strips has been performed. Heave added mass for sections are improved especially at the ship ends Fig.1, and also sway damping coefficients are well reproduced, Fig.2. However, roll is naturally predicted badly by both potential flow approaches.

In addition RANSE computations shall compute the drift force coefficients on the hull for various drafts and inclinations. These are again computed for the 3-d hull as a preprocessing step. It is crucial to include the speed effect here in the RANSE computations as the separation characteristics and thus drift force coefficients change drastically with speed and forward speed.

Currently we develop the interface between the 3-d preprocessors and the SIMBEL strip method and have prepared already a grid for an actual ro-ro ship. By the time of the workshop, we should have results of the standard strip method and the new "hybrid" approach to see how the changes in the individual hydrodynamic coefficients influence the global simulation.

REFERENCES

LANDRINI, M. (1996) *Implementation of a frequency domain code for zero forward speed seakeeping*, INSEAN Tech. Rep.

SÖDING, H. (1982), *Leckstabilität im Seegang*, IfS-Report 429, Univ. Hamburg

PEREIRA, R. (1988), *Simulation nichtlinearer Seegangslasten*, Schiffstechnik 35, pp.173-193

VUGTS, J.H. (1971), *The hydrodynamic forces and ship motions in oblique waves*, TNO report 150S, NSRC, Delft

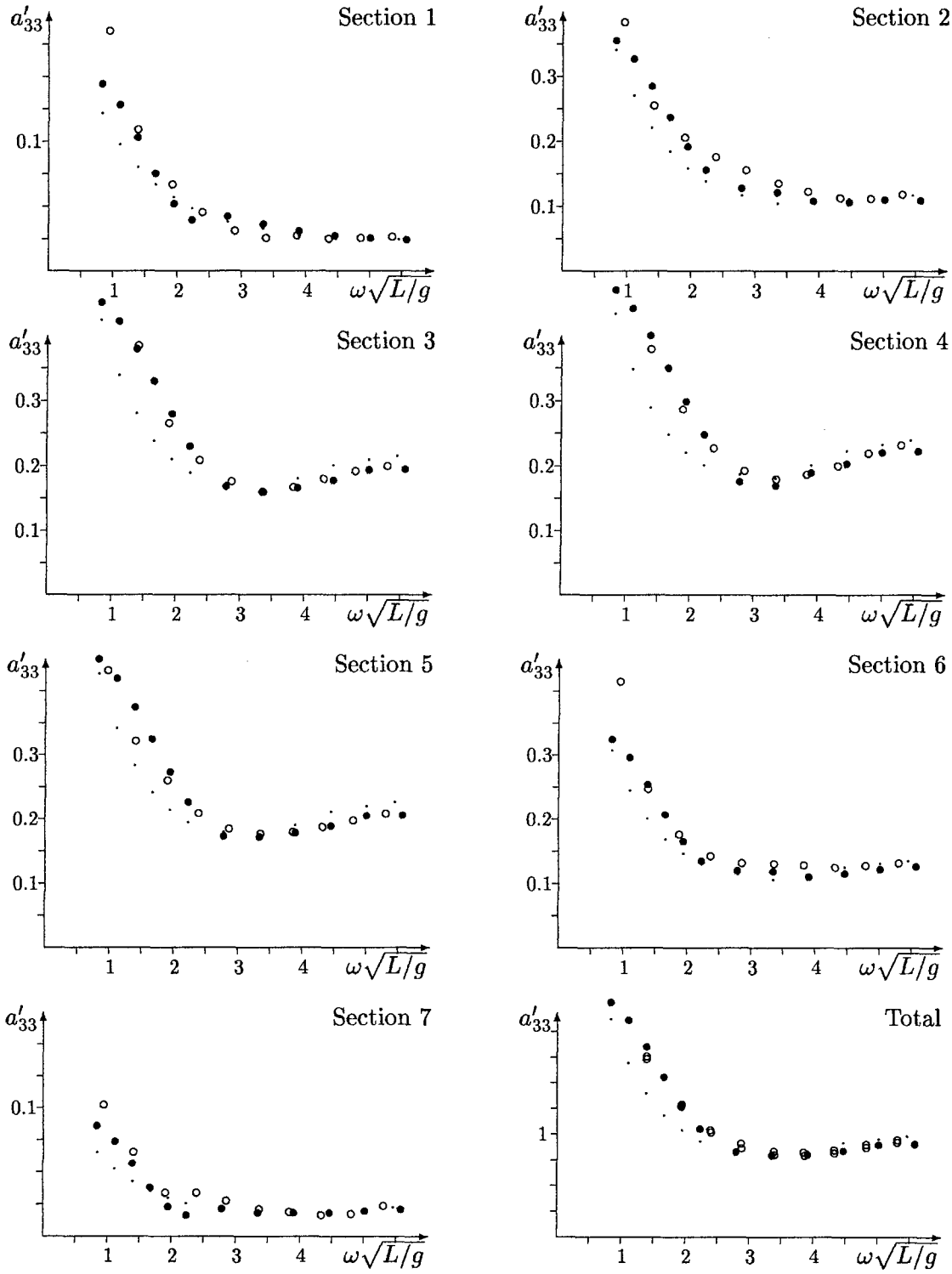

Fig.1: Series-60, $C_B = 0.7$, $F_n = 0$; added mass; $m = \nabla \cdot \rho$
$a'_{33} = a_{33}/m$ for vertical force due to heave motion for strips and total ship;
○ Exp., • GFM, · strip method

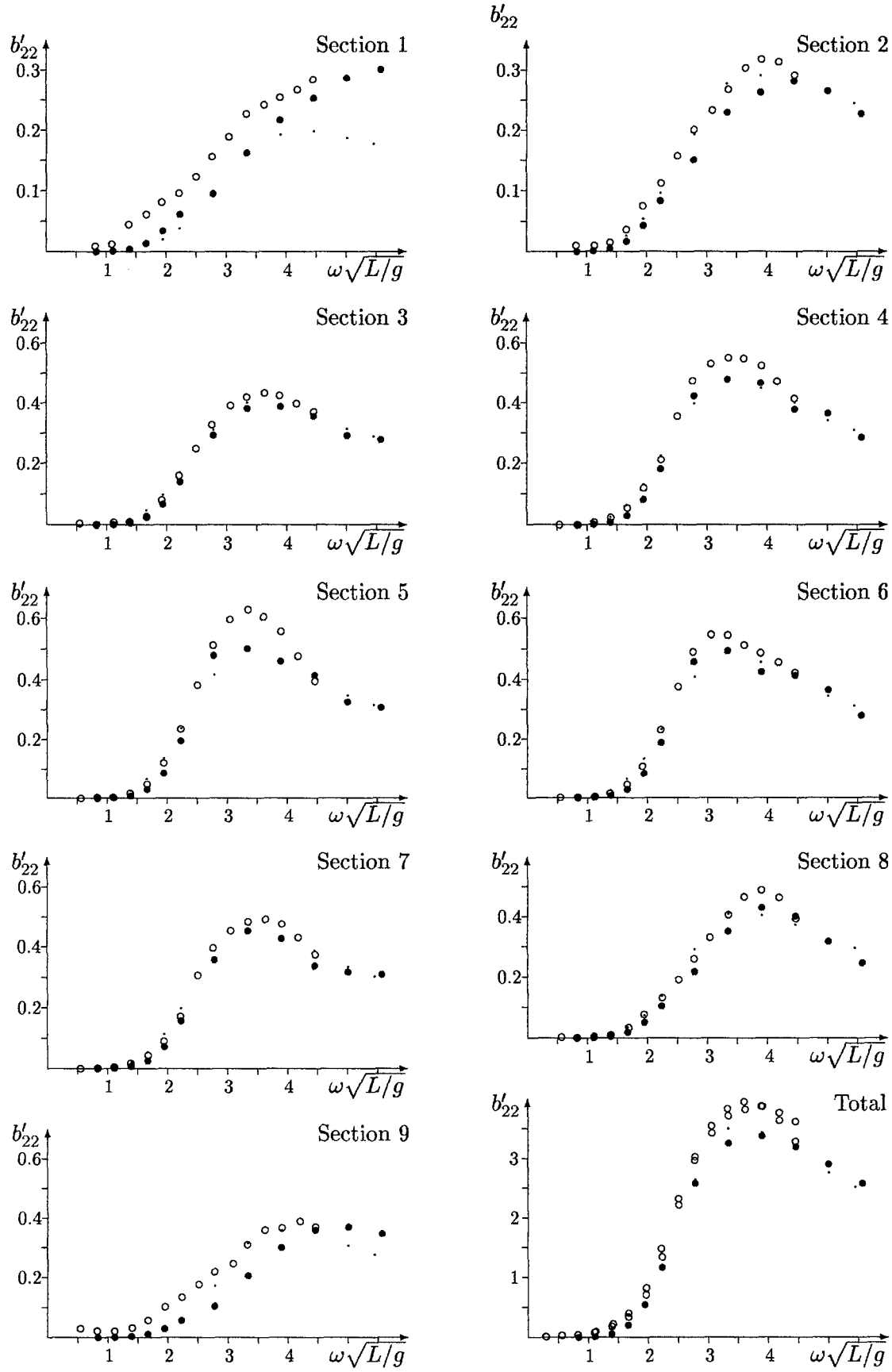

Fig.2: Series-60, $C_B = 0.7$, F_n; hydrodynamic damping
$b'_{22} = b_{22}/(m \cdot \sqrt{g/L})$ for sway force due to sway motion for strips and total ship;
○ Exp., • GFM, · strip method

UNSTEADY FREE SURFACE WAVES BY DOMAIN DECOMPOSITION APPROACH

E. F. CAMPANA AND A. IAFRATI
INSEAN - Italian Ship Model Basin - Rome, Italy

1 Introduction

Several numerical techniques have been recently developed to deal with the complex free surface topology induced by the wave breaking (*e.g.* Tulin & Landrini 2000, Sussman & Dommermuth 2000). However, although these approaches are strictly needed in the free surface region, their use far from the interface is expensive and neither really necessary. For instance, when studying the wave breaking induced by a submerged body an accurate description of the flow field close to the body is not needed while the computational effort can be focused about the free surface. For this reason, a domain decomposition approach is built which couple the Navier-Stokes solver, employed close to the interface, with a potential solver able to describe the flow in the body region.

In a previous work (Iafrati *et al.* 2001), an unsteady Navier-Stokes solver coupled with a Level-Set technique has been developed to study wave breaking induced by bodies moving beneath the free surface. In this work this approach is used in the free surface region, where the unsteady Navier-Stokes equations are solved by using a finite difference approach, while a Level-Set technique is used to follow the interface dynamics. Throughout the boundary of the computational domain velocity is assigned. In the body region, a boundary integral representation of the velocity potential is used with Neumann boundary conditions on the body contour and at inflow and outflow. Concerning the boundary conditions on the matching surface, two approaches are developed. In the first one, say Dirichlet type (DT), both the pressure and the velocity fields obtained from the Navier-Stokes solver are used within the unsteady Bernoulli's equation to obtain the velocity potential on the matching surface. In the second one, say Neumann type (NT), only the normal velocity obtained from the Navier-Stokes solver is used as a boundary condition on the matching surface. In both cases, the solution of the boundary integral formulation provides the velocity field on the matching to be used as boundary condition for the Navier-Stokes solver at the next time step. It is important to remark that, although here applied only in 2D problems, the proposed approaches are easily applicable also to 3D flows.

In the following a brief description of the Navier-Stokes solver and of the Level-Set technique is given while further details can be found in Iafrati *et al.* (2001) and in Iafrati *et al.* (2000). The domain decomposition approach is applied to the wave system generated by a bump on the bottom of a channel and by a submerged hydrofoil. Comparisons with the full Navier-Stokes solution and with results obtained by a fully non linear boundary element solution are presented.

2 Two fluid Navier-Stokes solver

The flow of air and water is approximated as that of a single incompressible fluid whose density and viscosity change across the interface. In an Eulerian frame of reference, local fluid properties changes with time only due to the interface motion. If surface tension and turbulence effects are neglected, the dimensionless unsteady Navier-Stokes equations in generalized coordinates are:

$$\frac{\partial U_m}{\partial \xi_m} = 0 \tag{1}$$

$$\frac{\partial}{\partial t}(J^{-1}u_i) + \frac{\partial}{\partial \xi_m}(U_m u_i) = -\frac{1}{\varrho}\frac{\partial}{\partial \xi_m}\left(J^{-1}\frac{\partial \xi_m}{\partial x_i}p\right) - J^{-1}\frac{\delta_{i2}}{Fr^2} + \frac{1}{Re\,\varrho}\frac{\partial}{\partial \xi_m}\left(\mu G^{mn}\frac{\partial u_i}{\partial \xi_n}\right) \tag{2}$$

where u_i is the $i-$th cartesian velocity component and δ_{ij} is the Kronecker delta. The quantity

$$U_m = J^{-1}\frac{\partial \xi_m}{\partial x_j}u_j \tag{3}$$

is the volume flux normal to the ξ_m iso-surface and J^{-1} is the inverse of the Jacobian. In equation (2)

$$Fr = \frac{U_r}{\sqrt{gL_r}}\ ,\ Re = (U_r L_r \varrho_w)/\mu_w$$

are the Froude and Reynolds number, respectively. U_r,L_r are reference values for velocity and length while ϱ_w, μ_w are the values of density and dynamic viscosity in water and are used as reference values. The quantity

$$G^{mn} = J^{-1}\frac{\partial \xi_m}{\partial x_j}\frac{\partial \xi_n}{\partial x_j} \tag{4}$$

is the mesh skewness tensor.

The numerical solution of the Navier-Stokes equations is achieved through a finite difference solver on a non staggered grid. Cartesian velocities and pressure are defined at the cell centers whereas volume fluxes are defined at the mid point of the cell faces and are computed by using a quadratic upwind scheme (QUICK) to interpolate cartesian velocities.

The momentum equation is integrated in time with a semi-implicit scheme: convective terms and the off-diagonal part of the diffusive ones are computed explicitly with an Adam-Bashfort scheme while a Crank-Nicolson discretization is employed for the diagonal part of the diffusive terms. A fractional step approach

is used: an auxiliary velocity field is obtained by neglecting the pressure term on the right hand side of the momentum equation (*predictor step*) and in a second stage (*corrector step*) the velocity field is updated by adding a pressure correction contribution. The latter is obtained by enforcing continuity thus yielding to a Poisson equation which is solved by using a multigrid technique. When the velocity is assigned at the boundary of the computational domain, Neumann boundary conditions are obtained for the Poisson equation.

3 Free surface motion via Level-Set technique

In order to reconstruct the distribution of fluid properties in the computational domain, the actual location of the interface has to be captured. In the level-set technique fluid properties are assumed to be related to the signed normal distance from the interface $d(\boldsymbol{x}, t)$. At $t = 0$ this function is initialized assuming $d > 0$ in water, $d < 0$ in air and $d = 0$ at the interface (Sussman *et al.* 1994). The generic fluid property f is assumed to be $f(d) = f_w$ if $d > \delta$, $f(d) = f_a$ if $d < -\delta$ and

$$f(d) = (f_w + f_a)/2 + (f_w - f_a)/2 \ \sin(\pi d/(2\delta))$$

otherwise. In the above expression δ is the half width of a transition region introduced to smooth the jump in the fluid properties and it is chosen so that the jump covers at least four cells. During the evolution the distance is transported by the flow, thus the equation

$$\frac{\partial d}{\partial t} + \boldsymbol{u} \cdot \nabla d = 0 \qquad (5)$$

is integrated to update the distribution of the distance function. The interface being a material surface, its location is captured by reconstructing the level $d = 0$. In order to damp disturbances outgoing from the computational domain, a numerical beach model is introduced in the equation for the distance. Two beach regions are introduced close to the two boundaries of the computational domain. If $y = 0$ is the still water level, in the beach regions equation (5) takes the following form:

$$\frac{\partial d}{\partial t} = \boldsymbol{u} \cdot \nabla d - \nu(d + y) \qquad (6)$$

where ν is zero at the inner limits of the beaches and grows quadratically toward the boundaries of the computational domain. Results presented below are obtained by using $\nu = 2$ at the end of the domain.

To keep constant in time the width of the transition region the distribution of the distance function is periodically reinitialized by computing, at each cell center, the minimum distance from the interface. This point is found to be very important when using the level-set technique in conjunction with the domain decomposition approach. First attempts (Iafrati *et al.* 2000) exhibited an excessive damping of the produced following wave. The reason for this excessive damping has been found to be in the need to use a time step smaller than the maximum Δt allowed by the Courant constraint ($CFL = 1$). Indeed, when integrating the motion of the interface with a time step much smaller than that allowed by the condition $CFL = 1$, a decay of the accuracy occurs (Sussman & Puckett 2000). On the basis of the above consideration, the re-initialization of the distance function is carried out with a period equal to the time step given by the respect of the condition $CFL = 1$.

4 Domain decomposition

The whole fluid domain is subdivided in two regions: a free surface region and a body region (Fig. 1). In the former the method described in the previous sections is used. In the latter, a potential flow is assumed and a boundary integral representation for the velocity potential ϕ is adopted. Two procedures, differing by the way in which the information are exchanged between the two domains, are developed. According to this, depending on the type of coupling, an overlapping (matching region) of the two domains can exist.

To illustrate the matching procedures, the wavy flow induced by a bump on the bottom of a channel is considered. The bump, whose shape is described by the formula

$$y(x) = -1 + 0.1(1 - 8x^2 + 16x^4) \quad x \in (-0.5, 0.5),$$

suddenly starts with a constant velocity, $\boldsymbol{U}_\infty = (-1, 0)$, from the right to the left. In the results presented below it is assumed $Fr = 0.707$ and $Re = 10000$.

The wavy flow is studied in a frame of reference attached to the body (Fig. 1). The computational domain extends in the horizontal direction from $x = -14$ to $x = 14$ with the numerical beach model (6) used in $x \in (-14, -8)$ and in $x \in (8, 14)$. In the vertical direction the domain extends from the bottom at $y = -1$ up to $y = 0.4$. The extension of the matching region depends on the type of approach used to couple the two solutions.

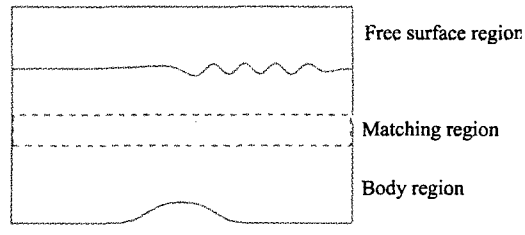

Figure 1: *Sketch of the zonal approach.*

With regard to the solution of the body region, Neumann boundary condition is applied on the body contour and at the inflow and outflow boundaries. Regardless of the type of coupling adopted, the solution of the body region provides the velocity field to be used as boundary condition on the bottom boundary of the free surface domain.

4.1 Dirichlet type

In this case the bottom boundary of the free surface region coincides with the upper boundary of the body region and panels coincide with the bottom face of the cells of the Navier-Stokes domain.

The Navier-Stokes solver provides the pressure and velocity distributions along the matching surface. Those are used within the unsteady Bernoulli's equation to update the distribution of velocity potential used as a Dirichlet boundary condition for the boundary element solution. The solution of the boundary integral problem provides the distribution of the velocity component normal to the matching surface, while the tangential component can be directly computed by the tangential derivative of the velocity potential along the matching surface.

4.2 Neumann type

For this type of coupling, an overlapping of the two domains is needed. In this case the panel distribution on the upper boundary of the body domain coincides with the bottom faces of the cell row $j = jo$ of the Navier-Stokes domain.

The solution of the Navier-Stokes equation provides the velocity distribution on the upper boundary of the body domain. This is used as a Neumann boundary condition for the boundary element solution. The latter gives back the distribution of the velocity potential all along the boundary, allowing the evaluation of the velocity field at any point inside the domain and in particular on the bottom boundary of the free surface region, where they are used as boundary condition for the Navier-Stokes solver at the next step.

5 Numerical results

To validate the domain decomposition and to compare the effectiveness of the two approaches, comparisons with the solution obtained by using the Navier-Stokes solver on the whole fluid domain (NS) are established. In applying the domain decomposition approach, the grid resolution employed in the free surface region is essentially the same of that used for the NS. Furthermore, to have a fair comparison, when using the Navier-Stokes solver in the whole fluid domain, a free-slip boundary condition is applied on the bottom of the channel.

In both the domain decomposition approaches the bottom boundary of the free surface region is located at $y = -0.35$. In the NT, the upper boundary of the body region is fifteen cells above ($jo = 15$, that is $y = -0.20$). A study of the dependence of the solution on the overlapping extension is performed.

A key issue of the unsteady domain decomposition is the control of the evolution of the boundary condition at the matching surface. To avoid that boundary conditions change too much from one step to another, the required time step is smaller than the maximum time step allowed by the stability limit $CFL = 1$. Results presented below are carried out at $\Delta t = 1/600$ while the stability limit would require, for the grid adopted, $\Delta t = 1/50$. Depencence of the solution on the time step is analysed.

In Fig. 2, the free surface profile at $t = 150$, obtained by the two different domain decomposition approaches and by the NS, are shown. In Fig. 3, the velocity components exchanged at the interface are compared with the corresponding values obtained by NS.

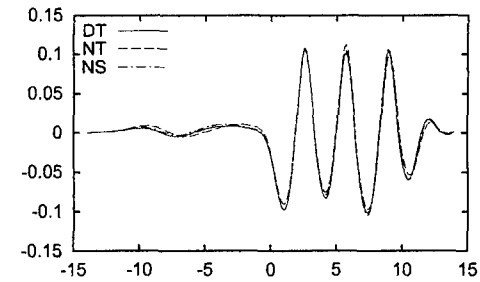

Figure 2: *Comparison between the DT and NT domain decomposition and the solution obtained by the Navier-Stokes solver throughout the fluid domain (NS).*

A very good agreement among the three solutions is observable, although the DT appears to perform slightly better.

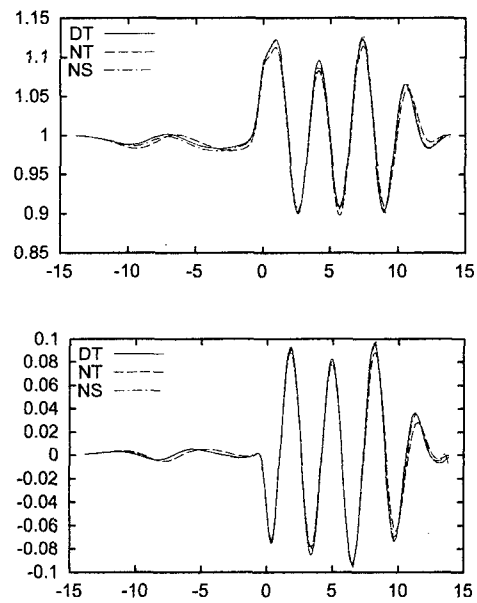

Figure 3: *Comparison of the u-velocity component* (top) *and v-velocity component* (bottom) *exchanged at the matching boundary.*

In Fig. 4, results obtained by using two different time steps are shown. The DT approach appears to be less sensitive to the time step. In Fig. 5, the effect of the width of the overlapping region in the NT approach is

shown. No substantial differences occur, provided the overlapping region is larger than ten cells (for $\Delta t = 1/600$).

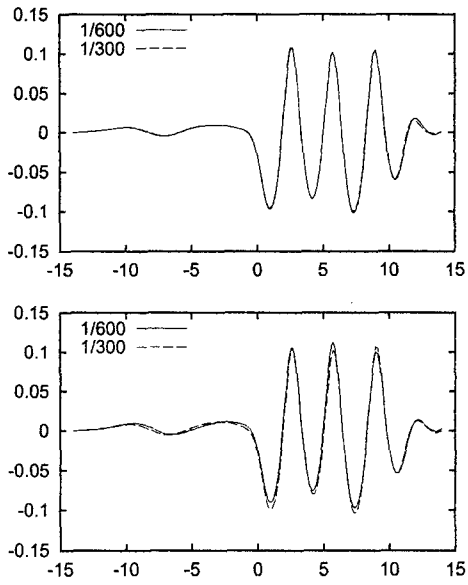

Figure 4: *Effect of the time step in the DT* (top) *and in the NT* (bottom) *approaches.*

As a case in which the advantages of using the domain decomposition are evident, the wavy flow generated by a submerged hydrofoil with an angle of attack is studied. Indeed, the use of a Navier-Stokes solver in the body region would require an important computational effort to correctly predict the flow about the hydrofoil, though one is much more interested in the free surface dynamics. This problem can be easily avoided by the domain decomposition approach described before, suitably modified by applying a Kutta condition at the trailing edge of the hydrofoil.

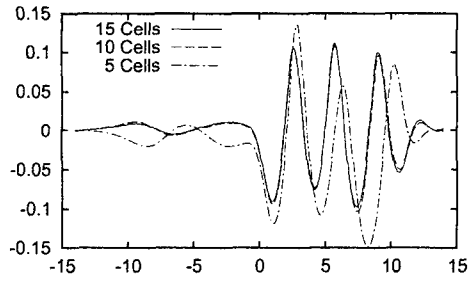

Figure 5: *Effect of the width of the overlapping region in the NT approach.*

The hydrofoil is a NACA 0012, 5 deg angle of attack and the submergence at the quarter of the chord is $y = -1.034$. The Froude number is $Fr = 0.567$ and the Reynolds number, based on the chord length, is $Re = 10000$. In Fig. 6, the wavy flow generated by the impulsive start of the hydrofoil is shown at $t = 11$ against the fully non linear boundary element solution (BEM) and the experimental data by Duncan (1983). Although numerical solutions have not yet reached a steady state, a good agreement is displayed by the domain decomposition approach.

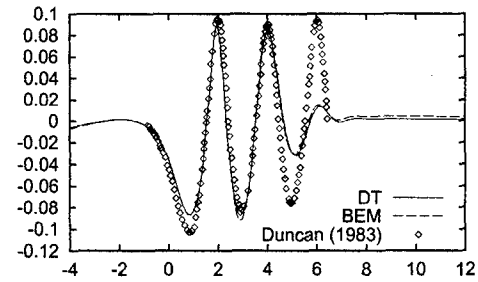

Figure 6: *Flow about a submerged hydrofoil: comparison with the fully non linear boundary element solution and the experimental results by Duncan (1983).*

Acknowledgments

This work was financially supported by the *Ministero Trasporti e Navigazione* in the frame of the INSEAN research plan 2000-02 and by the *Office of Naval Research*, under grant *N*.000140010344, through Dr. Pat Purtell. Authors also wish to thank Dr. D. Dommermuth for the useful discussions they had during his visit at INSEAN.

References

DUNCAN, J.: *The breaking and non - breaking wave resistance of a two-dimensional hydrofoil*, J. Fluid Mechanics, **126**, 507-520 (1983).

IAFRATI, A., DI MASCIO, A., CAMPANA, E.F.: *A level-set technique applied to unsteady free surface flows*, Int. Journal for Numerical Methods in Fluids, in press (2001).

IAFRATI, A., OLIVIERI, A., PISTANI, F., CAMPANA, E.F.: *Numerical and experimental study of wave breaking generated by a submerged hydrofoil*, Proc. 23rd ONR Symposium on Naval Hydrodynamics (2000).

SUSSMAN, M., SMEREKA, P., OSHER, S.J.: *A level set approach for computing solutions to incompressible two-phase flow*, Journal of Computational Physics, **114**, 146-159 (1994).

SUSSMAN, M., DOMMERMUTH, D.: *The numerical simulation of ship waves using cartesian grid methods*, Proc. 23rd ONR Symposium on Naval Hydrodynamics (2000).

SUSSMAN, M., PUCKETT, G.: *A coupled level-set and volume-of-fluid method for computing 3D and axisymmetric incompressible two-phase flows*, Journal of Computational Physics, **162**, 301-337 (2000).

TULIN, M., LANDRINI, M.: *Breaking waves in the ocean and around ships*, Proc. 23rd ONR Symposium on Naval Hydrodynamics (2000).

The bow wave of a vertical surface-piercing circular cylinder in a steady current

John CHAPLIN

Department of Civil & Environmental Engineering, Southampton University, UK

1. INTRODUCTION

The bow wave of a vertical surface-piercing cylinder in a steady current breaks at modest Froude numbers. A view of this flow is shown in figure 1, taken from experiments in which a 210mm diameter stainless steel cylinder was towed at constant speed through water initially at rest (Chaplin & Teigen, 2000). The bow wave is much like that of a blunt-bowed ship, where the resulting loss of momentum may represent a significant proportion of the wave resistance.

Figure 1 Flow upstream of a cylinder towed at Froude number $Fr = V/\sqrt{gd} = 1.64$, where V is the velocity and d the diameter, and Reynolds number $Re = Vd/\nu = 4.6\times10^5$

In the experiments, the wave resistance of the vertical cylinder was estimated from pressure measurements made at many points over its surface, and is plotted in figure 2 in the form of the equivalent loaded length ΔL. This is defined by

$$\text{(wave resistance)} = \Delta L \times \text{(drag per unit length far beneath the surface)}. \qquad (1)$$

The wave resistance increases rapidly once the Froude number has exceeded 0.5, and reaches a maximum at a Froude number of about 1. At the peak it is equivalent to the loading, at deeply submerged elevations, on a length of cylinder of about $0.8d$.

In working towards an understanding of these results, this paper is concerned with the problem of predicting the Froude number at which the bow wave of a vertical cylinder will first break. It is assumed that until this happens the flow upstream of the cylinder is represented reasonably well by potential flow analysis, even though in practice the downstream region will be dominated by the cylinder's wake.

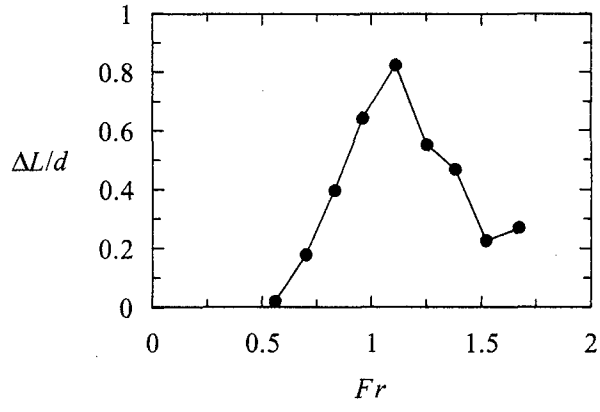

Figure 2. Wave resistance on a vertical surface-piercing cylinder expressed as the equivalent loaded length ΔL. $Re/Fr = 2.80 \times 10^5$.

In a reference frame (r, θ, z) fixed on the cylinder, the flow is steady. The origin is on the cylinder's axis at still water level; z is measured vertically upwards, and $\theta = 0$ is the direction of the incident flow. Velocities are normalised with respect to the incident velocity V, and lengths with respect to the cylinder's radius $d/2$. The free surface boundary conditions are

$$\eta = Fr^2(1 - v_r^2 - v_\theta^2 - v_z^2) \quad \text{and} \quad v_z = v_r \frac{\partial \eta}{\partial r} + v_\theta \frac{1}{r}\frac{\partial \eta}{\partial \theta} \,. \tag{2), (3)}$$

After describing an approximate model for the flow, a fully non-linear numerical solution is outlined, using the method of desingularised sources (Cao *et al.*, 1991). In the approach followed here, the boundary condition on the cylinder's surface is imposed by computing the three-dimensional image system associated with each source.

2. APPROXIMATE SOLUTION

As a first approximation, flow in any horizontal plane is assumed to be that corresponding to two-dimensional potential flow past a cylinder:

$$v_r = \cos\theta\,[1 - \frac{1}{r^2}] \,,\; v_\theta = -\sin\theta\,[1 + \frac{1}{r^2}] \,. \tag{4), (5)}$$

and v_z^2 is neglected in (2). The vertical velocity follows from (3), and the vertical acceleration of a particle is

$$\frac{dv_z}{dt} = v_r \frac{\partial v_z}{\partial r} + v_\theta \frac{1}{r}\frac{\partial v_z}{\partial \theta} = \frac{8Fr^4}{r^{10}}[-4 + 9r^2 - 4r^4 + (-3 + 8r^2 - 9r^4)\cos 2\theta + 3r^6 \cos 4\theta] \tag{6}$$

As the Froude number is increased, the expression on the right hand side of (6) first reaches a value of -1 (corresponding to a particle with a downwards acceleration of g) at a point on the surface of the cylinder $r = 1$, at 35.3° around from the stagnation point. This represent the conditions in which the water surface would first break, and occurs at a Froude number of 0.465.

3. FULLY NON-LINEAR SOLUTION

The fully non-linear solution for the steady bow wave flow uses a desingularised Eulerian approach, in which the velocity potential is represented partly by the sum of a large number of point sources distributed over the free surface. The sources are placed around the cylinder at regular radial and azimuthal intervals. As the solution develops, each source is moved vertically, maintaining a constant vertical offset from the free surface. A collocation point is placed on the free surface directly below each source.

At this point it would normally be necessary to introduce additional sources inside the cylinder to maintain its surface as a boundary. In two dimensions this problem can be solved explicitly by means of the circle theorem, but in three dimensions it is likely to involve the inclusion of a large number of extra sources and their corresponding collocation points. However, the aim of this work was to experiment with the idea of generating for each external source a three-dimensional image system which automatically preserves the boundary condition on the cylinder's surface.

The velocity potential of the three-dimensional image system associated with a single point source outside the cylinder can be constructed by using the method set out by Affes & Conlisk (1993) for the case of a cylinder in the neighbourhood of a vortex filament in free space. If ϕ_S is the potential due to the source, then the potential of the image system is

$$\phi_I = -\frac{1}{4\pi^2} \sum_{m=-\infty}^{\infty} e^{im\theta} \int_{-\infty}^{\infty} \frac{\partial \hat{\phi}_S}{\partial r}\bigg|_{r=1} \frac{K_m(|k|r)}{|k|K_m'(|k|)} e^{ikz}\, dz \tag{7}$$

where K_m is the modified Bessel function of order m, and $\hat{\phi}_S$ is the double Fourier transform of the source potential,

$$\hat{\phi}_S = \int_{-\infty}^{\infty} \int_{-\pi}^{\pi} \phi_S \exp(-ikz - im\theta)\, d\theta\, dz\,. \tag{8}$$

The transform in the z direction can be performed analytically to give

$$\frac{\partial \hat{\phi}_S}{\partial r}\bigg|_{r=1} = \int_{-\pi}^{\pi} e^{-im\theta} \frac{2k(R\cos\theta - 1)}{\sqrt{R^2 - 2R\cos\theta + 1}} K_1\left(k\sqrt{R^2 - 2R\cos\theta + 1}\right) d\theta \tag{9}$$

for a source of unit strength located at (R, 0, 0). The total velocity potential consists of the sum of the potentials due to the sources directly (making use of the symmetry of the flow about $\theta = 0$), the image systems of these sources, and the two-dimensional flow of which the velocity components are (4) and (5).

The solution proceeds iteratively, starting with a trial surface profile $\eta(r,\theta)$ obtained from (2), (4), (5), with $v_z = 0$. The source strengths are then obtained from the linear system (3), and each iteration is completed by updating the surface elevations from (2). Placing each source and collocation point on a fixed vertical line allows much of the computation involved in (7) to be carried out just once for a given mesh layout, and several of the subsequent operations can be done by using FFT routines.

Some results are shown in figure 3. At Fr = 0.36 and r = 1.2, only the vertical velocity differs markedly from the simple model. Since the computed vertical velocity is significantly reduced, it suggests that the critical Froude number will be rather greater than the figure of 0.465 mentioned above.

As described here the computational method for dealing with the boundary condition on the cylinder is not very efficient, since it requires more computer storage and time than the alternative of placing sources inside the cylinder. However, it does have some attractions, and there is scope for significant improvements.

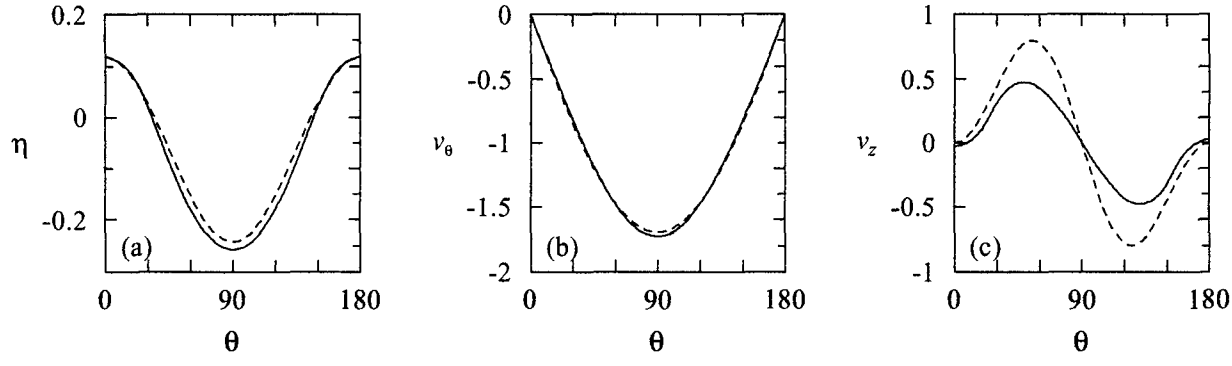

Figure 3. Approximate (broken line) and computed (continuous line) results at Fr = 0.36, and r = 1.2: (a) the water surface elevation; (b) the azimuthal velocity; (c) the vertical velocity. The upstream stagnation point is at $\theta = 180°$.

REFERENCES

AFFES, H., CONLISK, A. T.: *Model for rotor tip vortex-airframe interaction, Part 1, theory*, AIAA Journal, Vol. 31, Part 12, pp. 2263-2273 (1993).

CHAPLIN, J. R., TEIGEN, P.: *Drag on a vertical cylinder at a free surface*, Proc. of the IUTAM Symposium on Bluff Body Wakes and Vortex-Induced Vibrations, Marseille, June 2000.

CAO, Y., SCHULTZ, W. W., BECK, R. F.: *Three-dimensional desingularised boundary integral methods for potential problems*, International Journal for Numerical Methods in Fluids, Vol. 12, pp. 785--803 (1991).

Steady Free-Surface Flow in Water of Finite Depth

XIAO-BO CHEN[1] & RONG ZHAO[2]

[1]Bureau Veritas, DTA, 17bis, Place des Reflets, 92400 Courbevoie (France)
Fax: 33-1-4291.3395 Email: xiao-bo.chen@bureauveritas.com

[2]Marintek, Otto Nielsensv.10, PO Box 4125, N-7450 Trondheim (Norway)
Fax: 47-7359.5870 Email: rong.zhao@marintek.sintef.no

The steady free-surface potential flow generated by a source advancing at constant horizontal speed is considered by making use of the formulations developed by Chen & Nguyen (2000) in water of finite depth. Further to that work on the singular and highly-oscillatory properties of the steady free-surface potential near the track of the source located close to or at the free surface, another peculiar property is analyzed here. It is shown that the classical formulation suffers a non-uniformity when the waterdepth tends to infinity. A uniform formulation is then found by extracting the constant terms - one of them being infinity! Furthermore, the wave component of steady flow in subcritical and supercritical regimes is presented.

1. Green function of steady flow in water of finite depth

Under the reference system moving with the source at the speed U along the positive x-axis defined by its (x,y) plane coinciding with the mean free surface and z-axis oriented positively upward, the ship-motion Green functions $G(\vec{\xi},\vec{x}_s)$ representing the velocity potential of the flow created at a point $\vec{\xi}=(\xi,\eta,\zeta)$ by a steadily-advancing source of unit strength located at a point $\vec{x}_s=(x_s,y_s,z_s)$, can be expressed as

$$G = G^S + G^F \tag{1}$$

where G^F accounts for free-surface effects and G^S is defined in terms of simple singularities

$$4\pi\, G^S = \sum_{n=-\infty}^{\infty} (-1)^n \left\{ -1/\sqrt{r^2+(\zeta-z_s+2nh)^2} + 1/\sqrt{r^2+(\zeta+z_s+2nh)^2} \right\} \tag{2}$$

in which $r=\sqrt{(\xi-x_s)^2+(\eta-y_s)^2}$ and $h=H/L$ is the adimensional waterdepth with respect to the reference length L. The simple part G^S defined by (2) satisfies $G^S=0$ at the free surface ($\zeta=0$) and $\partial G^S/\partial\zeta=0$ at the sea bed ($\zeta=-h$). The free-surface part G^F in (1) is defined by a double integral representing the Fourier superposition of elementary waves

$$4\pi^2 G^F = \lim_{\epsilon\to+0} \int_{-\infty}^{\infty} d\beta \int_{-\infty}^{\infty} d\alpha \, \frac{A\, e^{-i(\alpha x+\beta y)}}{D+i\epsilon\Sigma_1} \tag{3}$$

with $(x,y)=(\xi-x_s,\eta-y_s)$ and A defined by

$$A = \cosh k(\zeta+h)\cosh k(z_s+h)/\cosh^2 kh \quad \text{with} \quad k=\sqrt{\alpha^2+\beta^2} \tag{4}$$

Furthermore, the dispersion function D in (3) is given by

$$D = F^2\alpha - k\tanh kh \tag{5}$$

in which $F=U/\sqrt{gL}$ is Froude number with g the acceleration of gravity. The function Σ_1 in (3) is given by $\Sigma_1=-\text{sign}(\alpha)$ and is significant in the region $D(\alpha,\beta)\approx 0$.

If we use the polar Fourier variables (k,θ), the equation (3) becomes

$$4\pi^2 G^F = \lim_{\epsilon\to+0} \int_{-\pi}^{\pi} d\theta \int_0^{\infty} dk \, \frac{A\, e^{-ik(x\cos\theta+y\sin\theta)}}{D/k - i\epsilon\,\text{sign}(\cos\theta)} \tag{6}$$

in which A is given by (4), and by using (5) D/k becomes :

$$D/k = k[F^2\cos^2\theta - \tanh(kh)/k] \tag{7}$$

Due to the symmetry properties of the dispersion function $D(k,\theta)$, it can be easily verified that the free-surface part of the Green function G^F given by (6) is symmetrical with respect to the axis $y=0$ and that its imaginary part is nil. The connection to the conventional form (eq.13.37 in Wehausen & Laitone, 1960) can be obtained by using the residue theorem and exploiting the symmetrical properties of the Fourier integral.

2. Non-uniformity of the Green function G^F

The free-surface component G^F is defined by the double Fourier integral (6) in which the amplitude function A and the dispersion function D are dependent on the waterdepth h as a parameter. It can be easily verified that the limit of the amplitude function $A(k,h)$ given by (4)

$$\lim_{k\to 0}\left\{\lim_{h\to\infty} A(k,h)\right\} = \lim_{h\to\infty}\left\{\lim_{k\to 0} A(k,h)\right\} = 1 \tag{8}$$

However, as far as the dispersion function $D(k,h)$ is concerned, we have from (7)

$$\lim_{k\to 0}\left\{\lim_{h\to\infty} D(k,h)\right\} = k(F^2 k\cos^2\theta - 1) = O(k) \tag{9a}$$

and

$$\lim_{h\to\infty}\left\{\lim_{k\to 0} D(k,h)\right\} = k^2(F^2\cos^2\theta - h) = O(-k^2 h) \tag{9b}$$

by using the development $\tanh(t) = t + O(t^3)$ as $t = kh \to 0$ in (7).

If the limit (9a) is used, we usually say that G^F given by (6) tends to the Green function in deep water. However, as the Fourier variable k is involved in the integral representation of G^F (6) and if the limit (9b) should be used, different values of G^F may be obtained since

$$\lim_{h\to\infty}\left\{\lim_{k=h^{-p}\to 0} D(k,h)\right\} = \begin{cases} 0 & p > 1/2 \\ -1 & p = 1/2 \\ -\infty & p < 1/2 \end{cases} \tag{10}$$

This non-uniform behavior of the dispersion function implies that the classical expression of the Green function G^F given by (6) may not be uniform in the limit of deep water, and that some undesirable terms such as constants may be embedded in (6). To identify them, we perform a local analysis of the Green function G^F corresponding to the Fourier integral in the region $k < \delta \ll 1$. We write

$$4\pi^2 G^F_\delta = \int_{-\pi}^{\pi} d\theta \int_0^{\delta} dk\, \frac{A_0}{D_0/k}\, e^{-ik(x\cos\theta + y\sin\theta)} \tag{11}$$

in which

$$A_0 = \left[A(k,h) + (e^{-k\sigma} - 1)\right]|_{k\to 0} = e^{-k\sigma}[1 + O(\delta^2)] \tag{12a}$$

with σ a positive real parameter and

$$D_0/k = D(k,h)/k|_{k\to 0} = k(F^2\cos^2\theta - h) + O(\delta^3) \tag{12b}$$

The parameter σ is introduced to facilitate the analysis as we will extend $\delta \to \infty$, and for the sake of numerical evaluation of the resultant integral. The value of σ is hoped to not affect on the results of the analysis. It will be shown that the undesirable terms are indeed independent of σ.

Introducing above expressions into (11), G^F_δ may be estimated as

$$\begin{aligned} 4\pi^2 G^F_0 = 4\pi^2 G^F_\delta|_{\delta\to\infty} &= \int_{-\pi}^{\pi} \frac{d\theta}{F^2\cos^2\theta - h} \lim_{\kappa\to 0}\int_{\kappa}^{\infty} dk\, \frac{e^{-k[\sigma + i(x\cos\theta + y\sin\theta)]}}{k} \\ &= \int_{-\pi}^{\pi} \frac{d\theta}{F^2\cos^2\theta - h} \lim_{\kappa\to 0} E_1\{\kappa[\sigma + i(x\cos\theta + y\sin\theta)]\} \end{aligned} \tag{13}$$

where $E_1\{\cdot\}$ is the exponential integral function defined in Abramowitz & Stegun (1967). At $\kappa \to 0$, the exponential integral function can be written

$$E_1\{\kappa[\sigma + i(x\cos\theta + y\sin\theta)]\} = -\log\kappa - \gamma - \log[\sigma + iR\cos(\theta - \phi)] + O(\kappa) \tag{14}$$

where $\gamma = 0.57721\ldots$ is Euler's constant, and (R,ϕ) defined as

$$R = \sqrt{x^2 + y^2} \quad \text{and} \quad \phi = \arctan(y/x)$$

Using (14) in (13), we have

$$4\pi^2 G^F_0 = C_\infty + C_0 + 4\pi^2 \tilde{G}^F_0 \tag{15}$$

with

$$C_\infty = \lim_{\kappa \to 0} \frac{2\pi \log \kappa}{h\sqrt{1-F^2/h}} \quad \text{for} \quad F/\sqrt{h} < 1 \quad ; \qquad C_\infty = 0 \quad \text{for} \quad F/\sqrt{h} > 1 \tag{16a}$$

$$C_0 = \frac{2\pi\gamma}{h\sqrt{1-F^2/h}} \quad \text{for} \quad F/\sqrt{h} < 1 \quad ; \qquad C_0 = 0 \quad \text{for} \quad F/\sqrt{h} > 1 \tag{16b}$$

$$4\pi^2 \tilde{G}_0^F = -\int_{-\pi}^{\pi} \frac{\log[\sigma + iR\cos(\theta-\phi)]}{F^2\cos^2\theta - h}\, d\theta \tag{16c}$$

Both C_∞ and C_0 are considered as constant since they are independent of the variables (ξ, η, ζ) and (x_s, y_s, z_s). They are zero in the supercritical regime ($F/\sqrt{h}>1$) but not in the subcritical regime ($F/\sqrt{h}<1$). Similar to the dispersion function analyzed in (10), the constant C_∞ at $F/\sqrt{h}<1$ given by (16a) is non-uniform and is equal to infinity if h is finite. The constant C_0 (16b) is finite and disappear in deep water while the term $\tilde{G}_0^F$ is represented by a single integral (16c).

3. Uniform formulation of the Green function

Further to the foregoing analysis, we may now define a uniform formulation of the Green function by simply subtracting the constant terms C_∞ and C_0 from the free-surface component G^F :

$$G = G^S + \bar{G}^F \quad \text{with} \quad \bar{G}^F = G^F - (C_\infty + C_0)/(4\pi^2) = \tilde{G}^F + \tilde{G}_0^F \tag{17}$$

with the new free-surface component $\bar{G}^F$ defined by

$$\tilde{G}^F = G^F - G_0^F = \lim_{\epsilon \to +0} \int_{-\pi}^{\pi} d\theta \int_0^\infty dk\, \mathcal{A}\, e^{-ik(x\cos\theta + y\sin\theta)} \tag{18}$$

with

$$\mathcal{A} = \frac{A}{D/k - i\epsilon\,\mathrm{sign}(\cos\theta)} - \frac{\exp(-k\sigma)}{k(F^2\cos^2\theta - h)} \tag{19}$$

It can be shown that $\mathcal{A} = O(1)$ at $k \to 0$ and has uniform limit for $h \to \infty$.

4. Wave component of the Green function

Following the analysis by Noblesse & Chen (1995), the free-surface part G^F can be decomposed as the sum of a wave component and a nonoscillatory component significant only in the near field. The wave component is defined by the single Fourier integral along the dispersion curves defined by the dispersion relation $D=0$

$$4\pi i\, G^W = \sum_{D=0} \int_{D=0} ds\, (\Sigma_1 + \Sigma_2) e^{-i(\alpha x + \beta y)} A/\|\nabla D\| \tag{20}$$

where $\sum_{D=0}$ means summation over all the dispersion curves and ds is a differential element of arc length of the dispersion curve. The function $\Sigma_1 = -\,\mathrm{sign}(\alpha)$ as already noted and the function Σ_2 is given by

$$\Sigma_2 = \mathrm{erf}(xD_\alpha + yD_\beta) \tag{21}$$

where $(D_\alpha, D_\beta) = (\partial D/\partial\alpha, \partial D/\partial\beta)$ and $\|\nabla D\| = \sqrt{D_\alpha^2 + D_\beta^2}$. The function $\mathrm{erf}\{\cdot\}$ in (21) is the usual error function defined in Abromowitz & Stegun (1967).

From (5), $D = 0$ defines two distinct curves in the left-half ($\alpha < 0$) and right-half ($\alpha > 0$) planes symmetrical with respect to $\alpha = 0$. Both dispersion curves are symmetrical with respect to $\beta = 0$ as well. The dispersion curves $k = k(\theta)$ for $0 \le \theta < \pi/2$ are depicted on Figure 1. The curves from right to left are associated with the value of $F/\sqrt{h} = (\mathbf{0}, 0.8, 0.9, 0.95, \mathbf{1}, 1.05, 1.1, 1.2, 2, 3, 5)$, respectively. It can be verified that the imaginary part of G^W given by (20) is nil due to the symmetrical properties of the dispersion curves, and the wave component G^W is depicted on Figures 2 and 3 for $F/\sqrt{h} = 0.95$ (subcritical regime) and 2.0 (supercritical regime), respectively.

References

[1] Abramowitz, M. & Stegun, I.A. (1967) Handbook of mathematical functions. *Dover Publications.*

[2] Wahausen J.V. & Laitone E.V. (1960) Surface waves. *Encyclopedia of Phisics*, Pringer-Verlag.

[3] Noblesse F. & Chen X.B. (1995) Decomposition of free-surface effects into wave and near-field components. *Ship Tech. Res.* 42, 167-185.

[4] Chen X.B. & Nguyen T. (2000) Ship-motion Green function in finite-depth water. *4th Intl Conf. on HydroDynamics*, Yokohama (Japan).

Figure 1: Dispersion curves depending on the values of $F/\sqrt{h}$

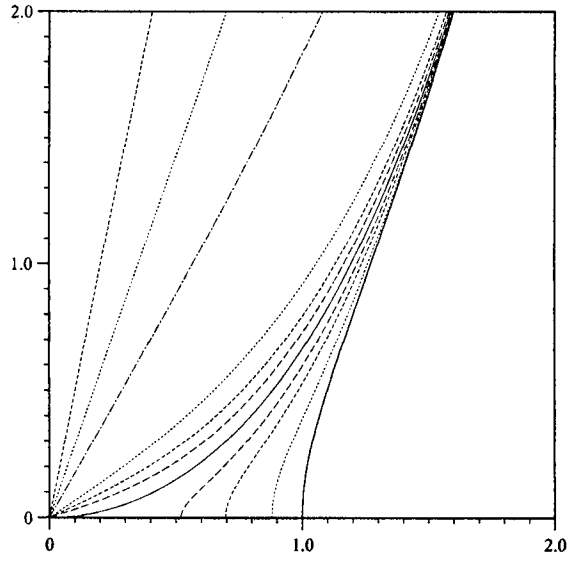

Figure 2: Wave component of the Green function at $F/\sqrt{h} = 0.95$ $(-10 \leq X \leq 2, -3 \leq Y \leq 3)$

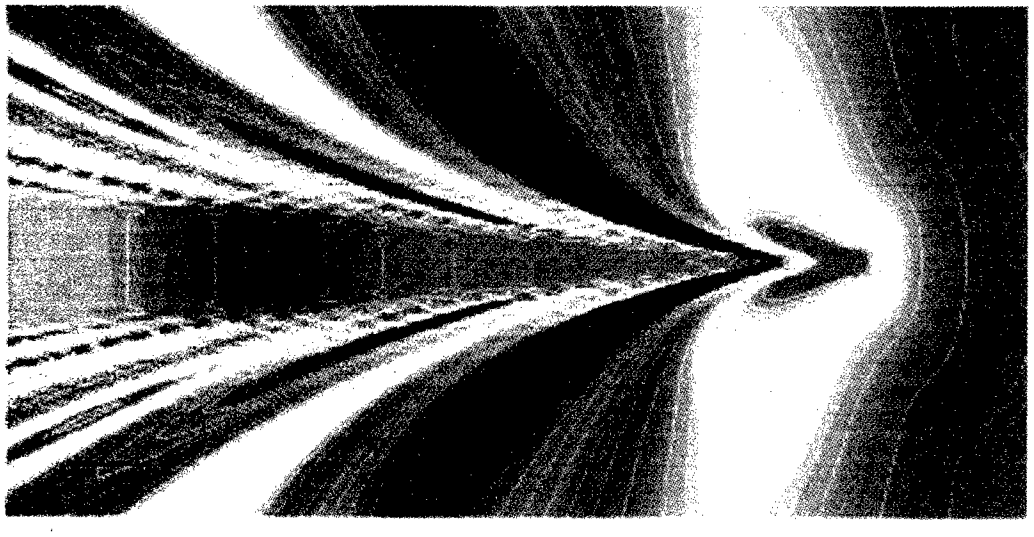

Figure 3: Wave component of the Green function at $F/\sqrt{h} = 2$ $(-10 \leq X \leq 2, -3 \leq Y \leq 3)$

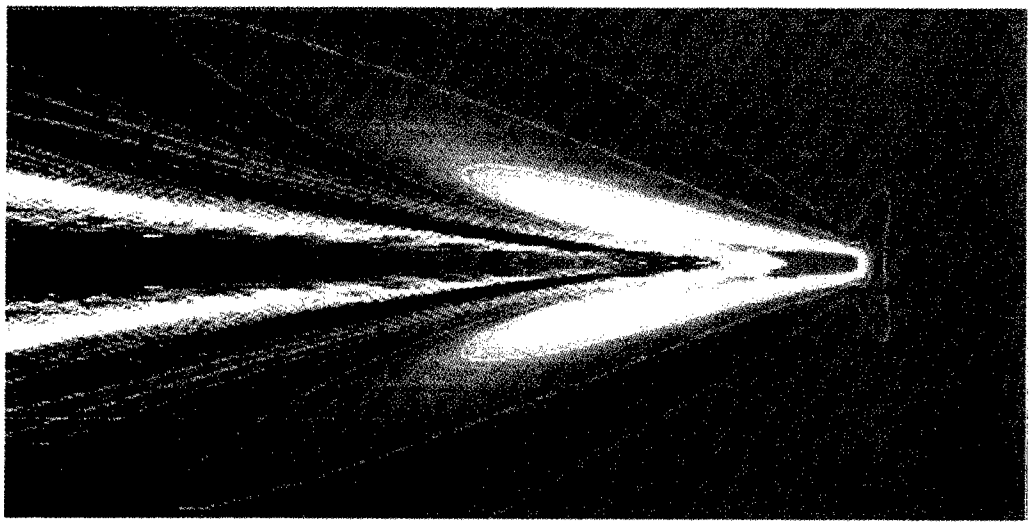

16th International Workshop on Water Waves and Floating Bodies
22-25 April 2001, AKI Grand Hotel, Hiroshima

Ship Entry into a Lock

Xue-Nong Chen
VBD - European Development Centre for Inland and Coastal Navigation
Duisburg, Germany

Som D. Sharma
Institute of Ship Technology
Mercator University, Duisburg, Germany

Abstract: The problem of ship entry into a very narrow lock is studied with attention to the interaction between the ship's motion and its waves. A one-dimensional unsteady hydraulic narrow-channel model for the flow coupled to the ship's motion in surge, heave and pitch is proposed and numerically implemented. The calculated ship motion is validated by comparison with model experiments carried out in the VBD shallow water tank by Zöllner and Broß (1993). As the ship begins to enter the lock it pushes a mass of water ahead so that a bore is generated. By way of reaction the ship experiences an impulse, decreasing its forward speed and increasing its trim and sinkage enormously. The accurate prediction of such motion is extremely relevant in practice. A movie animation is provided to illustrate this interesting phenomenon.

Introduction

The problem studied here concerns ship entry into a very narrow canal-lock. A typical example in Europe would be an inland ship of length $l = 110$ m, beam $b_m = 11.4$ m and draft $d_m = 2.5$ m moving at a speed of about 5 km/h into a rectangular canal-lock of length $L = 200$ m, breadth $B = 12$ m and water depth $h = 3$ m. We note in passing that this flow problem is analogous to that of a leaky piston pushing into a cylinder filled with a compressible fluid.

Before the ship reaches the lock it moves at a constant speed in a relatively wide lead-in canal. There it is in equilibrium since the net effective propeller thrust equals to the total hull resistance. Because of the low ship speed ($F_{nh} < 0.3$) the resistance is mainly frictional. As the ship-bow passes the lock-gate, it pushes a mass of water into the lock. Due to a piston effect, the free surface in the lock is at first greatly elevated and the resulting hump of water then slowly runs off through the narrow clearance between the ship and the lock. Owing to the inertia of water, the receding tendency goes on to form a depression in the lock. This process repeats itself becoming weaker and weaker in course of time. As a reaction the ship initially suffers a drastic deceleration, followed by decaying cycles of acceleration and deceleration.

An experimental investigation of this problem on model scale was carried out by Zöllner & Broß (1993) at the VBD in Duisburg. The motion recorded in the model experiments can be exploited to estimate the dominant effect. The average deceleration in the first phase amounts to 0.0025 g. The corresponding braking force is about 20 times larger than the steady frictional resistance according to the ITTC 1957 formula. This highlights the overwhelming importance of inertial effects in this phase.

Mathematical Model

Two coordinate systems are used: an earth-bound system $Oxyz$ and a system $\hat{O}\hat{x}\hat{y}\hat{z}$ moving horizontally with the ship. They are interrelated by

$$x = \hat{x} + \xi(t) - l/2, \quad y = \hat{y}, \quad z = \hat{z}, \quad t = \hat{t},$$

where l is the ship length and $\xi(t)$ is the distance covered in the lock (from the lock gate to the ship bow). The sinkage of the ship's center of gravity G is denoted by $s(t)$; the trim, by $\theta(t)$ (stern up positive). Therefore, its dynamic local cross-sectional area S_d under the undisturbed water level $z = 0$ can be derived from its static value S_0 as follows:

$$S_d(\hat{x},t) = S_0(\hat{x}) + b(\hat{x})[s(t) + (\hat{x} - \hat{x}_G)\theta(t)].$$

Here, only the strictly symmetric case is considered, i.e., a symmetric ship entering a symmetric lock along its centerline. Moreover, the problem is simplified to be one-dimensional, i.e., the free surface is $z=\zeta(x,t)$, the mean fluid velocity in x-direction is $u(x,t)$, and the dynamic local canal cross-sectional area filled with water is

$$A(x,t)=A_0(x)-S_d(\hat{x},t)+[B(x)-b(\hat{x})]\zeta(x,t)\,.$$

The flow is, therefore, modeled by the following mass-conservation and momentum equations:

$$\frac{\partial A}{\partial t}+\frac{\partial(uA)}{\partial x}=0 \tag{1}$$

$$\frac{\partial u}{\partial t}+\alpha_1\frac{U}{A}u-\alpha_2\frac{\partial^2 u}{\partial x^2}+u\frac{\partial u}{\partial x}+g\frac{\partial \zeta}{\partial x}=0 \tag{2}$$

and the pressure is given by

$$p=\rho g(\zeta-z). \tag{3}$$

The empirical α_1-term in Eq. (2) describes a mean local friction on the canal side-walls and the ship-hull surface; it has a dominant effect. The α_2-term represents a small viscous wave damping and may be neglected. Since by virtue of symmetry only three degrees of freedom (surge, heave and pitch) are involved, the relevant hydrodynamic forces and moment acting on the ship are generally expressed as

$$F_x=-\int_{S_w} pn_x dS\,,\quad F_z=-\int_{S_w} pn_z dS\,,\quad M_{\hat{y}G}=-\int_{S_w} p[\hat{z}n_x-(\hat{x}-\hat{x}_G)n_z]dS$$

and specially evaluated as

$$F_x=\rho g\int_{-l/2}^{l/2}\left\{\zeta\frac{d}{d\hat{x}}[S_0(\hat{x})+b(\hat{x})(s+\theta(\hat{x}-\hat{x}_G))]+\frac{\zeta^2}{2}\frac{db}{d\hat{x}}\right\}d\hat{x}$$

$$F_z=\rho g\int_{-l/2}^{l/2}[\zeta+s+\theta(\hat{x}-\hat{x}_G)]b(\hat{x})\,d\hat{x}$$

$$M_{\hat{y}G}=-\rho g\int_{-l/2}^{l/2}[\zeta+s+\theta(\hat{x}-\hat{x}_G)]b(\hat{x})(\hat{x}-\hat{x}_G)\,d\hat{x}.$$

The corresponding equations of motion are

$$m\frac{dU}{dt}=F_x+F_d\,,\qquad m\frac{dW}{dt}=F_z\,,\quad J_{\hat{y}\hat{y}G}\frac{d^2\theta}{dt^2}=M_{\hat{y}G}\,, \tag{4}$$

where

$$U=d\xi/dt,\quad W=-ds/dt,$$

and F_d is the excess of net effective propeller thrust over the hull frictional resistance. The thrust is assumed to remain constant throughout at its original equilibrium value before the ship reaches the gate. The frictional resistance is updated continuously using the ITTC 1957 formula with an empirical velocity-increase correction similar to Emerson's (1959).

Introducing static water-plane integrals

$$A_w = \int_{-l/2}^{l/2} b(\hat{x})d\hat{x}\,, \quad M_w = \int_{-l/2}^{l/2} (\hat{x}-\hat{x}_G)b(\hat{x})d\hat{x}\,, \quad I_w = \int_{-l/2}^{l/2} (\hat{x}-\hat{x}_G)^2 b(\hat{x})d\hat{x}$$

and dynamic auxiliary integrals

$$I_{sink}(t) = \int_{-l/2}^{l/2} \zeta(x,t)b(\hat{x})d\hat{x}, \qquad I_{trim}(t) = \int_{-l/2}^{l/2} (\hat{x}-\hat{x}_G)\zeta(x,t)b(\hat{x})d\hat{x},$$

the last two equations in Eq. (4) can be rendered in a compact form:

$$m\left(\frac{d^2 s}{dt^2} + \alpha_s \frac{ds}{dt}\right) + \rho g\left(A_w s + M_w \theta + I_{sink}\right) = 0 \tag{5}$$

$$J\left(\frac{d^2 \theta}{dt^2} + \alpha_t \frac{d\theta}{dt}\right) + \rho g\left(I_w \theta + M_w s + I_{trim}\right) = 0 \tag{6}$$

with $J = J_{\hat{y}\hat{y}G}$ for simplicity, and α_s and α_t as empirical damping coefficients for sinkage and trim, respectively.

Numerical Solution and Results

The coupled equations of motion of the fluid and the ship are solved simultaneously by an implicit finite difference method. Gourlay (1999) has given an analytic solution for the steady problem of a ship moving in an infinitely long narrow channel. We check our computer program by comparison with the analytic solution.

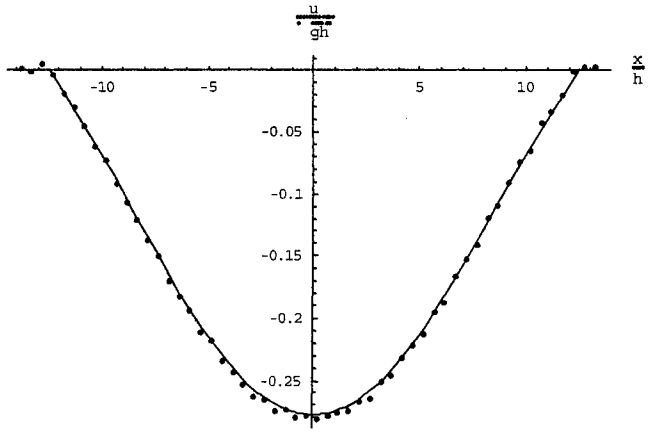

Fig. 1 Numerical and analytical results are represented by the dots and the line, respectively.

Fig. 1 shows a comparison of our numerical results with Gourlay's analytical solution for the velocity distribution along the ship's longitudinal axis for a Wigley hull of length 100 m , beam 11.4 m and draft 3 m at F_{nh} = 0.3 in a channel 12 m broad and 4 m deep. For simplicity, this comparison has been done for a captive hull (no sinkage or trim) and ignoring the empirical factors α_1 and α_2. Evidently, the agreement is satisfactory.

The problem of an inland ship entering a lock was investigated experimentally on model scale by Zöllner and Broß (1993) at VBD. One of their cases was chosen as the first example for our computations. The 1:16 ship model is VBD-M1343 and both horizontal and cross-sectional profiles of the lead-in canal are trapezoidal. The principal dimensions of the ship and lock were already cited in the Introduction. The ship speed is held at F_{nh} = 0.25 (about 5 km/h) as the ship approaches the lock. After the bow passes the lock gate the ship is free to surge.

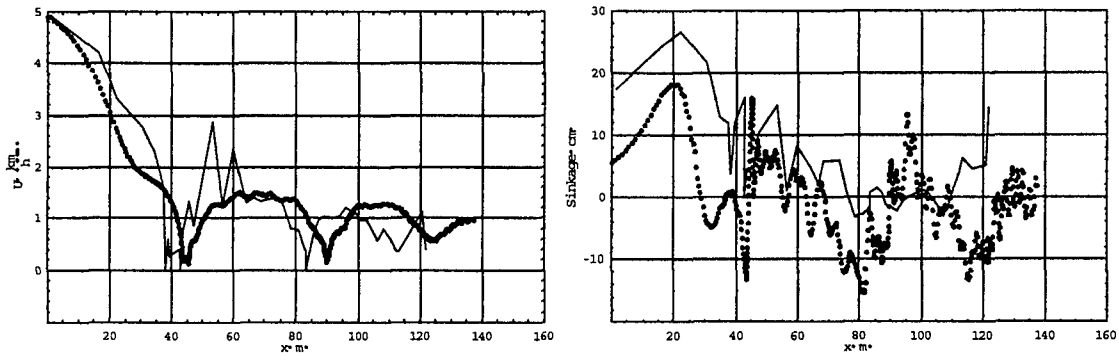

Fig. 2 Numerical and experimental speed and sinkage are represented by the dots and the lines, respectively.

Fig. 2 shows that the numerical computation captures the real unsteady forward motion of the ship with repeated deceleration and acceleration quite well. Even the two near-standstills are simulated with only a slight phase shift. (Note that with a higher initial speed or still larger blockage even aftward motion of the ship could occur temporarily.) On the other hand, the computed sinkage is mostly smaller than the measured one. A probable reason for this discrepancy is that our model does not take into account the propeller effect on the flow, which is further enhanced by the narrow lock. Fig. 3 shows three typical ship wave profiles in the lock at arbitrary instants.

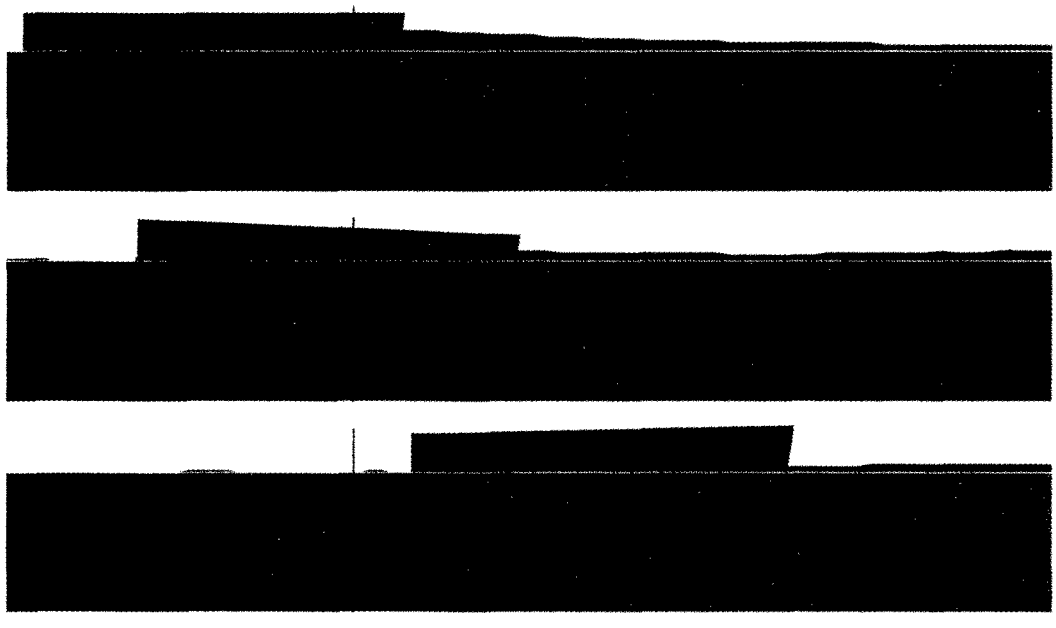

Fig. 3 Calculated ship wave profiles in the lock at three arbitrary instants.

References

Emerson, A. 1959 *Ship model size and tank boundary correction.* J. North East Coast Engineers 1959, Trans. North East Coast Institution of Engineers and Shipbuilders, 1959-60.

Gourlay, T. P. 1999 *The effect of squat on steady nonlinear hydraulic flow past a ship in a channel.* Schiffstechnik 46, No. 4, 217--222.

Zöllner, J. and Broß, H. 1993 *Einfluß der Bugformen von Binnenfahrzeugen auf das Einfahrverhalten in Schleusen.* VBD-Report 1338.

International Workshop on Water Waves and Floating Bodies, Hiroshima, 22-25 April 2001.

ON A FAST METHOD FOR SIMULATIONS OF STEEP WATER WAVES

Didier CLAMOND & John GRUE
Mechanics Division, Department of Mathematics, University of Oslo, Norway.

The dynamics of waves along the ocean surface plays an important role for safety of marine activity and operations. The waves determine the input parameters for dimensioning of oil-platforms and ships. Further, the waves determine the loads in tension-legs and risers connected to oil-platforms and floating production ships. The most common industrial analysis tools for waves at the sea surface (irregular waves) employ perturbation models, capturing nonlinear effects up to the second or the third order in wave steepness. Observations both in large scale and in laboratories reveal that weakly nonlinear methods have shortcomings in modelling moderately steep waves and the corresponding induced velocities and accelerations. Prominent examples are waves leading to ringing of offshore structures and highly nonlinear freak waves. Fully nonlinear methods which capture the weaknesses of weakly nonlinear methods have primarily been employed to study breaking waves. Here we focus an intermediate amplitude range, where perturbation models have poor performance, but the amplitudes are below those leading to breaking.

A common drawback of the existing fully nonlinear methods is that the computational schemes are slow. This means that long time simulations of wave-fields with appreciable size are unrealistic. While the integration of the prognostic equations can be made fast, the bottleneck is the solution of the Laplace equation which is required at each time step. Thus, a fully nonlinear model for water waves can only be fast provided that the Laplace equation solver is fast. Here the aim is to derive a rapid method for fully nonlinear non-overturning water waves. The formulation is two-dimensional, but the method may be extended also to the three-dimensional case. Making use of potential theory we introduce velocity potential and stream function (ϕ, ψ), and $(x,\ y,\ t)$ as horizontal, upward vertical and time variables, and let $\eta(x,t)$ be the surface elevation relative to the mean level $y=0$. In two dimensions we obtain ϕ and ψ by the Cauchy integral formula, split into real and imaginary parts, giving

$$\widetilde{\phi} = \frac{1}{\pi} \int_{-\infty}^{\infty} \frac{D\,(\widetilde{\phi}' - \eta_x' \widetilde{\psi}') - \widetilde{\psi}' - \eta_x' \widetilde{\phi}'}{1 + D^2} \frac{\mathrm{d}x'}{x' - x}, \tag{1}$$

$$\widetilde{\psi} = \frac{1}{\pi} \int_{-\infty}^{\infty} \frac{\widetilde{\phi}' - \eta_x' \widetilde{\psi}' + D\,(\widetilde{\psi}' + \eta_x' \widetilde{\phi}')}{1 + D^2} \frac{\mathrm{d}x'}{x' - x}, \tag{2}$$

where the 'tildes' denote the functions at $y=\eta$ and $\widetilde{\phi}=\widetilde{\phi}(x,t)$, $\widetilde{\phi}'=\widetilde{\phi}(x',t)$, etc. In (1)–(2) the function $D=(\eta'-\eta)/(x'-x)$ is introduced, where D decays according to $|x'-x|^{-1}$ for $|x'-x|\to\infty$ and $D\to\eta_x$ for $x'\to x$. The equation (2) is commonly used to determine $\widetilde{\psi}$, given $\widetilde{\phi}$ and η. $\widetilde{\psi}$ is then determined implicitly, and the equation is typically solved iteratively with

$\mathcal{O}(N^2)$ operations. This is the intensive part of the computations. An alternative, however, is to determine $\widetilde{\psi}$ from equation (1).

When the surface is horizontal, the integral equations are convolution products and can therefore be computed very quickly *via* Fast Fourier Transform. For a non-horizontal surface it is then tempting to reformulate the equation obtaining the form of convolutions. Splitting (1) into singular and regular integrals we obtain after one integration by parts

$$\begin{aligned}\widetilde{\phi} = &-\frac{1}{\pi}\fint_{-\infty}^{\infty}\frac{\widetilde{\psi}'}{x'-x}\,\mathrm{d}x' + \frac{1}{\pi}\int_{-\infty}^{\infty}\frac{\eta'\,\widetilde{\phi}'_x}{x'-x}\,\mathrm{d}x' - \frac{\eta}{\pi}\fint_{-\infty}^{\infty}\frac{\widetilde{\phi}'_x}{x'-x}\,\mathrm{d}x' \\ &+\frac{1}{\pi}\int_{-\infty}^{\infty}[\arctan(D)-D]\,\widetilde{\phi}'_x\,\mathrm{d}x' + \frac{1}{\pi}\int_{-\infty}^{\infty}\frac{D\,(D-\eta'_x)\,\widetilde{\psi}'}{1+D^2}\,\frac{\mathrm{d}x'}{x'-x}.\end{aligned} \tag{3}$$

Applying the Hilbert transform (i.e. $\mathcal{H}\{f\}\equiv\frac{1}{\pi}\int_{-\infty}^{\infty}\frac{f(x')}{x'-x}\,\mathrm{d}x'$), equation (3) becomes

$$\begin{aligned}\widetilde{\psi} = &\,\mathcal{H}\left\{\widetilde{\phi}\right\} + \eta\,\widetilde{\phi}_x + \mathcal{H}\left\{\eta\,\mathcal{H}\left\{\widetilde{\phi}_x\right\}\right\} \\ &-\mathcal{H}\left\{\frac{1}{\pi}\int_{-\infty}^{\infty}[\arctan(D)-D]\,\widetilde{\phi}'_x\,\mathrm{d}x' + \frac{1}{\pi}\int_{-\infty}^{\infty}\frac{D\,(D-\eta'_x)\,\widetilde{\psi}'}{1+D^2}\,\frac{\mathrm{d}x'}{x'-x}\right\}.\end{aligned} \tag{4}$$

This is another equation for $\widetilde{\psi}$. In (4), the singular integrals are convolutions and can thus be computed quickly. The remaining regular integrals have kernels that decrease rapidly, as $|x'-x|^{-3}$ and $|x'-x|^{-2}$, respectively. Therefore, integrations over $(-\infty,+\infty)$ can be approximated by integrations over a limited interval $(x-\lambda, x+\lambda)$. The parameter λ is choosen in accordance with the precision needed and depends on the wave characteristics and not on the length of the computational domain. Moreover, the contribution on the right hand side of (4) involving $\widetilde{\psi}$, is cubic in nonlinearity, while in equation (2) the corresponding term is quadratic. For nonbreaking waves, iterations with (4) thus converge faster than iterations with (2). The convergence is so fast that one iteration is enough for most of the practical computations (see below).

An iterative scheme is initialized by the explicit quadratic approximation

$$\widetilde{\psi}_1 = \mathcal{H}\left\{\widetilde{\phi}\right\} + \eta\,\widetilde{\phi}_x + \mathcal{H}\left\{\eta\,\mathcal{H}\left\{\widetilde{\phi}_x\right\}\right\}. \tag{5}$$

Applying one analytical iteration, neglecting integrals being of quartic nonlinearity, we get another approximation

$$\widetilde{\psi}_{2,\lambda} = \widetilde{\psi}_1 - \mathcal{H}\left\{\frac{1}{\pi}\int_{x-\lambda}^{x+\lambda}\frac{D\,(D-\eta'_x)\,\widetilde{\psi}'_1}{1+D^2}\,\frac{\mathrm{d}x'}{x'-x}\right\}. \tag{6}$$

The latter is explicit and does not involve transcendental functions. It is very accurate and quickly computable. Integration over one wavelength of steady periodic waves, with almost maximal slopes, cannot be distinguished from reference computations (fig. 1).

The formulation is also tested in unsteady simulations with the following method. The linear parts of the temporal evolution equations are solved analytically, while the remainding nonlinear parts are solved numerically with a variable step-size eight-order explicit Runge–Kutta scheme. A spectral method is used to compute the spacial derivatives, without smoothing or regridding. Evolution of a long wave packet, with initially small slope of the carrier wave ($ak_0 = 0.12$), is simulated. Very large waves — freak waves — are formed after some

while (fig. 2). The omitted term in (4) is quartic in nonlinearity with a small coefficient, and thus very small. This term may easily be included if needed. For most of the simulations it may be neglected. Therefore, the method is fully nonlinear in practice.

The method is $\mathcal{O}(N \log N)$ for practical computations, and thus very fast. Extensions include the three dimensional case and a finite (varying) fluid depth (Clamond & Grue 2001).

This work was conducted under the Strategic University Programme 'General Analysis of Realistic Ocean Waves' funded by the Research Council of Norway.

References

CLAMOND, D. & GRUE, J. 2001. A fast method for fully nonlinear water wave computations. Under consideration for publication in *J. Fluid Mech.*

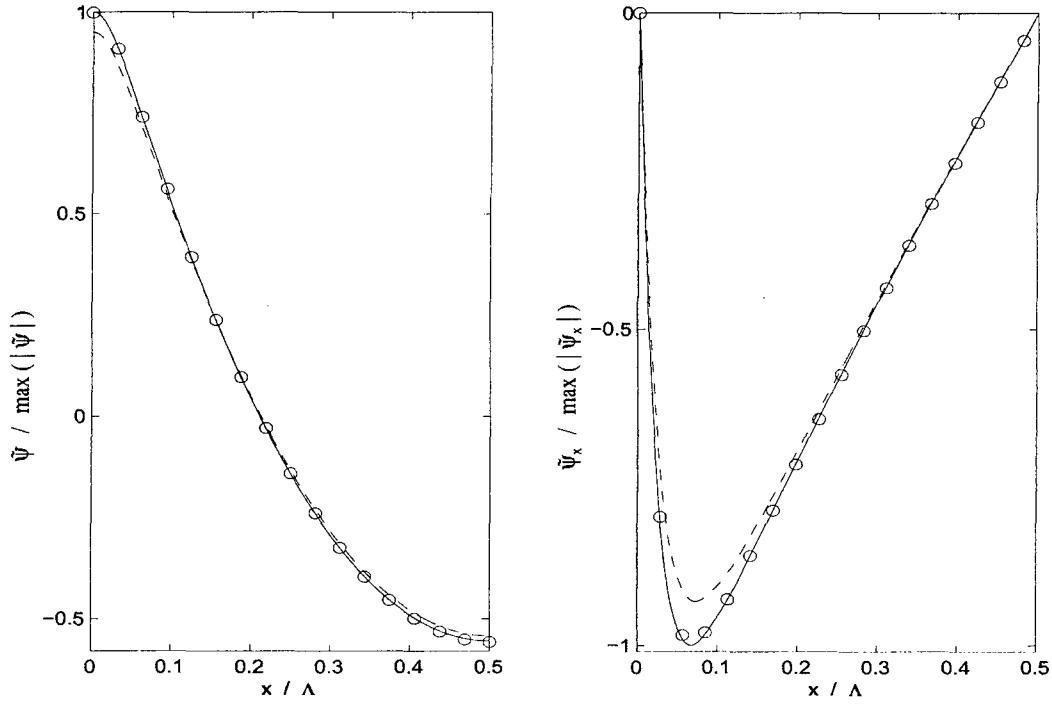

Figure 1: *Comparison of approximations for* $2\pi a/\Lambda = 0.41$ *(*Λ *wavelength).*

— exact, - - $\widetilde{\psi}_1$ (eq. 5), o $\widetilde{\psi}_{2,\lambda}$ (eq. 6 with $\lambda = \Lambda/2$).

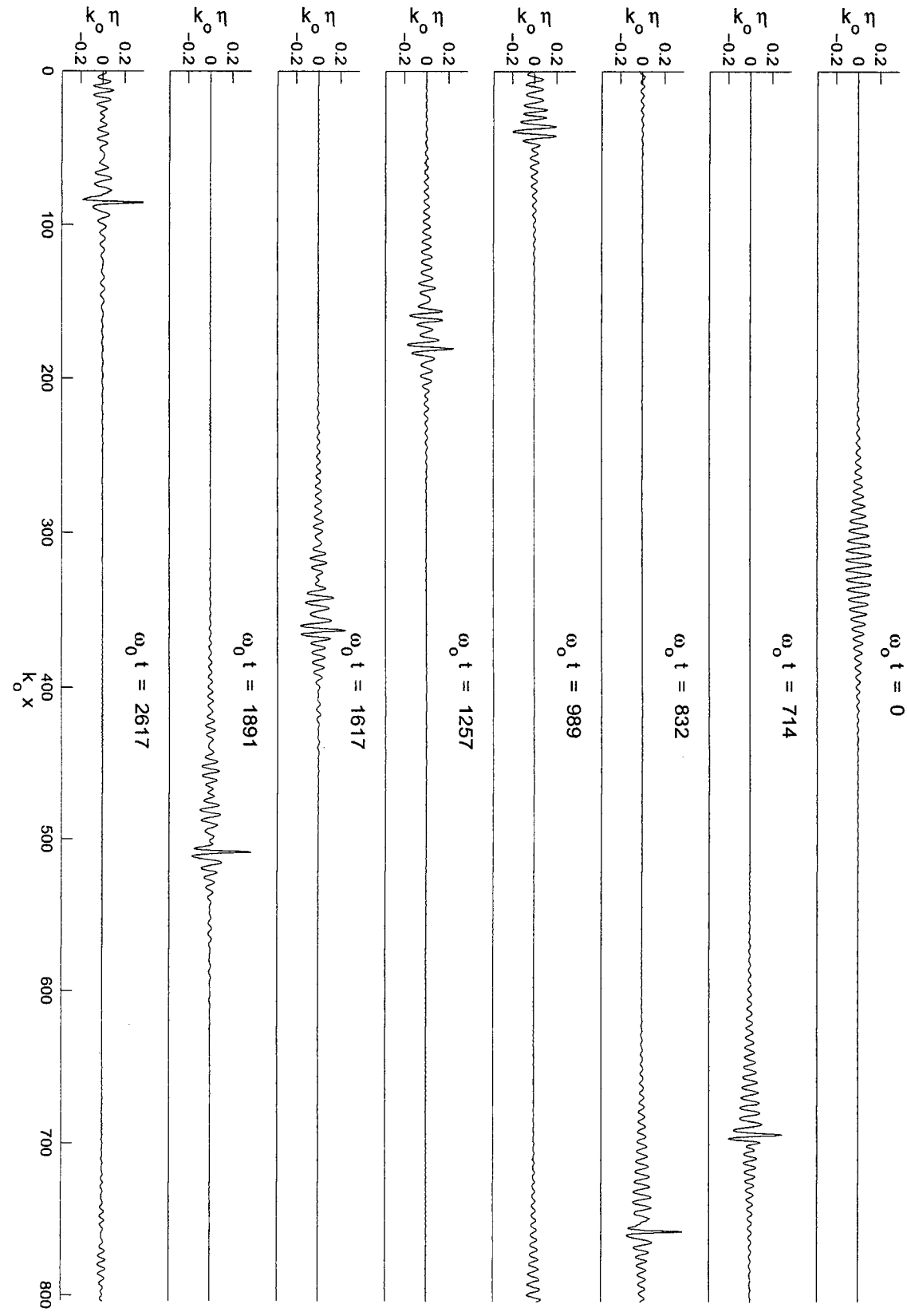

Figure 2: *Temporal evolution of a wave packet.*

Numerical Measurements of the Index of Wave Refraction through a Group of Vertical Cylinders

Alain H. CLÉMENT, Grégoire PIANET
Laboratoire de Mécanique des Fluides (CNRS UMR6598)
Ecole Centrale de Nantes - FRANCE

1 INTRODUCTION

The interaction of water waves with vertical cylinders has been investigated with special attention in our community those last years. Theses studies were mainly motivated by projects of very large floating structures, like airport, designed to be supported by a huge number of truncated vertical cylinders. When the cylinders are bottom standing, the velocity potential may be found by the semi analytical method of Linton and Evans (1989) [1]. This formulation was used to study some specific phenomenon linked to wave propagation in such regular pile network such as trapped mode [3]. Recently [2] P. McIver, applying the theory and results of solid-state physics to the propagation of water waves in such infinite network of cylinders, showed that the phenomenon of stopping band and passing band may occur also in this hydrodynamic context.

In the present study, the question was to determine if the equivalent of an index of refraction could be defined for the propagation of the water waves through an ocean area occupied by evenly spaced vertical piles when the number of cylinders increases while filling density is kept constant, like in fig.2.

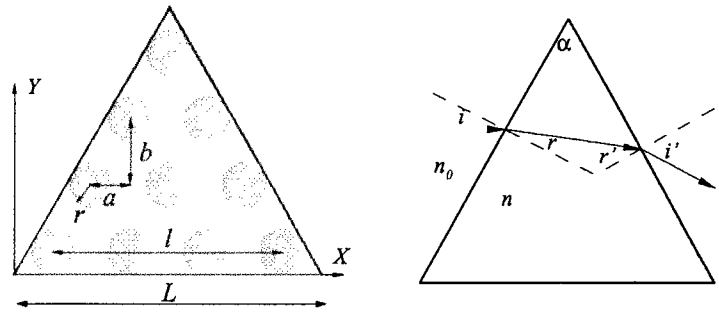

Figure 1: notations. *left*: cylinders filling a triangular area - *right*: refraction of a ray across a prism

To study this question, we have adopted an homogenization approach to the problem, as Evans & Shipway in [4], but using the ray theory of geometrical optics to define an experimental setup for the measurement of the index of refraction. We use the same classical experience as in the study of light propagation through a prism. It is well known that, if the prism medium has an index of refraction of says, n different from the index in the outer open ocean n_0, then the Snell-Descartes law states that:

$$\begin{cases} n_0 \sin i = n \sin r \\ n \sin r' = n_0 \sin i' \end{cases} \tag{1}$$

This law is usually expressed, in linear water wave refraction theory, using the wave celerity instead of the refraction index, reading: $(\sin i)/C_0 = (\sin r)/C$.

A prismatic area (i.e: a triangle view from the top fig.1), filled with cylinders of equal diameters, is exposed to an incident regular wave train described by the usual Airy potential. Two parameters may be used to describe the medium inside the prism: the density d (or *solidity factor* in [4]) which is the ratio of the total cross section area of the cylinders divided by the triangle surface, and the homogeneity factor h which will be defined here as the number of cylinders per unit surface.

Let L be the length of the base of the triangle, l the distance between the extreme circles centers on the base raw, a and b the horizontal and vertical distance between consecutive circles centers, r the radius of the circles (see fig.1). Let p denotes the number of cylinders on the base raw ($p = 4$ in fig.1), then N the total number of cylinders equals $N = \sum_{i=0}^{p-1}(i+1) = p(p+1)/2$. Choosing an equilateral triangle leads to the expression of the density $\sigma = 4\pi N r^2/\sqrt{3}L^2$, and the homogeneity factor $h = 4N/\sqrt{3}L^2$.

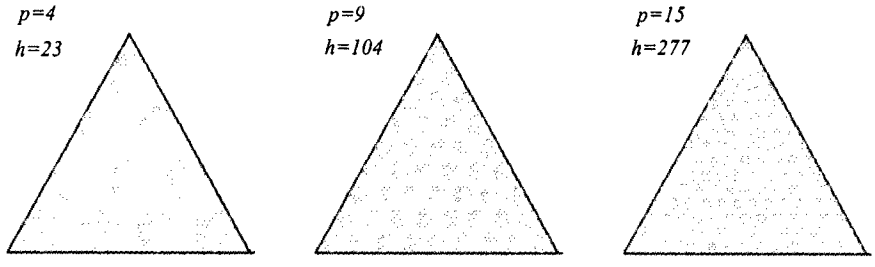

Figure 2: increasing the homogeneity factor h while keeping the density constant: $d = 0.5$

2 NUMERICAL EXPERIMENTS

The numerical experiments consists in first solving the above problem for the potential amplitude by the Linton-Evans method [1], and then by plotting and analyzing the downstream wave field in order to identify, when possible, a transmitted ray refracted of a certain angle to be measured. From this measured angle, the refraction index is derived through the Snell-Descartes law eq.(1).

The computation of the complex potential amplitude follows exactly the method described in [1]. The total potential is then given by

$$\phi = e^{i\kappa r\cos(\theta-\beta)} + \sum_{j=1}^{N}\sum_{n=-\infty}^{\infty} A_n^j Z_n H_n(\kappa r_j) e^{in\theta_j} \tag{2}$$

where we have kept the notations of the cited paper; H_n being the Hankel function of order n, and $Z_n = J_n'(\kappa a)/H_n'(\kappa a)$, with J_n the Bessel function of the first kind and order n. The coefficients A_n^j of the expansion (2) of the scattering potential are the solutions of the system

$$A_m^k + \sum_{j=1}^{N}\sum_{n=-M}^{M} A_n^j Z_n e^{i(n-m)\alpha_{jk}} H_{n-m}(\kappa R_{jk}) = -e^{i(\kappa x_k\cos\beta+\kappa y_k\sin\beta+m\frac{\pi}{2}-\beta)} \tag{3}$$

$$k = 1,\ldots,N \quad m = -M,\ldots,M$$

The first thing we did was to find a range of the parameters (density, homogeneity, wavelength,..) for which the phenomenon can be observed. It is not so evident, because due to other phenomena

like partial reflections, medium inhomogeneity, ..., at lot of rays emerge from the triangle, generating confuse refraction figures. Here, for $L = 1$, $d = 0.5$, $\beta = 0$ and $p = 15$, a large range of wavelengths was swept in order to find the best illustrative value. This occurs when the wavelength λ is approximately equal to the horizontal cylinders spacing a.

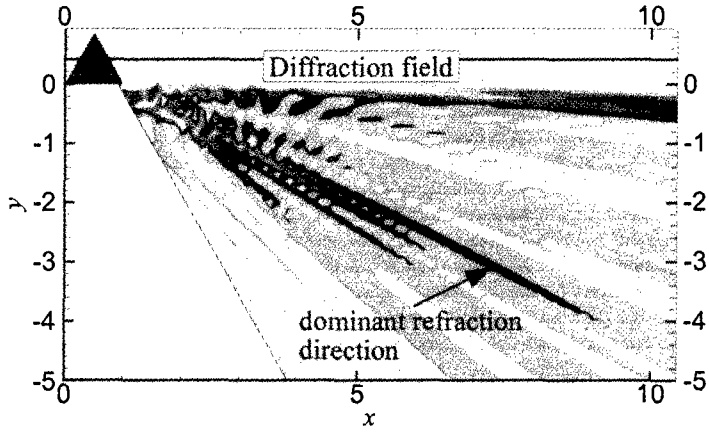

Figure 3: amplitude of the diffraction field showing the refracted ray direction $L = 1$, $d = 0.5$, $p = 15$, $\beta = 0$.

Measurements of the refraction angle are made directly on the plot of the wave field amplitude, in the quadrant where the ray must logically emerge. For the sake of legibility the scattering field is used for this analysis rather than the total wave field. An example of such a plot is given in fig.(3).

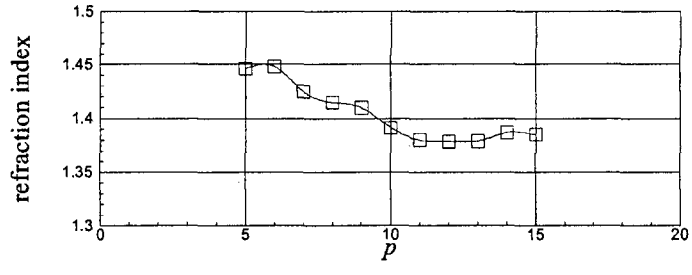

Figure 4: convergence with homogenisation

For this case, the measured refraction index was $n = 1.38$. The convergence to this value with increasing homogeneity is shown in figure (4) where the index is given as a function of the number p of cylinders on the base raw.

The next step was to investigate wether or not the observed phenomenon could be actually attributed to wave refraction. So, from the above case, we varied the incidence angle β and we checked the behavior of the refraction angle with regard to Snell-Descartes law eq.(1).Results obtained when varying the angle of incidence from -10 to 30 degrees are plotted in figure (5). The hydrodynamic results are in good agreement with the optical reference law; we can therefore conclude that the observed deviation phenomenon is most probably of refraction nature, in the common sense.

Finally, a comparison of our results was made with the continuum model proposed by Evans and Shipway at the last Workshop [4]. Their approach was based on an analogy of the equations of the 2D hydrodynamic problem with an acoustic model of the air flow in exchanger tube banks. Following their approach, the ratio between the wave velocity outside and the velocity inside the region filled by

cylinders, which is nothing but the refraction index as defined here, should be equal to $n = \sqrt{1+d^2}$. In order to compare our results with this proposal, we have performed a series of numerical experiments at zero incidence, with a fixed wavelength and a fixed homogeneity factor, and we varied the density in the range $[0, 0.5]$. Results are plotted in figure (6). Differences up to 20 percents are observed between these two approaches. It is difficult to conclude about these moderate discrepancies because on one side, our approach suffer from experimental uncertainties and numerical limitations of the number of cylinders, while the homogenisation technique used in the acoustical continuum model is based on several important assumptions.

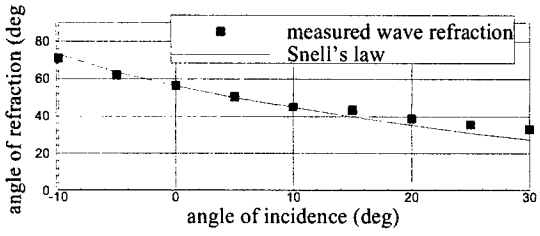

Figure 5: Hydrodynamical versus optical behaviour with varying incidence

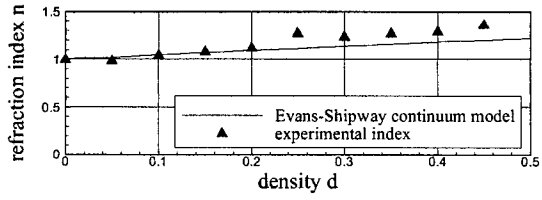

Figure 6: comparison with Evans-Shipway continuum model

3 CONCLUSION

We report here an attempt at verifying the homogenisation approach of wave propagation through an ocean area filled with vertical evenly spaced cylinders proposed by Evans and Shipway at the last Workshop [4]. The basic optical technique of light propagation across a prism is used as a model to analyse water wave propagation across a triangular zone of piles. First of all we had to localize the phenomenon in the whole parameters space; then, for cases where it was clearly observable, we verified that the deviation angle follows the Snell-Descartes law of refraction as expected. The convergence with the homogeneity factor has been tested for several cases, and the measured variation of the refraction index with the pile network density agrees reasonably well with the formula proposed by previous researchers. Nevertheless, it must be pointed out that the phenomenon appeared clearly only for few cases among all our attempts. In the other cases, many spurious rays made the refraction figure indecipherable, probably due to the isotropy of the network and the low level of homogenisation we used here, for computer time economy reasons. The Bragg scaterring phenomenon as described by McIver [2] in this application, could be also the source of unexplained results in some wavelength ranges.

References

[1] Linton, C.M., Evans, D.V. (1989). The interaction of waves with arrays of vertical circular cylinders. *J. Fluid Mech.*, vol215, pp.549-569.

[2] McIver, P. (2000). Water-Wave propagation through an infinite array of cylindrical structures. *J. Fluid Mech.*, vol.424, pp.101-125.

[3] Evans, D.V., Porter, R. (1997). Near-trapping of water waves by circular arrays of vertical cylinders. *Applied Ocean Research*, 19, pp.83-89.

[4] Evans, D.V., Shipway, B.B. (2000). A continuum model for multi-column structures in waves. in proc. 15th IWWWFB, Caesarea (Israel).

The Generation and Decay of Waves behind High-Speed Vessels

Lawrence J. Doctors
The University of New South Wales, Sydney, NSW 2052, Australia
Alexander H. Day
The University of Glasgow, Glasgow, G12 8QQ, Scotland

Summary

The inviscid linearized wave pattern generated by high-speed monohulls and catamarans is investigated theoretically with a particular view to determining the rate at which the maximal wave range on a longitudinal cut drops off with transverse offset from the track of the vessel. It is shown that the maximal wave range varies approximately with the offset raised to an exponent. The value of this exponent generally lies between -1.06 and -0.20, depending upon the speed of the vessel.

1 Introduction

The subject of the present investigation is the matter of the rate of decay of the waves generated by high-speed vessels. In the past, it has been suggested by some persons concerned with the damage caused by the waves behind river vessels, that the wave height varies with the inverse cube root of the transverse offset from the track of the vessel. This misconception presumably has its origins in a misunderstanding of the work of Wehausen and Laitone (1960, p. 487, Equation (13.42b)) and of Stoker (1966, p. 242, Equation (8.2.40)). Those equations are only applicable for the variation along the Kelvin angle in the linearized far-field wave system generated by a point source traveling in deep water.

This rate of decay has also been investigated by Day and Doctors (2000), with some emphasis being placed on an elementary tent-like element. In the current work, we shall investigate the effect of some fundamental parameters, such as the length of the vessel and the choice between monohull and catamaran.

2 Mathematical Formulation

The coordinate system and principal parameters defining the problem are shown in Figure 1(a). The vessel has a length L, a draft T, and the beam of the hull or demihull is B_1. The spacing between the demihulls, in the case of a catamaran, is s. The width of the river or the canal is w and the depth of the water is d. The density of the water is ρ, the acceleration due to gravity is g, and U is the speed of the vessel.

The formulas of Newman and Poole (1962) have been used to compute the wave resistance of the vessels. Regarding the wave elevation, one may consult the work of Tuck, Scullen, and Lazauskas (2000) and Doctors and Day (2000).

3 Computer Program

Advantage was taken of the obvious spatial recursion relationship between two corresponding terms in the summation for the wave elevation, for two points in the wave field. In this way, considerable computational effort was saved.

Calculations were extended to a distance of at least 30 fundamental wave lengths downstream of the vessel. It was also important to ensure that the downstream distance was sufficient in order to capture the relevant data for the longitudinal wave cuts with the greatest lateral offsets. At least 30 points were computed for each wave length.

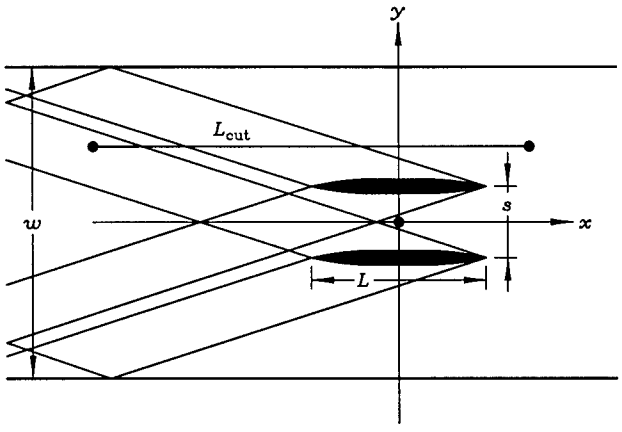

Figure 1: Definition of the Problem
(a) Coordinate System

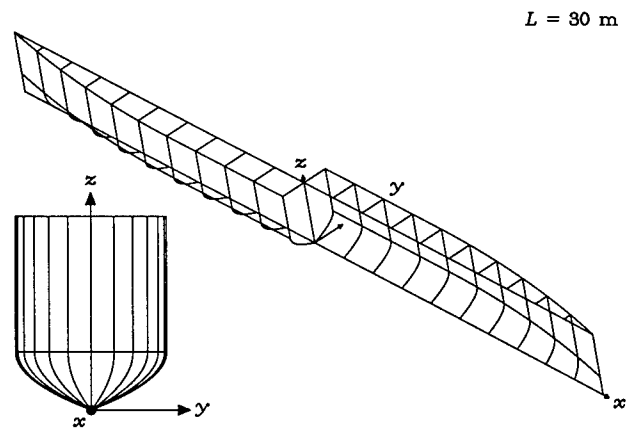

Figure 1: Definition of the Problem
(b) Modified Wigley Hull

In the case of deep water, it was found that the width of the canal could be chosen on the basis of the well-known Kelvin angle in order to avoid reflections from the side of the canal. Thus, in some cases, a width of up to 5000 m was chosen, in order to limit this source of error in the wave elevation to less than than 1 mm.

4 Test Vessels

A modified version of the hull defined by Wigley (1934) was used here to create a parent hull. The hull has parabolic section bilges and parabolic waterplane ends, as shown in Figure 1(b). The vessel has a variable amount L_1 of parallel middle body, which allows one to choose the prismatic coefficient. The vessel can also have a wall-sided region of draft T_1 near the waterplane.

All six of the vessels possess a displacement of 60 t and draft of 1.5 m in fresh water and have a maximal section coefficient of 0.8333. The three monohulls have a beam of 2.0 m. The three catamarans have a demihull beam of 1.0 m and a demihull spacing of 10.0 m. Overall vessel lengths of 24 m, 30 m, and 36 m were selected.

The analytic expressions for the wave functions for this vessel were presented by Doctors (1995).

5 Wave Resistance and Wave Elevation

The wave resistance for the three monohulls is plotted in Figure 2(a) and for the three catamarans in Figure 2(b). One should observe that selecting a series of vessels with the same effective wavemaking length $L_W = C_P L$ causes the humps and hollows of the curves to align horizontally. At the same time, the greater lengths lead to dramatic reductions in wave resistance.

The wave contours for a monohull are depicted in Figure 3(a). The different character of the wave pattern for the catamaran is noted in Figure 3(b).

6 Wave-Decay Curves

Four measures of the wave system were considered in this work. The "wave height", which is the greatest difference between a consecutive trough and a peak, is often used in practice to indicate the magnitude of the wave. For our principal measure, we shall use the "wave range" ζ_{range}. This is simply the difference between the highest and the lowest points in the wave cut.

Figure 4 shows the transverse decay of these wave measures for a monohull and for a catamaran. A curve of the type

$$\zeta/\zeta_1 = A(y/y_1)^N$$

has also been fitted; it is seen that the fit is excellent for these cases.

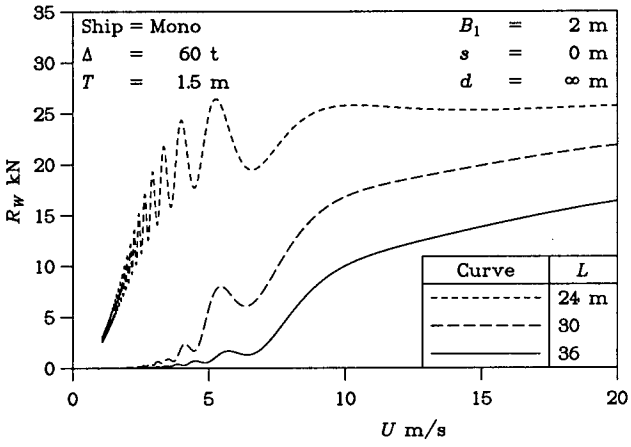

Figure 2: Wave Resistance
(a) Three Monohulls

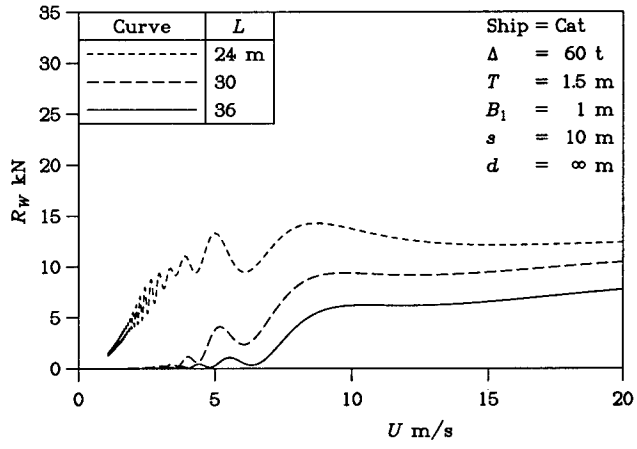

Figure 2: Wave Resistance
(b) Three Catamarans

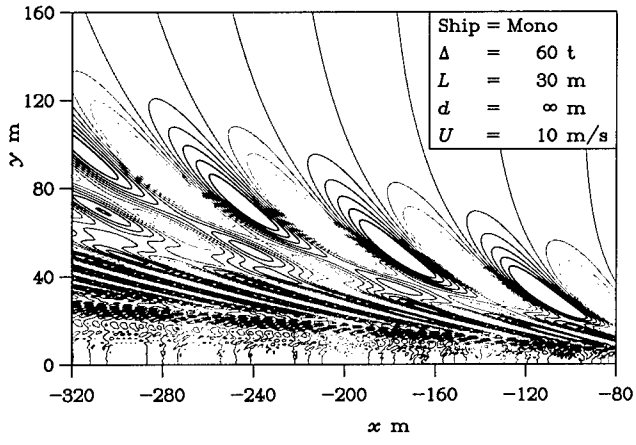

Figure 3: Wave Contours
(a) Monohull at a Speed of 10 m/s

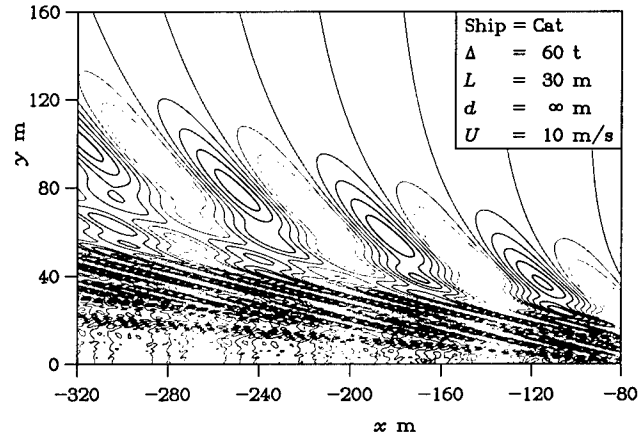

Figure 3: Wave Contours
(b) Catamaran at a Speed of 10 m/s

Finally, the "fitted" wave range ζ_1^* for all six vessels is shown in Figure 5(a). One can see, again, that the longer vessels always generate a lower wave range at the close cut where $y_1 = 100$ m, while catamarans generate smaller waves than monohulls do. This is particularly true at the lower speeds. The corresponding exponent N is shown in Figure 5(b). Here, it can be seen that a value of around -0.33 would actually be representative for speeds between 8.0 m/s and 13.0 m/s. However, a value of around -0.50 is certainly more applicable at the higher speeds. On the other hand, at some of the lower speeds, this exponent can reach values as low as -1.06.

7 Conclusions and Acknowledgments

Future work should include an extension of the numerical investigation to include the effects of finite depth. In this case, it will be necessary to take care regarding the spatial applicability of the simpler far-field wave elevation that was utilized.

The authors gratefully acknowledge the assistance of the Australian Research Council (ARC) Large Grant Scheme (via Grant Number A89917293).

8 References

DAY, A.H. AND DOCTORS, L.J.: "Rapid Estimation of Near- and Far-Field Wave Wake from Ships and Application to Hull-Form Design and Optimization", *J. Ship Research*, Accepted for publication, 28+ii pp (February 2000)

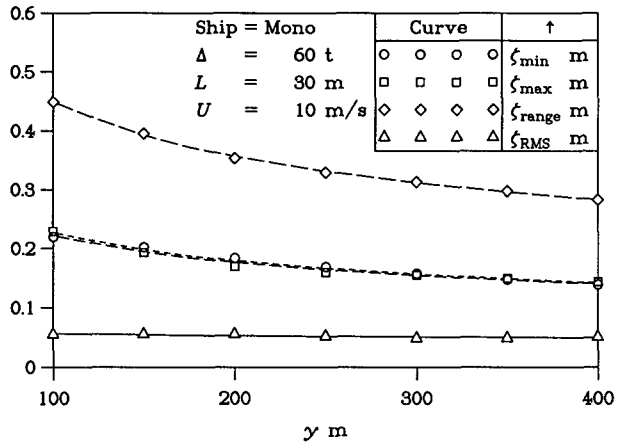

Figure 4: Curves of Wave Decay
(a) Monohull with a Length of 30 m

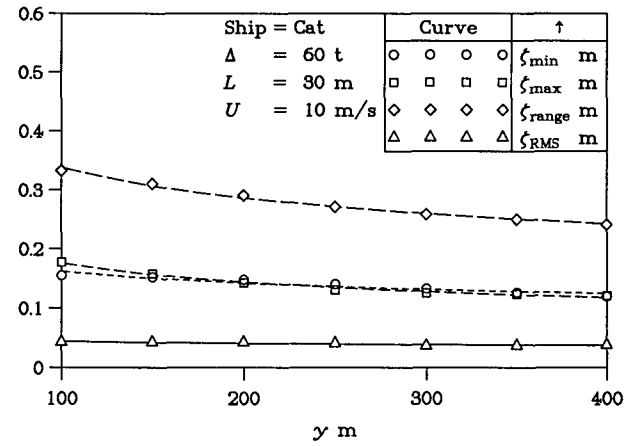

Figure 4: Curves of Wave Decay
(b) Catamaran with a Length of 30 m

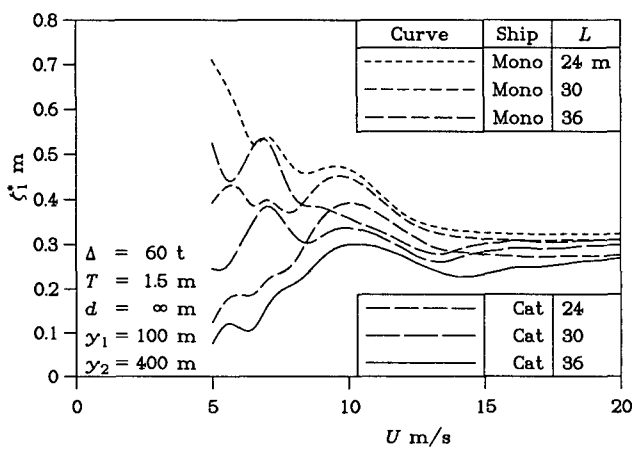

Figure 5: Decay Coefficients
(a) Magnitude of Range

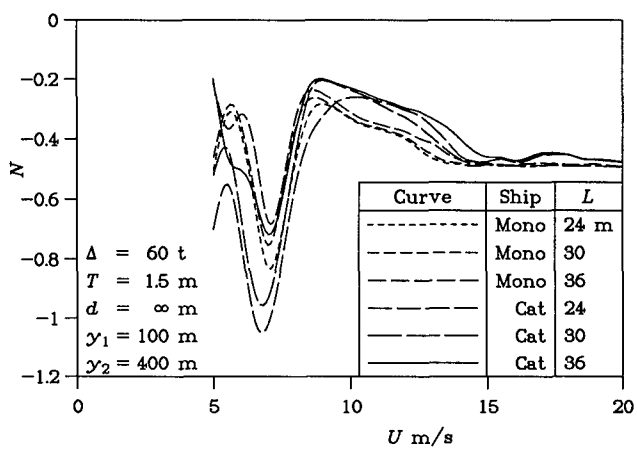

Figure 5: Decay Coefficients
(b) Decay Exponent

DOCTORS, L.J.: "A Practical Method of Prediction of Ship Resistance for Displacement Vessels", *Proc. Sixth International Symposium on Practical Design of Ships and Mobile Units (PRADS '95)*, Society of Naval Architects of Korea, Seoul, Korea, Vol. 1, pp 648–659 (September 1995)

DOCTORS, L.J. AND DAY, A.H.: "Wave-Free River-Based Air-Cushion Vehicles", *Proc. International Conference on Hydrodynamics of High-Speed Craft: Wake Wash and Motions Control*, Royal Institution of Naval Architects, London, England, pp 12.1–12.9 (November 2000)

NEWMAN, J.N. AND POOLE, F.A.P.: "The Wave Resistance of a Moving Pressure Distribution in a Canal", *Schiffstechnik*, Vol. 9, No. 45, pp 21–26 (1962)

STOKER, J.J.: *Water Waves*, Interscience Publishers, Inc., New York, 567+xxviii pp (1966)

TUCK, E.O., SCULLEN, D.C., AND LAZAUSKAS, L.: "Ship-Wave Patterns in the Spirit of Michell", *Proc. IUTAM Symposium on Free-Surface Flows*, Birmingham, England, 8 pp (July 2000)

WEHAUSEN, J.V. AND LAITONE, E.V.: "Surface Waves", *Encyclopedia of Physics: Fluid Dynamics III*, Ed. by S. Flügge, Springer-Verlag, Berlin, Vol. 9, pp 445–814 (1960)

WIGLEY, W.C.S.: "A Comparison of Experiment and Calculated Wave-Profiles and Wave-Resistances for a Form Having Parabolic Waterlines", *Proc. Royal Society of London*, Series A, Vol. 144, No. 851, pp 144–159 + 4 plates (March 1934)

Simulation of Sloshing Waves in a 3D Tank Based on a Pseudo-Spectral Method*

P. FERRANT & D. Le TOUZE

Division Hydrodynamique Navale/LMF, Ecole Centrale de Nantes, B.P.92101, 44321 Nantes Cedex 3

Abstract

Sloshing waves in a three dimensional tank are modelled using a pseudo spectral method based on fully non linear potential theory. The formulation is based on the expansion of the velocity potential in series of the natural modes of the tank geometry. Mode coefficients of the potential and nodal values of the free surface elevation are determined by accounting for the fully non linear kinematic and dynamic free surface conditions. The theoretical quasi-exponential convergence of the model with respect to the number of modes is verified in the case of free oscillations in a fixed 2D rectangular tank. Further results are given for 2D or 3D tanks submitted to forced motions. These results are found to be in very good agreement with available data.

Introduction

Spectral methods are characterized by the expansion of the solution in terms of global functions. When orthogonal functions are used, it can be shown that the approximation error decreases faster than algebraically. This behavior is referred to as exponential, or spectral convergence. The counterpart of this attractive feature is mainly found in the limitation to simple domains. However, their computational performances are such that spectral methods are prevailing for large scale computations in certain areas of fluid dynamics. This is for example the case in numerical weather forecast. For a review of the application of spectral methods in general computational fluid dynamics, see Hussaini & Zang (1987), or Fornberg (1995). In applications to free surface inviscid flows, it is possible to use orthogonal functions satisfying Laplace's equation, so that coefficients of the spectral expansions are determined through the free surface conditions only. Fenton & Rienecker (1982) solved nonlinear 2D wave propagation problems using spectral expansions both for the potential and the free surface elevation, under the assumption of space periodicity. In Dommermuth & Yue (1987) , three dimensional wave problems were simulated using a spectral method based on a perturbation expansion of free surface conditions. In Kim *et al* (1998) , fully non linear simulations in 2D rectangular tanks of infinite depth were reported. In Chern *et al* (1999), a spectral method based on Chebyshev polynomials was applied for solving fully nonlinear 2D free surface problems in a rectangular 2D tank, with the advantage of a fixed computational domain obtained by applying a time-depending σ-transform to the vertical co-ordinate. In the present paper, a spectral approach is applied to fully non linear sloshing waves in 2D or 3D rectangular tanks, using the natural modes of the fluid domain as a basis for the spectral expansion, and solving the boundary value problem in the physical space.

Mathematical Formulation and Numerical Solution

We consider a three dimensional tank, partially filled with an inviscid fluid. A cartesian fixed co-ordinate system $Oxyz$ is defined. Assuming potential flow, a problem for a scalar velocity potential Φ is set up. The potential has to satisfy Laplace's equation in the fluid domain, as well as Neumann conditions on the tank walls and bottom:

$$\Delta\Phi(M,t) = 0 \quad M \in D \tag{1}$$

*Abstract proposed for presentation at the 16th Workshop on Water Waves and Floating Bodies, Hiroshima, Japan, April 2001.

$$\frac{\partial \Phi}{\partial n} = U.n \quad on\ solid\ boundaries \tag{2}$$

In the present formulation, we suppose a single-valued free surface F, represented by $z = \eta(x,y,t)$. The kinematic and dynamic conditions at the free surface are thus formulated as follows (with implicit non-dimensionalization with respect to the mean water depth h and the acceleration of gravity g):

$$\frac{\partial \eta(x,y,t)}{\partial t} = \frac{\partial \Phi}{\partial z} - \frac{\partial \Phi}{\partial x}\frac{\partial \eta}{\partial x} - \frac{\partial \Phi}{\partial x}\frac{\partial \eta}{\partial x} \ ; \ M(x,y,z,t) \in F \tag{3}$$

$$\frac{\partial \Phi(M,t)}{\partial t} = -z - \frac{1}{2}|\vec{\nabla}\Phi|^2 \ ; \ M(x,y,z,t) \in F \tag{4}$$

Then, we introduce a spectral expansion of Φ in series of natural modes of the tank:

$$\Phi(x,y,z,t) = \sum_{m=0}^{\infty}\sum_{n=0}^{\infty} a_{mn}(t)\Psi_{mn}(x,y,z) \tag{5}$$

where Ψ_{mn} are eigen functions of the fluid domain, satisfying equations (1) and (2), and a_{mn} are time depending modal amplitudes. Here we consider a parallelepipedic tank, for which eigen functions are given by:

$$\Psi_{mn}(x,y,z) = \frac{cosh(k_{mn}(z+1))}{cosh(k_{mn})} cos(\overrightarrow{k_{mn}}\,\vec{x}) \tag{6}$$

where $\vec{x} = (x,y)$ and $\overrightarrow{k_{mn}} = (m\pi/L_x, n\pi/L_n)$ is the wave number associated to each mode.

After truncation of the spectral expansion, equation (5) is fed in the dynamic free surface condition:

$$\sum_{m=0}^{N_x}\sum_{n=0}^{N_y} \frac{da_{mn}(t)}{dt}\Psi_{mn}(x,y,\eta) = -\eta(x,y,t) - \frac{1}{2}|\vec{\nabla}\Phi(x,y,\eta,t)|^2 \tag{7}$$

In the solution of wave propagation problems using a spectral approach, the assumption of space periodicity may be introduced to further expand the free surface elevation in spectral Fourier series [3]. Here for fully non linear sloshing problems, the free surface elevation cannot a priori be expanded in Fourier series of horizontal co-ordinates. Thus $\eta(x,y,t)$ is represented by its nodal values at free surface collocation points, on which free surface conditions are imposed.

Starting from given initial conditions, the initial boundary value problem is thus solved for N_Φ modal amplitudes of the potential and N_η nodal values of the free surface elevation. A standard 4th order Runge-Kutta scheme is applied for advancing the solution in time, by integrating the free surface conditions as ODE for a_{ij} and η_k.

The system of first order differential equations for a_{ij} is obtained at each substep of the time marching procedure by solving a system of linear algebraic equations resulting from the application of the dynamic condition (7) at a sufficient number of collocation points on the free surface. This is in contrast with other schemes for inviscid free surface flows in which nodal potential values are updating by directly applying the dynamic condition. Derivatives of the potential appearing at the right-hand sides of the FSC's are computed from the spectral expansions, while finite difference formulas are applied for the derivatives of the wave elevation.

When the problem is solved on the basis of a perturbation expansion procedure, see e.g. [4], the resulting time-invariant kernel is the same at each order of the expansion, and a FFT procedure can be applied, with a $O(N_\Phi Log(N_\Phi))$ effort at each time step. In the present fully nonlinear scheme, the kernel of the linear system formed of values of $\Psi_{mn}(x,y,\eta)$ is solution-dependent and has to be reevaluated at each sub-step. A preconditioned GMRES iterative solver is applied for solution of linear systems. The resulting cost is $O(N_\Phi^2)$ for a well-conditioned system, i.e. when the number of iterations at convergence is only weakly dependent on the size of the problem. The other significant part of the computational effort is devoted to the assembly of the kernel and to the computation of potential derivatives, thus the global effort is also $O(N_\Phi^2)$.

Numerical Results

2D free motion

In this section we consider a 2D tank, with initial conditions $\eta(x,y,0) = \eta_0(x,y)$ and $\Phi(x,y,z,0) = 0$. The fluid is initially at rest, and the initial free surface profile corresponds to the first linearized eigen

mode, with an initial steepness $(\eta_{max} - \eta_{min})/Lx = 10\%$. The tank length is $L_x/h = 2$. This simple test case aimed at a verification of the convergence properties of the scheme. Free motion simulations over 7 dominant periods were repeated with increasing number of modes and free surface nodes: $N_\Phi = N_\eta =$ 11, 21, 31, 41, 51, 61, 71 . The maximum difference between the instantaneous fluid energy and the initial (potential) energy has been computed in each case. Results are plotted in figure 1. The expected spectral convergence is obtained, with a max relative error of 10^{-4} on the energy with 71 modes. The error on the fluid volume is about 10^{-7}, and does not vary significantly with N_Φ. Free surface profiles corresponding at each successive maxima of the free surface elevation are collected in figure 2.

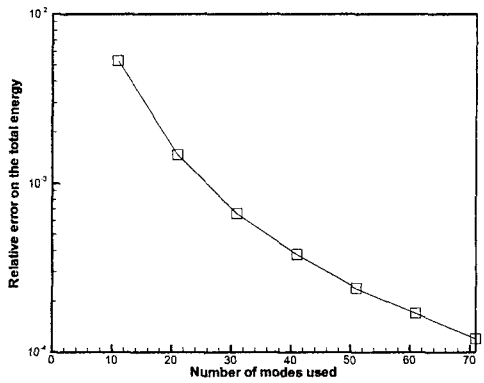

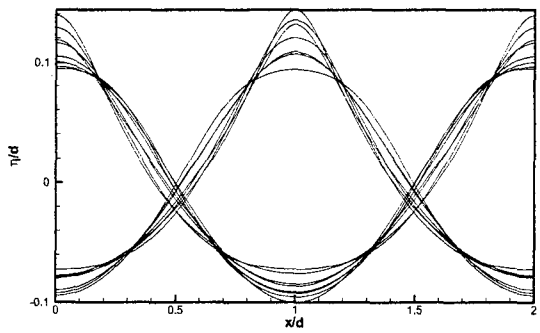

***Figure 1** (left): Convergence of the relative energy error with respect to number of modes*
***Figure 2** (right): Successive extrema of the free surface profile*

2D forced motions

Here we consider a 2D tank with fluid initially at rest, submitted to a forced motion $x(t) = a\,sin(\omega t)$. The problem formulation is modified to account for the moving co-ordinate system, following closely the approach of Wu *et al* (1998), in which nonlinear sloshing problems are solved using a finite element method. The tank length is $L_x/h = 25.$, a very shallow water case, for which strong nonlinear effects are anticipated. The reduced motion amplitude is $a/h = 2.5$. The angular frequency is $\omega = 0.9973\omega_0$, where ω_O is the frequency of the first linearized natural mode. This is just a case presented in [7]. The simulation has been run with 40 modes . Figure 3 below is the equivalent of figure 9 in [7], plotted with the results of our spectral model. A bore is formed at the end of the simulation (figure 3-b). Results from both approaches seem very similar up to the formation of the bore, at about $t = 26.$ (figure 3-a). Then results differ slightly. With the present spectral method, a steeper wave front followed by very short waves are exhibited. However, no convergence tests have been performed to date on this case. Such tests will be available for presentation at the workshop.

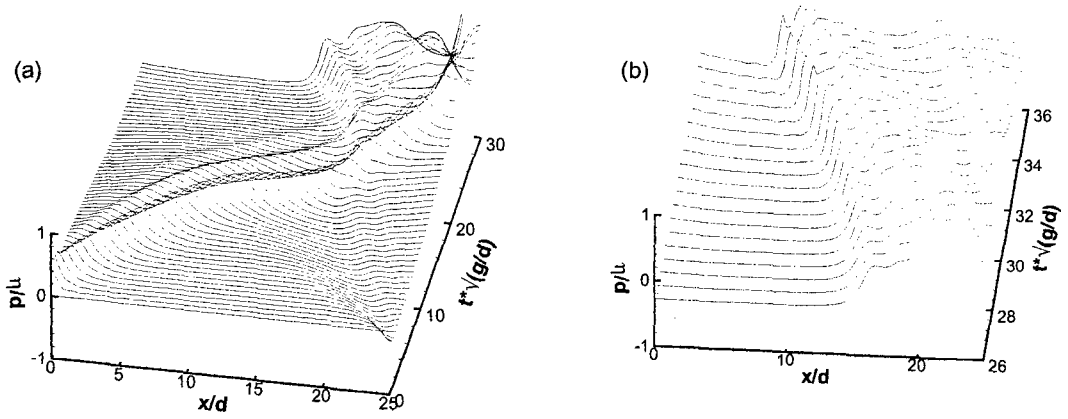

***Figure 3**: Wave profiles for forced motions, $L_x/h = 25.$, $\omega = 0.9973\,\omega_0$, $a/h = 2.5$. (a): $t = 0 \sim 30$. (b): $t = 26 \sim 36$.*

3D forced motions

A shallow water case is now considered in the case of a 3D tank: $L_x/h = 25.$, $L_y/h = 25$. The parameters corresponding to case (H) in table 1 of Wu et al (1998) have been selected. The tank is subject to a sine motion along the first diagonal of the undisturbed free surface, $x = a_x\, sin(\omega_x t)$; $y = a_y\, sin(\omega_y t)$, with $a_x = a_y = 1.2h$ and $\omega_x = \omega_y = 0.998\omega_{0x}$. The simulation was performed with 1600 (40x40) modes. We give below four examples of free surface profiles in the tank. Longer simulations and comparisons with results given in [7] are underway and will be presented at the workshop, together with energy and volume checks.

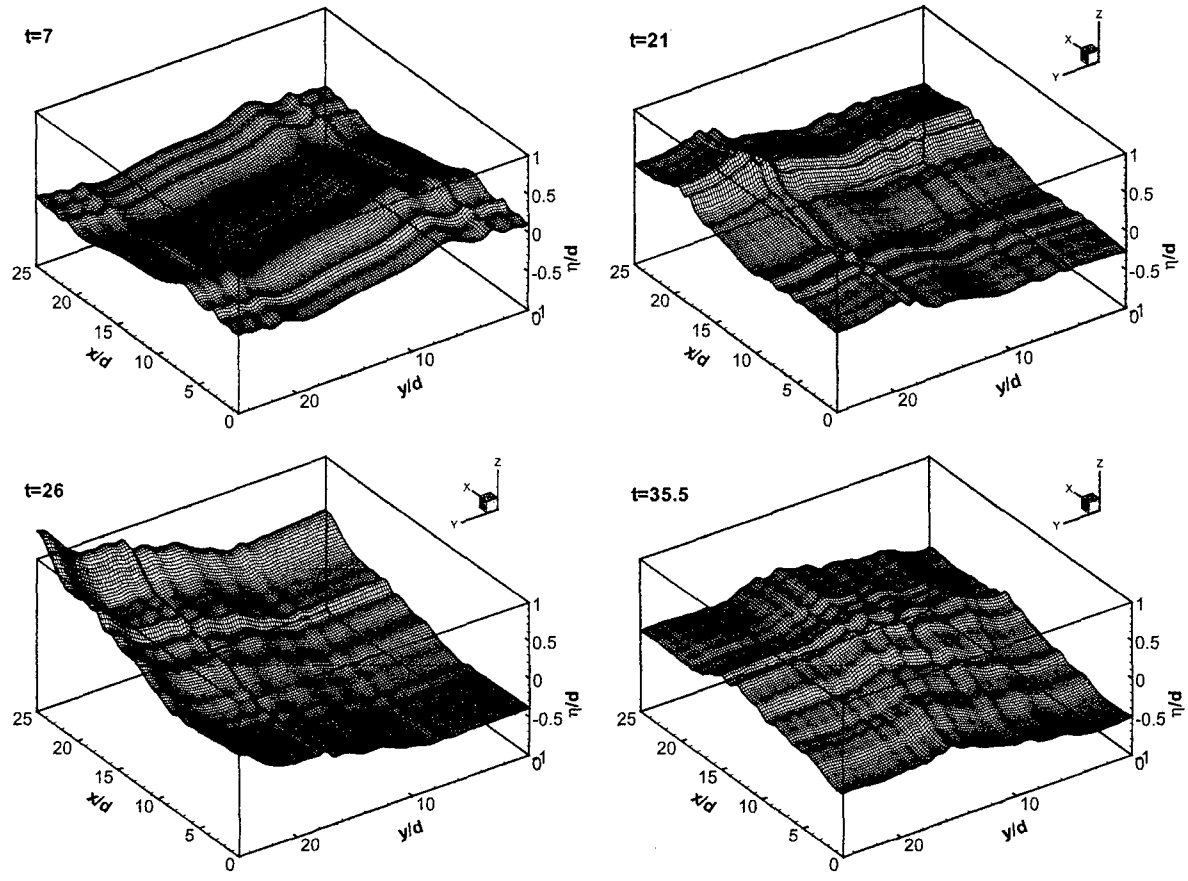

References

[1] Hussaini, M.Y. & Zang, T.A., 1987, Spectral methods in fluid dynamics, *Ann. Rev. Fluid. Mech.*, **19**:339-367

[2] Fornberg, B., 1995, *A practical guide to pseudo spectral methods*, Cambridge University Press, ISBN 0-521-49582-2

[3] Fenton, J.D. & Rienecker, M.M., 1981, A Fourier method for solving nonlinear water-wave problems: application to solitary-wave interactions., *J. Fluid Mech.*, **118**: 411-443.

[4] Dommermuth & D.G., Yue, D.K.P., 1987, A higher-order spectral method for the study of nonlinear gravity waves, *J. Fluid Mech.*, **184**:267-288.

[5] Kim, M.J., Moon, H.T., Lee, Y.B., Choi, S.K., Kim, Y.K., Nam, H.Y. & Cho, M., 1998, A spectral method for free surface flows of inviscid fluids, *Int. J. Num. Meth. in Fluids*, **28**:887-902

[6] Chern, M.J., Borthwick, A.G.L. & Eatock-Taylor, R., 1999, A pseudo-spectral σ-transformation model of 2D non linear water waves. *J. Fluids & Struct.*, **13**:607-630

[7] Wu, G.X., Ma, Q.W., Eatock-Taylor, R., 1998, Numerical simulation of sloshing waves in a 3D tank based on a finite element method. *Applied Ocean Res.*, **20**:337-355.

GREEN WATER LOADING ON A DECK STRUCTURE

M.Greco,
Dep.of Marine Hydrodynamics, NTNU
7491, Trondheim, Norway
Email: marilena@marin.ntnu.no

O.M.Faltinsen
Dep.of Marine Hydrodynamics, NTNU
7491, Trondheim, Norway
Email: oddfal@marin.ntnu.no

M.Landrini
INSEAN, The Italian Ship Model Basin
Via di Vallerano 139, 00128, Roma, Italy
Email: maulan@waves.insean.it

At the previous Workshop, a numerical investigation of water-on-deck phenomena was presented by the same authors. A two-dimensional problem was considered. The effect of main wave- and body-parameters was studied. The fully nonlinear problem was solved by boundary-integral equations. Here, we discuss a continuation of that activity. Results from an on-going experimental investigation are presented, together with the analysis of the interaction of the fluid on the deck with superstructures.

Experiments Two-dimensional water-on-deck (w.o.d.) model tests are on-going in a narrow wave flume (13·5 m long, 1 m deep, 0·6 m wide). Incoming waves are generated by a flap wavemaker hinged at 0·1 m from the bottom. The selected body-parameters are: draft $D = 0{\cdot}2$ m, length $L = 1{\cdot}5$ m, freeboard $f = 0{\cdot}05$ m. The bottom corner at the bow was rounded with a radius of curvature 0·08 m to avoid significant vortex shedding. Body motions are restrained. Since the generated wave system is highly transient, with the first crest generally steeper than the following ones, we decided to focus on the first w.o.d. event.

Fig. 1 is representative of the behavior when the fluid invades the deck. The nominal incoming wave length is $\lambda = 2$ m and the wave height $H = 0{\cdot}16$ m. At the beginning the fore-part of deck remains dry, and the shipping of water starts in the form of a rounded jet plunging directly onto the deck. A cavity is formed with air trapped inside. This behavior has been observed in all the test-conditions we studied. Moreover, though for the case shown the jet hits the deck rather close to the bow edge, cases are recorded were the fluid organizes itself to plunge on the deck further from the bow. Finally, in a few cases even blunter impacts have been observed. In all cases, the front view of the event confirmed the two-dimensionality of the phenomenon and excluded that the cavity formation is related to localized three-dimensional instabilities. As a consequence, the initiation of deck-wetting should be characterized by localized high impact pressures. In the reported example, the time scale involved is rather short, about 0·12 s, and at the instant of impact the entrapped cavity has length $l_{cav}/D \simeq 0{\cdot}16$ and height $h_{cav}/D \simeq 0{\cdot}05$. This fluid behavior was not mentioned in the two–dimensional experiments reported in Cozijn (1995). This may be due to the small time and space scales involved. A consequence of the presence of the cavity is that capacity wave probes do not estimate correctly free-surface height.

As time increases (*cf.* bottom plots in Fig. 1) two horizontal jets develop after the impact of the plunging fluid front. One of the two moves backwards towards the bow edge and reduces the cavity volume. The other propagates forward along the deck and increases the wetting velocity relative to a dam-breaking type analysis. As time passes, the cavity moves forward, convected together with the shipped water. Also, the water level above the cavity increases and contributes to squeeze it. This combined actions are responsible, together with surface tension, of the fragmentation of the cavity, though we cannot document this evolution because of the limited frame rate of the video camera.

We used fluorescent material injected in front of the bow edge to detect a possible vortex-shedding in the initial stage of the phenomenon. In particular, we observed that, after the air entrapment, when the cavity starts to move forward, the gravity has already organized the run–down of the fluid in front of the model, preventing the beginning of vortex shedding, at least of strength large enough to be detected by the used method. At this stage, the flow pattern can be sketched as one stream wetting the deck and one involved in the run–down, with negligible cross-flow at the bow edge.

These new features observed in the experiments are not modeled in our computations, where the fluid is allowed to wet the deck as soon as it exceeds the freeboard. A better modeling would probably require the use of a Kutta-like condition, with the fluid leaving tangentially the front bow-edge, and the description of the jet plunging onto the deck. The free surface shape close to the separation point at the bow can be found by a local analysis, Zhao & Faltinsen (1998). This gives $z_1 = C(t)x_1^{2/3}$. Difficulties related to high fluid velocity are expected during impact, and may be alleviated by locally using a Wagner-type of analysis. The final collapse of the cavity would require other methods.

In spite of this, we applied our method to simulate the experiments, and results (solid lines) for later stages of the phenomenon are compared in Fig. 2 with experimental free-surface profiles, ∘. In particular, to reproduce as close as possible the experimental set-up, the actual wave flume has been modeled numerically and the motion of the physical flap has been used to drive the numerical one. However a mathematical damping region different from the physical wave beach was used. This difference matters initially when a seiching

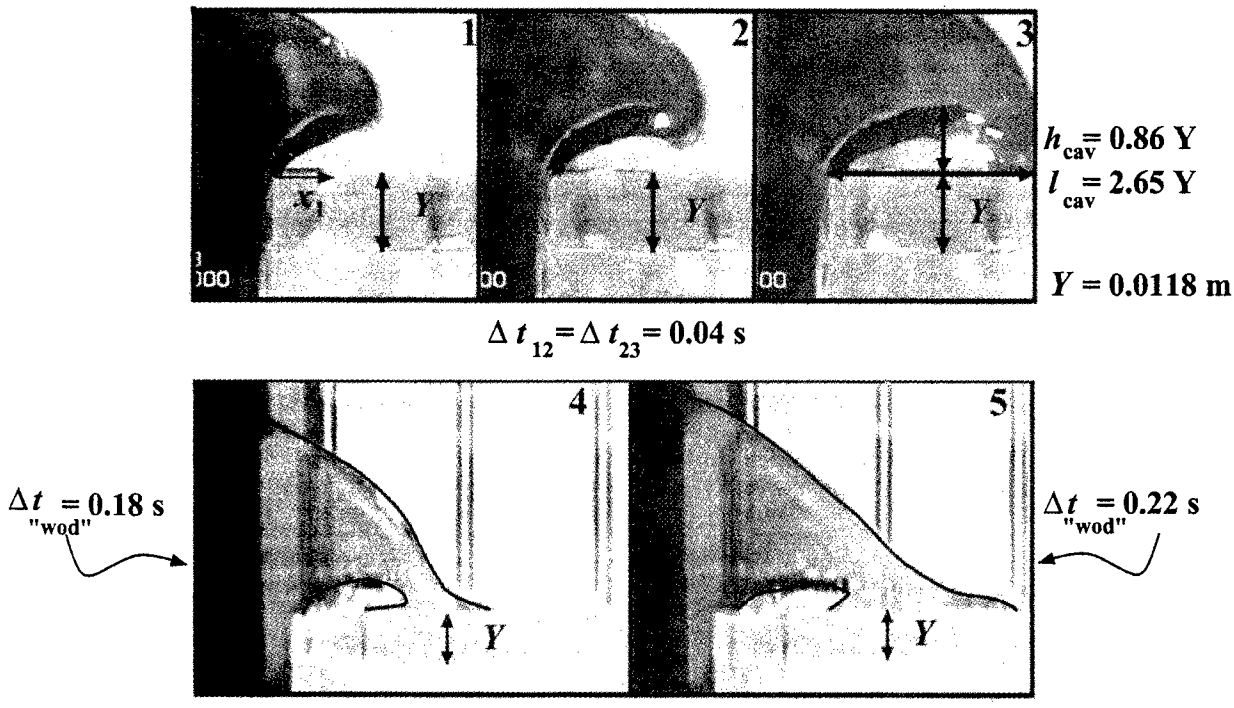

Figure 1. Water-on-deck at the bow of a 2-D ship. Top: initial stage of the wetting. Bottom: cavity formation and transition to dam-breaking type of flow.

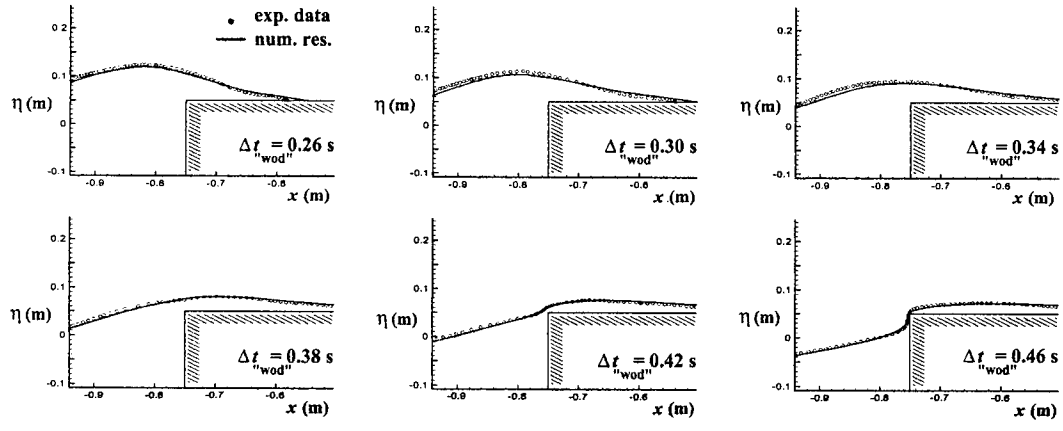

Figure 2. Water-on-deck on a 2-D ship. Comparison of numerical simulation with experimental free-surface profiles. Nominal incoming waves conditions: $\lambda = 2$ m, $H = 0{\cdot}16$ m.

motion is set up in the tank. However the seiching amplitude is small and minimized by the automatically controlled wavemaker. Apparently, though we neglected the details of the initial stages of water shipping and of the wave beach, results agree well with measured profiles (obtained through the digital record of the video camera) with the exception of the wave front region were the numerical method predicts a higher velocity. This suggests that the gross flow evolution is not significantly affected by the phenomena connected with the initial plunging. The instant t_{wod} in Figs. 1–2 indicates the instant of water-on-deck starting in the numerical simulation. Future tests will include the impact of the green water on a vertical deck structure. Relevant numerical studies of the phenomenon are reported in the following text.

Fluid–structure interaction Greco *et al.* (2000) studied the two-dimensional impact of water on a rigid vertical superstructure after a dam break. Here, we investigate the influence of hydroelasticity. The left plot in Fig. 3 gives an example of longitudinal steel stiffeners adopted for the deck house of a FPSO unit. We focus on the effects of those between deck 8 and deck 9 by using an equivalent Euler beam. The upper portion of the deck house is assumed rigid. The cross section is shown in the right plot. Recent accidents for FPSO units documented in Ersdal & Kvitrud (2000), suggest

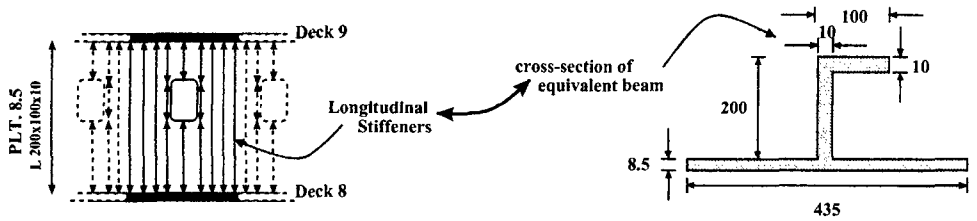

Figure 3. Example of stiffeners of a deck structures. Lengths are in millimeters.

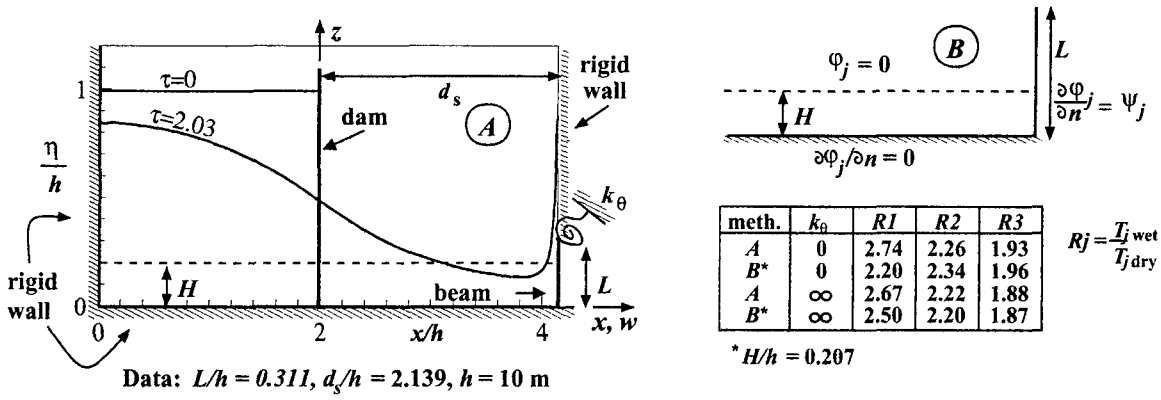

meth.	k_θ	R1	R2	R3
A	0	2.74	2.26	1.93
B*	0	2.20	2.34	1.96
A	∞	2.67	2.22	1.88
B*	∞	2.50	2.20	1.87

$Rj = \frac{T_j \text{ wet}}{T_j \text{ dry}}$

* H/h = 0.207

Figure 4. Impact with a vertical wall after a dam-break (left). In the table, the 'exact' solutions (A) for natural periods are compared with results from the simplified analysis (B) sketched in the top-right plot.

to use a freeboard exceedence of 10 m. The flow is originated as the breaking of a dam located at the bow, with height $h = 10$ m and length $2h$ (*cf.* Fig. 4). The beam is located $d_s = 2{\cdot}139h$ from the dam, with length $L = 0{\cdot}311h$. The lower edge is clamped, while rotations at the upper edge are constrained by a spring with constant k_θ. The deformation $w(z,t)$ of the beam is expressed in terms of the known dry modes $\psi_j(z)$ of the beam with unknown amplitudes $\zeta_j(t)$. Structural damping is neglected.

The fluid-structure interaction is studied by coupling the nonlinear potential fluid model with the linear beam. For a given time, w and w_t are known and the b.v.p. for the potential φ is solved by imposing $\varphi_n = w_t$ along the beam. For the hydrodynamic pressure at the wall, φ_t is found by solving a similar b.v.p. with the exception of the boundary condition at the beam, where the Neumann condition is substituted by a non-homogeneous Robin condition. The latter follows by inserting the condition for φ_{tn} into the beam equation and represents the fluid-structure coupling. Once the φ_t is known, w_{tt} can be evaluated and fluid motion and structural deformation can be prolonged in time. A similar procedure was applied by Tanizawa (1999) to analyze the impact of a flexible body on a free surface.

The initial conditions, $\tau = t\sqrt{g/h} = 0$, are shown in Fig. 4, together with a later free-surface configuration, when the wetted portion of the vertical wall is almost $3L$. The flow generated after the impact is characterized by a narrow jet of water rising along the wall, also observed in case of rigid wall.

The numerical solution can be negatively affected by a variety of difficulties: spatial and time resolutions decrease progressively for higher-order modes and confluence of different boundary conditions at the edges of the beam implies locally a poorer convergence. Therefore, a simplified analytical analysis (top-right plot in Fig. 4) is also considered to check the present results. The incoming water is approximated by a strip of fluid with constant height H, and the potential φ_j due to j-th mode oscillations with unit amplitude is computed with $\varphi_j = 0$ along the free surface. A solution is found by separation of variables and a Fourier expansion of the mode over the wetted surface. The height H is a free parameter chosen by the following considerations. In the approximate problem, it is found that the fluid further away than $\sim 0{\cdot}79L$ from the beam is practically not affected by vibrations. Therefore H is determined by imposing that masses of fluid involved in the approximate and exact problems are the same. In this procedure, particles above the beam are neglected because their role in the hydroelastic problem is expected to be small. This procedure gives an $H/h = 0{\cdot}207$. The ratio natural wetted-period to natural dry-period $Rj = T_{j\text{wet}}/T_{j\text{dry}}$ is computed and compared with results obtained by the 'exact' problem. This comparison is tabulated for $j = 1,2,3$ in Fig. 4 for $k_\theta = 0, \infty$ and shows a promising agreement, more evident for the higher modes, as we can expect since their sensitivity to the fluid details is smaller. Left plots in Fig. 5 give the time evolution of ζ_j for the first two modes, in the case of $k_\theta = 0$. Late stages are presented for $j = 1,\ldots,4$. After the beam is completely wetted, $\Delta\tau_{\text{imp}} \simeq 0{\cdot}12$, the modes oscillate with almost constant period and amplitude. Both the value of ζ_j and the amplitude of oscillations decrease as the order of mode increases. This behavior does not change substantially when the parameter $K_\theta = k_\theta L/EI$ is varied (EI is the beam

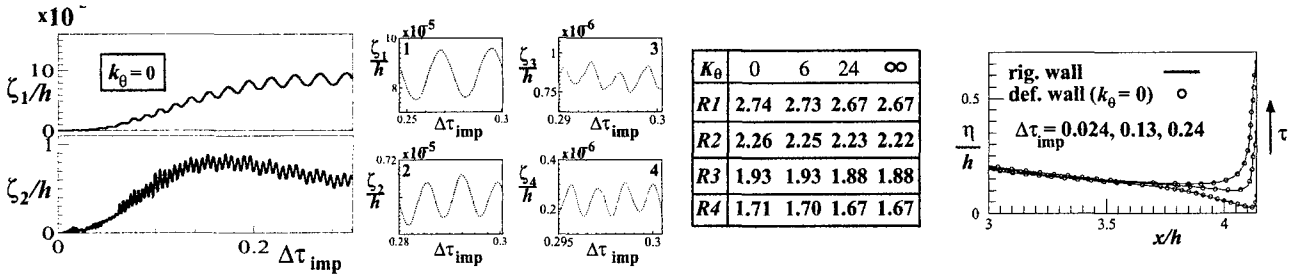

K_θ	0	6	24	∞
R1	2.74	2.73	2.67	2.67
R2	2.26	2.25	2.23	2.22
R3	1.93	1.93	1.88	1.88
R4	1.71	1.70	1.67	1.67

Figure 5. Left: Amplitude of the first four modes as a function of time. Table: ratio of natural wetted-periods to natural dry-periods for the first four modes of the beam. $K_\theta = k_\theta L/EI$. Right: free surface for three different instants after the impact (solid lines: rigid wall, ○: $k_\theta = 0$).

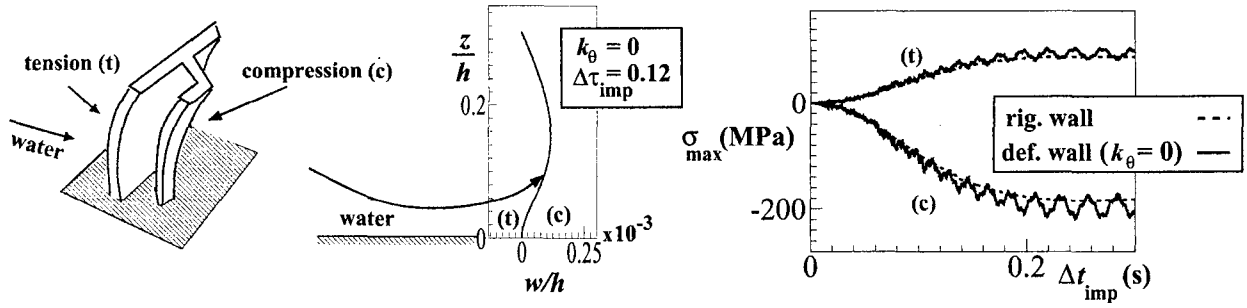

Figure 6. Left: sketch of the loaded beam. Center: deformation of the beam for $\Delta\tau = 0{\cdot}12$ after the impact. Right: maximum tension and compression stresses as a function of time. Quasi-steady (dashed lines) and hydroelastic (solid lines) analyses ($k_\theta = 0$).

bending stiffness). Qualitatively we observe smaller amplitudes as it increases and a minor influence for higher modes, which are less sensitive to the boundary conditions. In general, Rj decreases as K_θ increases and it is smaller for higher j (see the table). The highest natural wetted-period changes from $\sim 0{\cdot}018$ to $\sim 0{\cdot}026\sqrt{h/g}$ as we go from $K_\theta = \infty$ to 0. This means $T_{1\text{wet}}$ is small compared to the time duration for the beam to be wetted. It implies that the hydroelasticity does not play an important role for the resulting maximum strains (*cf.* Faltinsen (2001)).

The rigid wall results, solid lines, are compared with the clamped-supported beam results, ○, in the right plot of Fig. 5 for the free-surface configurations at three instants of time after the impact. The overall pattern is not affected by wall deformation.

In Fig. 6, we analyze maximum stresses on the beam based on hydroelastic and quasi-steady analyses. The latter means rigid structure from a hydrodynamic point of view and resulting static structural deformations. Fifteen modes are used in the calculations. For the considered cases, maxima are always observed at the bottom end. In particular, left plot, the fluid-induced bending moment gives tension stresses (t) in the wetted side, and compression stresses (c) in the opposite side. The deformation of the beam for $\Delta\tau = 0{\cdot}12$ after the impact is given in the center-plot, where it is also sketched the direction of the incoming water. The right plot gives the maximum tension and compression bending stresses. Compression stresses reach larger values than tension ones. This is because the cross-sectional neutral axis is closer to the wetted side. We note that magnitude of hydroelastic results oscillates around a mean value close and above the quasi-steady analysis. This documents the unimportance of hydroelasticity in this case.

This research activity has taken place at the Strong Point Centre on Hydroelasticity in Trondheim, supported by NTNU and MARINTEK. The research has also been supported by the Italian *Ministero dei Trasporti e della Navigazione* through INSEAN Research Program 2000-02. The mobility of M.L. is partly supported by ONR through University of Hiroshima.

REFERENCES

Cozijn, J. L., " Development of a calculation tool for green water simulation", MARIN Wageningen / Delft Univ. of Technology, the Netherlands, 1995.

Ersdal, G. & Kvitrud, A., "Green water on Norwegian production ships", Proc. 10th Int. Conf. Offshore and Polar Engg, ISOPE'2000, Seattle, 2000.

Faltinsen, O.M., "Hydroelastic slamming", J. Marine Science and Technology, Vol. 5, No. 2, 2001.

Greco, M., Faltinsen, O.M. & Landrini, M., "Basic Studies of Water on Deck", Proc. 23rd Symp. on Naval Hydrod., Val de Reuil, National Academy Press, Washington D.C., 2000.

Tanizawa, K., "A Numerical Simulation Method of Hydroelastic Water Surface Impact Based on Acceleration Potential", Proc. FEDSM99, 3rd ASME/JSME Joint Fluids Eng. Conf., San Francisco, 1999.

Zhao, R. & Faltinsen, O.M., "Water Entry of arbitrary Axisymmetric Bodies With and Without Flow Separation", Proc. 22nd Symp. on Naval Hydrod., National Academy Press, Washington D.C., 1998.

AIR CUSHION UNDER FLOATING OFFSHORE STRUCTURE

R. Gueret and A. J. Hermans
Department of Applied Mathematics, Delft University of Technology, The Netherlands

1 Introduction

In this paper, we present a new integral equation to describe the motion of an air cushion supported platform. These platform are studied as a design concept for floating airports. The amplitudes of motion of such body are expected smaller and a better repartition of pressure on the body reduces the mechanical structural loads. In this paper, we study the behavior of an air cushion supported floating platform exited by waves. The platform consists of a rigid body and an air cavity beneath it. We assume that there is no air leakage. For clarity, we restrict our theory to heave motion.
We assume the flow being potential reducing the problem to the determination of a potential Φ and use usual assumptions of linearized potential theory. The platform's boundary Σ is split into the boundary Σ_1 for the wetted part of the platform, and Σ_2 which is the free surface underneath the platform and submitted to air cushions pressure. An integral equation is then given for the determination of the potentials of diffraction and radiation. It is possible to extend the method to several air cushions, connected or not, and to take into account the pitch motion.

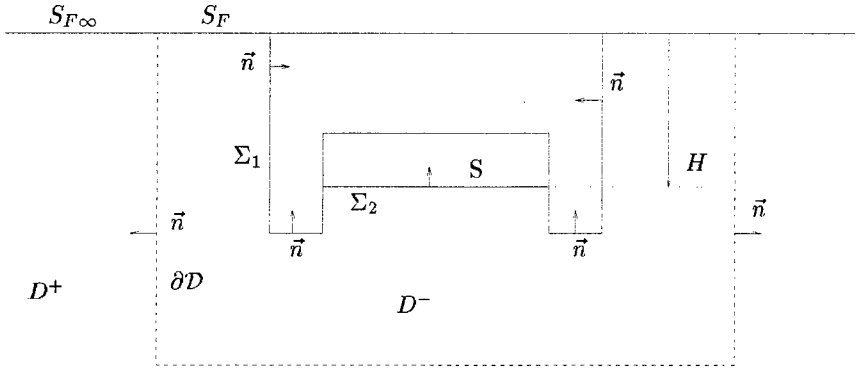

Figure 1: Definition of the geometry

2 Boundary conditions

We define η to be the surface elevation under the cavity, S the interface of this cavity at a distant of H meter from the free surface, V_{cs} and p_{cs} the volume and pressure in the cavity when the platform is at rest. The instantaneous pressure p_c is supposed to be uniform in the platform cavity. We have the following kinematic and dynamic condition at the interface Σ_2:

$$p_c = -\rho g H - \rho g \eta - \rho \frac{\partial \Phi}{\partial t} \quad , \quad \frac{\partial \eta}{\partial t} = \frac{\partial \Phi}{\partial z} \tag{1}$$

The change of pressure can be determined by the change of the volume of cavity. The air compression obeys the adiabatic law and we can write:

$$\frac{\Delta p}{p_{cs}} = -\gamma \frac{\Delta V}{V_{cs}} \quad , \quad \Delta V = -\iint_{\Sigma_2} (\eta - \xi)\, dS \tag{2}$$

where ξ is the platform heave motion and $\gamma = 1.4$. Combining relations [1] and [2] leads to the boundary condition on Σ_2.

$$\frac{\partial^2\Phi}{\partial t^2} + g\frac{\partial\Phi}{\partial z} - \frac{\gamma p_{cs}}{\rho V_{cs}}\frac{\partial \Delta V}{\partial t} = 0$$

$$\text{or} \qquad \frac{\partial^2\Phi}{\partial t^2} + g\frac{\partial\Phi}{\partial z} + \frac{\gamma p_{cs}}{\rho V_{cs}}\iint_{\Sigma_2}\frac{\partial\Phi}{\partial z}\,dS - \frac{\gamma p_{cs} S}{\rho V_{cs}}\frac{\partial\xi}{\partial t} = 0$$

$$\text{Let} \quad \alpha = \frac{\gamma p_{cs}}{\rho g V_{cs}}$$

αS, which is a non-dimensional number, represents the ratio of the force due to air compression by the buoyancy force.
In frequency domain, we write $\Phi(\underline{x},t) = \phi(\underline{x})\,e^{-i\omega t}$ and we have then the boundary conditions:

$$\left\{-\nu\phi + \frac{\partial\phi}{\partial z} + \alpha\iint_{\Sigma_2}\frac{\partial\phi}{\partial z}\,dS + i\omega\alpha S\xi = 0\right\}_{\Sigma_2} \quad ; \quad \left\{\frac{\partial\phi}{\partial n} = -i\omega\xi n_z\right\}_{\Sigma_1} \tag{3}$$

We also add the usual linearized free surface condition at $z = 0$ and the Sommerfeld radiation condition at infinity.

3 Boundary value problem

The fluid domain is split in two regions, separated arbitrary by an interface ∂D. The platforms stays in the region D^- and the region towards infinity is defined as D^+. The potential function in D^+ is written as the superposition of the incident wave potential and a diffracted wave potential as follows

$$\phi(\underline{x}) = \phi^{inc}(\underline{x}) + \phi^{+}(\underline{x})$$

In D^+, the total potential is denoted as $\phi^-(\underline{x})$. At the dividing surface ∂D we require continuity of the total potential and its normal derivative.
We introduce the Green's function $\mathcal{G}(\underline{x},\underline{\xi})$ that fulfills $\Delta\mathcal{G} = 4\pi\delta(\underline{x}-\underline{\xi})$, the free surface and the radiation condition.
Applying Green's theorem for ϕ^+ and ϕ^- leads to the following formula:

for x $\in D^-$:

$$0 = -\iint_{S_{F\infty}\cup\partial\mathcal{D}}(\phi^+\frac{\partial\mathcal{G}}{\partial n} - \mathcal{G}\frac{\partial\phi^+}{\partial n})\,dS$$

$$4\pi\phi^- = \iint_{S_F\cup\Sigma\cup\partial\mathcal{D}}(\phi^-\frac{\partial\mathcal{G}}{\partial n} - \mathcal{G}\frac{\partial\phi^-}{\partial n})\,dS \tag{4}$$

The integrals over $S_{F\infty}$ and S_F become zero, due to the free surface condition for $\mathcal{G}$, ϕ^+ and ϕ^-. Adding up the two expressions in [4], leads to:

$$4\pi\phi^- = \iint_{\Sigma}(\phi^-\frac{\partial\mathcal{G}}{\partial n} - \mathcal{G}\frac{\partial\phi^-}{\partial n})\,dS + \iint_{\partial\mathcal{D}}([\phi]\frac{\partial\mathcal{G}}{\partial n} - \mathcal{G}\,[\frac{\partial\phi^-}{\partial n}])\,dS \qquad \text{for x} \in D^-$$

$$\text{or} \qquad 4\pi\phi^- = \iint_{\Sigma}(\phi^-\frac{\partial\mathcal{G}}{\partial n} - \mathcal{G}\frac{\partial\phi^-}{\partial n})\,dS + 4\pi\phi^{inc}$$

When $\underline{x}$ tends to Σ, we have then

$$2\pi\phi^- = 4\pi\phi^{inc} + \iint_{\Sigma_1 \cup \Sigma_2} (\phi^- \frac{\partial \mathcal{G}}{\partial n} - \mathcal{G}\frac{\partial \phi^-}{\partial n})\, dS \tag{5}$$

We decompose the potential into a potential of diffraction and a potential of radiation

$$\phi = \phi^D - i\omega\xi\phi^R$$

diffraction:
From [3], we write the boundary conditions for ϕ^D:

$$\left\{ -\nu\phi^D + \frac{\partial \phi^D}{\partial z} + \alpha \iint_{\Sigma_2} \frac{\partial \phi^D}{\partial z}\, dS = 0 \right\}_{\Sigma_2} \qquad \left\{ \frac{\partial \phi^D}{\partial n} = 0 \right\}_{\Sigma_1}$$

$$\text{let} \quad \tau_D = \iint_{\Sigma_2} \frac{\partial \phi^D}{\partial z}\, dS$$

Integrating [3] on Σ_2 and re injecting the result in the equation, we obtain:

$$\tau_D = \frac{\nu}{1+\alpha S} \iint_{\Sigma_2} \phi^D\, dS \qquad \text{and} \qquad \frac{\partial \phi^D}{\partial n} = \nu\phi^D - \frac{\nu\alpha}{1+\alpha S} \iint_{\Sigma_2} \phi^D\, dS$$

Following Noblesse, we can write:

$$\left(\frac{\partial \mathcal{G}}{\partial n} - \nu\mathcal{G}\right)_{\Sigma_2} = \mathcal{H}(r, r_1) = -\left(\frac{1}{r} + \frac{1}{r_1}\right)_\zeta + \nu\left(\frac{1}{r} - \frac{1}{r_1}\right)$$

The potential ϕ^D is then found to be solution of the integral equation:

$$2\pi\phi^D - \iint_{\Sigma_1} \phi^D \frac{\partial \mathcal{G}}{\partial n}\, dS - \iint_{\Sigma_2} \mathcal{H}\, \phi^D\, dS - \frac{\alpha\nu}{1+\alpha S} \iint_{\Sigma_2} \mathcal{G}\, dS \times \iint_{\Sigma_2} \phi^D\, dS = 4\pi\phi^{inc} \tag{6}$$

radiation:
We apply the same procedure for the radiated potential. The boundary equations read:

$$\left\{ -\nu\phi^R + \frac{\partial \phi^R}{\partial z} + \alpha \iint_{\Sigma_2} \frac{\partial \phi^R}{\partial z}\, dS - S\alpha = 0 \right\}_{\Sigma_2} \qquad \left\{ \frac{\partial \phi^R}{\partial n} = n_z \right\}_{\Sigma_1}$$

and we find:

$$\tau_R = \frac{1}{1+\alpha S}\left\{ \nu \iint_{\Sigma_2} \phi^R\, dS + S^2\alpha \right\} \qquad \frac{\partial \phi^R}{\partial n} = \nu\phi^R - \frac{\nu\alpha}{1+\alpha S} \iint_{\Sigma_2} \phi^R\, dS + \frac{\alpha S}{1+\alpha S}$$

We obtain the integral equation for ϕ^R :

$$2\pi\phi^R - \iint_{\Sigma_1} \phi^R \frac{\partial \mathcal{G}}{\partial n}\, dS - \iint_{\Sigma_2} \mathcal{H}\, \phi^R\, dS - \frac{\alpha\nu}{1+\alpha S} \iint_{\Sigma_2} \mathcal{G}\, dS \times \iint_{\Sigma_2} \phi^R\, dS$$
$$= -\frac{\alpha S}{1+\alpha S} \iint_{\Sigma_2} \mathcal{G}\, dS - \iint_{\Sigma_1} \mathcal{G} n_z\, dS \tag{7}$$

4 Numerical results

We apply our model to a 250m long and 78m wide rectangular platform. The total height is 15m and the water free surface in the air cushion is at distance of 10m from the mean sea level. The vertical walls thickness, surrounding the air cavity, is 4m for the 250m long side walls , and 6m for the 78m long end walls. With these values, we find $\alpha = 2.4310^{-5}$. In Figure [2] and [3], we compute the added mass and damping coefficients for heave motion. In figure [4] we compare the amplitude of the platform elevation for a unit height incoming head wave with the experimental results of Pinkster. The agreement is good. In figure [5], we compute the wave elevation amplitude in the air cushion. We check that, in agreement with our assumptions, no resonant mode will generate waves that hit the horizontal deck of the air cushion platform.
We first note that we obtain a negative added mass for a large range of frequency and also with discontinuities. This is due to the small width/length ratio. For wider platform this phenomenon never occurs.

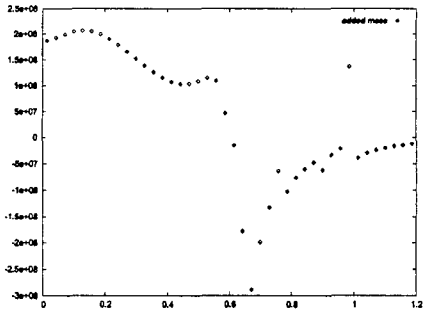

Figure 2: Added mass

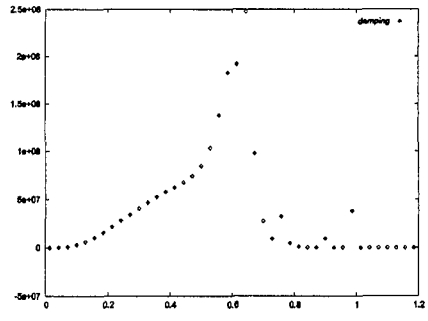

Figure 3: Damping

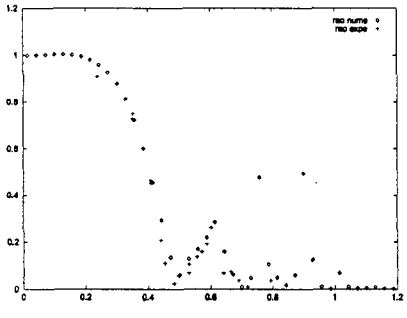

Figure 4: RAO

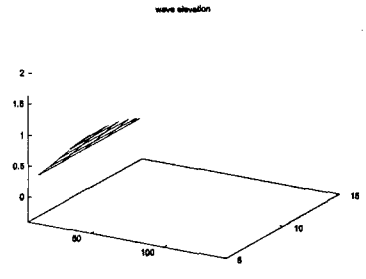

Figure 5: Wave elevation

References

[1] Aad J. Hermans. A boundary element method for the interaction of free-surface waves with a very large floating flexible platform, *J. of fluids and structures*, to appear.

[2] Malenica Š. & Zalar M. An alternative method for linear hydrodynamics of air cushion supported floating bodies. *15th International Workshop on Water Waves and Floating Bodies.*

[3] Pinkster J.A & Meevers E.J.A. The behavior of a large air-supported mob at sea. *15th International Workshop on Water Waves and Floating Bodies.*

[4] Noblesse F. The green function in the theory of radiation and diffraction of regular waves by a body. *J.Engg.Math, 16,137-169 (1982).*

16th International Workshop on Water Waves and Floating Bodies
22.-25. April 2001, AKI Grand Hotel, Hiroshima

Influence of Canal Topography on Ship Waves in Shallow Water

Rupert Henn and Som D. Sharma
Institute of Ship Technology
Mercator University, Duisburg, Germany

Tao Jiang
VBD - European Development Centre for Inland and Coastal Navigation
Duisburg, Germany

1 INTRODUCTION

The waves generated by ships sailing on rivers or canals differ much from those in the open deep sea. Shallow water waves are typically steeper and, hence, nonlinear. They can damage river banks and endanger other ships. Natural rivers and artificial canals are getting increasingly too small for the present and future traffic. To survive in today's aggressive competition between different modes of transport inland ships have to become larger and faster. With increasing ship size the ratio of water depth to draft is getting smaller and, hence, fairways need to be dredged.
In this work the influence of the bottom topography of a canal on the waves generated by a ship at near-critical speed is studied. The wave pattern is found to differ significantly from the horizontal bottom case. Moreover, the danger arising from a ship sailing in a canal at an ill-adapted speed is pointed out. The calculations are based on shallow-water wave equations of the Boussinesq type, which have been previously used to successfully simulate the waves generated by a ship in a canal with a horizontal bottom, see Jiang & Henn (1999).

2 MATHEMATICAL FORMULATION

2.1 Coordinate System

A right-handed ship-bound coordinate system *Oxyz* is used. The origin *O* lies at the stern in the intersection of the undisturbed water-plane and the ship's longitudinal center-plane. The *x*-axis points in the direction of ship's forward motion; the *z*-axis, vertically upwards. The ship sails at speed *V* along the centerline of the canal. Running trim and sinkage are ignored.

2.2 Field equations

The fluid motion is described by the modified Boussinesq equations as given by Jiang (1998):

$$\zeta_t - V\zeta_x + (\zeta_x + h_x)u + (\zeta + h)(u_x + v_y) + (\zeta_y + h_y)v = 0$$

$$u_t - Vu_x + uu_x + vu_y + g\zeta_x$$
$$-\frac{h}{2}[h_{xx}u_t + 2h_x u_{tx} + hu_{txx} + h_{xy}v_t + h_y v_{tx} + h_x v_{ty} + hv_{txy}$$
$$- V(h_{xx}u_x + 2h_x u_{xx} + h_{xy}v_x + h_y v_{xx} + h_x v_{xy})]$$
$$-\frac{h^2}{3}[u_{xxt} + v_{xyt} - V(u_{xxx} + v_{xxy})] = 0$$

$$v_t - Vv_x + uv_x + vv_y + g\zeta_y$$
$$-\frac{h}{2}[h_{xy}u_t + h_x u_{ty} + h_y u_{tx} + hu_{txy} + h_{yy}v_t + 2h_y v_{ty} + hv_{tyy}$$
$$- V(h_{xy}u_x + h_x u_{xy} + h_y u_{xx} + h_{yy}v_x + 2h_y v_{xy})]$$
$$-\frac{h^2}{3}[u_{txy} + v_{tyy} - V(u_{xxy} + v_{xyy})] = 0$$

Here, $h(x,y)$ is the water depth, $\zeta(x,y,t)$ is the wave elevation, $u(x,y,t)$ and $v(x,y,t)$ are the depth-averaged perturbation velocity components in the x and y directions, respectively, t is the time, and g is the acceleration due to gravity.

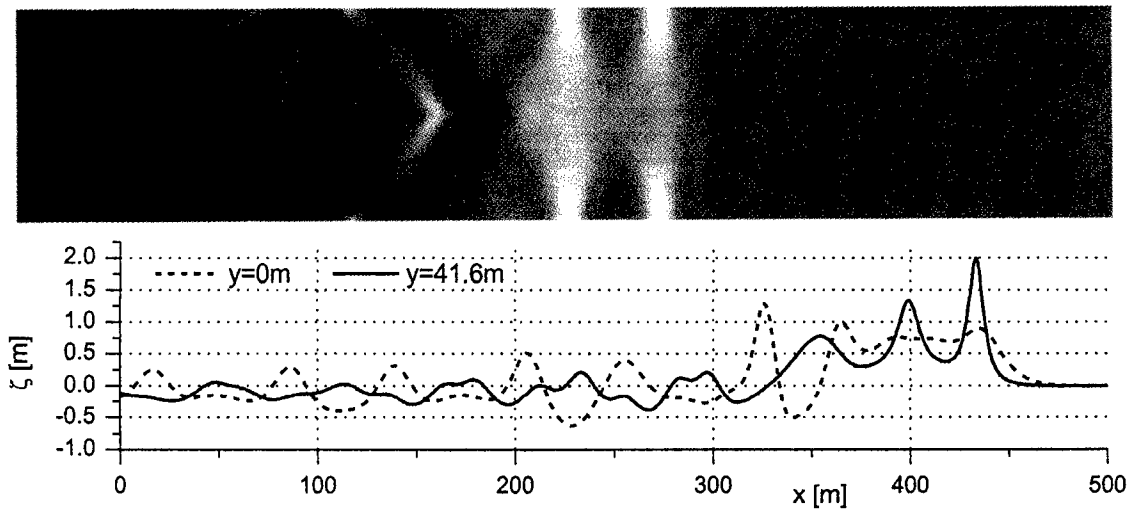

Fig. 4 Wave pattern and longitudinal wave-cuts at locally critical speed in a river-like canal

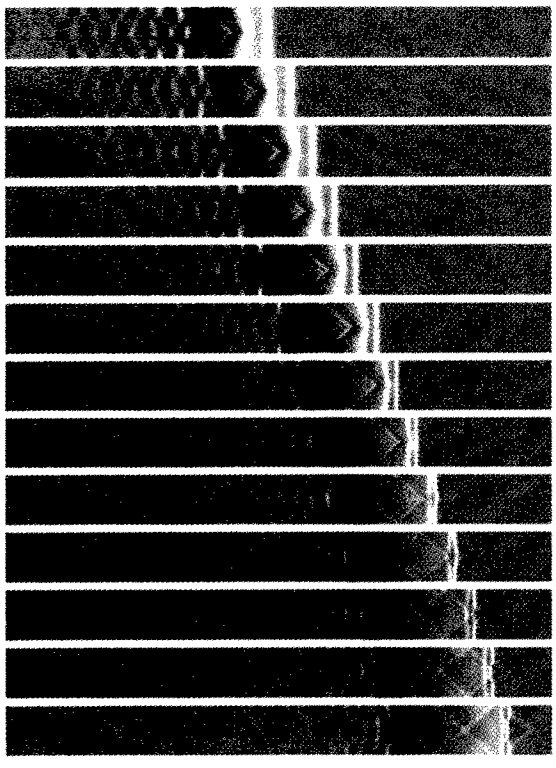

Fig. 5 Density plots of wave pattern generated by a ship moving onto a beach

5.3 Ship moving into a gradually shallower region

Fig. 5 shows a time series of density plots of the wave pattern produced by a ship sailing steadily into shallower water on the center-line of a rectangular canal with longitudinally sloping bottom. It is somewhat like running onto a beach. The ship starts its run in water of depth 5 m. Soon two solitary waves are generated. Before more solitary waves can be generated the water gets shallower. The second solitary wave being on deeper water is always faster and finally catches up with the first, while the ship overtakes them both. In the last plot in Fig. 5 the ship has reached the right edge of the calculation domain where the water is 1 m deep.

6 CONCLUSIONS

It has been shown that the bottom topography has an important influence on the waves generated by a ship in a shallow canal. The typical solitary waves generated by ships moving at near-critical speeds in shallow canals and easily observed in model tests acquire a more complex geometry if the canal bottom is uneven. The local depth Froude number is not the simple criterion for their occurrence. The specially high waves prevailing in the shallow bank zones of the canal may endanger other ships and damage the embankment. As a precaution ships must not sail at transcritical speeds in rivers and canals with river-like profiles.
Although wave resistance was not explicitly considered in this work, it is reasonable to expect that it will also be subject to the influence of bottom topography. It would be of much interest to model a more natural river bank as a partially reflecting boundary in future studies.

7 REFERENCES

Jiang, T.: Investigation of waves generated by ships in shallow water, Proc. 22nd Symposium on Naval Hydrodynamics, Washington D.C./USA, 1998

Jiang, T. & Sharma, S. D.: Wavemaking of flat ships at transcritical speeds, Proc. 19. Duisburger Kollqium Schiffstechnik/Meerestechnik, Duisburg 1998 (in german)

Jiang, T. & Henn, R.: Numerical investigation shallow-water wave equations of Boussinesq type, Proc. 14th Intl. Workshop on Water Waves and Floating Bodies, Port Huron/MI, USA 1999

2.3 Boundary conditions

On the boundaries of the computational domain sufficiently ahead of and behind the ship the Sommerfeld radiation condition

$$q_t + \sigma q_x = 0$$

is applied, where q stands for each of the variables ζ, u and v, with $\sigma = -V + \sqrt{gh}$ ahead of the ship and $\sigma = -V - \sqrt{gh}$ behind the ship. The ship and canal are assumed to be both symmetric about their common longitudinal center-plane. So the entire flow is symmetric:

$$\zeta(y) = \zeta(-y),\ u(y) = u(-y),\ v(y) = -v(-y).$$

Therefore, the computational domain may be restricted to the half-plane $y \geq 0$. The vertical canal side-walls are supposed to be impermeable and perfectly reflecting.

2.4 Ship modeling

The flow perturbation caused by the ship hull is locally approximated by the slender-body theory. Therefore, the transverse velocity component v on the center-plane $y = +0$ is given by

$$v = \begin{cases} -\dfrac{1}{2}\dfrac{V}{h}\dfrac{dS}{dx} & ,\ 0 \leq x \leq L \\ 0 & ,\ \text{elsewhere} \end{cases}$$

An inland passenger ferry (Main dimensions: $L = 39.29$ m, $B = 8.84$ m and $T = 1.2$ m) is used as an exemplary ship; for further details see Jiang & Sharma (1998).

3 NUMERICAL METHOD

The field equations are discretized in space and time using the (symmetric) Crank-Nicolson finite difference scheme. The resulting sparse matrix is solved by a standard SOR (Successive Over-Relaxation) method, namely, the Gauss-Seidel algorithm. A detailed description can be found in Jiang (1998).

4 CANAL TOPOGRAPHY

Two essentially different types of canal-bottom topography are simulated: (i) A set of polygonal cross-sectional profiles which are uniform over the whole length of the canal; (ii) A rectangular profile with linearly decreasing water depth in the direction of ship's motion.

4.1 Configuration A

In configuration A the canal is 100 m wide; the water depth is 5 m in the central portion between two symmetric knuckle lines from where it decreases linearly to 1 m at the vertical side-walls. The y-coordinate of the knuckle varies from 50 m in case (a) – that is a rectangular profile – through 37.5 m (b), 25 m (c) to 12.5 m (d), see Fig. 1. Such profiles occur in many inland water canals.

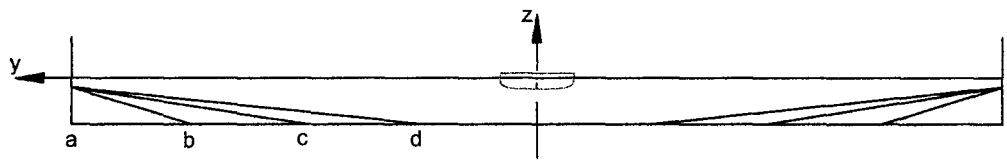

Fig. 1 Four different profiles of the canal configuration A

4.2 Configuration B

In configuration B the canal is also 100 m wide; the water depth varies from 5 m in the center to 3 m at the side walls as shown in Fig. 2, simulating a natural river with a deepened fairway.

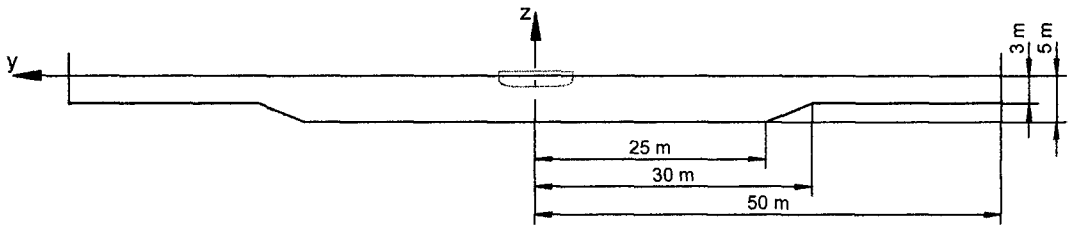

Fig. 2 Profile of the canal configuration B

5 RESULTS

5.1 Configuration A

Fig. 3 shows calculated wave patterns at ship speed 7 ms^{-1} corresponding to local depth Froude number unity. In other words, the ship is sailing at critical speed for the depth at the canal center. In the rectangular profile (a) solitary waves running ahead of the ship can be clearly observed. They vanish gradually as the shallower outer region of the profile gets larger: (b) → (c) → (d), probably because the Froude number based on mean depth grows increasingly supercritical.

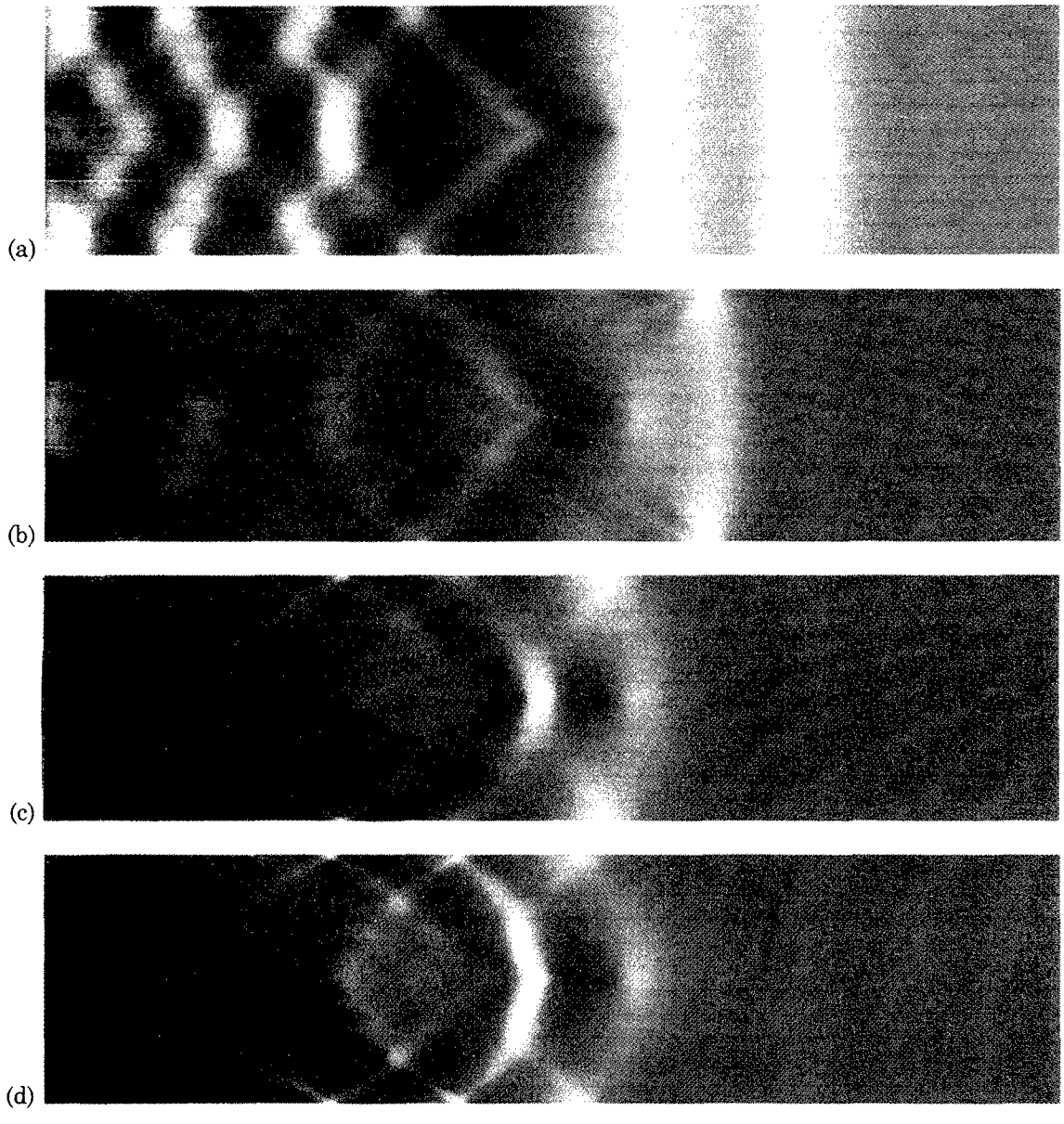

Fig. 3 Density plots of wave patterns at the same (locally critical) speed in different canal profiles

5.2 Configuration B

The ship moves again at a speed of 7 ms^{-1}. Fig. 4 shows the calculated wave pattern and longitudinal wave cuts at two chosen transverse locations. Looking first at the wave pattern, two solitary waves are evident. But whereas in the canal with a horizontal bottom (Fig. 3a) the amplitude of the solitary wave is constant over the full canal width, here the wave amplitude increases dramatically toward the side-walls. This may be hazardous for ambient traffic, specially for small craft that preferably sail in the outer shallower region of the canal to evade heavier vessels at the center. Comparing now the wave cut along the canal center-line ($y = 0$) with that near the side-wall ($y = 41.6$ m), it is seen that the maximum wave elevation in the latter is twice as high. Such high waves near the side-walls are, of course, also a menace to the river banks.

The bow wave of a vertical surface-piercing circular cylinder in a steady current

John CHAPLIN

Department of Civil & Environmental Engineering, Southampton University, UK

1. INTRODUCTION

The bow wave of a vertical surface-piercing cylinder in a steady current breaks at modest Froude numbers. A view of this flow is shown in figure 1, taken from experiments in which a 210mm diameter stainless steel cylinder was towed at constant speed through water initially at rest (Chaplin & Teigen, 2000). The bow wave is much like that of a blunt-bowed ship, where the resulting loss of momentum may represent a significant proportion of the wave resistance.

Figure 1 Flow upstream of a cylinder towed at Froude number $Fr = V/\sqrt{gd} = 1.64$, where V is the velocity and d the diameter, and Reynolds number $Re = Vd/\nu = 4.6\times10^5$

In the experiments, the wave resistance of the vertical cylinder was estimated from pressure measurements made at many points over its surface, and is plotted in figure 2 in the form of the equivalent loaded length ΔL. This is defined by

$$\text{(wave resistance)} = \Delta L \times \text{(drag per unit length far beneath the surface)}. \qquad (1)$$

The wave resistance increases rapidly once the Froude number has exceeded 0.5, and reaches a maximum at a Froude number of about 1. At the peak it is equivalent to the loading, at deeply submerged elevations, on a length of cylinder of about $0.8d$.

In working towards an understanding of these results, this paper is concerned with the problem of predicting the Froude number at which the bow wave of a vertical cylinder will first break. It is assumed that until this happens the flow upstream of the cylinder is represented reasonably well by potential flow analysis, even though in practice the downstream region will be dominated by the cylinder's wake.

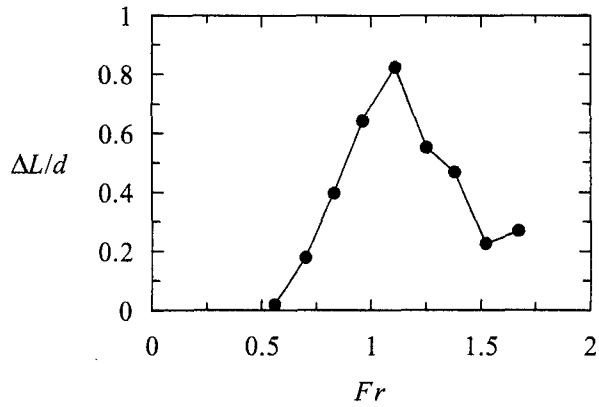

Figure 2. Wave resistance on a vertical surface-piercing cylinder expressed as the equivalent loaded length ΔL. $Re/Fr = 2.80 \times 10^5$.

In a reference frame (r, θ, z) fixed on the cylinder, the flow is steady. The origin is on the cylinder's axis at still water level; z is measured vertically upwards, and $\theta = 0$ is the direction of the incident flow. Velocities are normalised with respect to the incident velocity V, and lengths with respect to the cylinder's radius $d/2$. The free surface boundary conditions are

$$\eta = Fr^2(1 - v_r^2 - v_\theta^2 - v_z^2) \quad \text{and} \quad v_z = v_r \frac{\partial \eta}{\partial r} + v_\theta \frac{1}{r}\frac{\partial \eta}{\partial \theta} \ . \qquad (2), (3)$$

After describing an approximate model for the flow, a fully non-linear numerical solution is outlined, using the method of desingularised sources (Cao *et al.*, 1991). In the approach followed here, the boundary condition on the cylinder's surface is imposed by computing the three-dimensional image system associated with each source.

2. APPROXIMATE SOLUTION

As a first approximation, flow in any horizontal plane is assumed to be that corresponding to two-dimensional potential flow past a cylinder:

$$v_r = \cos\theta\,[1 - \frac{1}{r^2}] \ , \ v_\theta = -\sin\theta\,[1 + \frac{1}{r^2}] . \qquad (4), (5)$$

and v_z^2 is neglected in (2). The vertical velocity follows from (3), and the vertical acceleration of a particle is

$$\frac{dv_z}{dt} = v_r \frac{\partial v_z}{\partial r} + v_\theta \frac{1}{r}\frac{\partial v_z}{\partial \theta} = \frac{8Fr^4}{r^{10}}[-4 + 9r^2 - 4r^4 + (-3 + 8r^2 - 9r^4)\cos 2\theta + 3r^6 \cos 4\theta] \qquad (6)$$

As the Froude number is increased, the expression on the right hand side of (6) first reaches a value of -1 (corresponding to a particle with a downwards acceleration of g) at a point on the surface of the cylinder $r = 1$, at 35.3° around from the stagnation point. This represent the conditions in which the water surface would first break, and occurs at a Froude number of 0.465.

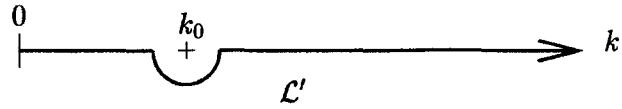

Figure 1: Contour of integration

For the half-plane problem the solution will be sought as a superposition of exponential functions of the form:

$$w(x) = \frac{i}{\omega}\phi_z^- = w_1(x) + w_2(x) = \sum_n a_n \exp\{i\kappa_n x\} + w_2(x) \tag{8}$$

where for the platform with homogeneous physical properties it is expected that the constant '**amplitudes**' a_n and '**wave numbers**' κ_n can be determined. It turns out that, for large values of $\mathcal{D}$, $w_1(x)$ is a good numerical approximation of the geometrical-optics solution. If the physical parameters are not constant the method has to be extended according to the more general '**ray**' approach. Due to the fact that we consider a half-plane the real part of κ_n has to be negative or if the real part equals zero it must obey the outgoing condition. The inhomogeneous term in the equation behaves like $\exp(ik_0x)$ this does not indicate that the solution behaves accordingly. The physics of the problem shows that, for the semi-infinite plate, the wavy part of the solution in the far field has a different real wave-number κ_1, as has been made visible in the numerical simulations as well.

We introduce (8) in (6) and carry out the integration with respect to ξ. This leads to the relation:

$$\sum_n a_n \left(\mathcal{D}\kappa_n^4 - (\mu - 1)\right) \mathrm{e}^{i\kappa_n x} =$$
$$i\sum_n a_n \frac{k_0}{2\pi}(\mathcal{D}\kappa_n^4 - \mu) \int_{\mathcal{L}'} \frac{1}{k - k_0}\left(\frac{\mathrm{e}^{ikx}}{k - \kappa_n} - \frac{\mathrm{e}^{-ikx}}{k + \kappa_n}\right) \mathrm{d}k + \zeta_\infty \mathrm{e}^{ik_0x} \tag{9}$$

The integral has to be evaluated vor positive values of x. We transform the integral to integrals along the vertical axis in the complex k-plane, we then obtain the contribution to the modes in $w_1(x)$ explicitly. It turns out that the well known dispersion relation see HERMANS (1997) is recovered. There are three physically realistic solutions for κ:

$$\left(\mathcal{D}\kappa^4 - \mu + 1\right)\kappa = \pm k_0 \tag{10}$$

The two boundary conditions give two relations for the unknown values of the 'amplitudes' a_n and $w_2(0)$. In the first integral we also obtain a contribution of the pole, $k = k_0$, of the integrand. The contribution of this pole has to cancel the inhomogeous term $\zeta_\infty \mathrm{e}^{ik_0x}$. This leads to a third relation for a_n ,we obtain:

$$\sum_{n=1}^{3} k_0(\mathcal{D}\kappa_n^4 - \mu)\frac{1}{\kappa_n - k_0}a_n + \mathcal{I}\{w_2\} + \zeta_\infty = 0 \tag{11}$$

The influence of $w_2(x)$ can be taken into account iteratively. Extension to a finite width problem is straight forward. It will be explained how three-dimensional cases and the case of obligue incident waves can be treated.

4. Results

In the figures below a comparison is shown of the results obtained, for the semi-infinite plate,

by this method where the first iterate of $w_2(x)$ is taken into account with results obtained by TKACHEVA by means of an asymptotic evaluation of Wiener-Hopf results. The numerical results obtained by means of a boundary element method for a finite platform of width (l = 300 m. and $D/\rho g = 10^5$ m^4.) are shown. Next the asymptotic values for the reflection

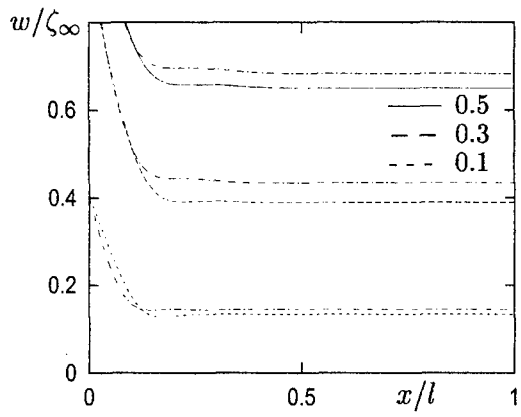

(a) asymptotic results for a semi-infinite platform (TKACHEVA – · –)

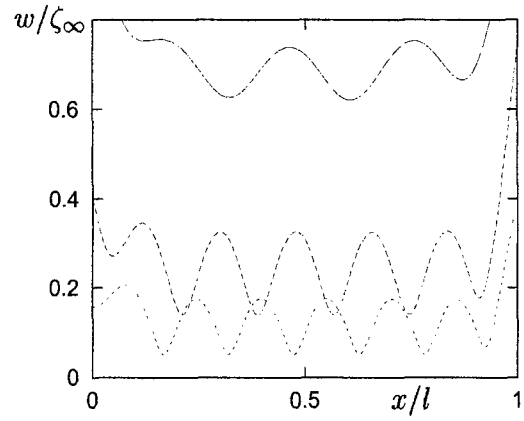

(b) numerical results for a platform with length l = 300 m.

and transmission coefficients for the finite plate, where we neglected the influence of $w_2(x)$ are shown. The final result is a comparison of the values of the deflection near the resonance frequency are shown. In figure (c) one also gets an impression about the accuracy of the zeroth order method. The coefficients may deviate about 5% from those obtained by the direct computations.

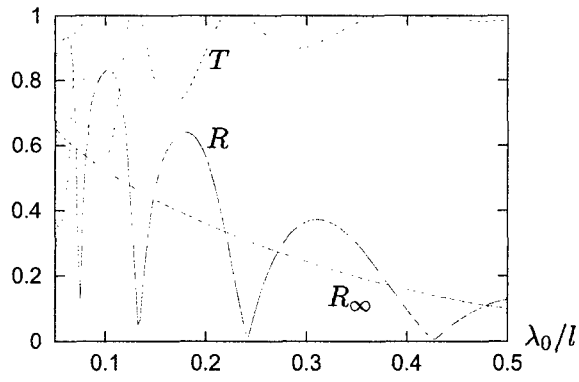

(c) Reflection and transmission coefficients for finite (l = 300 m.) and semi-infinite plate

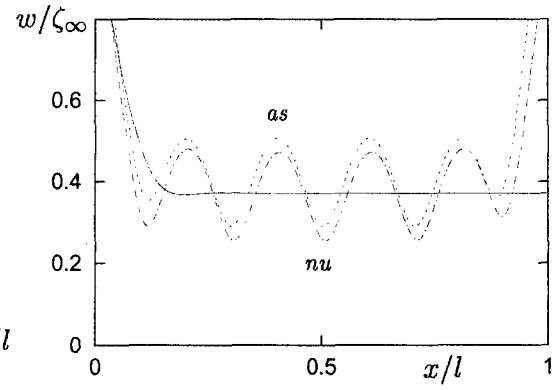

(d) Comparison of the numerical and the asymptotic results for a finite (l = 300 m.) and a semi-infinite platform with $\lambda_0/l = 0.2425$.

References

HERMANS A.J. (1997). An asymptotic method in ship hydrodynamic, in: *Differential Equations Theory, Numerics and Applications*, edited by E. van Groesen and E. Soewono, Kluwer Acad. Publ. p. 103-125.

HERMANS A.J. (2000). A Boundary Element Method for the Interaction of Free-Surface Waves with a Very Large Floating Flexible Platform. *J. of Fluids and Structures*, vol. 14, 2000, p 943-956.

OHKUSU M. and NANBA Y. (1996). Analysis of hydroelastic behavior of a large floating platform of thin plate configuration in waves, *Proceedings of the International Workshop on Very Large Floating Structures*, Hayama, Japan, p. 143-148.

TKACHEVA (private communication with A. A. Korobkin). Diffraction of surface waves at the floating elastic plate, (in Russian) submitted to: *Mechanics of Liquids and Gases*

STARTING FLOW GENERATED BY A FLOATING WEDGE IMPACT

A. IAFRATI[1] AND A.A. KOROBKIN[2]

[1] *INSEAN - Italian Ship Model Basin - Rome, Italy*
[2] *Lavrentyev Institute of Hydrodynamics - Novosibirsk, Russia*

1 Introduction

The small time analysis of the starting flow close to the intersection between the liquid surface and a floating wedge is considered. The liquid and the body are initially at rest. At some instant of time taken as the initial one ($t = 0$), the floating wedge with deadrise angle γ impulsively starts to move down with a constant velocity V. The liquid is assumed ideal and incompressible, and its flow potential. We shall determine both the liquid flow and position of the free surface, which are uniformly valid during the initial stage, where $Vt/h_0 \ll 1$, h_0 is the initial draft of the floating wedge.

The pressure-impulse theory was used by Sedov (1935) to obtain the liquid flow just after the impact instant. Within this theory the boundary conditions are linearised and imposed on the initially undisturbed liquid boundary. The theory predicts the flow singularity at the intersection points. The right-hand side intersection point, $x = x_c$, $y = 0$, where $x_c = h_0 \cot\gamma$, is considered below. In a small vicinity of this point, $r/h_0 \ll 1$, the velocity potential $\phi(x, y, t)$ behaves like (Iafrati & Korobkin 2000)

$$\phi \simeq -Ar^{\sigma_0}\cos(\sigma_0\theta) \ , \tag{1}$$

where $\sigma_0 = \pi/(2\beta)$, $\beta = \pi - \gamma$ and (r, θ) are the cylindrical coordinates with the origin at the intersection point (see figure 1). The coefficient A depends on the entry velocity V, the deadrise angle γ and the initial draft h_0. Here $\frac{1}{2} < \sigma_0 < 1$, which implies that the solution by Sedov predicts non-physical behavior of the flow close to the intersection point and has to be considered as the first-order 'outer' solution. The higher-order 'outer' solution can be derived using the small-time expansion procedure. In order to obtain uniformly valid description of the flow during the initial stage, an 'inner' solution must be considered within stretched variables.

It is shown that in the leading order as $Vt/h_0 \to 0$ the inner solution is non-linear, self-similar and depends only on the wedge deadrise angle γ. Deflection of the inner free surface cannot be neglected even in the leading order in contrast to the Sedov's solution. The solution of the inner problem is achieved by decomposing the fluid domain in three parts: the far-field region, the intermediate region and the jet region. Asymptotic methods are used to evaluate both the shape of the free surface and the velocity potential in the far-field region. The flow in the jet region is described within the shallow-water approximation. The solution in the intermediate region is determined numerically by iterations. A boundary integral representation is used for the velocity potential. Shape of the free surface in the intermediate region is obtained using a pseudo-time stepping procedure developed. The shallow-water solution in the jet region is updated at each step of the iterations and is directly incorporated into the solution of the boundary-value problem in the intermediate region. It is shown that the developed procedure is stable and provides the combined numerical-asymptotic solution of the inner problem with a given accuracy.

2 Formulation of the inner problem

The starting flow close to the intersection point $x = x_c$, $y = 0$ is considered with the help of the stretched non-dimensional variables

$$x = x_c + a(t)\lambda, \quad y = a(t)\mu, \quad \phi(x, y, t) = Aa^{\sigma_0}(t)\varphi(\lambda, \mu, t), \quad a(t) = [(2 - \sigma_0)At]^{\frac{1}{2-\sigma_0}}. \tag{2}$$

Substituting (2) into the original equations and the boundary conditions, we obtain that in the leading order as $a(t)/h_0 \to 0$ the inner flow is quasi-stationary, $\varphi \approx \varphi(\lambda, \mu)$, and the entry velocity can be neglected compared to velocity of the flow close to the intersection point.

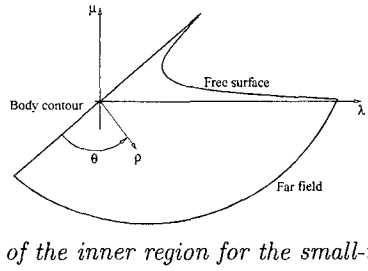

Figure 1: *Sketch of the inner region for the small-time analysis.*

It is convenient to introduce the modified velocity potential $S = \varphi - \frac{1}{2}\rho^2$, where $\rho = \sqrt{\lambda^2 + \mu^2}$, which satisfies the following equations (Iafrati & Korobkin 2000)

$$\nabla^2 S = -2 \qquad \text{in the flow region,} \tag{3}$$

$$S_n = 0 \qquad \text{along both the free surface and the wedge surface,} \tag{4}$$

$$S_\tau^2 + 2\sigma_0 S = (1-\sigma_0)\rho^2 \qquad \text{along the free surface,} \tag{5}$$

$$S \simeq -\frac{1}{2}\rho^2 - \rho^{\sigma_0}\cos(\sigma_0\theta) \qquad (\rho \to \infty), \tag{6}$$

where S_n and S_τ are the normal and tangential derivatives of the unknown function $S(\lambda,\mu)$ on the boundary. The far-field condition (6) follows from matching the 'inner' solution (2) and the 'outer' solution (1). Therefore, in the leading order the flow near the intersection point is self-similar and depends only on the parameter σ_0.

The inner problem (3) - (6) is non-linear and complicated. Moreover, the shape of the free surface is unknown in advance and has to be determined together with the liquid flow. If the free surface is known, the dynamic boundary condition (5) can be integrated providing the velocity potential along the free surface and, therefore, the velocity field throughout the inner flow region in quadratures.

3 Asymptotic behavior of the inner solution in the far field

In order to reduce the size of the computational domain required to solve the inner problem (3) - (6), the asymptotic behavior of the solution in the far field is estimated. It should be noted that the Stokes' procedure does not work in this case and we have to map the far-field region onto a canonical one to find the asymptotic expansion of the modified potential $S(\lambda,\mu)$. The free-surface shape in the far field is described by the equation $\theta = \tilde\theta(\rho)$, where $\tilde\theta(\rho) \to \beta$ as $\rho \to \infty$. It is useful to introduce the new angular variable $\alpha = \theta\beta/\tilde\theta(\rho)$ so that the fluid domain in the far field corresponds to $0 \le \alpha \le \beta$. Three cases are distinguished: (i) $\gamma > \pi/4$, (ii) $\gamma = \pi/4$ and (iii) $\gamma < \pi/4$. In the case $\gamma > \pi/4$, we obtain

$$\tilde\theta(\rho) = \beta + \frac{\sigma_0}{2-\sigma_0}\rho^{\sigma_0-2} - \frac{\sigma_0^2(1-\sigma_0)}{2(2-\sigma_0)^2}\tan(2\gamma)\rho^{2\sigma_0-4} + o(\rho^{2\sigma_0-4}), \quad \theta = \alpha\frac{\tilde\theta(\rho)}{\beta},$$

$$S(\rho,\theta) = -\frac{1}{2}\rho^2 - \rho^{\sigma_0}\cos(\sigma_0\alpha) + \frac{\sigma_0^2}{2-\sigma_0}\left[\frac{\alpha}{\beta}\sin(\sigma_0\alpha) + \frac{\cos[2(1-\sigma_0)\alpha]}{2\cos(2\gamma)}\right]\rho^{2\sigma_0-2} + o(\rho^{2\sigma_0-2}), \tag{7}$$

$$S(\rho,\tilde\theta(\rho)) = -\frac{1}{2}\rho^2 + \frac{\sigma_0^2}{2(2-\sigma_0)}\rho^{2\sigma_0-2} - \frac{\sigma_0^3(1-\sigma_0)}{2(2-\sigma_0)^2}\tan(2\gamma)\rho^{3\sigma_0-4} + o(\rho^{3\sigma_0-4}).$$

The corresponding expansions for the blunt-wedge case, $\gamma \le \pi/4$, have been also derived. They are more complicated than expansions (7) due to eigensolutions, orders of which are comparable with the orders of other terms appeared in the expansions.

4 Mass conservation

The inner solution has to be determined in the unbounded region, whose shape is unknown in advance. The matching condition (6) shows that the mass flux incoming into the inner flow domain from the outer region is infinite. This infinite flux has to be balanced in some sense by deflection of the free surface in the inner region and by the mass outflow through the jet. In order to understand better the mechanism of this balance, let us consider a point E located on the free surface in the far-field region and a point F located on the free surface in the jet region. We consider the finite part $\mathcal{D}_{EF}$ of the flow domain, which is bounded in the far field by the circumference $\rho = R_E$, in the jet region by a straight line orthogonal to the body contour through the point F, on the top by the free surface and on the left-hand side by the body contour. Equation (3) gives

$$\int_{\mathcal{D}_{EF}} \nabla^2 S \, d\lambda d\mu = \int_{\partial\mathcal{D}_{EF}} \frac{\partial S}{\partial n}\, ds = -2|\mathcal{D}_{EF}|,$$

where $|\mathcal{D}_{EF}|$ is the area of the finite region $\mathcal{D}_{EF}$. According to the boundary conditions (4) on the free surface and on the body contour, the normal derivative of S differs from zero only along the far-field boundary and on the jet cut at F. When E tends to infinity both the mass flux from the far-field boundary and the area $|\mathcal{D}_{EF}|$ are unbounded. However, with the help of the asymptotic expansions (7), it can be shown that the two contributions balance each other for any finite R_E, thus leading to a finite flux of mass through the jet cut.

Concerning the behavior of the solution in the jet region, there are two possibilities: (i) the jet is of finite length and (ii) the jet is of infinite length. Whatever is the case, we assume that the fluid flows from the intermediate region into the jet region through the cut F. In order to satisfy both the kinematic condition on the free surface and the

body boundary condition (4) in the case of finite length of the jet and a non-zero angle at the jet tip, it must be $S_\tau(0) = 0$, where τ is the coordinate along the free surface with $\tau = 0$ at the jet tip. By differentiating the dynamic boundary condition (5) with respect to τ, we obtain

$$\lim_{\tau \to 0^+} \frac{S_\tau^2(\tau) - S_\tau^2(0)}{\tau} = 2(1-\sigma_0)\rho\rho_\tau(0) - 2\sigma_0 S_\tau(0).$$

Since $S_\tau(0) = 0$, the left-hand side is positive and the equality implies $\rho_\tau(0) > 0$. On the other hand, $\varphi_\tau(0) = S_\tau(0) + \rho(0)\rho_\tau(0) > 0$, which shows that in this case the liquid particles move in the jet region from the jet tip. This result contradicts to the assumption about the flow pattern in the jet region. Therefore, infinite length of the jet is expected.

5 Asymptotic behavior of the inner solution in the jet region

Asymptotic analysis of the flow in the thin jet region is carried out by using ideas from the shallow-water theory. It is convenient to introduce the new Cartesian coordinate system $O\xi\eta$ with the axis $O\xi$ directed along the body surface and the axis $O\eta$ towards the liquid region. The jet cut F is given now as $\xi = \xi_0$, $0 < \eta < h(\xi_0)$, where equation $\eta = h(\xi)$ describes the free-surface shape in the jet region, $\xi \geq \xi_0$. Within the stretched variables $\eta = h(\xi)z$, $h(\xi) = h(\xi_0)T(\xi)$ and $s(\xi, z) = S(\xi, h(\xi)z)$ the jet region corresponds to the strip, $\xi \geq \xi_0$, $0 < z < 1$, and the unknown functions $T(\xi)$ and $s(\xi, z)$ can be found in the forms $T(\xi) = T_0(\xi) + h^2(\xi_0)T_1(\xi) + \ldots$ and $s(\xi, z) = s_0(\xi, z) + h^2(\xi_0)s_1(\xi, z) + \ldots$, where $h^2(\xi_0)$ is considered as a small parameter. Substituting these asymptotic expansions into (3) - (6), we obtain

Eq. (3)	$s_{0zz} =$	$0,$	$s_{1zz} =$	$-2T_0^2 - T_0^2 s_{0\xi\xi}$	$0 < z < 1$
KBC (4)	$s_{0z} =$	$0,$	$s_{1z} =$	$T_{0\xi} T_0 s_{0\xi}$	$z = 1$
BBC (4)	$s_{0z} =$	$0,$	$s_{1z} =$	0	$z = 0$
DBC (5)	$s_{0\xi}^2 =$	$(1-\sigma_0)\xi^2 - 2\sigma_0 s_0,$	$2s_{0\xi}s_{1\xi} =$	$(1-\sigma_0)T_0^2 - 2\sigma_0 s_1 + T_{0\xi}^2\left[(1-\sigma_0)\xi^2 - 2\sigma_0 s_0\right]$	$z = 1$

in the leading and for the second order, respectively. The system of the differential equations is numerically solved with a space-marching procedure for $\xi > \xi_0$, starting from ξ_0 and a given thickness $h(\xi_0)$ provided by the solution in the intermediate region.

6 Numerical solution in the intermediate region

In order to solve completely the inner problem, the numerical iterative procedure is developed to find the shape of the free surface in the intermediate region. Both the inner potential φ and the modified potential S, where $\varphi = S + \frac{1}{2}\rho^2$, are used. The inner potential φ satisfies the Laplace equation, solution of which is sought by using a boundary integral formulation in the computational domain bounded by the far-field boundary, the body contour and the free surface. The far field boundary (FF) is located at $\rho = R$ with R being large enough so that the asymptotic expansion (7) is expected to represent the solution with a given accuracy for $\rho \geq R$. The same expansion is used also to assign the value of the velocity potential along the far-field boundary.

The main issue is related to the free surface (FS) shape that is unknown and must be determined as a part of the solution. To this aim a pseudo time-stepping procedure is adopted by using the asymptotic expansion (7) as a first guess. Once the free surface shape is assigned, the distribution of the velocity potential along the free surface is obtained by integrating the dynamic boundary condition (5), which is rewritten as $S_\tau = -\sqrt{(1-\sigma_0)\rho^2 - 2\sigma_0 S}$, and then using the relation $\varphi = S + \rho^2/2$. On the wetted part of the body contour (BC) the impermeability condition, $\partial\varphi/\partial n = 0$, is applied.

The solution of the boundary-value problem provides the velocity potential along the wetted part of the body and its normal derivative along both the free surface and the far-field boundary. This allows us to compute ∇S on the free surface and to verify then if the kinematic boundary condition, $\partial S/\partial n = 0$, is satisfied. If not, the free surface shape is updated by using ∇S as a free-surface velocity. Special treatment of the intersection between the free surface and the body contour is required. The angle at the intersection progressively decays and, when it drops below a limit value, the jet is cut off and is replaced by the jet region, where the flow is described within the shallow-water approximation (see section 5). In this way we obtain the shape of the free surface and the distribution of the velocity potential along both the body contour and the free surface. The shallow-water (SW) part is directly included into the boundary integral formulation. In order to clarify the numerical procedure, the boundary integral representation is written for a point $\boldsymbol{x}$ on the boundary of the computational domain, which leads to the following boundary integral equation

$$\frac{1}{2}\varphi(\boldsymbol{x}) + \int_{BC} \varphi(\boldsymbol{y})\frac{\partial G}{\partial n}(\boldsymbol{x}-\boldsymbol{y})ds(\boldsymbol{y}) - \int_{FS\cup FF} \frac{\partial \varphi}{\partial n}(\boldsymbol{y})G(\boldsymbol{x}-\boldsymbol{y})ds(\boldsymbol{y}) = \tag{8}$$

$$\int_{BC\cup SW} \frac{\partial \varphi}{\partial n}(\boldsymbol{y})G(\boldsymbol{x}-\boldsymbol{y})ds(\boldsymbol{y}) - \int_{FS\cup FF\cup SW} \varphi(\boldsymbol{y})\frac{\partial G}{\partial n}(\boldsymbol{x}-\boldsymbol{y})ds(\boldsymbol{y}),$$

where the Cauchy principal value of the integral is taken for the singular ones. It must be noted that for $\boldsymbol{x} \in FF \cup FS$ the velocity potential is assigned and the first term on the left-hand side of (8) is moved to the right-hand side of the equation.

In Fig. 2 a close up view of the region about the matching between the intermediate region and the shallow water part is shown. On the left picture the geometry is shown whereas the distribution of the modified velocity potential versus λ is shown on the right. In both cases the transition between the two regions is very regular.

Two different checks were performed to evaluate the convergence of the solution and its accuracy (Fig. 3). The integral of $(\partial S/\partial n)^2$ along the free surface can be regarded as a measure of the accuracy at which the kinematic boundary condition is satisfied. Moreover, the area enclosed between the disturbed free surface and its initial level, $\mu = 0$, is computed and compared with the incoming flow from the far field boundary, in order to check the mass conservation. Results show that convergence is achieved after about 1500 iterations (Fig. 3).

Finally, calculations are performed by varying the far field extension of the computational domain ($R = 40$ and 28) and different values of the limit angle (10° and 5°) for the matching with the shallow-water solution. In both cases results show that the solution is essentially independent of those parameters (see Fig. 4), provided they are properly chosen so that the corresponding asymptotic expansions hold.

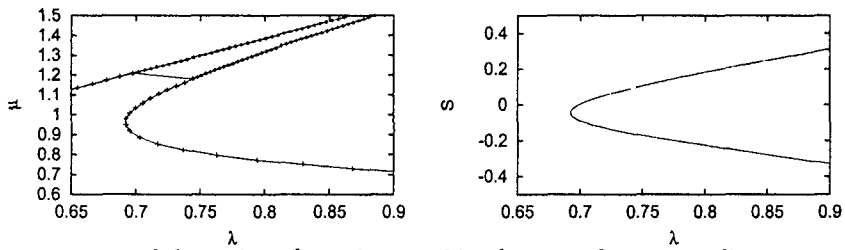

Figure 2: *Close up view of the region about the matching between the intermediate region and the shallow water part.* ($\gamma = 60°$)

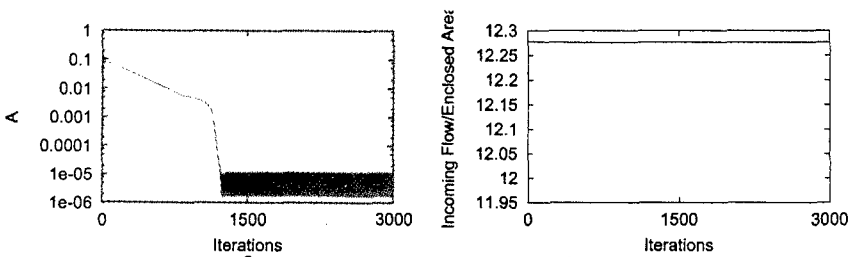

Figure 3: left) *Integral of* $(\partial S/\partial n)^2$ *along the free surface;* right) *Incoming flow and area enclosed by the free surface.*

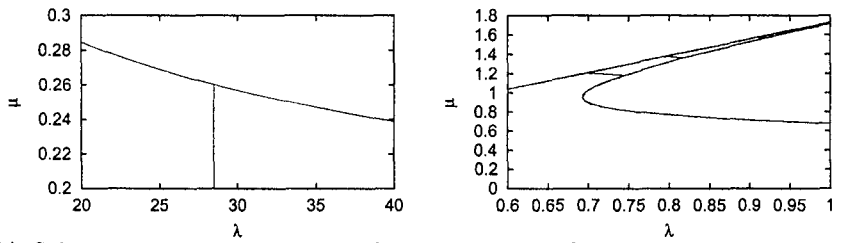

Figure 4: left) *Solutions obtained with two different extension of the computational domain are compared close to the end of the shorter domain;* right) *Solutions obtained by using two different values of the limit angle for the cut of the jet are compared in the matching region.*

Acknowledgments

A.A.K. acknowledges the support from RFBR (projects No. 00-01-00839 and No. 00-15-96162) and SB RAS (integrated grant No. 1). A.I. acknowledges the support from *Ministero dei Trasporti e Navigazione* in the framework of the INSEAN research plan 2000-02.

References

SEDOV, L.I.: *Floating wedge impact*, Tr. Tsentr. Aerodin. Inst., 152, pp. 27-31 (1935).

IAFRATI, A., KOROBKIN, A.A.: *Liquid flow close to intersection point*, Proc. 15th Workshop on Water Waves and Floating Bodies, (2000).

(Abstract for the 16th International Workshop on Water Waves and Floating Bodies, April 2001)

Side Wall Effects of a Towing Tank on Measured Unsteady Waves in Low Frequency Range

Hidetsugu IWASHITA
Engineering Systems, Hiroshima University
1-4-1 Kagamiyama, Higashi-Hiroshima 739-8527, JAPAN

1. INTRODUCTION

Several kinds of numerical method to estimate hydrodynamic forces and motions of ships advancing in waves have been developed up to now. Typical examples, for instance, will be the Green function method and the Rankine panel method in the three dimension. Especially the Rankine panel method may be the main current of the most recent studies from the reason that it enables to apply more exact free surface condition. It also enables to apply the numerical beach tequnique for the radiation condition when the method is extended to the time domain. It is reported that it works well even for the low frequency range. In those methods, the Rankine source is used as the kernel function of the integral equation. Therefore adequate numerical techniques must be introduced for satisfying the radiation condition and some techniques have been already proposed. The validation of the numerical accuracy due to those teqniques, however, have not been attempted enoughly for the low frequency range. This comes from few experimental data because of the difficulty of the experiment in the low frequency range.

On the other hand, it is suggested that the comparison of the numerical results with experiments on hydrodynamic forces and motions is not sufficient for the validation of the computation codes based on advanced and complicated methods proposed nowadays[1][2]. Actually it is very few to see the remarkable advantage of such advanced methods against the strip method if we adopt those physical values for an index of validation. The local physical value such as pressures should be used to make clear the advantage of advanced methods.

From these backgrounds, Iwashita et al.[1][2] carried out a systematic experiment for a blunt VLCC and measured not only the hydrodynamic forces but also the wave pressure acting on the ship advancing in oblique waves. In the experiment the low frequency range where the reduced frequency $\tau(= U\omega_e/g)$ takes smaller value than 0.25 appears in wide range depending on the attack angle of the incident wave, and the importance of the low frequency range has been realized. Experiments were compared with some kinds of computation and the importance of the comparison on the wave pressure has been also pointed out in the paper. Similar experiments have been performed in the same way by some companies in Japan. However most of the hull forms are confidential. We therefore can not utilize their experimental data for the validation of our computation codes. One of the reason why companies hesitate to present their experimental data may be related to the expensive cost and much time to get experimental data on the wave pressure. This may be settled if the local physical value can be measured more easily and cheaply.

Iwashita [3] carried out the experiment for popular hull forms, Series-60 ($C_b = 0.6$ and 0.8), in order to get data which everybody can use. The unsteady waves measured by Ohkusu's method [5] were adopted as the local physical value and plenty of wave patterns were obtained through the experiments carried out in 1999 and 2000. The unsteady wave pattern physically means the unsteady pressure distribution on the free surface and its measurement is not so difficult and expensive. In the experiment, so called k_2 wave system which propagates from the ship to the forward direction and k_1 wave system which propagates from downstream toward the ship have been observed for $\tau = 0.23$. The k_1 wave with large amplitude which propagates from downstream toward the ship and disappears at bow region has been also observed for $\tau = 0.28$. These are very interesting phenomena in the low frequency range arround $\tau = 0.25$. In order to utilize those measured unsteady waves for

the validation of the computation codes, measured data itself must be validated on the effect of the side wall of the towing tank, which will be involved in the obtained data.

In this study the side wall effect of the towing tank on measured unsteady waves is investigated by simulating the actual experiment numerically. The thin ship theory is applied in the time domain and the radiation problem is solved corresponding to the experiment. The numerical result obtained considering side wall effect is compared with the result obtained excluding side wall effect, and the effect of the side wall is made clear.

2. FORMULATION

The problem is simplified restricting our interest only in the radiation problem since both radiation and diffraction wave systems generated by the ship takes the same pattern as understood by the asymptotic theory. Then we consider a thin ship advancing at arbitrary forward speed $U(t)$ and oscillating with cirlular frequency ω_e in the towing tank. The space fixed coordinate system is taken allocating its origin at beach side of the tank. The ship motions are restricted in heave and pitch modes corresponding to the experiment and we express them by $\xi_3(t)$ and $\xi_5(t)$. The linear theory is employed for this problem assuming ideal potential flow.

The velocity potential $\phi(x,y,z;t)$ of the fluid must satisfy the following initial and boundary conditions[4]:

$$[\mathrm{L}] \quad \nabla^2\phi = 0 \qquad \text{in } V(t) \text{ for } t > \tau \tag{1}$$

$$[\mathrm{F}] \quad \Big(\frac{\partial^2}{\partial t^2} + g\frac{\partial}{\partial z}\Big)\phi = 0 \qquad \text{on } z = 0 \text{ for } t > \tau \tag{2}$$

$$[\mathrm{H}] \quad \frac{\partial\phi}{\partial n} = V_n \qquad \text{on } S_H \text{ for } t > \tau \tag{3}$$

$$[\mathrm{W}] \quad \frac{\partial\phi}{\partial n} = 0 \qquad \text{on } S_W \text{ for } t > \tau \tag{4}$$

$$[\mathrm{I}] \quad \phi = \frac{\partial\phi}{\partial t} = 0 \qquad \text{on } z = 0 \text{ for } t = \tau \tag{5}$$

S_H and S_W denote the ship surface and the side wall of the towing tank respectively. When we assume a thin ship which body shape is expressed by $F(x,y,z) = y - f(x,z) = 0$, the body boundary condition (3) can be simplified as

$$\frac{\partial\phi}{\partial y} = \Big\{-[U(t) + z\,\xi_5(t)]f_x - [\xi_3(t) - x\,\xi_5(t)]f_z\Big\}\Big/\sqrt{1 + f_x^2 + f_z^2} \tag{6}$$

Applying the Green's second identity to the fluid domain, we obtain the following two sets of equation:

$$\sigma(P;t) = 2\Big\{-[U(t) + z\,\xi_5(t)]f_x - [\xi_3(t) - x\,\xi_5(t)]f_z\Big\}\Big/\sqrt{1 + f_x^2 + f_z^2} \quad \text{for } P \text{ on } S_H \tag{7}$$

$$\begin{aligned}\frac{\partial\phi(P;t)}{\partial n_P} =& -\iint_{S_H(t)} \sigma(Q;t)\frac{\partial G_0(P,Q)}{\partial n_P}\,dS_Q \\ &- \int_0^t \Big\{\iint_{S_H(\tau)} \sigma(Q;\tau)\frac{\partial G_T(P,Q;t-\tau)}{\partial n_P}\,dS_Q\Big\}\,d\tau \\ &+ \frac{\sigma_W(P;t)}{2} - \iint_{S_W(t)} \sigma_W(Q;t)\frac{\partial G_0(P,Q)}{\partial n_P}\,dS_Q \\ &- \int_0^t \Big\{\iint_{S_W(\tau)} \sigma_W(Q;\tau)\frac{\partial G_T(P,Q;t-\tau)}{\partial n_P}\,dS_Q\Big\}\,d\tau \quad \text{for } P \text{ on } S_W\end{aligned} \tag{8}$$

where P and Q show the field point and the source point respectively. G_0 and G_T are the impulse response functions defined by

$$G_0(P,Q) = \frac{1}{4\pi}\Big(\frac{1}{r} - \frac{1}{r'}\Big), \quad G_T(P,Q;t-\tau) = \frac{1}{2\pi}\int_0^\infty \sqrt{gk}\sin(\sqrt{gk}(t-\tau))e^{k(z+z')}J_0(kR)\,dk \tag{9}$$

$$\left.\begin{matrix} r \\ r' \end{matrix}\right\} = \sqrt{R^2 + (y-y')^2 + (z \mp z')^2}, \quad R = \sqrt{(x-x')^2 + (y-y')^2} \tag{10}$$

We need not to solve the integral equation to determine the source distribution on S_H since it is determined explicitly by eq.(7).

If the source distribution is determined on the side wall for every time step, the wave elevation $\zeta(P;t)$ is evaluated by

$$-g\zeta(P;t) = -\int_0^t \left\{ \iint_{S_H(\tau)} \sigma(Q;\tau) \frac{\partial G_T(P,Q;t-\tau)}{\partial t} \, dS_Q \right\} d\tau$$
$$- \int_0^t \left\{ \iint_{S_W(\tau)} \sigma_W(Q;\tau) \frac{\partial G_T(P,Q;t-\tau)}{\partial t} \, dS_Q \right\} d\tau \quad \text{on } z = 0 \tag{11}$$

The forward speed $U(t)$ and motions $\xi_3(t)$, $\xi_5(t)$ are arbitrary functions in the present study. Therefore the kernel functions G_0 and G_T must be calculated for all P and Q at each time step.

3. NUMERICAL CALCULATION

The numerical calculation is carried out simulating the actual measurement of radiation waves experimented at RIAM in Kyushu University by the author. The towing tank ($L \times B \times D = 65\text{m} \times 5\text{m} \times 7\text{m}$) is descretized into the finite number of elements, and the forward speed $U(t)$ and motions $\xi_3(t)$, $\xi_5(t)$ are given refering measured results.

Computations are performed mainly for $\tau = 0.23$ and $\tau = 0.28$. For $\tau = 0.23$, k_2 wave system and k_1 wave system progressing in forward direction has been observed remarkably in the experiment, Figs.1,3. For $\tau = 0.28$ the wave progressing in forward direction with large amplitude and disappearing in front of the ship has been observed, Figs.2,4. Present numerical simulations are compared with those results, and we validate how the side wall of the towing tank affects the measured results and whether the measured results are reliable or not. If it is confirmed that the side wall effect is not so significant, we can utilize measured radiation waves for the validation of arbitrary numerical methods in the low frequency range.

4. SAMPLE OF RESULTS

Figs.5 and 6 show the wave elevation due to the point source advancing at forward speed $U(t)$ and pulsating as a function $\sigma(t)$. $U(t)$ and $\sigma(t)$ are given by $U(t) = U_0(1 - e^{-dt})$ and $\sigma(t) = (1 - e^{-ct})(a + b\cos\omega_e t)$. Constants are $a = 0.0(\text{m}^3/\text{s})$, $b = 1.0(\text{m}^3/\text{s})$, $c = d = 2.0$, $U_0 = 0.886(\text{m/s})$, $\omega_e = 2.55(1/\text{s})$ in this example. The point source is located at $Q = (x'(t), 0, -0.2)$ and starts from $x'(0) = 5.0(\text{m})$. The wave elevation is computed along the longitudinal axis of $y = 0.2(\text{m})$.

Figures show that the present computation ('TD' in figures) near the source point converges to the result of the frequency domain ('FD') around $t > 30$. The correponding results considering side wall effect are illustrated in Figs.7 and 8. The wave reflection from the side wall can be seen by comparing them with Figs.5 and 6.

Further calculations for the thin ship and for other conditions are now in progress, and all the results will be presented in the workshop.

REFERENCES

[1] IWASHITA, H., ITO, A., OKADA, T., OHKUSU, M., TAKAKI, M., MIZOGUCHI, S. (1993), *Wave Forces Acting on a Blunt Ship with Forward Speed in Oblique Sea (2nd Report)*, J. Soc. Naval Arch. Japan, Vol. 173 (in Japanese)

[2] IWASHITA, H., ITO A. (1998), *Seakeeping Computations of a Blunt Ship Capturing the Influence of the Steady Flow*, Ship Technology Research, Vol. 45/4

[3] IWASHITA, H., (2000), *On Unsteady Waves Generated by a Blunt Ship with Forward Speed*, Proc. of 15th IWWWFB, Israel

[4] LIN, W. M. & YUE D. (1990), *Numerical Solutions for Large-Amplitude Ship Motions in the Time Domain*, Proc. 18th Symposium on Naval Hydrodynics

[5] OHKUSU, M. (1977), *Analysis of Waves Generated by a Ship Oscillating and Running on a Calm Water with Forward Velocity*, Jounal of The Society of Naval Architects of Japan, Vol.142

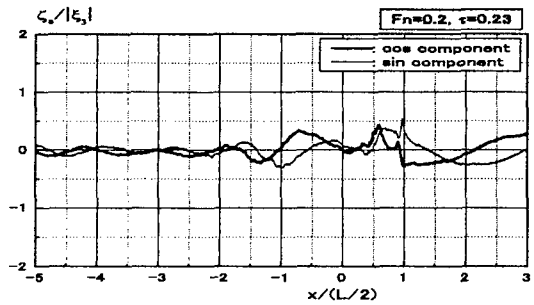

Fig.1 Heave radiation wave for Series-60 ($C_b = 0.8$) measured at $y/(B/2) = 1.32$, $F_n = 0.2$, $\tau = 0.23$

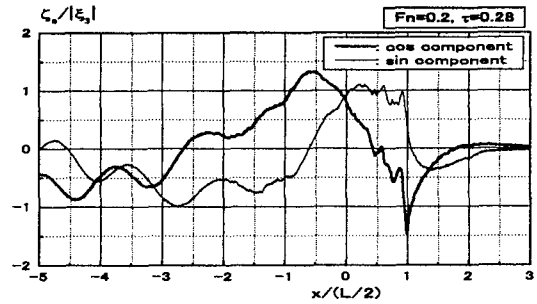

Fig.2 Heave radiation wave for Series-60 ($C_b = 0.8$) measured at $y/(B/2) = 1.32$, $F_n = 0.2$, $\tau = 0.28$

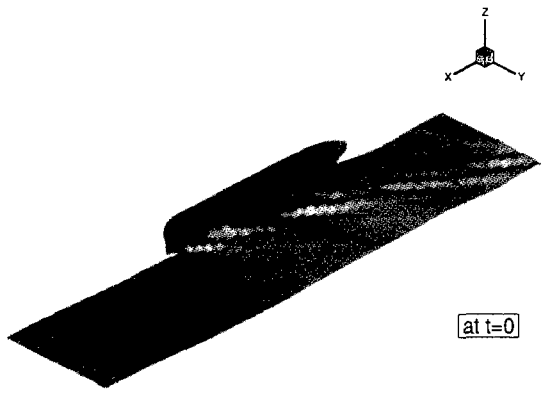

Fig.3 Perspective view of heave radiation wave for Series-60 ($C_b = 0.8$) measured at $F_n = 0.2$, $\tau = 0.23$

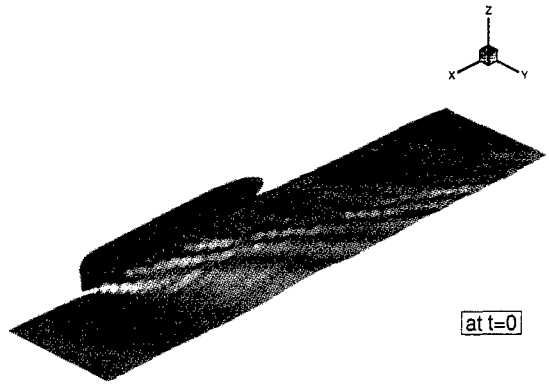

Fig.4 Perspective view of heave radiation wave for Series-60 ($C_b = 0.8$) measured at $F_n = 0.2$, $\tau = 0.28$

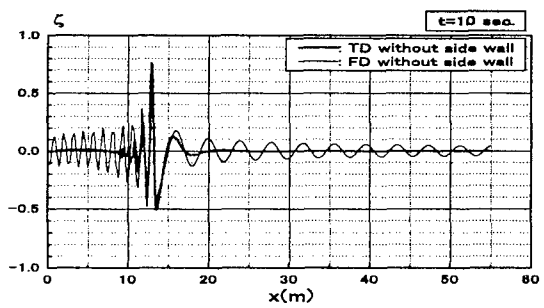

Fig.5 Unsteady wave generated by a point source at $y = 0.2$, $t = 10$ sec.

(corresponding to $F_n = 0.2$, $\tau = 0.23$)

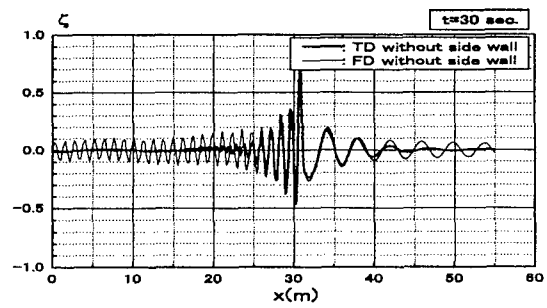

Fig.6 Unsteady wave generated by a point source at $y = 0.2$, $t = 30$ sec.

(corresponding to $F_n = 0.2$, $\tau = 0.23$)

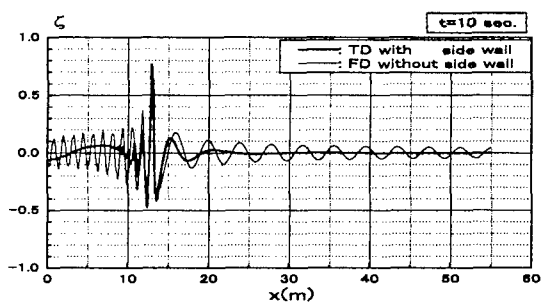

Fig.7 Unsteady wave generated by a point source in the tank at $y = 0.2$, $t = 10$ sec.

(corresponding to $F_n = 0.2$, $\tau = 0.23$)

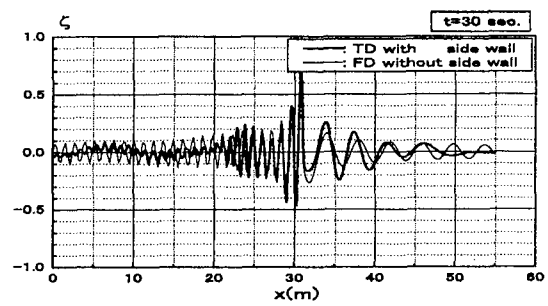

Fig.8 Unsteady wave generated by a point source in the tank at $y = 0.2$, $t = 30$ sec.

(corresponding to $F_n = 0.2$, $\tau = 0.23$)

WATER WAVE SCATTERING BY INCLINED BARRIER SUBMERGED IN FINITE DEPTH WATER

Mridula Kanoria[1] and B.N. Mandal[2]

[1] Department of Applied Mathematics, Calcutta University,India

[2] Physics and Applied Mathematics Unit, Indian Statistical Institute,India

1. Introduction : Water wave scattering problems involving thin barrier of arbitrary shape submerged in finite depth water are generally tackled by some approximate techniques assuming linear theory. The technique of hypersingular integral equation is demonstrated here in tackling the problem of water wave scattering by an inclined thin barrier submerged in *finite depth water*. The corresponding *deep water* problem was earlier investigated by Parson and Martin[1]. An appropriate use of Green's integral theorem produces a representation of the velocity potential describing the irrotational motion in the fluid region, in terms of the unknown dicontinuity of the potential across the submerged barrier. Utilization of the boundary condition on the barrier gives rise to an integro-differential equation for the discontinuity, which is interpreted as equivalent to a hypersingular integral equation. This is solved numerically by approximating the discontinuity in terms of a finite series involving Chebysev polynomials of the second kind followed by a collocation method. The reflection and transmission coefficients are then estimated numerically using this solution. The force and moment(about the origin) acting on the barrier per unit width are also estimated for various positions of the barrier. Comparison is made with available deep water results. It is observed that if the mid point of the barrier is submerged to the order of one-tenth of the bottom depth, then the deep water results effectively hold good, and in that case, the finite depth problem can be modelled as deep-water problem.

2. Mathematical formulation : Let a thin straight inclined barrier Γ be submerged in water of uniform finite depth h, and let d be the depth of its mid point below the mean free surface and the co-ordinate system be so chosen that the position of Γ is described by $y = d + ta\cos\theta, x = ta\sin\theta (-1 \leq t \leq 1, d > a\cos\theta, h > d + a\cos\theta, 0 \leq \theta \leq 90^0, \theta$ being the angle of inclination of the barrier with the vertical). A train of surface water waves of amplitude b_0 and circular frequency σ is incident from the direction of $x = -\infty$ on the barrier. The incident wave potential $Re\{\phi_0(x,y)e^{-i\sigma t}\}$ with

$$\phi_0(x,y) = \frac{gb_0}{\sigma}\frac{\cosh k_0(h-y)e^{ik_0x}}{\cosh k_0 h}$$

where k_0 is the unique positive real root of the transcendental equation $k\tanh kh = K$, with $K = \sigma^2/g$, g being the gravity. The ensuing motion in the fluid region described by velocity potential $Re\{\phi(x,y)e^{-i\sigma t}\}$ where $\phi(x,y)$ satisfies

$$\nabla^2\phi = 0, \quad 0 \leq y \leq h$$

$$K\phi + \frac{\partial\phi}{\partial y} = 0 \quad \text{on } y = 0,$$

$$\frac{\partial\phi}{\partial n} = 0 \quad \text{on } \Gamma$$

where $\frac{\partial}{\partial n}$ denotes normal derivatives on Γ,

$$r^{1/2}\nabla\phi \text{ is bounded as } r \to 0$$

where r is the distance from the submerged edges of Γ,

$$\frac{\partial \phi}{\partial y} = 0 \quad \text{on } y = h$$

$$\phi(x,y) \to \begin{cases} T\phi_0(x,y) & \text{as } x \to \infty, \\ \phi_0(x,y) + R\phi_0(-x,y) & \text{as } x \to -\infty \end{cases}$$

where R and T are respectively the unknown reflection and transmission coefficients (complex) which will be determined in the course of mathematical analysis.

3. The method of solution : By an appropriate use of Green's integral theorem in the fluid region a representation of $\phi(\xi,\eta)$ at a point $p \equiv (\xi,\eta)(0 < \eta < h)$ is found to be

$$\phi(\xi,\eta) = \phi_0(\xi,\eta) - \frac{1}{2\pi}\int_\Gamma F(q)\frac{\partial G}{\partial n_q}(x,y:\xi,\eta)ds_q \tag{3.1}$$

where $F(q)$ the discontinuity of $\phi(x,y)$ across Γ and $q \equiv (x,y)$ is a point on Γ, and $\frac{\partial}{\partial n_q}$ denotes the normal derivatives at q on Γ, and $G(p;q)$ is given by (cf Banerjea *et al* [2])

$$G(x,y:\xi,\eta) = ln\frac{r}{r'} - 2\int_{C_1}\frac{e^{-k(y+\eta)}}{k-K}\cos k(x-\xi)dk - 2\int_{C_2}\frac{e^{-kh}L(k,y)L(k,\eta)}{k(k-K)\Delta(k)}\cos k(x-\xi)dk \tag{3.2}$$

where $r, r' = \{(x-\xi)^2 + (y \mp \eta)^2\}^{1/2}$,

$$L(k,y) = k\cosh ky - K\sinh ky, \;\; \Delta(k) = k\sinh kh - K\cosh kh, \tag{3.3}$$

and the paths C_1, C_2 are along the positive real axis in the complex k-plane indented below the pole at $k = K$ for C_1 and below the poles at $k = K$, k_0 for C_2.The boundary condition on Γ produces an integro-differential equation, which can be interpreted as the following *hypersingular* integral equation in [1]

$$\frac{1}{2\pi}\not\int_\Gamma F(q)\frac{\partial^2 G(p;q)}{\partial n_p \partial n_q}ds_q = \frac{\partial \phi_0}{\partial n_p}, \;\; p \in \Gamma \tag{3.4}$$

for the determination of $F(q)$, where the cross on the integral sign indicates that it is to be interpreted as a Hadamard finite part integral.

Denoting ξ, η by $\xi = ua\sin\theta, \;\; \eta = d + ua\cos\theta, \;\; -1 \le u \le 1$ it can be shown that

$$\frac{\partial^2 G(p;q)}{\partial n_p \partial n_q} = -\frac{1}{a^2}\left[\frac{1}{(u-t)^2} - \mathcal{K}(u,t)\right]. \tag{3.5}$$

where $\mathcal{K}(u,t)$ is a regular function of u,t, and can be expanded in a form suitable for numerical computation. The details of this expansion is ommitted here. However, this expansion is an important step in this work.

The hypersingular integral equation (3.4) can be rewritten as

$$\not\int_{-1}^{1}\left[\frac{1}{(u-t)^2} + \mathcal{K}(u,t)\right]f(t)dt = l(u), \quad -1 < u < 1 \tag{3.6}$$

$$f(t) = \frac{gb_0}{\sigma}F(t) \tag{3.7}$$

and $l(u)$ is a known function (it is related to ϕ_0). The equation (3.6) is to be solved subject to the condition that

$$f(\pm 1) = 0. \tag{3.8}$$

As in [1] $f(t)$ is approximated as

$$f(t) = (1-t^2)^{1/2} \sum_{n=0}^{N} a_n U_n(t) \tag{3.9}$$

where $U_n(t)$ is Chebyshev polynomial of the second kind. and $a_n (n = 0, 1, ..N)$ are unknown complex constants. Substituting (3.9) into (3.6), we obtain

$$\sum_{n=0}^{N} a_n A_n(u) = l(u), \quad -1 < u < 1, \tag{3.10}$$

where $A_n(u) = -\pi(n+1)U_n(u) + \int_{-1}^{1} (1-t^2)^{1/2} \mathcal{K}(u,t) U_n(t) dt.$

To find the unknown constant $a_n (n = 0, 1, ...N)$ we put $u = u_j (j = 0, 1, ..N)$ in the relation (3.10) to obtain the linear system

$$\sum_{n=0}^{N} a_n A_n(u_j) = l(u_j) \quad j = 0, 1, ...N \tag{3.11}$$

The collocation points $u_j (j = 0, 1, ..N)$ are chosen as [1]

The reflection and transmission coefficients R and T can be found in terms of a series involving a_n by making $\xi \to \mp\infty$ in the expression for $\phi(\xi, \eta)$ given in (3.1). Expressions for R, T involve certain integrals which can be evaluated numerically for different values of the physical parameters $Ka, h/a, d/a$ and the angle θ of inclination of the barrier with the vertical. Thus once the complex constants $a_n (n = 0, 1, ..N)$ are found by solving the linear system (3.11), numerical estimates for $|R|$ and $|T|$ can be obtained. Also $|R|^2 + |T|^2$ must be unity from the consideration of energy principle, this can be used to check the correctness of numerical estimates obtained for $|R|$ and $|T|$. The amplitudes of the force and moment (about the origin) per unit width of the barrier can also be estimated numerically once $a_n (n = 0, 2, ..N)$ are obtained.

4. Numerical results : The numerical estimates for $|R|$ converges fairly rapidly with N. An accuracy of almost five decimal places has been achieved by choosing $N = 3$ or 4. Also the correctness of the numerical method is checked by estimating $|R|$ for the case of a submerged vertical plate ($\theta = 0^0$) and comparing with known results obtained earlier in [3] by eignefunction expansion method. Again, for $\theta = 45^0, a/h = 0.4, d/h = 0.4$, $|R|$ and $|T|$ are estimated by the present method, and it has been verified that $|R|^2 + |T|^2$ almost coincide with unity.

$|R|$ is depicted against the wave number Ka in figure 1 taking $\theta = 45^0$ for different values of d/h keeping d/a fixed. It is observed that when the depth of the mid point of the inclined barrier is one-tenth of the bottom depth ($d/h = 0.1$), the results almost coincide with deep-water results given in [1] and shown in the same figure by crosses. The bottom effect appears to be significant in the low wave number range. This may be attributed due to the fact that in the low wave number range, the wave length of the incident wave train is large enough to have adequate penetration below the free surface so as to be affected significantly by the bottom while in the large wave number range the reverse phenomenon occurs and as such there is no appreciable effect is observed.

In figure 2 $|R|$ depicted against Ka for an almost horizontal barrier by taking $\theta = 89^0$. As observed in [1] for the case of deep water, zero of $|R|$ are seen to occur for the case of finite depth water. The zeros of $|R|$ begin to appear only when the inclination of the barrier with the vertical is of the order of 80^0. This is not shown here. The non-dimensional amplitude of the force and moment(about the

origin) acting on the barrier per unit width are depicted in figure 3 and 4 respectively. It is observed from these figures that the amplitudes decrease with the increase of θ. These results are plausible.

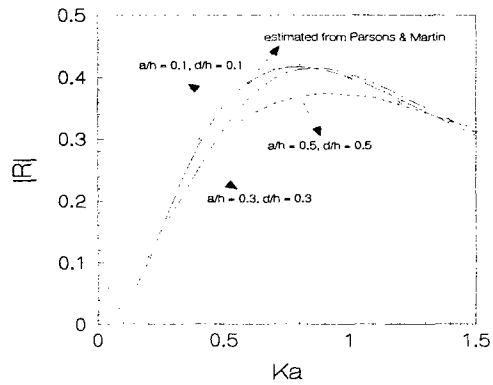

Fig. 1: Reflection coefficient vs wave number, $\theta = 45^0$

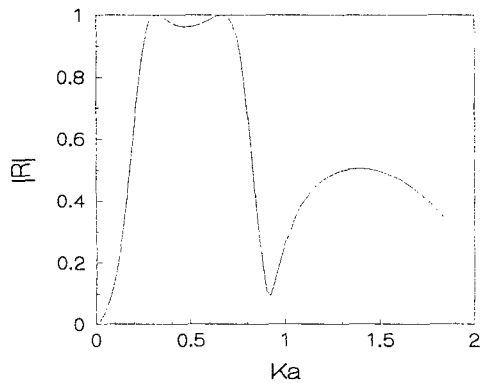

Fig. 2: Reflection coefficient vs wave number, a/h = 0.8,d/h = 0.1,$\theta = 89^0$

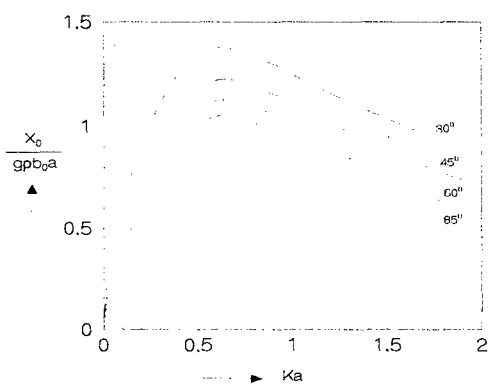

Fig. 3: Amplitude of the force per unit width vs wave number a/h=.3,d/h=.3

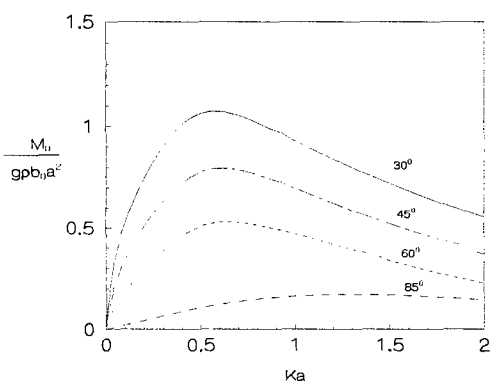

Fig. 4: Amplitude of moment per unit width vs wave number d/h=0.3,a/h=0.3

5. Conclusion : Water wave scattering by an inclined barrier plate submerged in *finite depth* water is investigated by using a hypersingular integral equation formulation. Numerical estimates for the reflection coefficient, amplitudes of force and moment acting on the barrier are obtained fairly accurately and are depicted graphically against the wave number and compared with deep-water results. Also, some numerical results for an almost horizontal barrier are obtained as special cases, and these agree with known results obtained by other methods. The technique used here is now being used to tackle water wave scattering problems involving a *curved* barrier in the form of an arc of a circle, ellipse etc. submerged in finite depth water . The method can also be used with some modification for a surface piercing curved barrier.

This work is partially supported by CSIR, New Delhi.

References

1. Parsons, N. F.; Martin, P. A. ,*Appl. Ocean Res.* **14** (1992) 313-321.
2. Benerjea, S.; Dolai, D.P. ; Mandal, B.N. ,*Arch. Appl. Mech.* **67** (1996) 35-43.
3. Mandal, B.N. and Dolai, D.P., *Appl. Ocean Res.* **16** (1994) 195-203.

Abstract for the 16th Intl Workshop on Water Waves and Floating Bodies, Hiroshima, April 2001

Second-Order Steady Forces on Multiple Cylinders in a Rectangular Periodic Array

by Masashi KASHIWAGI
Research Institute for Applied Mechanics, Kyushu University
6-1 Kasuga-koen, Kasuga-city, Fukuoka 816-8580, Japan

1. Introduction

Effects of hydrodynamic interactions among multiple cylinders must be expected not only on the first-order forces and wave-induced motions but also on higher-order hydrodynamic quantities. The present paper is concerned with the characteristics of second-order steady forces on each cylinder in a rectangular array composed of many identical cylinders with equal separation distance.

Recently, Kashiwagi (2000) presented an effective calculation method for the wave drift force on the basis of the momentum conservation principle. However, this method (referred to as the far-field method) gives only the total forces in the horizontal plane and the yaw moment on the whole structure.

Meanwhile, the wave drift force can also be computed by integrating the pressure over the wetted surface of a structure, which enables us to evaluate the local forces on each cylinder. Based on this direct pressure-integration method, an accurate numerical calculation method is presented in this paper. Validity and numerical accuracy of the method are confirmed by comparison with the results of the far-field method and experimental results measured using 64 truncated circular cylinders arranged in 4 rows and 16 columns.

2. Formulation and Second-Order Forces

A column-supported large floating structure is considered, which comprises a thin upper deck and a large number of identical and equally-spaced buoyancy columns. The elementary column considered here is a truncated circular cylinder with radius a and draft d. The distance between centerlines of adjacent cylinders is $2s$ in both x- and y-axes of a Cartesian coordinate system. The positive z-axis is directed downward, with $z = 0$ the undisturbed free surface and $z = h$ the constant water depth.

The structure is allowed to move with unsteady motions of six degrees of freedom in response to the wave excitation. The vectors of the translational and rotational motions are denoted by $\boldsymbol{\xi}(t)$ and $\boldsymbol{\alpha}(t)$, respectively; the magnitudes of which are assumed to be small. Under the usual potential-flow assumptions, we introduce the velocity potential, Φ, with which the hydrodynamic pressure can be computed from Bernoulli's equation. Then the wave force on a body can be obtained by integrating the pressure multiplied by the unit normal vector over the instantaneous body's wetted surface, say $S(t)$.

Assuming weak nonlinearities, the velocity potential and the motion vectors can be written as a perturbation series in a small parameter which is usually taken as the wave slope. Furthermore, using Taylor's expansion for the pressure and unit normal vector on $S(t)$ with respect to the mean body surface, S_B, the wave forces on a body can be expressed also in a perturbation series. Skipping details of the derivation (see Ogilvie (1983) for example), the calculation formulae for the first-order and second-order forces can be summarized as follows:

$$\boldsymbol{F}^{(1)} = \rho \iint_{S_B} \frac{\partial \Phi^{(1)}}{\partial t} \boldsymbol{n}\, dS - \rho g \iint_{S_B} \Xi_3^{(1)} n_3 \boldsymbol{k}\, dS, \tag{1}$$

$$\boldsymbol{F}^{(2)} = \rho \iint_{S_B} \frac{\partial \Phi^{(2)}}{\partial t} \boldsymbol{n}\, dS - \rho g \iint_{S_B} \Xi_3^{(2)} n_3 \boldsymbol{k}\, dS + \boldsymbol{F}_q^{(2)}, \tag{2}$$

where

$$\begin{aligned} \boldsymbol{F}_q^{(2)} = {} & \frac{1}{2}\rho \iint_{S_B} \left|\nabla \Phi^{(1)}\right|^2 \boldsymbol{n}\, dS - \frac{1}{2}\rho g \oint_{C_B} \{\zeta_R^{(1)}\}^2 \boldsymbol{n}\, d\ell \\ & + \rho \iint_{S_B} \boldsymbol{\Xi}^{(1)} \cdot \nabla\Big(\frac{\partial \Phi^{(1)}}{\partial t}\Big) \boldsymbol{n}\, dS + \boldsymbol{\alpha}^{(1)} \times \boldsymbol{F}^{(1)} \\ & - \rho g \iint_{S_B} \alpha_3^{(1)} \big(\alpha_1^{(1)} x + \alpha_2^{(1)} y\big) n_3 \boldsymbol{k}\, dS. \end{aligned} \tag{3}$$

Here $\zeta_R^{(1)}$ in (3) denotes the first-order relative wave elevation given by

$$\zeta_R^{(1)} = \frac{1}{g} \frac{\partial \Phi^{(1)}}{\partial t}\bigg|_{z=0} - \Xi_3^{(1)}, \tag{4}$$

which must be evaluated along the mean waterline C_B; ρ is the fluid density; g is the gravitational acceleration; $\boldsymbol{n}$ is the unit normal vector directing into the fluid from the mean body surface S_B; $\boldsymbol{\Xi}^{(1)} = \boldsymbol{\xi}^{(1)} + \boldsymbol{\alpha}^{(1)} \times \boldsymbol{r}$ and thus $\Xi_3^{(1)} = \xi_3^{(1)} + \alpha_1^{(1)} y - \alpha_2^{(1)} x$; $\boldsymbol{k}$ is the unit vector in the z-direction of the space-fixed coordinate axes. The corresponding expressions for the moment can be obtained in a similar form.

The present paper is concerned with the second-order steady forces, which can be computed by taking time-average over one period of $\boldsymbol{F}_q^{(2)}$ which contains only quadratic products of first-order quantities.

3. Solution of First-Order Problem

The first-order quantities are assumed to be time-harmonic with circular frequency of the incident wave, ω, and are expressed as

$$\Phi^{(1)} = \mathrm{Re}\Big[\frac{gA}{i\omega} \big\{ \phi_I + \phi_S - K \sum_{k=1}^{6} X_k \big(\phi_k + \varphi_k\big) \big\} e^{i\omega t} \Big], \tag{5}$$

$$\xi_k^{(1)} = \mathrm{Re}\Big[A\, X_k\, e^{i\omega t} \Big], \quad \alpha_k^{(1)} = \mathrm{Re}\Big[\frac{A}{a}\, X_{k+3}\, e^{i\omega t} \Big], \tag{6}$$

where A is the amplitude of the incident wave, $K = \omega^2 a/g$ is the nondimensional wavenumber, and X_j $(j = 1 \sim 6)$ is the complex motion amplitude expressed in a nondimensional form.

ϕ_I and ϕ_S are the incident-wave and scattering potentials, respectively, and the sum, $\phi_I + \phi_S \equiv \phi_D$, is referred to as the diffraction potential. For plane waves propagating in the direction with angle β relative to the positive x-axis, ϕ_I is given by

$$\phi_I = \frac{\cosh k_0(z-h)}{\cosh k_0 h}\, e^{-ik_0(x\cos\beta + y\sin\beta)}, \tag{7}$$

where k_0 is the solution of the wave dispersion relation, $k_0 \tanh k_0 h = K$.

In the radiation problem, ϕ_k in (5) denotes the velocity potential of a single body oscillating in the k-th mode (with no interactions), and φ_k represents the remaining part due to hydrodynamic interactions with radiated and scattered waves by the other bodies, which are essentially the same as the scattering problem.

Therefore the boundary conditions to be satisfied on the body surface, S_B, are given as

$$\frac{\partial \phi_D}{\partial n} = 0, \quad \frac{\partial \phi_k}{\partial n} = n_k, \quad \frac{\partial \varphi_k}{\partial n} = 0, \quad (k = 1 \sim 6) \qquad \text{on } S_B \tag{8}$$

where $\boldsymbol{n} = (n_1, n_2, n_3)$ and $\boldsymbol{r} \times \boldsymbol{n} = (n_4, n_5, n_6)$.

Solutions satisfying (8) and other free-surface and radiation conditions may be obtained by Kagemoto & Yue's interaction theory (1986). The expressions of the velocity potentials appropriate near the j-th body can be summarized as follows:

$$\phi_D^j = \phi_I + \big\{A_S^j\big\}^T \big\{\psi_S^j\big\}, \tag{9}$$

$$\phi_k^j = \big\{\mathcal{R}_k^j\big\}^T \big\{\psi_S^j\big\}, \quad \varphi_k = \big\{A_k^j\big\}^T \big\{\psi_S^j\big\}, \tag{10}$$

where $\big\{A_S^j\big\}$ in (9) and $\big\{A_k^j\big\}$ in (10) are unknown coefficient vectors of scattered waves to be determined, and $\big\{\psi_S^j\big\}$ is the vector comprised of the progressive and evanescent wave components, which are expressed as

$$\big\{\psi_S^j\big\} = \left\{ \begin{array}{l} \dfrac{\cosh k_0(z-h)}{\cosh k_0 h}\, H_m^{(2)}(k_0 r_j)\, e^{-im\theta_j} \\ \dfrac{\cos k_n(z-h)}{\cos k_n h}\, K_m(k_n r_j)\, e^{-im\theta_j} \end{array} \right\}. \tag{11}$$

Here k_n $(n = 1, 2, \cdots)$ denotes the evanescent-mode wavenumbers satisfying $k_n \tan k_n h = -K$. The local cylindrical coordinate system $(r_j,\ \theta_j,\ z)$ has been used, with the origin placed at the center of the j-th body. The number of Fourier series in the θ-direction, m, is taken as 0, ± 1, ± 2, $\cdots$.

Once the velocity potentials are determined, it is straightforward to compute the first-order forces, $\boldsymbol{F}^{(1)}$ defined by (1), on each of the cylinders in the array. The complex amplitude X_k defined in (6) will be determined by solving the motion equations of the structure consisting of many buoyancy cylinders.

4. Outline of Numerical Computations

As the first step of numerical computations, the first-order boundary-value problems for a single cylinder were solved by the boundary element method using 9-point quadratic representations for the surface geometry and velocity potential.

In computing the wave interactions by Kagemoto & Yue's theory, the number of Fourier series in the θ-direction (M) and of evanescent wave modes (N) were determined to be $M = 5$ and $N = 3$ after a convergence check. In this case, the total unknowns for $N_B = 64$ cylinders are $(2M+1) \times (N+1) \times N_B = 2816$. To enhance numerical efficiency, the double symmetry relations with respect to the x- and y-axes were exploited, reducing the number of unknowns to 1/4 (i.e. $2816/4 = 704$).

In computing the second-order steady forces, the spatial derivatives of the velocity potential over the submerged surface, S_B, and the line integral along the waterline, C_B, were evaluated using the boundary condition (8) and quadratic isoparametric representations for the velocity potential and coordinates (x, y, z).

5. Outline of Experiments

A truncated circular cylinder with diameter $D\,(=2a) = 114$ mm was used as an elementary float, and 64 cylinders were arranged in a rectangular array with 4 rows (in the y-axis) and 16 columns (in the x-axis) with equal separation distance of $2s = 2D$ between the centerlines of adjacent cylinders in both x- and y-axes. The draft of cylinders was set to $d = D$ and $2D$, but the results of $d = 2D$ will be mainly shown because there were no essential differences.

Although the effects of wave-induced motions can be taken into account in the calculation method, the motions of the structure were completely fixed, and the experiments were carried out in head waves ($\beta = 0°$). The wave forces were measured by dynamometers at 6 different positions; No. 1, No. 9, and No. 15 Columns. (16 columns are numbered from the upwave side.) By symmetry in head waves, the lines at $y = \pm D$ are called the inside and the lines at $y = \pm 3D$ are called the outside. Then the positions of measured cylinders are distinguished with the column number and the inside or outside line. The frequency range in the measurements was $Ks\,(=\omega^2 s/g) = 0.2 \sim 1.6$ and the wave steepness H/λ (the ratio of wave height to wave length) was set to approximately $1/50$.

6. Results and Discussion

Numerical accuracy of the present method was checked by comparing the sum of the local steady forces on 64 cylinders with independent results by the far-field method developed by Kashiwagi (2000). Some results are shown in Table 1 for the case of $\beta = 30°$, $s = D$, $d = 2D$, and $h = 7.5\,d$. In computing the wave-induced motions, the center of gravity was assumed to be on the water plane, and the radii of gyration in roll, pitch, and yaw modes were set to $0.25B$, $0.25L$, and $0.25L$, respectively, with B and L being the breadth and length of the structure.

Table 1 Steady forces in surge, sway, and yaw on a structure with 64 circular cylinders arranged periodically in the array of 4 rows and 16 columns, computed by the far-field method and the pressure integration method. ($d = 2D$, $s = D$, $h = 7.5\,d$, $\beta = 30°$)

By Far-Field Method (Momentum-Conservation Principle)

	Diffraction Problem			Including Motion Effects		
Ks	FX	FY	MZ	FX	FY	MZ
0.50	0.05413	0.00876	0.00412	0.14638	0.01407	-0.10189
1.00	0.08821	0.04253	0.02977	0.08946	0.04258	0.03098
1.50	1.6217	0.08032	-0.00668	1.6218	0.08030	-0.00606
1.75	3.9364	0.27782	0.40703	3.9369	0.27766	0.40795
2.00	3.2052	0.70410	-0.26574	3.2048	0.70387	-0.26517
2.50	0.98615	0.50644	-0.37112	0.98633	0.50677	-0.37146

By Near-Field Method (Direct Pressure Integration)

	Diffraction Problem			Including Motion Effects		
Ks	FX	FY	MZ	FX	FY	MZ
0.50	0.05576	0.00874	0.00343	0.17035	0.01336	-0.10203
1.00	0.08868	0.04209	0.02975	0.08997	0.04213	0.03099
1.50	1.6222	0.08027	-0.00664	1.6223	0.08025	-0.00602
1.75	3.9368	0.27791	0.40708	3.9373	0.27775	0.40799
2.00	3.2056	0.70419	-0.26571	3.2052	0.70396	-0.26513
2.50	0.98646	0.50627	-0.37130	0.98664	0.50661	-0.37164

We can see from Table 1 that very good agreement exists between the far-field method and the present pressure-integration method. For higher frequencies, the steady surge (FX) and sway (FY) forces and steady yaw moment (MZ) were dominated by the diffraction component, because the structure considered here is large in size compared to the wavelength of the incident wave and thus the wave-induced motions are relatively small.

Computed local steady forces acting on elementary cylinders are shown from Fig. 1 through Fig. 6 together with measured results. From these figures we can observe the followings:

1) At the upwave side (Column No. 1), variation of the steady force is rapid in the frequency range lower than the near trapped-mode frequency ($Ks \simeq 1.24$ in the present case), but this variation becomes mild as the position of the cylinder concerned goes downstream.

2) For frequencies higher than $Ks = 1.24$, the local steady forces on upwave cylinders become positive and large, dominating the total drift force on the structure.

3) The steady force on a cylinder along the inside line in the array is larger than that on a cylinder along the outside line in the variation amplitude with respect to the frequency.

4) Computed results by the present method are in good agreement with measured results, except for the very narrow frequency range just below the near trapped-mode frequency.

References

[1] Kashiwagi, M. (2000): "Wave Drift Force and Moment on a VLFS Supported by a Great Number of Floating Columns", *Proc. 10th International Offshore and Polar Engineering Conf.*, Seattle, Vol. 1, pp. 49–56

[2] Ogilvie, T.F. (1983): "Second Order Hydrodynamic Effects on Ocean Platforms", *International Workshop on Ship and Platform Motion*, Berkeley, pp. 205–265

[3] Kagemoto, H. and Yue, D.K.P. (1986): "Interactions among Multiple Three-Dimensional Bodies in Water Waves: An Exact Algebraic Method", *Journal of Fluid Mechanics*, Vol. 166, pp. 189–209

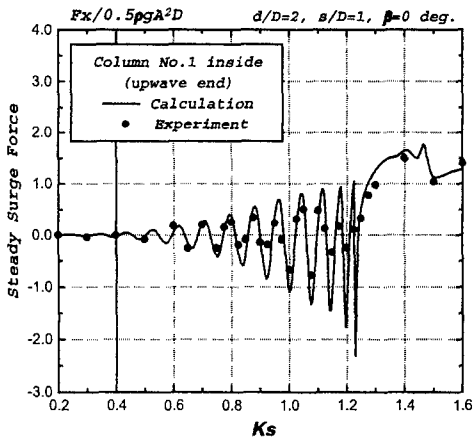

Fig. 1 Steady surge force on the cylinder at Column No. 1 along the inside line

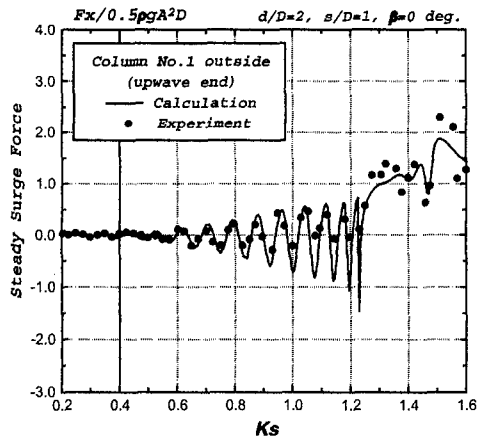

Fig. 2 Steady surge force on the cylinder at Column No. 1 along the outside line

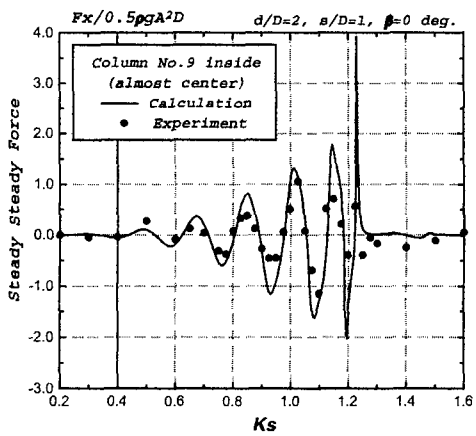

Fig. 3 Steady surge force on the cylinder at Column No. 9 along the inside line

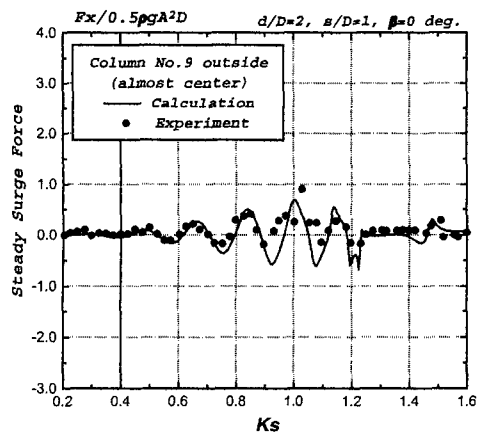

Fig. 4 Steady surge force on the cylinder at Column No. 9 along the outside line

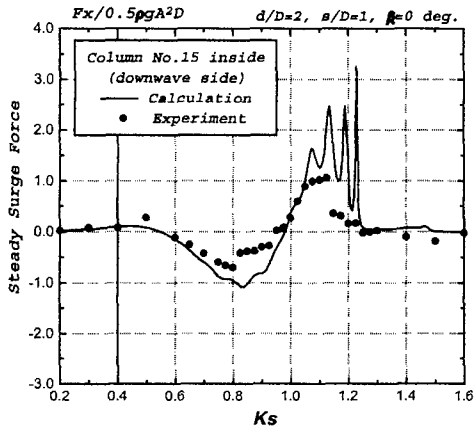

Fig. 5 Steady surge force on the cylinder at Column No. 15 along the inside line

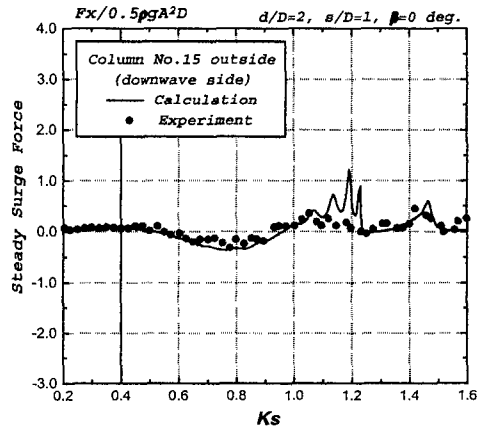

Fig. 6 Steady surge force on the cylinder at Column No. 15 along the outside line

REDUCTION OF HYDROELASTIC RESPONSE OF FLOATING PLATFORM IN WAVES

T.I. Khabakhpasheva and A.A. Korobkin

Lavrentyev Institute of Hydrodynamics,
Novosibirsk, 630090, RUSSIA

1. Introduction

A very large floating structures are considered as an alternative of such land-based large facilities as, for example, airport. A proposed design of floating airport has a thin plate configuration of large horizontal extend. Bending rigidity of such a floating plate is small, and wave-induced motion of the plate is significantly affected by its elastic deflection. Analysis of floating plate behaviour in waves is based on hydroelasticity, in which the coupled hydrodynamics and structural dynamics problems are solved simultaneously. A goal of the analysis is to predict accurately both the plate deflection and stresses in the plate and to find a way for their reduction. The latter is of great importance for securing safety and the structure performance. Reduction of the motion of an floating elastic plate in waves by surrounding it by an breakwater was studied numerically in [1,2]. It was shown that breakwaters effectively reduce the plate response for long waves but in the case of short waves the reduction is not well-pronounced. The idea to put a floating structure in the shadow of a breakwater for reduction of the structure response is clear and practical. However, the behaviour of a structure in restricted water might be affected by its hydrodynamic interaction with the breakwater and resonance phenomena might occur. Another way to reduce the floating plate response was suggested in [6] that is to adjust to the front side of the elastic plate a wave reflector – vertical submerged plate, the height of which is about three times less than the water depth – or a wave-breaking structure – multi-column floating structure of small extend. Experiments [6] revealed that both the wave reflector and the wave-breaking structure decrease deflections of the main structure in the case of short incident waves. However, for long incident waves which provide greater deflections of the main structure than short waves, the experiments did not detect well-pronounced effects of the additional structures. Both approaches [2,6] are based on the idea to protect (to shield) a floating elastic structure from the incident wave action, in order to reduce a part of the wave energy which can be absorbed by the structure.

In order to test possible approaches aimed to reduce floating plate response in waves, direct numerical simulations of hydroelastic behaviour of the plate are very attractive. Three-dimensional numerical simulation of the linear response of an elastic plate in waves is the most accurate approach. Three-dimensional numerical simulations of floating rectangular plate in waves were performed in [3,4]. However, at present these simulations are still time-consuming and expensive to use them at the design stage. At the very initial stage of design it looks reasonable to use the simplest models of floating plate behaviour, in order to discover main trends and to distinguish main features of the problem. If an effect is well-pronounced within a simple model, it is expected to be of importance also within more accurate models.

In this paper two approaches to reduce elastic deflection of floating plates are described within the two-dimensional linear theory. In the two-dimensional problem the plate is modeled by an Euler homogeneous beam. Developed method is applied also to the problem of cracked floating beam. The first approach is based on the concept of vibration absorber well-known in many engineering applications. Within the second approach the floating beam is connected to the sea bottom with a spring, rigidity of which can be adjusted in such a way that the beam deflection due to incident waves is reduced.

Four 2D-problems on hydroelastic behaviour of a floating beam in waves are considered, where the beam is (**i**) homogeneous, (**ii**) cracked, (**iii**) compound with an elastic connection between the parts of the beam, (**iv**) homogeneous and elastically connected to the sea bottom. The problems are treated by the common method described below. The formulation is given for the third problem on compound beam behaviour, which is the most general one. The scheme of the flow and the main notations are given in the figure

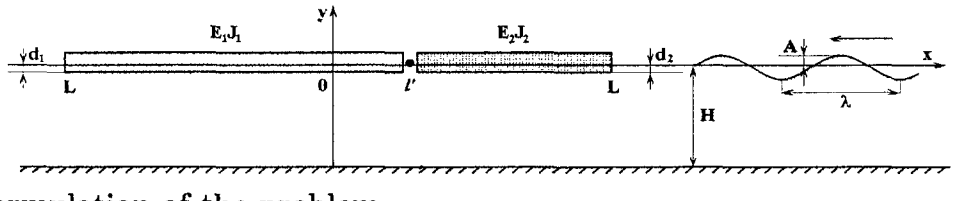

2. Formulation of the problem

The plane linear problem of a floating beam in waves is considered. The beam vibration is caused by periodic incident wave of frequency ω and small amplitude A. The beam consist of two parts (see figure) with their bending stiffnesses E_iJ_i and drafts d_i (i=1,2) being prescribed. The beam drafts are assumed

much smaller than both the total beam length $2L$ and the liquid depth H. We shall determine the beam deflection and the stress distribution in the beams and study their dependence on characteristics of the beam parts and conditions of their connection.

Non-dimensional variables are used below: L is taken as the length scale, $1/\omega$ as the time scale, the amplitude of the incident wave A as the deflection scale, the product ρgA, where ρ is the liquid density and g is the acceleration due to gravity, as the pressure scale, $2Ld\rho g$ as the scale of bending stresses, and the product $A\omega L$ as the scale of the velocity potential. Within the linear wave theory the non-dimensional hydrodynamic pressure $p(x,0,t)$ along the beam , $-1 < x < 1$, and the beam deflection $w(x,t)$ are given as $p(x,0,t) = \Re[e^{it}P(x)]$ and $w(x,t) = \Re[e^{it}W(x)]$, respectively. The new unknown complex-valued functions $P(x)$ and $W(x)$ satisfy the following equations and the boundary conditions:

$$P(x) + \frac{\gamma}{2\pi}\int_{-1}^{1} P(x_0)K(x-x_0)dx_0 = e^{ikx} - W(x), \tag{1}$$

$$\beta(x)W^{IV} - \alpha(x)W = P(x) \qquad (-1 < x < 1), \tag{2}$$

$$W''(\pm 1) = 0, \qquad W'''(-1) = 0, \qquad W'''(+1) = -k_l W(+1), \tag{3}$$

$$W(l-0) = W(l+0), \qquad \beta_1 W''(l-0) = \beta_2 W''(l+0), \qquad \beta_1 W'''(l-0) = \beta_2 W'''(l+0), \tag{4}$$

$$W''(l-0) + k_T[W'(l-0) - W'(l+0)] = 0, \tag{5}$$

where $\alpha(x) = \begin{cases} \alpha_1 & \text{for } x \in [-1,l), \\ \alpha_2 & \text{for } x \in (l,1], \end{cases} \qquad \beta(x) = \begin{cases} \beta_1 & \text{for } x \in [-1,l), \\ \beta_2 & \text{for } x \in (l,1]. \end{cases}$

The problem (1) - (5) contains eight parameters:

$$k_l = K_l L^3/E_1J_1, \quad k_T = K_T L/E_1J_1, \quad \gamma = L\omega^2/g, \quad \alpha_j = \gamma d_j/L, \quad \beta_j = E_jJ_j/(\rho g L^4), \quad (j = 1,2)$$

and k which is the positive solution of the dispersion equation $k\tanh(kH_0) = \gamma$, $H_0 = H/L$. The function $K(z)$ in (1) is given as

$$K(z) = -2\pi i \frac{ke^{-ik|z|}}{H_0(k^2-\gamma^2)+\gamma} + 2\pi\sum_{j=1}^{\infty}\frac{s_j e^{-s_j|z|}}{H_0(s_j^2+\gamma^2)-\gamma},$$

where $s_j = (\pi j - \delta_j)/H_0$ and δ_j is the solution of the equation $\delta_j = \arctan(\gamma H_0/(\pi j - \delta_j))$, $j \geq 1$.

The boundary-value problem (1)-(5) describes the hydroelastic behaviour of a free-free homogeneous beam in waves with $\alpha_1 = \alpha_2$, $\beta_1 = \beta_2$, $k_l = 0$ and $k_T = \infty$, of a free-free cracked beam with $\alpha_1 = \alpha_2$, $\beta_1 = \beta_2$, $k_l = 0$ and $k_T \geq 0$, of a free-free compound beam with $\alpha_1 \neq \alpha_2$, $\beta_1 \neq \beta_2$, $k_l = 0$ and $k_T \geq 0$, and of an homogeneous beam connected elastically to the sea bottom, with $\alpha_1 = \alpha_2$, $\beta_1 = \beta_2$, $k_l \neq 0$ and $k_T = \infty$.

3. Method of solution

Problem (1) - (5) can be solved with the help of the normal mode method in the same manner as in [7]. This method reduces the integral equation (1) to infinite system of algebraic equations with respect to the principle coordinates of the pressure $P(x)$. However, the eigenfunctions of the compound beam are rather complicated and, moreover, they do not correspond to the features of the hydrodynamic pressure distribution along the beam. A main idea of the present study is to use different basic functions for the pressure and the beam deflection. Trigonometric functions are used as basic functions to present the pressure in the form

$$P(x) = \frac{1}{2}a_0 + \sum_{n=1}^{\infty} ac_n \cos\pi nx + \sum_{n=1}^{\infty} as_n \sin\pi nx. \tag{6}$$

Substitution of expansion (6) into equation (2) leads to the following expansion for the beam deflection

$$W(x) = \frac{1}{2}a_0 wc_0(x) + \sum_{n=1}^{\infty} ac_n wc_n(x) + \sum_{n=1}^{\infty} as_n ws_n(x). \tag{7}$$

The functions $wc_j(x)$ and $ws_j(x)$ satisfy conditions (3)-(5) and equation (2) with $P(x)$ being replaced by $\cos(j\pi x)$ and $\sin(j\pi x)$, respectively. The functions $wc_j(x)$ and $ws_j(x)$ are considered here as basic functions for the beam deflection. The integral equation (1) with account for expansions (6) and (7) leads to the infinite system of algebraic equations with respect to the coefficients ac_n and as_n.

$$(\mathbf{I} + \frac{\gamma}{2\pi}\mathbf{S} + \mathbf{A})\,\vec{a} = \vec{e}. \tag{8}$$

Here $\mathbf{I} = \mathrm{diag}(2,1,1,...)$ is diagonal matrix, symmetric matrix $\mathbf{S}$ comes from the integral term in (1), symmetric matrix $\mathbf{A}$ comes from the term $W(x)$, and $\vec{a} = (ac_0/2, ac_1, ac_2, ...ac_n, as_1, as_2, ...as_n)^T$. The elements of the vector $\vec{e}$ are the coefficients in the expansion of $\exp(ikx)$ with respect to the trigonometric functions. All elements of the matrices $\mathbf{S}$ and $\mathbf{A}$ and those of the vector $\vec{e}$ are given by analytical formulae.

4. Free-free homogeneous beam

Problem (1) - (3) with $\alpha_1 = \alpha_2$, $\beta_1 = \beta_2$ and $k_l = 0$ corresponds to that of hydroelastic behaviour of the homogeneous free-free beam in waves and was studied in [5] by the domain decomposition method, in [7] by

the normal mode method and in [8] with the help of a combination of these methods. The obtained numerical results are in good agreement for low frequencies of incident waves but differ each other for high frequencies. The problem of high-frequency excitation of floating elastic plates is not solved yet. The low-frequency case is considered here only.

Numerical calculations were performed for the conditions of the experiments carried out by Wu *et al* [8] for homogeneous narrow plate in a channel: d =8.36mm, H =1.1m, h =38mm, EJ =471kg m^3/s^2, L =5m. The frequency of incident wave is equal to 4.4s^{-1} (period of the wave T = 1.429s) and 2.2s^{-1} (period of the wave T = 2.875s). In this cases $\beta = 7.7 \cdot 10^{-5}, \alpha = 0.016$ and $\alpha = 0.004$, $\gamma = 9.85$ and $\gamma = 2.43$, $k = 10.1$ and $k = 3.654$, respectively, depending on the incident wave frequency. Convergence of the numerical algorithm was checked by changing the number of terms taken into account in each sum of (6) and (7). Ninety terms were used to plot the obtained numerical results. The present results for the homogeneous beam, are identical with those obtained in [5,7,8] by other methods. The amplitude of the beam deflection $|W(x)|$ is shown below only for $T = 1.429$s.

5. Free-free compound beam

The linear problem of two floating beams is considered. The beams are connected with the help of a torsional spring. Vibrations of the beams are caused by periodic incident wave of small amplitude. The longer beam is referred to as the main structure, characteristics of which are prescribed. The shorter beam is referred to as the auxiliary plate, length of which is given. Both characteristics of the auxiliary plate and the torsional spring stiffness which essentially reduce the vibration amplitude of the main structure are determined. The auxiliary plate can be adjacent either in front of the structure (case *a*) or at the rear side of it (case *b*).

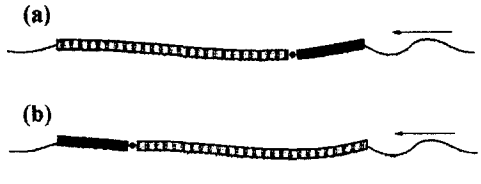

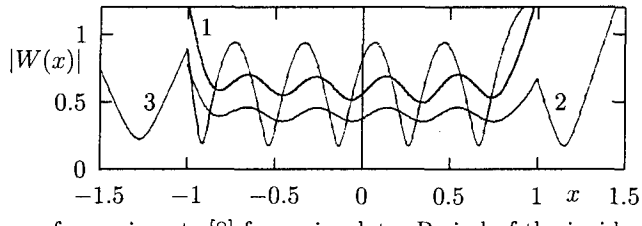

Calculations were performed for the conditions of experiments [8] for main plate. Period of the incident wave is equal to 1.429s (line 1 is for a single plate, line 2 is for case *a*, line 3 is for case *b*, length of the auxiliary plate is equal to 0.25 of the main plate length, $(EJ)_{aux} = 100(EJ)_{main}$). It was revealed that:

- auxiliary plates adjacent in front of the main structure (case *a*) decrease the structure vibrations;
- vibrations of the main structure are increased with auxiliary plates attached to its rear side (case *b*);
- reduction of the vibration is strongest if the plates are simply connected ($k_T = 0$);
- auxiliary plate of length 1.5m decrease the deflections by 20% (case *a*) and increase them by 10% (case *b*);
- essential reduction (35%) of the structure vibrations was obtained in the case of rigid auxiliary plates of length 2.5m simply connected in front of the main structure.

Roughly speaking, in order to reduce the floating plate vibrations, a rigid plate of smaller length has to be simply connected in front of the main structure.

6. Free-free cracked beam

In order to model the cracked beam problem, the method of matched asymptotic expansions is used. According to this method, the beam is divided into the 'inner' region which surrounds the crack, and the 'outer' region, where the transverse variation of the stresses is not important and the plate is modeled by an elementary homogeneous beam. In the leading order as $h/L \to 0$, reduction in stiffness of the beam due to the presence of a crack is modeled with the help of a torsional spring (see figure).

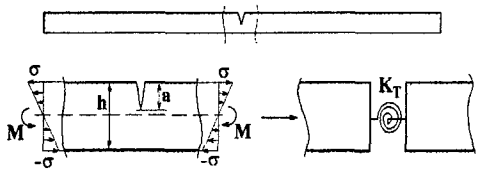

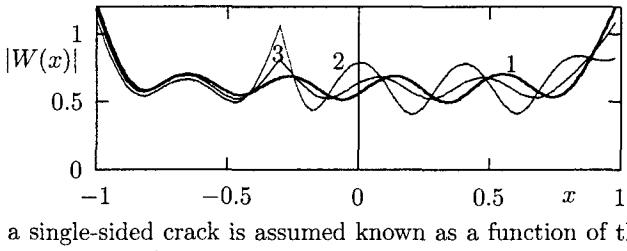

The equivalent torsional spring stiffness K_T for a single-sided crack is assumed known as a function of the beam parameters and the crack length a. The 'outer' solution for the floating free-free beam which is divided by the torsional spring into two parts, provides the bending stresses outside the crack region. Therefore the 'outer' solution is described by the problem considered in Section 5, where $\alpha_1 = \alpha_2$, $\beta_1 = \beta_2$, $k_l = 0$, $k_T \geq 0$.

As a result of numerical calculations, the distribution of beam deflections and bending moments were obtained outside the crack region for different positions of the crack and its length. Analysis of numerical calculations gives:

• Presence of a crack changes the distributions of both the plate deflections and stresses, if the crack is longer than a half of the plate thickness. The longer the crack, the more pronounced are the changes.

• Local maximum of the deflections and local minimum of the bending stresses occur at the crack position.

• These changes are much more pronounced if a crack is located at the points of maximum bending stresses of the equivalent homogeneous plate.

Calculations were performed for the conditions of the experiments [8]. The results are depicted for homogeneous beam ($a = 0$, curve 1), broken beam ($a = h$, $l = -0.3$, curve 2) and cracked beam ($a/h = 0.8$, $l = -0.3$, curve 3). It is seen that the presence of the crack increases locally the deflections but decreases the stresses in the beam. The 'outer' solution gives necessary data to evaluate the stress intensity factor at the crack tip and to predict the evolution of the crack length in time.

7. Floating beam with its edge being elastically connected to the sea bottom

Numerical solution of problem (1)-(5) with $\alpha_1 = \alpha_2$, $\beta_1 = \beta_2$, $k_T = \infty$ and $k_l > 0$ revealed that elastic connection of the front edge of the floating beam to the bottom can essentially reduce the beam deflections in the main part of the beam. Rigidity of the elastic connector can be adjusted in an optimal way for a given frequency of incident wave.

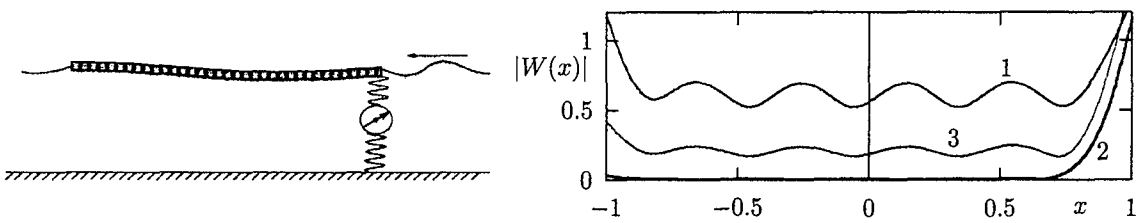

In the figure the amplitudes of the beam deflections are shown for the free-free beam ($k_l = 0$, curve 1) and for elastically connected beam ($k_l = 1000$, curve 2 and $k_l = 700$, curve 3). Parameters of numerical calculations are given in Section 4, $T = 1.429$s. The curve with $k_l = 1300$, is similar to the curve with $k_l = 700$. It is seen that the dimensional rigidity of the elastic connector $K_l \approx 3800 kg/s^2$ can be considered as optimal for the conditions of experiment [8]. For another frequency of incident wave the connector rigidity has to be changed, which can be done with an active control system.

8. Conclusion

The method of numerical solution of the floating beam problem is based on expansions of the hydrodynamic pressure and the beam deflection with respect to different basic functions. This makes it possible to simplify the treatment of the hydrodynamic part of the problem and at the same time to satisfy accurately the beam boundary conditions. Two approaches aimed to reduce the beam vibrations are described. The effect of the vibration reduction is well pronounced and can be utilized at the design stage. Combination of the presented approaches is expected to be perspective.

This work was supported by the RFBR (projects N00-01-00842, N00-01-00850 and N00-15-96162) and SB RAS (integration grant N1).

References

1. Nagata S., Yoshida H., Fujita T. & Isshiki H. Reduction of the motion of an elastic floating plate in waves by breakwaters. *2 Int. Conf. on Hydroelasticity in Marine Technology* Fukuoka, Japan, 1-3 Decem. 1998. pp.229-238.

2. Seto H. & Ochi M. A hybrid element approach to hydroelastic behavior of a very large floating structure in regular wave. Ibid pp.185-194.

3. Kashiwagi M. Hydrodynamic interactions among a great number of columns supporting a very large flexible structure. Ibid pp.165-176.

4. Kim J.W. & Ertekin R.C. An eigenfunction-expansion method for predicting hydroelastic behavior of a shallow-draft VLFS. Ibid pp.47-60.

5. Sturova I.V. The oblique incidence of surface waves onto the elastic band. Ibid pp.239-245.

6. Yago K., Endo H., Ohmatsu S. On the hydroelastic response of box-shaped floating structure with shallow draft (2nd report). *J. of the Soc. of Nav. Arch. of Japan* 1997. V.182. pp.307-317.

7. Korobkin A. A. Numerical and asymptotic study of the two-dimensional problem on hydroelastic behavior of a floating plate in waves. *J.Appl.Mech.Tech.Phys.* 2000, V.41, No. 2, pp.286-293.

8. Wu C., Watanabe E. & Utsunomiya T. An eigenfunction expansion-matching method for analyzing the wave-induced responses of an elastic floating plate. *Appl. Ocean Res.* 1995. V.17(5). P.301-310.

Hydroelastic Analysis of a Floating Runway with Inhomogeneous Structural Properties

Jang Whan Kim[1], Jian Ma[2] and William C. Webster[2]
[1]Department of Ocean and Resources Engineering, University of Hawaii at Manoa, USA
[2]Department of Civil and Environmental Engineering, University of California at Berkeley, USA

1. INTRODUCTION

The hydroelastic analysis of the floating runway has usually been made under the assumption that the structural properties, such as mass and stiffness, are uniform over the runway (see, Mamidipudi & Webster, 1994; Newman, 1996; Kashiwagi, 1998; Ertekin & Kim, 1999). Recently, Webster (1998) proposed an optimization scheme to minimize the cost of the floating runway by re-distributing the mass and stiffness of the runway. In this scheme, the hydroelastic response of the runway for a given wave spectrum should be evaluated at each stage of the optimization process. An efficient numerical method is necessary to reach to the optimal design within reasonable computing time and cost.

In this paper we present a numerical method to obtain hydroelastic response of inhomogeneous runway in waves. The runway is modeled as an orthotropic plate following Mamidipudi & Webster (1994) and the fluid is modeled by Green-Naghdi theory as has been done previously by Ertekin & Kim (1999). The finite-difference method is used to discretize the governing equations of the plate and fluid in the runway region. The flow in the fluid domain outside the runway is solved by the use of Green's function, to obtain radiation condition for the fluid under the runway. Preliminary numerical results are presented by applying the present numerical scheme to a runway with the stiffness varying transversely.

2. FORMULATION

Runway structure

Following Mamidipudi & Webster (1994), the floating runway is modeled as an orthotropic plate with variable mass and stiffness. The vertical deflection $\zeta(x,y)$ of the runway of length L and width B is governed by

$$-\omega^2\rho_p(x,y)\zeta + D_x(x,y)\frac{\partial^4\zeta}{\partial x^4} + 2H(x,y)\frac{\partial^4\zeta}{\partial x^2\partial y^2} + D_y(x,y)\frac{\partial^4\zeta}{\partial y^4} = p_b(x,y)\ , \qquad (1)$$

where $D_x(x,y), D_y(x,y)$ and $H(x,y)$ are the bending and the torsional rigidities, $\rho_p(x,y)$ is the mass per unit area, and $p_b(x,y)$ is the pressure at the bottom of the runway. Along the edges of the runway and corners, additional conditions are imposed to make sure that the runway is 'free'. Details of the conditions can be found in Webster (1998). The pressure at the bottom of the runway should be equal to the pressure at the upper surface of the fluid, which will be given later in the formulation of the fluid.

Fluid layer under the runway

We adopted the Green-Naghdi equations following Ertekin and Kim (1999) to model the fluid underneath. The equations can be written in terms of the depth-integrated potential $\phi(x,y)$ from which the velocity field of the fluid is defined by

$$\mathbf{u}(x,y) = \nabla\phi, \quad w(x,y,z) = -(z+h)\nabla^2\phi \qquad (2)$$

where h is the water depth. The conservation of mass is stated as

$$h_1\nabla^2\phi - i\omega\zeta = 0 \qquad (3)$$

where $h_1 = h - d$ is the clearance between the runway and the sea bottom. The equation for conservation of momentum can be integrated as

$$p_f = i\omega\rho\phi + \left(\frac{\omega^2 \rho h_1}{3} - \rho g\right)\zeta \tag{4}$$

where $p_f = p_f(x,y)$ is the pressure at the upper surface of the fluid, which should be equal to $p_b(x,y)$ in Eq.(1).

Fluid layer outside the runway

In the outer region where there is no runway on the top of the fluid layer, the Green-Naghdi equation reduces to a simple Helmholtz equation (see, Ertekin & Kim, 1999). The general solution of the Helmholtz equation in the outer domain can be represented as the plane wave plus the line integral along the edge of the runway by Green's identity. A radiation condition for $\phi(x,y)$ along the edge can be derived by enforcing the continuity of the mass and energy flux across the edge (Bai et al, 2000). The radiation condition can be written as

$$\phi = \frac{1}{\pi}\int_J H_0^{(1)}(k|\mathbf{x} - \boldsymbol{\xi}(s)|)\left(\frac{\partial\phi}{\partial n} - \frac{\partial\phi_0}{\partial n}\right)ds + \phi_0 \tag{5}$$

where $\mathbf{x} = (x,y)$ is the field point and $\boldsymbol{\xi}(s)$ is the source point on J, $H_0^{(1)}$ is the Hankel function of the first kind. The wave number, k, is given by the dispersion relation of the Green-Naghdi equation as,

$$k^2 = \frac{3\omega^2}{3gh - h^2\omega^2} \quad \text{or} \quad \omega^2 = \frac{3ghk^2}{3 + h^2k^2}. \tag{6}$$

3. NUMERICAL METHOD

Webster (1998) derived the finite-difference formula for the structural equation using the fifth-order polynomial interpolation. On the edge panels, special formulas have been derived to satisfy the free edge conditions. In this study, we use the same formula for every panel by introducing additional exterior panels along the peripheral of the runway. Satisfying edge conditions can eliminate the extra unknowns due to these panels. Similarily, the Laplacian operator in the fluid equation in Eq. (3) is also discretized by finite difference formula with additional strip of panels along the peripheral. Imposing the radiation condition, Eq. (5), eliminates the extra unknowns. The discretized equations can be given as

$$\begin{bmatrix} \mathbf{S}_0 + \mathbf{S}_B - \omega^2\mathbf{M} + \rho g\mathbf{I} & -i\omega\rho\mathbf{I} \\ i\omega\mathbf{I} & -h_1\mathbf{L}_0 + \mathbf{L}_R \end{bmatrix} \begin{Bmatrix} \boldsymbol{\zeta} \\ \boldsymbol{\phi} \end{Bmatrix} = \begin{Bmatrix} 0 \\ \mathbf{f}_w \end{Bmatrix} \tag{7}$$

where $\mathbf{S}_0$ is the stiffness matrix and $\mathbf{S}_B$ is the correction due to the edge conditions, $\mathbf{M}$ is the virtual mass matrix that includes the inertia due to mass of the plate and the added mass term, $\rho h_1 / 3$, given in Eq. (3). The matrix $\mathbf{L}_0$ is due to the Laplacian operator in Eq. (3) and $\mathbf{L}_R$ is contribution by the radiation condition, Eq. (5). The forcing vector $\mathbf{f}_w$ is due to the forcing by incident wave. Note that the matrices that appear in Eq. (7) are sparse, except $\mathbf{S}_B$ and $\mathbf{L}_R$, which are dense for the unknowns along the edge of the plate.

We tried both iterative and direct scheme to solve the algebraic equation, Eq. (7). As an iterative scheme, we tried a PFFT method. The preconditioning is made by the FFT solution of the infinitely wide floating plate with uniform stiffness and mass distribution. The stiffness and mass of the uniform system are given by the averaging the original system to solve. Numerical test showed that this iterative scheme was successful only when the structural properties of the runway is close to uniform. Otherwise the convergence was quite slow and even non-convergent when the non-uniformity was severe.

As the second approach, we tried direct scheme after eliminating ϕ from Eq. (7):

$$\left(\omega^2\mathbf{I}+\mathbf{LS}\right)\boldsymbol{\zeta}=-i\omega\mathbf{f}_w \tag{8}$$

where $\mathbf{S}=\left(\mathbf{S}_0+\mathbf{S}_B-\omega^2\mathbf{M}+\rho g\mathbf{I}\right)/\rho$ and $\mathbf{L}=-h_1\mathbf{L}_0+\mathbf{L}_R$. The matrix $\mathbf{LS}$ is still sparse at the internal panels. It is dense only on the three lanes of the panel strips from the edge. Sparse solver has been used to save the computer memory and CPU time.

4. RESULTS

As a numerical example, an isotropic plate with the stiffness varying in y-direction is studied. The bending and torsional rigidity is given by

$$D_x=D_y=H_{xy}=D_0\left(1+\varepsilon\cos\frac{2\pi y}{B}\right),\ D_1=\nu D_0\left(1+\varepsilon\cos\frac{2\pi y}{B}\right). \tag{9}$$

The dimensions and the structural properties of the runway are given by

$L=5$ km, $B=1$ km, $d=5$ m, $h=50$ m, $D_0=1.96\times10^{11}$ N-m, $\nu=0.3$.

In Fig 1., the deflections at four different incident wave angle, β, which is defined as the angle between x-axis and the wave angle, are compared for three different value of ε (see Eq. (9)): $\varepsilon=-0.5$, 0 and 0.5. The deflections are normalized by the amplitude of incoming wave, A. The incoming wavelength is 125 m or $L/\lambda=20$. Total 150 by 30 panels are used to discretize the runway.

In the head sea, the runway with the centerline stiffened ($\varepsilon=0.5$) has a calmer runway surface. The runway with edges stiffened has undulations of greater height along the center of the runway, presumably because the transmitted waves are guided by the stiffened edges and not radiate to the water outside. On the other hand, in the oblique and beam seas, the runway with the stiffened edges is more calm.

REFERENCES

Bai, K. J., Yoo, B. S. and Kim, J. W. 2000 "A Localized Finite-Element Analysis of a Floating Runway in a Harbor," (*in print*) *Marine Structures.*

Ertekin, R.C. and Kim, J.W. 1999, "A Hydroelastic Response of a Floating, Mat-Type Structure in Oblique, Shallow-Water Waves," *Journal of Ship Research*, Vol. 43, No.4 , pp. 241-254.

Kashiwagi, M., 1998 "A B-Spline Galerkin Scheme for Calculating the Hydroelastic Response of a Very Large Floating Structure in Waves," *J. Marine Science and Technology*, Vol. 3, pp37-49.

Mamidipudi, P. and Webster, W. C. 1994 "The Motions Performance of a Mat-Like Floating Airport," *Hydroelasticity'94,* Trondheim, Norway.

Newman, J. N., Maniar, H. D. and Lee, C. H. 1996 "Analysis of Wave Effects for Very Large Floating Structures," International Workshop on Very Large Floating Structures, Hayama, Japan, pp. 135-142.

Webster, W. C. 1998 "Optimal Structure for Large-Scale Floating Runways," *Hydroelasticity in Marine Technology*, Kashiwagi et al. (eds), RIAM, Kyushu University, pp. 15-26.

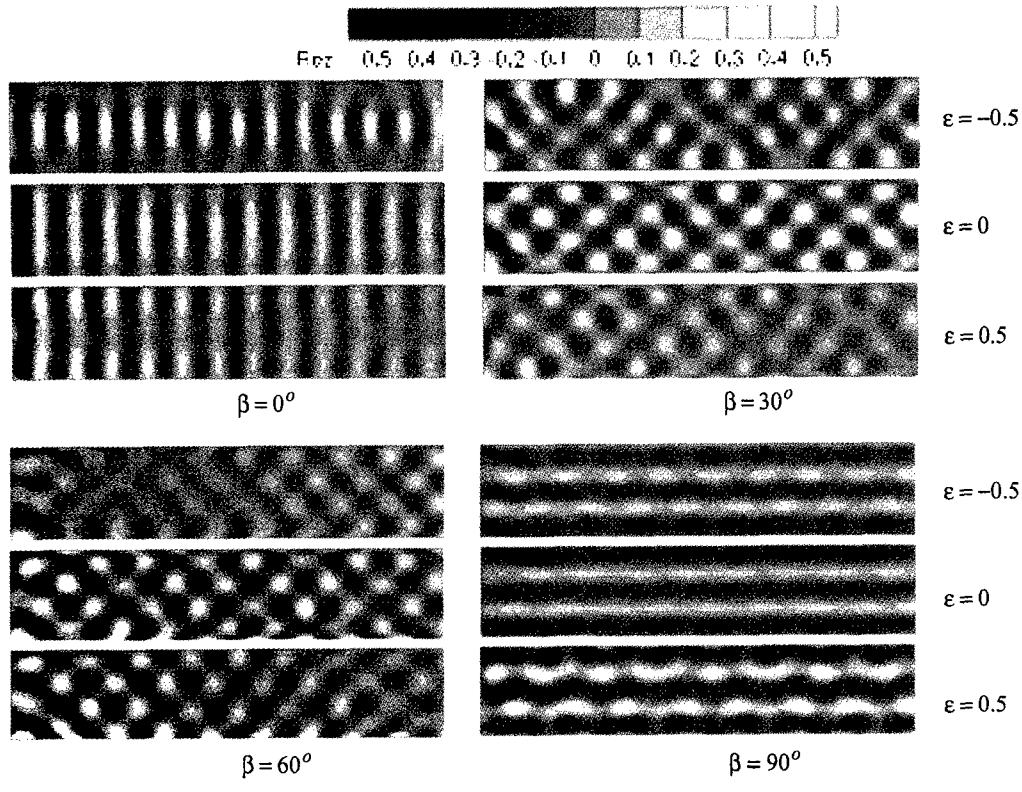

Fig. 1 Contour plots of $\mathrm{Re}\zeta / A$ at four different incident wave angles.

Coupled Analysis of Ship Motions and Sloshing Flows

Yonghwan KIM
American Bureau of Shipping, Research Department
Houston, TX, USA

1. INTRODUCTION

Ships with liquid cargo experience the slosh-induced internal loads during their operation. In some ships like LNG carriers, the impulsive local load is a major concern for safe structural design, whereas the global forces and moments are of interest in some types of ships. Although the ship motion excites the sloshing flow, the sloshing flow also affects the ship motion in return. Sometimes these slosh-induced forces and moments are significant, so that the coupling effect is critical in the prediction of seakeeping performance for such cases. The anti-rolling tank (ART) is a good example which utilizes this coupling effect. Moreover, the coupling effect between the motion response and fluid flow on deck plays a key role in the dynamic instability problem of small fishing vessels.

This study concentrates on the coupling problem of the ship motions and sloshing flows. In order to solve the coupling problem, two distinct problems - ship motion and sloshing - should be solved at the same time. Generally, the sloshing phenomena in the tank or the deck are strongly nonlinear, so that the time-domain approach seems the right way to tackle. In this study, the finite difference method has been applied to solve the sloshing problem. Particularly, this study adopts the same scheme with [1] and [2]. For the ship motion problem, the Large Amplitude Motion Program (LAMP) has been used. Two programs have been combined, so that the slosh-induced moment affects the ship motion in waves, and vice versa.

The test models are a modified S175 hull equipped with rectangular anti-rolling tanks of passive type and a VLCC with 17 oil tanks. The computational results for the anti-rolling tanks have been compared with experimental data for a supply vessel with the same beam-length and draft-length ratios. The present method is directly applicable to the design of ARTs and sloshing analysis in LNG carriers and FPSOs.

2. BACKGROUND

Consider a freely floating ship equipped with a partially-filled tank. Two Cartesian coordinate systems are defined at the center of ship motion and the tank bottom, as shown in Figure 1. The ship is in the 6-D.O.F. motion which is excited by the incident wave and also the internal forces and moments due to sloshing. The equation of the ship motion can be written as follows:

$$[M_{ij}]\frac{\partial^2\vec{\xi}}{\partial t^2}+[B_{ij}]\frac{\partial\vec{\xi}}{\partial t}+[C_{ij}]\vec{\xi}=\vec{F}_{ext}(t)+\vec{F}_{slosh}(t) \tag{1}$$

where $\vec{\xi}$ is the displacement of ship motion and $[M_{ij}]$, $[B_{ij}]$ and $[C_{ij}]$ represent the matrices of mass, damping and restoring coefficients. The external excitation force vector $\vec{F}_{ext}(t)$ includes all the forces on the external hull surface by incident waves and hydrodynamic reactions. Moreover, $\vec{F}_{slosh}(t)$, the slosh-induced component, contributes to the excitation. In the present study, the ship motion problem has been considered in the realm of linear theory. Therefore, the linear surface conditions as well as the body boundary condition have been considered in the boundary value problem for the ship motion.

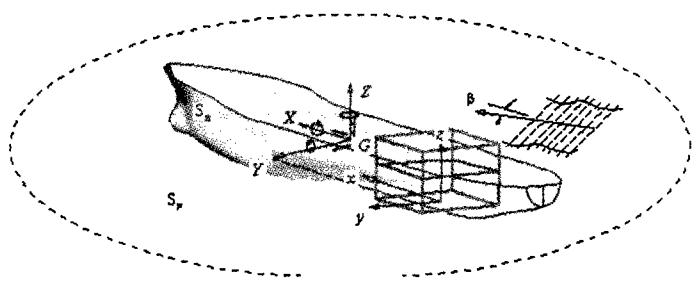

Figure 1. Coordinate system

The continuity and Euler equations are assumed to govern the fluid flow inside of the tank:

$$\nabla\cdot\vec{u}=0 \qquad \text{and} \qquad \frac{\partial\vec{u}}{\partial t}+\vec{u}\cdot\nabla\vec{u}=-\frac{1}{\rho}\nabla\vec{p}+\vec{f} \tag{2}$$

where $\vec{u}(u,v,w)$ is the velocity vector, defined in the tank-fixed coordinate. Moreover, ρ, p and $\vec{f}$ are the liquid density, pressure and external force vectors, respectively. The external force consists of the gravitational force, translational and rotational inertia forces, which can be written as

$$\vec{f}=[T(\xi_4,\xi_5,\xi_6)]\cdot\left(\vec{g}-\frac{d^2\vec{\xi}_{1,2,3}}{dt^2}-\frac{d\vec{\Omega}}{dt}\times\vec{r}_G-2\vec{\Omega}\times\frac{d\vec{r}_G}{dt}-\vec{\Omega}\times(\vec{\Omega}\times\vec{r}_G)\right) \tag{3}$$

where $\bar{g}$, $\bar{\xi}_{1,2,3}$ and $\bar{\Omega}$ are the gravitational force vector, the translational motion vectors (ξ_1,ξ_2,ξ_3) and rotational velocity vectors $(\dot{\xi}_4,\dot{\xi}_5,\dot{\xi}_6)$ of the ship motion. [T] is the transform matrix from ship-fixed coordinate to tank-fixed coordinate. In addition, $\bar{r}_G$ is the position vector of the considered point from G. On the free surface, both the kinematic and dynamic conditions should be satisfied.

$$\frac{\partial \eta}{\partial t} + \bar{u} \cdot \nabla \eta = 0 \qquad \text{and} \qquad p = p_{atm} \tag{4}$$

where η indicates the free surface profile and p_{atm} is the air pressure inside of the tank. In addition, a proper wall condition is necessary on the tank walls and internal members. Then the slosh-induced forces and moments on the tank can be obtained by integrating the pressure on the tank surface S_{tank}.

$$\vec{F}_{slosh}(t) = \int_{S_{tank}} p \begin{pmatrix} \vec{n} \\ \vec{r}_G \times \vec{n} \end{pmatrix} dS \tag{5}$$

where $\vec{n}$ is the normal vector on the surface.

The ship motion has been solved using a three-dimensional panel method. Particularly, the Large Amplitude Motion Program (LAMP) program has been used for the time-domain solution. In this computation, the Rankine source has been distributed on the hull surface and local free surface near the body, and the transient wave Green function has been distributed on the matching surface for the radiation condition. The detailed numerical scheme for this mixed-singularity can be found in [3].

The sloshing flow has been solved using the finite difference method described in [2] without viscosity. The key concept of this method is to predict the global fluid motion, and hence some local phenomena have been ignored. This numerical method adopts the SOLA scheme in the fluid domain and SURF scheme for the free surface conditions. The impact pressure on the tank top is also predictable using the scheme introduced in [1] and [2].

3. COMPUTATIONAL RESULTS

The numerical tests have been carried out two models, a modified S175 hull and a VLCC with 17 oil cargo holds. Figure 2 shows the hull form equipped with an ART. The beam(B)-length(L) and draft-length ratios are 0.288 and 0.084, respectively. Bai [4] has reported the experimental data for a supply vessel with the same length characteristics, although the hull forms are not the same. In his experiment, two types of ART, with and without pillars, have been considered. The present computation has been applied for the same size of ART, and its lengths are shown in Figure 3. In this experiment, the five circular pillars have been equipped as shown in the left figure, while the flat plates have been considered in the numerical computation. Only the beam sea condition has been considered for this ship, since the roll motion is of major interest. The linear damping coefficient has been applied for roll motion, and 2.5% of the critical damping has been used in all computation.

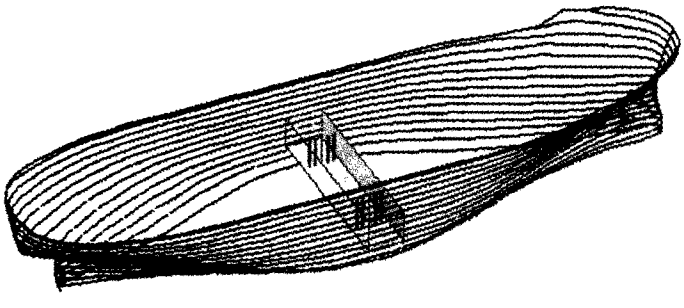

Figure 2. Modified S175 hull equipped with an ART

The essence of ART design is to tune the ship motion and sloshing flows. That is, the natural frequency of sloshing mode should be well tuned with that of roll motion. Figure 4 shows the time-histories of the wave-induced moment, slosh-induced moment and the resultant roll response. In this case, the filling ratio is 50%. At this filling condition, the natural frequency of fundamental sloshing mode is close to that of the roll motion. From this figure, it can be observed that the phase difference of the wave excitation and slosh-induced moment is close to 180 degrees, resulting in the cancellation of the total roll moment. Therefore, it is obvious that the ART can provide a significant reduction of roll amplitude.

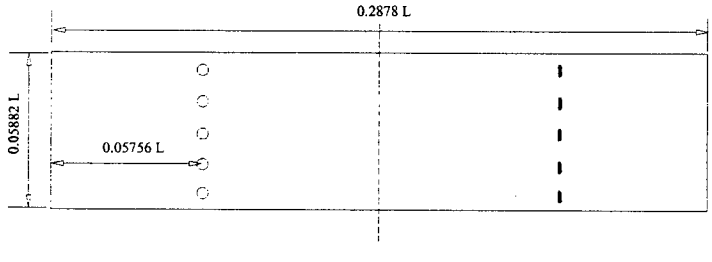

Figure 3. Characteristic lengths of ART with pillars; experimental (left) and computation (right)

Figure 5 shows the instantaneous ship positions at three time steps with and without ART for the same wave condition to Figure 4. As expected, the reduction of the roll motion is very significant. Therefore, a dramatic change of the roll amplitude can be expected when the tuning of two frequencies is successful.

Figure 6 shows the roll RAOs for two ships, the modified S175 hull for the present computation and the supply vessel that was tested by Bai. Since the hull forms of two ships are not the same, the RAO curves should be compared for not quantities but trend. The RAO curves for the cases with ARTs show a dramatic reduction near the roll natural frequencies,

but the roll motion can be larger than the case without an ART at out-of-resonance frequencies. This is because the phase difference of the slosh-induced and wave-induced moments is no longer close to 180 degrees, so that the slosh-induced moment can increase the total roll excitation. From this comparison, we can conclude that the present numerical method provides the correct solution of the coupling problem.

The reduction of the roll amplitude using an ART depends on the wave condition. In the realm of linear theory, the wave-induced excitation is linearly proportional to the wave amplitude. However, the slosh-induced moment varies with a nonlinear manner ([5]). Furthermore, in the random ocean, an ART does not guarantee the dramatic reduction as seen in Figure 5. A good survey about the efficiency of ARTs can be found in [6].

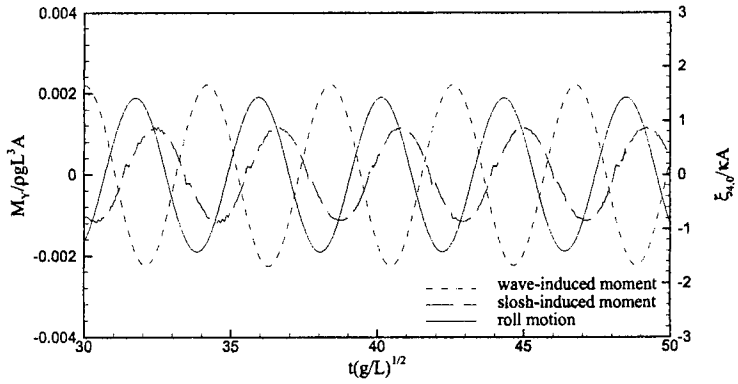

Figure 4. Time-histories of the wave-induced and slosh-induced roll moments; ART without pillars, $\omega\sqrt{L/g}=1.5$, A/L=0.005

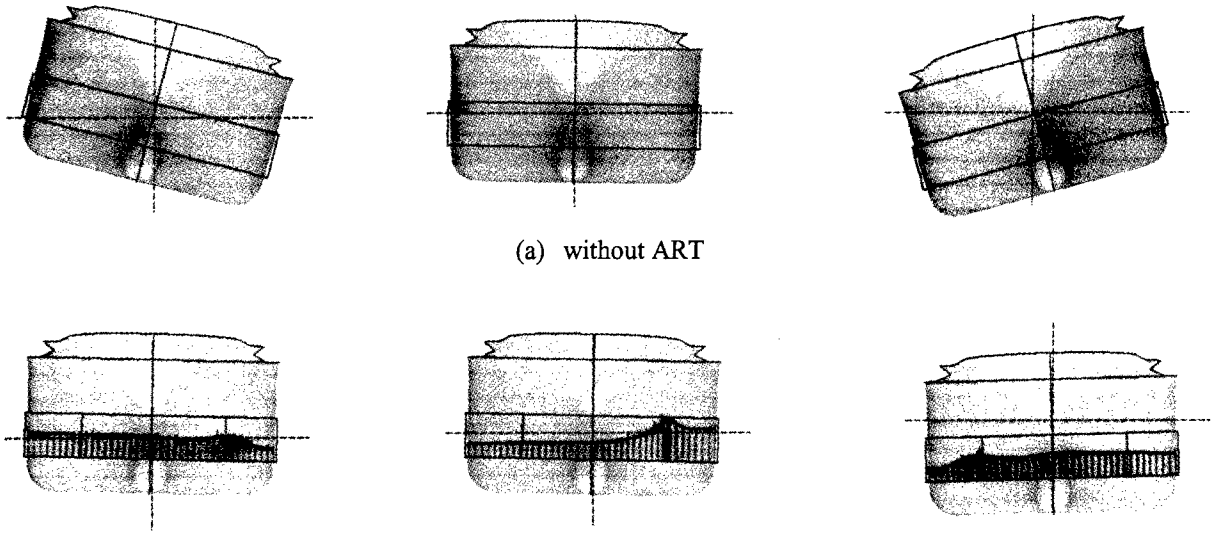

(a) without ART

$t\sqrt{g/L}=22.8$ $t\sqrt{g/L}=23.8$ $t\sqrt{g/L}=24.8$

(b) with ART (with pillars)

Figure 5. Instantaneous ship positions and sloshing flows at three time steps; $\omega\sqrt{L/g}=1.5$, A/L=0.05, 50% filling

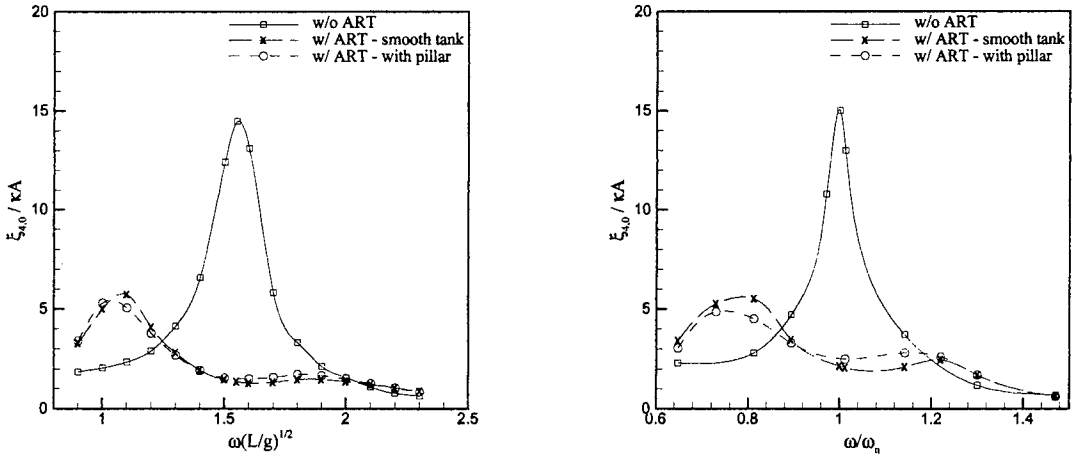

(a) Computational result for modified S175 hull (b) Experimental result for the supply vessel

Figure 6. Motion RAOs of two ships, A/L=0.005

The present method can also be applied to a cargo ship with liquid holds. Figure 7 shows the hull profile (half) and cargo holds for a real ship application. This ship is a typical VLCC of 320-meter long and has 17 oil tanks. Zero speed has been applied, so this ship can be considered as a FPSO also. The center tanks have transverse webs and the wing tanks have

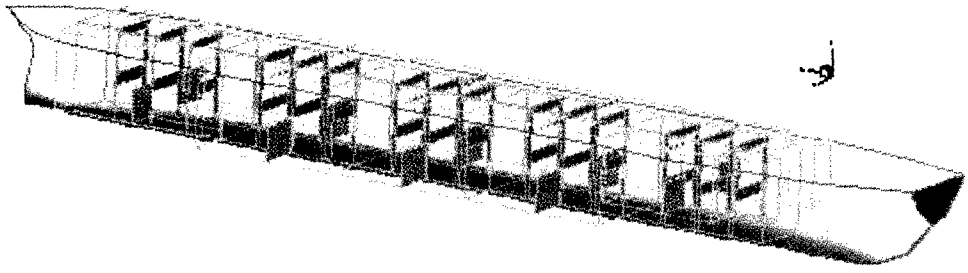

Figure 7. Ship and tank for a real ship computation; 300K VLCC

large swash bulkheads at the tank center. In this computation, the random incident waves were applied to excite the freely floating body with zero speed. The modal wave period was 15.0 seconds and significant wave height was 7.5 meters. The filling ratio was fixed to 80% for most tanks. Figure 8 shows an instantaneous snapshot of the liquid profiles inside of the tanks. The corresponding motion histories are in Figure 9. The difference between two motion signals is significant, therefore the coupling effects may play an important role in ships with liquid cargo.

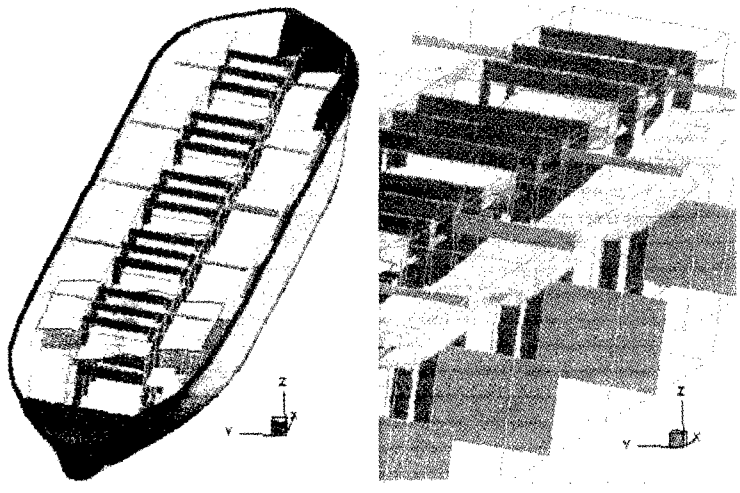

Figure 8. Snapshot of the liquid surface in 17 tanks; 320m VLCC, sea sate 7

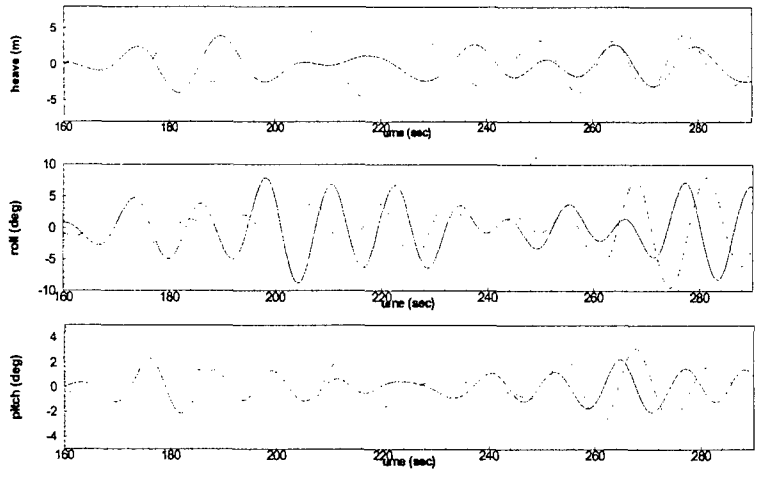

Figure 9. The motion histories at random waves; VLCC, Sea Sate 7, dashed line: without coupling, solid line: with coupling, from above: heave, roll, and pitch

References

[1] KIM, Y., PARK, Y.J., LEE, H.R.: *A numerical study on the prediction of sloshing impact pressure,* Trans. of the Society of Naval Architects of Korea, vol.30 (1994)

[2] KIM, Y.: *Numerical simulation of sloshing flows with impact load,* Applied ocean Research (will appear) (2000)

[3] W.M. LIN et al: *LAMP User's manual,* SAIC (1998)

[4] BAI, K.J., RHEE, K.P.: *Roll-damping tank test,* Seoul National University, Project Report (1987)

[5] VAN DAALEN, E.F.G., GERRITS, J., LOOTS, G.E., VELDMAN, A.E.P.: *Free surface anti-rolling tank simulations with a volume of fluid based Navier-Stokes solver,* Proc. International Workshop on Water Waves and Floating Bodies, Israel, (2000)

[6] MILLER, E.R., SLAGER, J.J., WEBSTER, W.C.: *Phase I report on the development of a technical practice for roll stabilization system selection,* NAVSEC Report 6136-74-280 (1974)

Wave interactions in the coastal zone

Gert Klopman[1] and Maarten W. Dingemans[2]

1. Introduction. In the coastal zone free-surface waves are often quite non-linear, due to shoaling from deeper water where they have been generated by wind or other means. To understand and predict the further evolution in the coastal zone wave-interaction processes are studied by several means. The results of such studies may be applicable to spectral wave models like WAM (*e.g.* see Komen *et al.*, 1994) and SWAN (Booij *et al.*, 1999), as well as to the drift motion of ships moored in shallow water.

2. Cumulant-closure approaches. In the coastal zone we usually have water of restricted depth, for which case Boussinesq-like equations form an adequate description, *e.g.* Dingemans (1997). For simplicity of the discussion we now treat only 1D horizontal wave propagation in this section. Examples of this approach have been given, amongst others, by Rasmussen (1998) and by Becq-Girard *et al.* (1999). Also approaches based on the Laplace equations are followed, *e.g.* Eldeberky and Madsen (1999). See also Dingemans (2000) for a discussion on the above models. Starting with the Boussinesq-like equations given by Madsen and Sørensen (1993) for a slowly-varying bottom formulated in the free-surface elevation $\zeta(x,t)$ and the vertically integrated velocity $q = \int dz\, u(x,z,t)$. The Fourier expansions of ζ and q are written as:

$$\begin{pmatrix} \zeta(x,t) \\ q(x,t) \end{pmatrix} = \sum_{m=-\infty}^{\infty} \begin{pmatrix} 1 \\ \dfrac{\omega_m}{k_m(x)} \end{pmatrix} A_m(\beta x) \exp\left[i\left(\omega_m t - \psi_m(x)\right)\right] \tag{2.1}$$

where $k_m = \partial\psi_m/\partial x$ and $\beta \ll 1$ denotes the slow variation of the amplitudes. Inserting these series in the Boussinesq-like equations and keeping only the lowest-order terms in β leads to an amplitude equation of the following form

$$\frac{dA'_q}{dx} = \left(\sigma_q \frac{dh}{dx} - ik_q(x)\right) A'_q + i \sum_{m=-\infty}^{\infty} J_{m,q-m} A'_m A'_{q-m}\,, \tag{2.2}$$

where $A'_q = A_q \exp\left[-i\psi_q(x)\right]$ and the linear shoaling coefficient σ_q and the interaction coefficient $J_{m,q-m}$ are long expressions, independent of the bottom slope. Notice that reflection has been neglected.

To obtain a model in terms of the (discrete) variance (power spectrum) $E_q = \langle A'_q A'^*_q \rangle$ the evolution equation (2.2) is multiplied with A'^*_q; the conjugate evolution equation is multiplied with A'_q and the averaged. Both contributions are added and of the results the ensemble average is taken. The result is an evolution equation for the discrete spectral values:

$$\frac{dE_q}{dx} = 2\sigma_q \frac{dh}{dx} E_q - 2 \sum_{-\infty}^{\infty} J_{m,q-m}\, \mathrm{Im}\left\{B_{m,q-m}\right\}\,, \tag{2.3}$$

where the bi-spectrum is defined by $B_{m,q-m} = \langle A'_m A'_{q-m} A'^*_q \rangle$.

In the same way an evolution equation for the bi-spectrum can be derived (*e.g*, see Rasmussen, 1998):

$$\begin{aligned} \frac{dB_{m,q-m}}{dx} &= \left[\left(\sigma_m + \sigma_{q-m} + \sigma_q\right)\frac{dh}{dx} - i\delta k(x)\right] B_{m,q-m} \\ &+ i \sum_{-\infty}^{\infty} \left(J_{n,m-n} T_{n,m-n,q-m,-q} + J_{n,q-m-n} T_{n,q-m-n,m,-q} - J_{n,q-n} T_{-n,n-q,m,q-m}\right)\,, \end{aligned} \tag{2.4}$$

where $\delta k(x) = k_m(x) + k_{q-m}(x) - k_q(x)$ is the wave-number mismatch, and $T_{n,m-n,q-m,-q}$ is the discrete tri-spectrum defined as $T_{n,m-n,q-m,-q} = \langle A'_n A'_{m-n} A'_{q-m} A'^*_q \rangle$.

3. Closure hypotheses. Some closure is needed now because the tri-spectrum is in principle unknown. What is usually done is to assume the wave field to be Gaussian, which allows one to discard the fourth-order cumulant. An n-th order moment of random quantities $a_1 \cdots a_n$ can be reduced to a sum of products of lower-order moments, plus a irreducible term, the n-th order cumulant:

$$\langle a_1 \cdots a_n \rangle = \sum_{j=1}^{n-1} \langle a_1 \cdots a_j \rangle \langle a_{j+1} \cdots a_n \rangle + \langle a_1 \cdots a_n \rangle^C\,. \tag{3.1}$$

[1]Albatros Flow Research, The Netherlands, email: Gert.Klopman@afr.nl
[2]WL|Delft Hydraulics, The Netherlands, email: Maarten.Dingemans@wldelft.nl

For a discussion of cumulants[1] for both random variables and random fields is referred to Monin and Yaglom (1975, pp. 223 ff.) or to Kendall and Stuart (1977, Chapter 3).

When also near-stationarity is assumed and when shallow-water wave approximations are used to simplify the coefficients, the following evolution equation for the bi-spectrum results (*i.e.* see Rasmussen[2], 1998, Eqs. (9.20) and (9.21)):

$$\frac{dE_q}{dx} = 2\left(\sigma_q \frac{dh}{dx}\right) E_q - 2\sum_{m=-\infty}^{\infty} J_{m,q-m}\,\mathrm{Im}\left\{B_{m,q-m}\right\}\,, \tag{3.2a}$$

and

$$\begin{aligned}\frac{dB_{m,q-m}}{dx} &= \left[\left(\sigma_m + \sigma_{q-m} + \sigma_q\right)\frac{dh}{dx} - i\delta k(x)\right] B_{m,q-m} \\ &\quad + 2iJ_{m,q-m}\left(\frac{k_m}{k_q}E_q E_{q-m} + \frac{k_{q-m}}{k_q}E_q E_m - \frac{k_q}{k_m}E_m E_{q-m}\right)\,.\end{aligned} \tag{3.2b}$$

For use in wave models like WAM and SWAN it is advantageous to decouple these equations.However, this can only be done in a very approximate way and the resulting spectral energy evolution equation gives no evolution in case of a horizontal bottom. The fourth-order cumulant discard hypothesis has been used extensively, see, *e.g.* Rasmussen (1998) and Eldeberky and Madsen (1999).

In turbulence research it is well known that the fourth-order cumulant discard hypothesis (also known as the Millionschikov hypothesis, see, *e.g.*, Monin and Yaglom, 1975, p. 241 and §19.3). Applying this hypothesis leads to an evolution equation for the energy which leads to negative energies eventually because of the viscous damping. In water waves a similar damping is present because usually a cut-off frequency is used and increasingly shorter waves come in the region beyond the cut-off frequency and lead to a form of damping. The inconsistency in using the Gaussianity assumption can be made clear in the following way. The energy density evolution equation shows the generation of bound waves. With the presence of bound and free waves in the wave field, it cannot be true anymore that the totality of the wave field remains Gaussian (or, otherwise stated, uncoupled and therefore linear). Janssen (1991) shows that it is a necessity for having transfer of energy over the various components of the spectrum to have the fourth-order cumulant to be different from zero. He therefore takes the sixth-order cumulant to be zero.

A different, but related view has been given by Holloway (1980). Instead of taking the n-th order cumulant to be zero, $\langle a_1 \cdots a_n\rangle^C = 0$, Holloway (1980) substitutes for the n-th order cumulant a term linear in the $(n-1)$-th cumulant $\langle a_1 \cdots a_{n-1}\rangle^C$ with a fore-factor which is an unknown function of lower-order cumulants. Effectively what is happening is that instead of supposing the fourth-order cumulant to be zero, the difference between the fourth-order cumulant and some linear functional of the triple correlation is supposed to be zero. Following Holloway (1980), the kinetic equation for the spectral action density N_ℓ can be written in the following general form:

$$\frac{\partial N_\ell}{\partial t} = \int_\Delta dk_m dk_n \Gamma_{\ell mn}\left(N_m - N_\ell\right) N_n \theta_{\ell nm}\,, \tag{3.3}$$

with $\int_\Delta$ denoting the integration over the wave numbers satisfying $\boldsymbol{k}_\ell + \boldsymbol{k}_m + \boldsymbol{k}_n = 0$, the $\Gamma_{\ell mn}$ are the interaction coefficients depending on the specific model and $\theta_{\ell mn} = \mathrm{Re}\left\{\left[\mu_{\ell mn} + i\left(\omega_{\ell mn}\right)\right]^{-1}\right\}$. The coupling coefficient thus appears as an frequency uncertainty coefficient among three interaction waves, indicating a broadening of the resonance condition. For the determination of $\mu_{\ell mn}$ Holloway suggests to identify it with the sum of the individual interaction rates $\mu_{\ell mn} = \eta_\ell + \eta_m + \eta_n$ with the fundamental interaction rate η_ℓ given by $\eta_\ell = \int_\Delta dk_m dk_n \Gamma_{\ell mn} N_n \theta_{\ell mn}$. Equation (3.3) together with the relations for $\theta_{\ell mn}$, $\mu_{\ell mn}$ and η_ℓ constitute a closed set of equations describing the evolution of strongly-interacting waves. In the approach of Becq-Girard em et al. (1999) an approximate version of the approach of Holloway has been followed. Here the parameter $\mu_{\ell mn}$ has been replaced by a fixed parameter K to be chosen beforehand. No simple prescription how to choose K is available.

4. Perturbation-series approaches. Another approach to describe the non-linear triad interactions is by the direct application of Stokes' second-order wave theory to directional random waves. This has been done in a classical Stokes' second-order perturbation-series approach for deep-water waves by *e.g.* Masuda *et al.* (1979), and for an arbitrary water depth with a horizontal bed by *e.g.* Dean and Sharma (1981) and Laing (1986). Willebrand (1975) started from a variational principle and derived similar results which are also applicable to mildly sloping sea beds.

[1] In the Russian literature *cumulant* is also termed *semi-invariant*.

[2] Rasmussen also considers effects of wave dissipation due to wave breaking, which effects we here ignore.

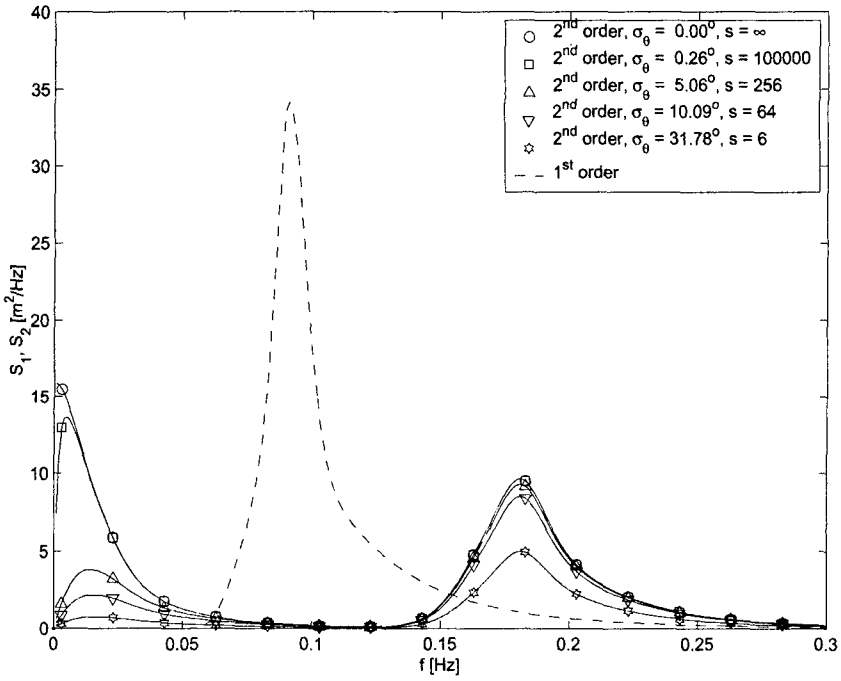

FIG. 4.1. *Influence of the amount of directional spreading on the second-order spectrum.*

The perturbation-series approaches make distinction at a certain frequency between free wave-components satisfying the wave dispersion relationship and bound components forming a non-resonant triad with two free components. The bound wave-components are traveling with a celerity not satisfying the wave dispersion relationship. This multi-component description per wave frequency and direction is different from the approaches described in Section 2 (*e.g.* Becq-Girard *et al.*, 1999; Eldeberky and Madsen, 1999; Herbers and Burton, 1997; Rasmussen, 1998) which consider only one wave component per wave frequency and direction.

Using the nomenclature of Laing (1986), the free surface elevation $\zeta(\boldsymbol{x},t)$ in the perturbation-series approach can be described as:

$$\text{(4.1a)}\qquad \zeta(\boldsymbol{x},t) = \sum_{m=-\infty}^{\infty} A_m \exp[\, i\,(\omega_m t - \boldsymbol{k}_m\cdot\boldsymbol{x})] \;+ \\ + \sum_{m=-\infty}^{\infty}\sum_{n=-\infty}^{\infty} \frac{D_2(\omega_m,\boldsymbol{k}_m;\omega_n,\boldsymbol{k}_n)}{g\,[1-\Omega_{m,n}^2/(g\,\kappa_{m,n}\,\tanh\kappa_{m,n}\,h)]}\, A_m\, A_n\, \exp[\, i\,(\Omega_{m,n}t - \boldsymbol{\kappa}_{m,n}\cdot\boldsymbol{x})],$$

with $\Omega_{m,n} = \omega_m + \omega_n$ and $\boldsymbol{\kappa}_{m,n} = \boldsymbol{k}_m + \boldsymbol{k}_n$ respectively the angular frequency and the wave number of the bound-wave components with kernel D_2, $\kappa_{m,n} = |\boldsymbol{\kappa}_{m,n}|$, (ω_m,ω_n) and $(\boldsymbol{k}_m,\boldsymbol{k}_n)$ the angular frequency and wave number of the free-wave components. Further we have for the negative-indexed quantities the following symmetry relations in order to get a real-valued free surface elevation $\zeta(\boldsymbol{x},t)$:

$$\text{(4.2)}\qquad \omega_{-m} = -\omega_m, \qquad \boldsymbol{k}_{-m} = -\boldsymbol{k}_m, \qquad \text{and} \qquad A_{-m} = A_m^*.$$

Assuming the first-order wave components A_m to be due to a stationary Gaussian process, it is easy to derive an expression for the (two-sided) power spectrum $\Phi(\omega,\boldsymbol{k})$ of the free surface elevation $\zeta(\boldsymbol{x},t)$:

$$\text{(4.3a)}\qquad \Phi(\omega,\boldsymbol{k}) = \Phi_1(\omega,\boldsymbol{k}) + \Phi_2(\omega,\boldsymbol{k}),$$

$$\text{(4.3b)}\qquad \Phi_2(\omega,\boldsymbol{k}) = \int\!\!\int d\boldsymbol{k}_1\, d\omega_1\; D_{20}(\omega_1,\boldsymbol{k}_1;\omega-\omega_1,\boldsymbol{k}-\boldsymbol{k}_1)\;\Phi_1(\omega_1,\boldsymbol{k}_1)\;\Phi_1(\omega-\omega_1,\boldsymbol{k}-\boldsymbol{k}_1),$$

$$\text{(4.3c)}\qquad D_{20}(\omega_1,\boldsymbol{k}_1;\omega_2,\boldsymbol{k}_2) = 2\left\{\frac{D_2(\omega_1,\boldsymbol{k}_1;\omega_2,\boldsymbol{k}_2)}{g\,[1-\hat{\Omega}_{1,2}^2/(g\,\hat{\kappa}_{1,2}\,\tanh\hat{\kappa}_{1,2}\,h)}\right\}^2,$$

with $\Phi_1(\omega,\boldsymbol{k})$ the two-sided first-order spectrum of the free wave components, $\hat{\Omega}_{1,2} = \omega_1+\omega_2$, $\hat{\kappa}_{1,2} = |\hat{\boldsymbol{\kappa}}_{1,2}|$ and $\hat{\boldsymbol{\kappa}}_{1,2} = \boldsymbol{k}_1 + \boldsymbol{k}_2$.

For waves with a first-order JONSWAP spectrum and $\cos^{2s}(\theta/2)$ directional distribution in a water depth of 8 meter and a peak frequency of 0.91 Hz, Figure 1 gives an example of the influence of the amount of direction spreading on the wave-number integrated one-sided frequency spectra $S_1(f)$ and $S_2(f)$:

$$S_1(f) = 4\pi \int \Phi_1(2\pi f, \boldsymbol{k})\, d\boldsymbol{k} \qquad \text{and} \qquad S_2(f) = 4\pi \int \Phi_2(2\pi f, \boldsymbol{k})\, d\boldsymbol{k}. \tag{4.4}$$

For a given first-order free-wave spectrum $\Phi_1(\omega, \boldsymbol{k})$ the associated second-order bound-wave spectrum $\Phi_2(\omega, \boldsymbol{k})$ can be determined in a straightforward manner. However, in general the total spectrum $\Phi(\omega, \boldsymbol{k})$ is given and $\Phi_1(\omega, \boldsymbol{k})$ and $\Phi_2(\omega, \boldsymbol{k})$ are unknown. Laing (1986) used an iterative procedure to split a given spectrum into a (first-order) free-wave part and a (second-order) bound-wave part.

5. Concluding remarks. In the coastal zone wave non-linearity is dominated by non-resonant and near-resonant interactions between wave triads. This in contrast with the situation in deep water, where the energy content of the bound sub-harmonics is neglegible and the bound super-harmonics also become much less important (but do not vanish).

Two approaches are being studied: cumulant-closure approaches and perturbation-series approaches. At the moment there exist no well-proven cumulant-closure relationships, while the perturbation-series approaches are self-contained at a certain order and do not need additional closure. At this moment the inclusion of a perturbation-series approach (*e.g.* Laing, 1986; Willebrand, 1975) into a spectral model for coastal regions like SWAN (Booij *et al.*, 1999) seems the most straight-forward method for the inclusion of the major non-resonant bound-wave triad interactions.

For a horizontal bed both the cumulant-closure approaches and the perturbation-series approaches are both supposed to include a description of second-order bound waves. So, a carefull comparison of both approaches for this horizontal bed case can lead to more insight into their working and into their weak and strong points.

Another point which still needs further research is the description of near-resonant triad interactions other than the bound waves.

References.

Becq-Girard, F., Forget, P. and Benout, M., 1999. Non-linear propagation of unidirectional wave fields over varying topography. *Coastal Engineering* **38(2)**, pp. 91-113.

Booij, N., Ris, R.C. and Holthuijsen, L.H., 1999. A third-generation wave model for coastal regions. Part I.: Model description and validation. *J. Geophys. Res.* **104(C4)**, pp. 7649-7666.

Dean, R.G. and Sharma, J.N., 1981. Simulation of wave systems due to nonlinear directional spectra. *Proc. Int. Symp. Hydrodynamics in Ocean Eng.*, Trondheim, Norway, **2**, pp. 1211-1222.

Dingemans, M.W., 1997. *Water Wave Propagation over Uneven Bottoms.* World Scientific, Singapore, 967 pp.

Dingemans, M.W., 2000. *Modelling of wave-triad interactions for use in SWAN.* WL|Delft Hydraulics, Note H3528.20, April 2000, 13 pp.

Eldeberky, Y. and Madsen, P.A., 1999. Deterministic and stochastic evolution equations for fully dispersive and weakly nonlinear waves. *Coastal Engineering* **38(1)**, pp. 1-24.

Herbers, T.H.C. and Burton, M.C., 1998. Nonlinear shoaling of directionally spread waves on a beach. *J. Geophys. Res.* **102(C9)**, pp. 21101-21114.

Janssen, P.A.E.M., 1991. On non-linear wave groups and consequences for spectral evolution. In: *Directional Ocean Wave Spectra*, Editor Beal, R.C., The John Hopkins University, pp. 46-52.

Holloway, G., 1980. Oceanic internal waves are not weak waves. *J. Phys. Ocean.* **10(6)**, pp. 906-914.

Kendall, M. and Stuart, A., 1977. *The Advanced Theory of Statistics.* Vol. 1: *Distribution Theory*, Fourth Edition. Charles Griffin, London, 472 pp.

Komen, G.J., Cavaleri, L., Donelan, M., Hasselmann, K., Hasselmann, S. and Janssen, P.A.E.M., 1994 *Dynamics and Modelling of Ocean Waves.* Cambridge Univ. Press, 532 pp.

Laing, A.K., 1986. Nonlinear properties of random gravity waves in water of finite depth. *J. Phys. Ocean.* **16(12)**, pp. 2013-2030.

Masuda, A., Kuo, Y.Y. and Mitsuyasu, H., 1979. On the dispersion relation of random gravity waves. Part 1: Theoretical framework. *J. Fluid Mech.*, **92**, pp. 717-730.

Monin, A.S. and Yaglom, A.M., 1975. *Statistical Fluid Mechanics: Mechanics of Turbulence*, Vol. 2. The MIT Press, Cambridge, Ma., 769 pp.

Rasmussen, J.H., 1998. Deterministic and stochastic modelling of surface gravity waves in finite depth. *Ph.D. Thesis*, ISVA, Denmark, 245 pp.

Willebrand, J., 1975. Energy transport in a nonlinear and inhomogeneous random gravity wave field. *J. Fluid Mech.*, **70(1)**, pp. 113-126.

BREAKING BOW AND STERN WAVES: NUMERICAL SIMULATIONS

M. Landrini,
INSEAN, The Italian Ship Model Basin
Via di Vallerano 139, 00128, Roma, Italy
Email: maulan@waves.insean.it

A. Colagrossi
Ocean Engineering Laboratory, UCSB
6740 Cortona Dr., Goleta 93117 (CA)
Email: andreac@catena.mee.ucsb.edu

M. P. Tulin
Ocean Engineering Laboratory, UCSB
6740 Cortona Dr., Goleta 93117 (CA)
Email: mpt@engineering.ucsb.edu

Ship-generated waves have always fascinated scientists, and played a key role in surface-ship hydrodynamics for contributing to hull resistance, generating sounds and radiating very long narrow wakes remotely visible. Some of these phenomena originate abeam the ship through extensive breaking of diverging bow and stern waves, forming a wake.

In this paper we summarize and extend our recent research activity aimed to understand the complex fluid dynamics involved in bow- and stern-wave radiation, including wave breaking. The analysis is limited to practical slender ships, with a sharp stem, for which basic insight can be achieved by an approximate quasi three-dimensional model based on the idea that longitudinal gradients of relevant flow quantities are small compared with vertical and transverse gradients. A historical recollection of slender-body theory for ship hydrodynamics is given by Maruo (1989), Tulin and Wu (1996), Fontaine and Tulin (2001).

In this framework, two methods have been developed at the OEL. One based on a potential flow model, where the velocity field is given through the Laplace equation solved by a Boundary Element Method (BEM), and the evolution in time is obtained by integration of free-surface boundary conditions. Specific details of the latest code are documented in Landrini and Colagrossi (2001 a). The method has the advantage of high resolution, sufficient to capture breaking, and to trace jet overturning up to the impact against the underlying free surface.

Post-breaking evolution is studied by a gridless method, called SPH and developed by Monaghan and co-authors (see *e.g.* Monaghan (1988)), which we applied to breaking waves since the previous Workshop. In this case, Euler equations for a weakly compressible fluid have been considered. Further developments led to a code named *SPlasH*, applied to a variety of free-surface problems, and presented in Tulin and Landrini (2000), Colagrossi *et al.* (2000). A detailed description of the algorithm is given in Landrini *et al.* (2001 b)

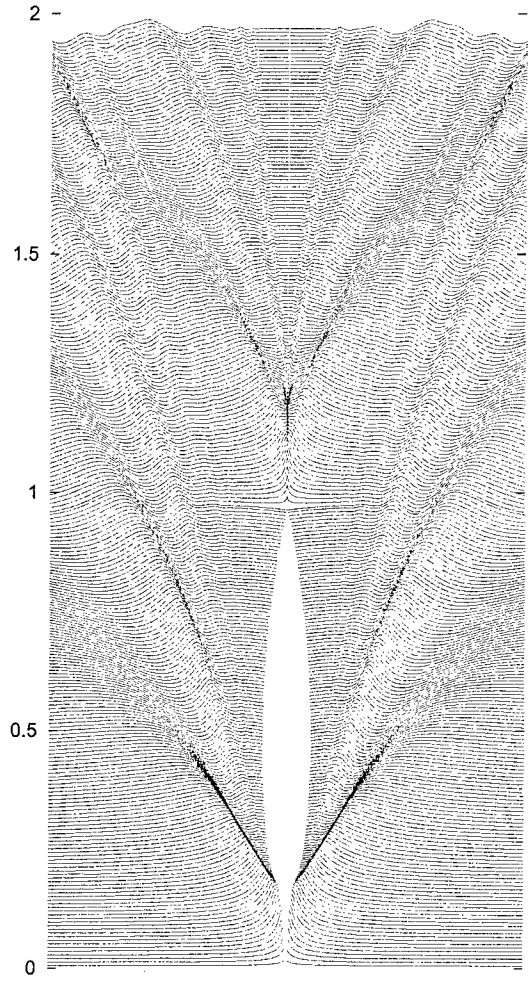

Figure 1. Wave pattern around a Wigley hull ($B/L = 0{\cdot}1$, $D/L = 0.1$, $\mathrm{Fr} = 0{\cdot}3$) by 2D+t (BEM) computations.

The global picture by BEM In the 2D+t method, calculations are carried out in two dimensions, vertical and transverse to the ship, and successively in time. Fig. 1 shows the three-dimensional steady wave pattern around a Wigley hull reconstructed by collecting successive free-surface configurations.

Two key features of the flow are evidenced: first, the system of diverging waves radiated at the bow as a result of the collapse of the "splash", and second the "rooster tail" due to the gravity rebound of the free surface just past the stern which, in turn, is the source of another system of diverging waves.

A thorough analysis of the genesis of diverging bow waves is given by Tulin and Wu (1996). The collapse of

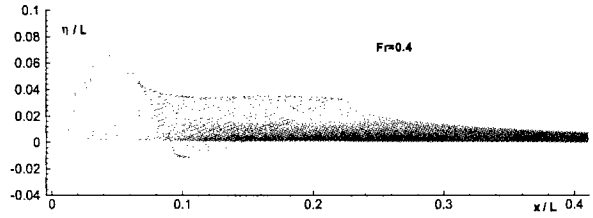

Figure 2. Evolution of the splash at the bow of a Wigley hull ($B/L = 0{\cdot}2$, $D/L = 0{\cdot}1$, Fr$= U/\sqrt{gL} = 0{\cdot}4$) by 2D+$t$ (BEM) computations.

splash at the bow is detailed through Fig. 2: the free-surface flow is not much decelerated before the stem, but upon reaching it, is deviated sharply upwards, rises on and eventually levels off and falls down. An entire thin sheet is formed in this process and appears as a splash on either side of the hull. The relaxation of these splashes is the prime source of diverging waves. In the present case, radiated waves are large enough to break, following the typical evolution: crest-rising, front-steepening and jet formation.

Diverging breaking waves can be radiated also by transom sterns. This is shown in the case of a Wigley hull, suitably tapered to have a deep transom stern (*cf.* top-plot in Fig. 3). The computation is performed as in previous cases up to the last section. We then assume that the transom is dry and the potential is continuous across it, this provides the initial conditions for the following free-surface evolution. The resulting wave pattern for Fr$=U/\sqrt{gL} = 0{\cdot}3$ is shown in the center-plot. Beside the already mentioned bow wave system, here we observe a sharp rooster tail, surrounded by steep breaking diverging waves. The analysis of the flow field shows that the rooster tail is caused by i) the inward motion of the fluid in proximity of the ship associated with the contraction of the hull cross section and eventually colliding after the end of the ship, and ii) the gravity rebound of the free surface. Both features are also detected in the case of Fig. 1, but for a dry transom stern the cavity left in the free surface gives rise to a stronger rebound. The growth of stern waves is better shown in the perspective view in the bottom plot. At first, the free surface move inwards and upwards, creating a sort of triangular hump. Later, the main bulk of fluid starts to collapse down, leaving a thinner and thinner jet, and a couple of steep waves propagating outwards emerge, breaking soon after.

Post-breaking analysis through *SPlasH* In practical cases ship-generated waves break, and further analysis by BEM would require special treatment of the free surface, often unphysical or not practical. The reasons for ship waves to break can be found in ship geometry (bow-flare, transom stern), higher speed of advance, interaction with ambient waves.

The gridless code *SPlasH* has been developed to handle these breaking cases. The evolution of a breaking bore, shown in Fig. 4, gives an idea of the capabilities of the method. The flow is generated by a piston moving horizontally with constant speed. After a while an energetic jet appears, impacting with the underlying free surface and

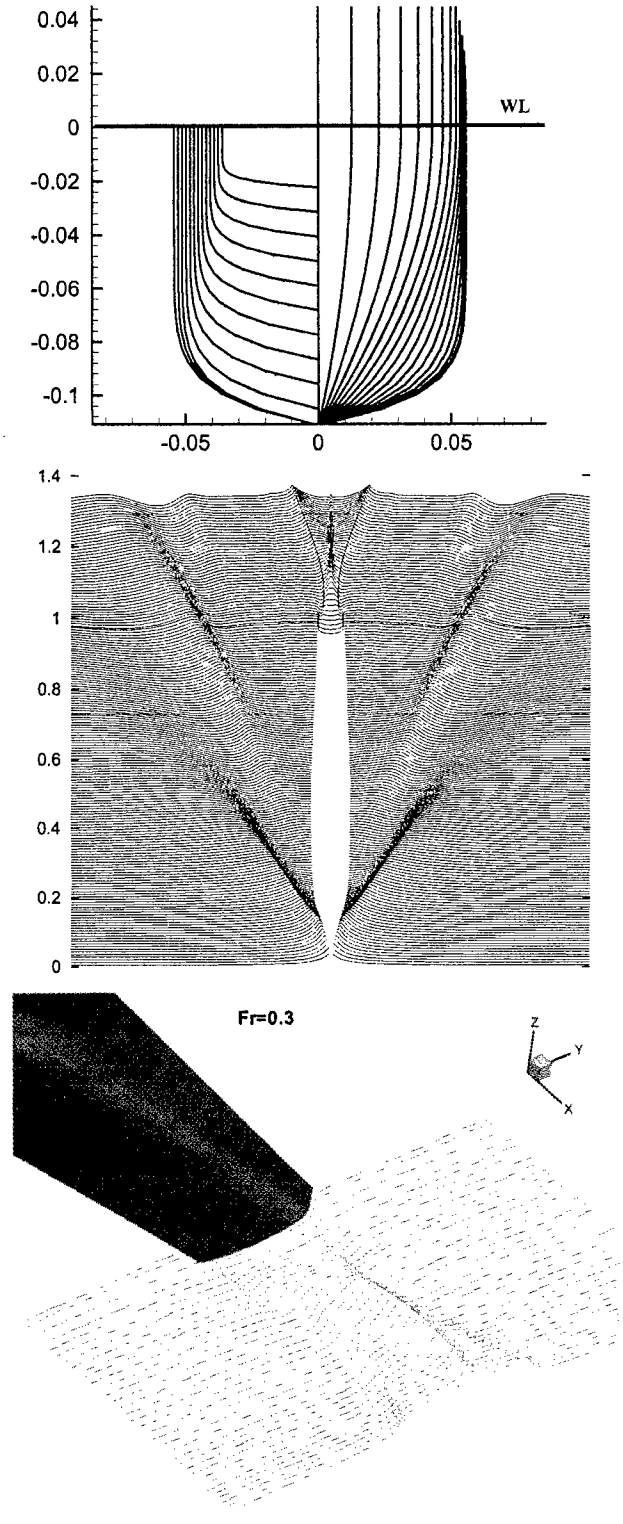

Figure 3. Wave pattern around a modified Wigley hull with a transom stern by 2D+t (BEM) computations. Top: ship cross sections; center: wave pattern; bottom: detail of rooster tail and breaking waves past the stern.

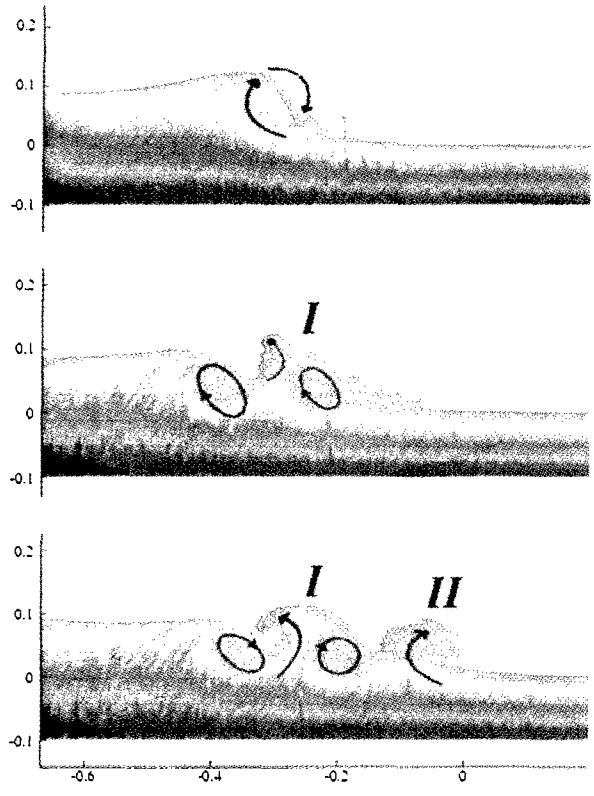

Figure 4. Breaking bore and splash-up cycles forced by a piston moving from left to right in finite depth water. Computations by SPH method.

creating a cavity and therefore circulation (here clockwise). The strong splash-up *I* appears, center-plot, evolving into a counter-rotating vortical structure and another forward splash up *II*, bottom-plot. The strength of the plunging jet is crucial in determining that of the following splash-up and the entire resulting process, which for the breaking bore here considered is characterized by several splash-up cycles, Tulin and Landrini (2000).

We have discovered similar features in breaking ship waves by analyzing pictures of model testing (pictures taken by Penna and Guerra at the INSEAN model basin). In particular, Fig. 5 shows the bow wave generated by a frigate (DDG51-type of the US Navy) with a strong flare. For Fr= 0·41, the splash readily evolves into a plunging jet, creating the splash-up shown in the enlarged detail which reveals also the surface scar associated with the backward facing jet to be compared with the bottom-plot in Fig. 4.

We applied *SPlasH* in a 2D+*t* fashion to study the post-breaking behavior of ship waves. We first discuss the case of a Wigley hull. The initial evolution has been already shown in Fig. 2 and, in this case, the computations are initialized by those BEM results. This procedure simplified the modeling, increased the efficiency and allowed an optimal resolution of the computation, with a high number of particles clustered into the jet. The three-dimensional wave pattern is reconstructed in Fig. 6, where only the upper layer of particles is represented. Only the portion around the breaking is

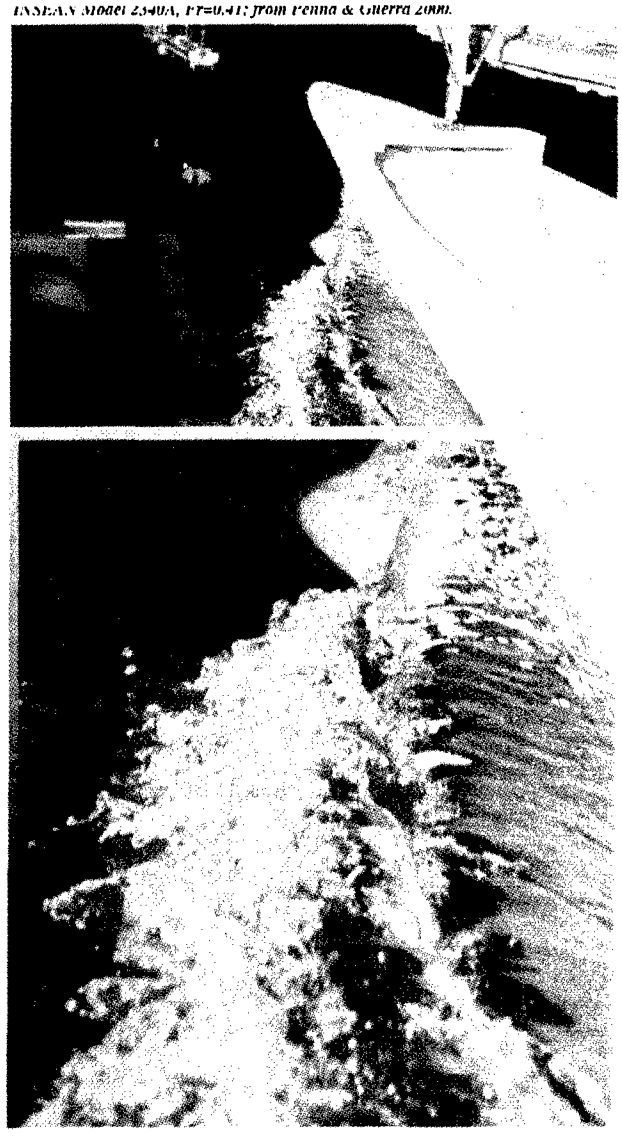

Figure 5. Breaking bow waves in model testing. INSEAN Model 2412 of the US Navy DDG51 (Fr=0·41).

shown, with the ship center plane located at $y = 0$, and the mid-ship cross section at $x = 0$. The impacting jet generates a splash-up, evolving into i) a vortical structure left behind the crest, and ii) remaining particles riding on the crest emerging after the breaking which resemble the steady eddy used by Cointe and Tulin (1994) to model two-dimensional steady spilling breakers. This flow pattern is better visible in the two-dimensional bottom plot, and is remarkably similar to pictures of (two-dimensional) breaking waves shown in Melville (1996).

On this ground, in breaking ship-wave patterns, we can distinguish a TYPE I breaking, resulting from less energetic breaking waves, and resembling the steady spilling breaking observed *e.g.* past hydrofoils at small incidence, and a TYPE II breaking, with strong (possibly multiple) splash-up, causing larger air entrapment and vortex generation.

TYPE II breaking is (usually) generated at the bow of

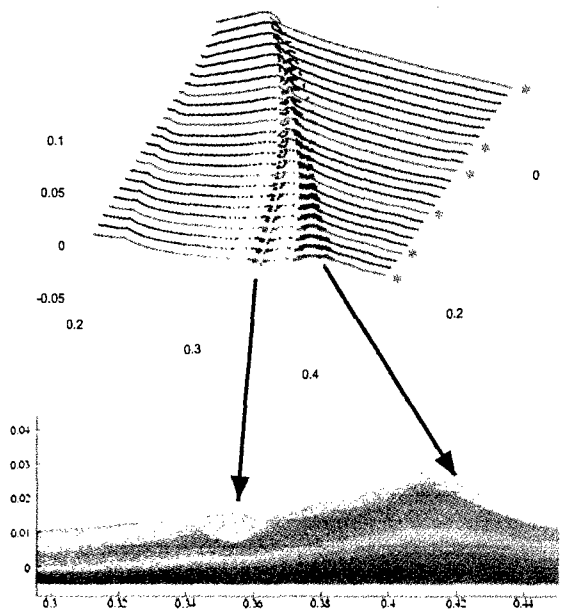

Figure 6. Top: perspective view of 2D+t computation by *SPlasH* of the wave pattern generated by a Wigley hull ($B/L = 0{\cdot}2$, $D/L = 0{\cdot}1$, Fr= 0·46); bottom: two-dimensional view of late evolution.

ships with pronounced flare, and the numerical simulation by SPH requires the modeling of arbitrary curved boundaries. This extension of *SPlasH* has been recently accomplished by generalizing the concept of "ghost particles", and a preliminary result is given in Fig. 7 for a frigate-type ship (used by O'dea and Walden in their analysis of deck wetness). The flare is less pronounced than in Model 2412, and the collapse of the splash, top plot, causes a weaker breaking than that observed in Fig. 5. The resulting three-dimensional wave pattern is reconstructed in the bottom plot.

Results for Model 2412 and for the post-breaking evolution of stern waves will be discussed at the Workshop.

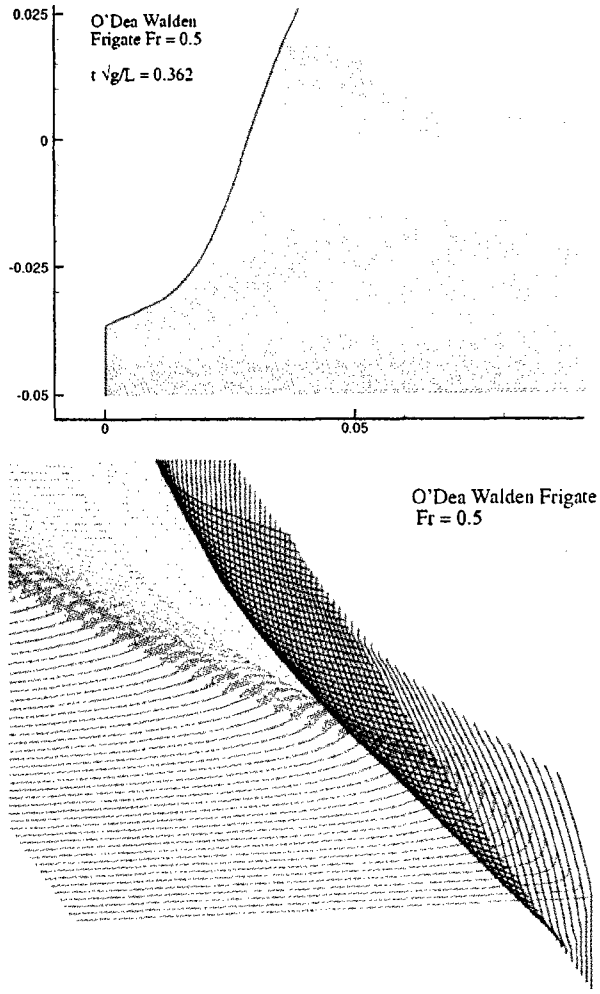

Figure 7. 2D+t computation by *SPlasH* of wave pattern around a frigate. Top: the collapsing splash at the bow; bottom: perspective view of the resulting wave pattern.

ACKNOWLEDGEMENTS

This work has been supported as part of a program for the simulation of ship breaking waves by the Ship Hydrodynamics Program of ONR, initiated by Dr. Ed Rood and now supervised by Dr. Pat Purtell. The research acitivity of M.L. is also supported by the Italian *Ministero dei Trasporti e della Navigazione* through INSEAN Research Program 2000-2002.

REFERENCES

R. Cointe R., M.P. Tulin "A theory of steady breakers", *J. Fluid Mech.*, Vol. 276, 1994.

A. Colagrossi, M. Landrini, M.P. Tulin "Near Shore Bore Propagation and Splashing Processes: Gridless Simulations", Monterey (CA), OEL Tech. Report 00-224, 2000.

E. Fontaine, M. Landrini, M.P. Tulin On modeling the post-breaking phase: splashing. Proc. of *15th Int. Work. Water Waves Float. Bodies*, Eds. T. Miloh and G. Zilman, 2000.

E. Fontaine, M.P. Tulin "On the prediction of free-surface flows past slender hulls using the 2D+t theory: the evolution of an idea", *Ship Tech. Res.*, 2001.

M. Landrini, A. Colagrossi "TwoDPT: a 2D+t code for ship hydrodynamics", OEL Technical Report, 2001

M. Landrini, A. Colagrossi, M.P. Tulin "Gridless simulation of sloshing flows in tank", OEL Technical Report, 2001

H. Maruo H. "Evolution of the theory of slender Ships", *Ship Tech. Res.*, Vol. 36, pp. 107-133, 1989.

W.K. Melville W.K. "The role of surface-wave breaking in air-sea interaction", *Ann. Rev. Fluid Mech.*, Vol. 28, 1996, pp. 279-321, 1996.

Monaghan J.J., "An Introduction to SPH", *Comp. Phys. Comm.* 48, pp. 89-96, 1988.

M. P. Tulin, M. Landrini "Breaking waves in the ocean and around ships" Proc. of *23rd ONR Symp. on Naval Hydrodynamics*, Val de Reuil, France, 2000.

M.P. Tulin, M. Wu "Divergent bow waves" Proc. of *21st ONR Symp. on Naval Hydrodynamics*, Trondheim, Norway, National Academy Press, Wash. D.C., pp. 99–117, 1996.

SOLUTION OF RADIATION PROBLEMS WITH EXACT GEOMETRY

by C.-H. Lee[1] and J. N. Newman[2]
[1] WAMIT, Inc., Chestnut Hill, MA USA (chlee@wamit.com)
[2] MIT, Cambridge, MA USA (jnn@mit.edu)

(16th Workshop on Water Waves and Floating Bodies – Hiroshima, Japan – 22-25 April 2001)

The panel method is used frequently to solve three-dimensional radiation and diffraction problems in the frequency domain. In the usual numerical procedure the submerged surface of the body is represented by small elements. Both the solution for the velocity potential or source strength, and also the body geometry, are approximated on each element.

In most practical cases the number of elements needed to achieve the desired accuracy is large, on the order of 1000. Significant effort may be required to develop a suitable set of elements for input to the program. Generally this requires the use of special pre-processing software. Several input files with systematically smaller elements may be required to establish convergence. Despite these problems, the low-order panel method is widely used for radiation/diffraction analyses, even for simple bodies such as spheres and cylinders.

It is not strictly necessary to approximate the body geometry, if it can be represented explicitly in the program. This avoids the effort of developing appropriate input files with small elements, and provides a more accurate description of the geometry. The explicit representation is most useful in conjunction with a higher-order representation of the solution. Some modifications are required in the numerical implementation and coding, particularly with respect to the evaluation of the influence functions.

In some cases one explicit algorithm is sufficient to describe the entire body surface. A much wider class of bodies can be represented by subdividing the submerged surface into patches, with separate algorithms corresponding to each patch. The truncated circular cylinder is an example, where two separate patches are required to represent the cylindrical side and circular flat bottom. The fundamental property of each patch is that its surface is smooth, continuous, and differentiable. The most general definition of the class of bodies we include here is that the submerged surface can be subdivided into a set of patches, where a pair of parametric coordinates (u, v) is used to define the position on each patch, the boundaries of the patch map to a square in the parametric space, and an explicit transformation $\mathbf{x}(u, v)$ exists between the Cartesian space (x, y, z) and the parametric space.

This procedure has been used to extend the capabilities of the radiation/diffraction code WAMIT. Except for the use of explicit geometry we follow the approach developed by Maniar (1995), and described by Lee *et al* (1996). In that work B-splines are used to represent both the geometry and the velocity potential on each patch. Here we use B-splines only to represent the velocity potential. The accuracy of the solution can be systematically refined by controlling the degree of the B-splines, and/or subdividing each patch into 'panels' with B-spline knots at the panel boundaries. Three examples follow, with brief descriptions of the body representation and hydrodynamic results.

Truncated vertical cylinder with an oblate spheroidal bottom

The family of bodies shown in Figure 1 is generated by a simple subroutine. Quadratic B-splines are used to represent the solution. On each patch, 2×2 or 4×4 panels are used. In the case $R = 0$, corresponding to a submerged oblate spheroid, one patch is used with 16 or 36 unknowns. In the cases $R > 0$ two patches are used and the total number of unknowns (B-spline coefficients) is 32 or 72, respectively.

Figure 2 shows the heave added-mass and damping coefficients. For the three intermediate cases ($R = 0.25, 0.5, 0.75$) the damping coefficient (and also the heave exciting force) vanish at ($k = 0.045, 0.22, 0.74$), respectively.

The McIver toroid

The McIver toroid shown in Figure 3 was analyzed by Newman (1999), using the low-order panel method. The results of that work confirmed the existence of a singular solution at the first zero of the Bessel function $J_0(k)$ ($k = 2.4048$). However the convergence of the low-order analysis is relatively slow near the singular wavenumber, and up to 8192 panels were used (2048 unknowns). For the present higher-order analysis an explicit representation of the geometry has been developed. The procedure described by Newman (1999) is used to compute the loci of points on a cross-section. These points are expressed in terms of the toroidal coordinates R and θ about the axis of the ring source and the radius $R(\theta)$ is approximated by an economized polynomial of degree 10. The maximum error in this approximation is a radial difference on the order of 0.00001. Only one patch is required to represent one quadrant of the toroid, as shown in Figure 3. Quadratic B-splines are used to represent the velocity potential.

Figure 4 shows the heave added mass in the vicinity of the singular wavenumber, and the convergence of the singular wavenumber with increasing numbers of panels using both the low- and higher-order methods. (The singular wavenumber is defined here as the value of k where the added-mass coefficient changes sign from positive to negative values.) It is apparent that the higher-order solution is more accurate, and requires a much smaller number of unknowns.

Rectangular barge with moonpool

A rectangular barge with two planes of symmetry and a rectangular moonpool at its center is represented by six flat rectangular patches (end, side, moonpool end, moonpool side, bottom forward of the moonpool, and bottom outboard of the moonpool). The principal dimensions are length=16m, beam=4m, moonpool length 8m, and moonpool width 2m. The draft is varied between 0.125m and 2.0m to illustrate its effect on the moonpool resonant frequencies. The table below shows the peak amplitude and wavenumber for the first five Fourier coefficients of the free-surface elevation in the moonpool. In the 'radiation' data the barge oscillates in the surge/heave modes in calm water, and the Fourier coefficients are evaluated directly from the resulting free-surface elevation on the centerline of the moonpool. In the 'diffraction' data the barge is fixed in incident head waves. Most of the resonant amplitudes are greater in the radiation problem, due to the stronger forcing by the body motions.

The last line in the table shows the asymptotic limits of the resonant wavenumbers for infinite draft. In this limit the resonant modes $n > 0$ correspond to standing waves with n nodes, in a basin with the same horizontal dimensions as the moonpool. As the draft is reduced the resonant wavenumber increases, corresponding to a reduction in the resonant wave period. This was first noted and explained by Molin (1999). For the 'pumping mode' ($n = 0$) the resonant wavenumber $k \simeq 1/T$ for large draft T.

	draft(m)	k_0	$\|c_0\|$	k_1	$\|c_1\|$	k_2	$\|c_2\|$	k_3	$\|c_3\|$	k_4	$\|c_4\|$
radiation:	0.125	0.82	3.0	1.00	0.4	1.27	14	1.60	5.1	1.93	89
	0.25	0.76	3.0	0.92	1.1	1.18	15	1.49	16	1.82	127
	0.5	0.64	3.2	0.78	3.4	1.03	21	1.34	84	1.68	310
	1.0	0.48	3.9	0.62	16	0.89	56	1.22	1115	1.59	465
	2.0	0.32	5.0	0.48	127	0.81	500	1.18	35000	1.57	3300
diffraction:	0.125					1.28	0.6	1.61	1.0	1.95	1.0
	0.25			0.92	1.1	1.18	1.1	1.49	2.3	1.82	3.8
	0.5			0.78	1.3	1.03	3.1	1.34	7.2	1.68	16
	1.0	0.46	1.0	0.62	4.3	0.89	12	1.22	32	1.59	91
	2.0	0.31	3.5	0.48	17	0.81	72	1.18	572	1.57	225
	∞	0		0.39		0.79		1.17		1.57	

Table 1: Resonant wavenumbers k_n and amplitudes $|c_n|$ of Fourier modes in the moonpool of a rectangular barge. The last line shows the infinite-draft limits.

REFERENCES

Lee, C.-H., Maniar, H., Newman, J., & Zhu, X. 1996. 'Computations of wave loads using a B-spline panel method,' *Proc. 21st Symp. on Naval Hydrodynamics,* Trondheim, pp. 75-92.

Maniar, H. 1995. *A three dimensional higher order panel method based on B-splines,* Ph.D. thesis, MIT.

Molin, B., 2000. 'On the sloshing modes in moonpools, or the dispersion equation for progressive waves in a channel through the ice sheet,' *Proc. 15th Intl. Workshop on Water Waves and Floating Bodies,* Caesaria, Israel, pp. 122-125.

Newman, J. N. 1999. 'Radiation and diffraction analysis of the McIver toroid,' *J. of Engineering Maths.* Vol. 35, pp. 135-147.

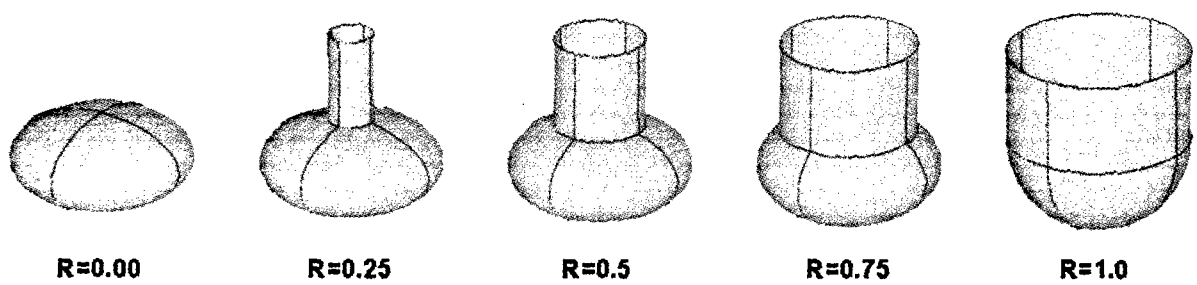

Figure 1: Perspective views of the truncated vertical cylinder of radius $R \leq 1$, extending from the free surface ($z = 0$) to $z = -1$, with an oblate spheroidal bottom which has a radius equal to 1.0, and extends from $z = -1$ to $z = -2$. The boundaries of the patches and their images are shown by dark lines.

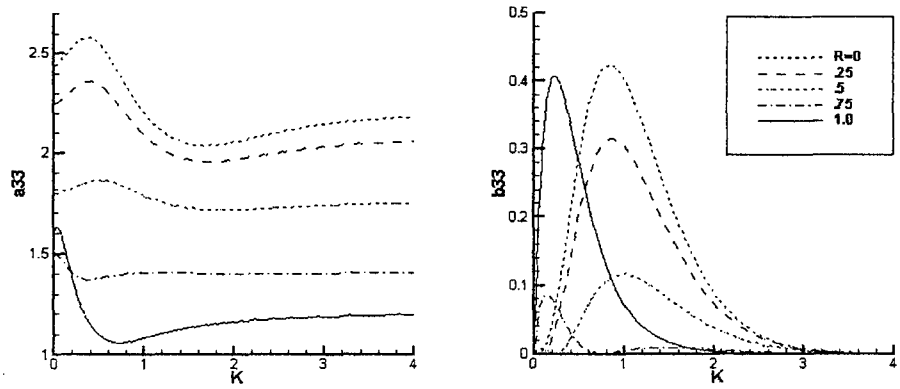

Figure 2: Heave added-mass and damping coefficients for the family of bodies shown in Figure 1.

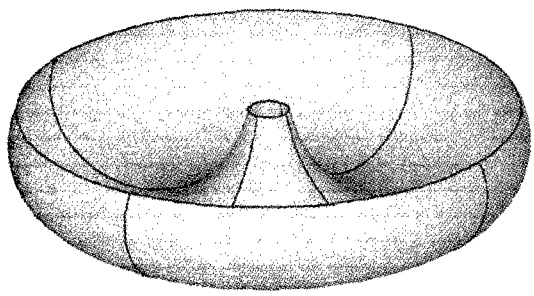

Figure 3: Perspective view of the McIver toroid generated by a ring source of unit radius, with the inner waterline at $r = 0.2$ and the outer waterline at $r = 2.4687$.

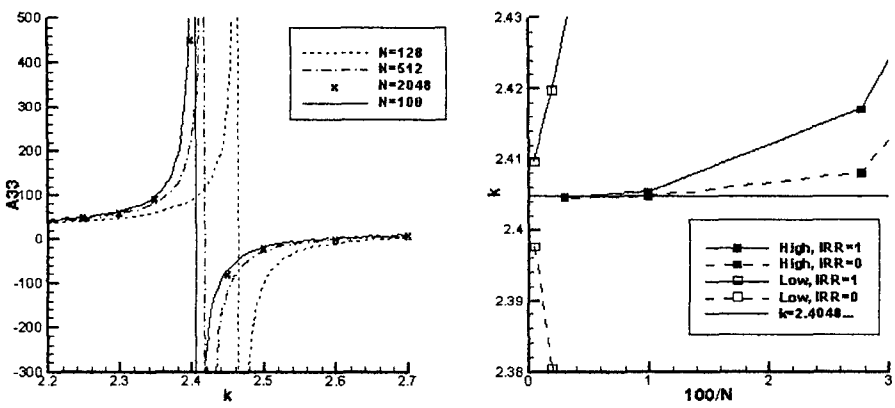

Figure 4: Results for the McIver toroid. The left figure shows the heave added-mass coefficient, including results from the low-order analysis with N=128, 512, 2048 panels on one quadrant of the body surface, and the higher-order results with explicit geometry definition (N=100 unknowns). The latter results are converged within graphical accuracy. The right figure shows the convergence of the low- and higher-order results to the singular wavenumber $J_0(k) = 0$. IRR=1 denotes that the irregular-frequency effects are removed.

The 16th International Workshop on Water Waves and Floating Bodies, Hiroshima, Japan, April 2001

Investigation of the Mathieu Instability of Roll Motion by a Time-Domain Viscous-Fluid Method

S.-W. Liao and R. W. Yeung
Mechanical Engineering & Ocean Engineering
University of California at Berkeley, Berkeley, California 94720-1740, USA

Introduction

Correct predictions of response of floating bodies in waves have been of great interest in the field of naval architecture and ocean engineering. Time-domain analysis based on potential-flow theory remains a popular approach (see e.g., Vinje and Brevig, 1980, Tanizawa and Naito, 1997, Van Daalen 1993, Wu & Eatock-Taylor, 1996, Celebi & Beck, 1997), even though in many occasions viscous effects cannot be ignored.

Roll response near its resonance condition, in particular, is strongly affected by viscous damping, not only in terms of the steady-state response amplitude, but also in terms of the stability or boundedness of the response itself, as we will address in this paper. It is possible to account for viscous effects but introducing damping in an empirical way (see, e.g., Himeno, 1981, Cointe et al., 1990, Sen ,1993). Nonetheless, it would be highly desirable to remove such empiricism by including the consideration of viscosity at the outset of the flow problem. This has been successfully pursued by Yeung and Liao (1999) in their FSRVM (Free-Surface Random-Vortex Method) method. In this paper, we explore the analysis and the computational basis of how the coupled multiple-degrees of freedom response of a floating body can critically depend on the presence of viscous damping.

The interesting phenomenon of Mathieu instability, arisen from the coupling between heave and roll motion (Paulling and Rosenberg, 1959) is investigated. The effects associated with the presence of bilge keels and fluid viscosity on the response near a "troublesome" resonant condition are addressed. The nonlinear coupling between heave and roll is vital, thus the issue is very much related to large-amplitude motion. A cylinder having interesting geometrical properties is devised for both experiments and computations. This cylinder is shown to be dynamically unstable under certain conditions according to the Mathieu equation.

Nonlinear heave-roll coupling

It was known from the time of Froude (1863) that the coupling between heave and roll can result in unstable ship motion. The phenomenon was investigated experimentally and theoretically by Paulling and Rosenberg (1959) for a ship undergoing forced oscillation in heave with an initial roll angle. The instability is related to the geometrical properties of a ship, the location of center of gravity, and the amplitude of the heave motion. This instability in roll is most likely to occur at the heave resonance frequency ω_y when the heave amplitude is sufficiently large.

Based on the equilibrium between inertia and restoring moment, the roll equation of a cylinder about its center of gravity (Paulling and Rosenberg, 1959) can be written as

$$(I_g + \mu_{33})\frac{d^2\alpha}{dt^2} + M_b g\overline{GM}\alpha + K_{\alpha y}\alpha y_o \cos(\omega_y t) = 0, \quad (1)$$

where I_g is the moment of inertia, μ_{33} the added moment of inertia, M_b the mass, $\overline{GM}$ the metacentric height, α the roll displacement, y the heave displacement, and y_o the amplitude of heave displacement (see Fig. 1). The last term of the equation, $K_{\alpha y}$, is the nonlinear restoring moment per unit roll and unit heave displacements. The nonlinear coefficient $K_{\alpha y}$ was given in terms of body geometry by Paulling and Rosenberg (1959). However, for a wall-sided cylinder, it is not difficult to show that $K_{\alpha y} = \rho g\overline{OG}A_w$, where $\overline{OG}$ is the distance between the center of gravity and the body center and A_w=B being the (two-dimensional) waterplane area for the cylinder. Equation (1) can be nondimensionalized to obtain the standard Mathieu equation (see for example, Jordan and Smith, 1988):

$$\frac{d^2\alpha}{d\tau^2} + (\delta + \epsilon\cos\tau)\alpha = 0, \quad (2)$$

$$\delta \equiv (\omega_\alpha/\omega_y)^2, \quad \epsilon \equiv \delta(y_o/\overline{GM})(K_{\alpha y}/M_b), \quad (3)$$

and $\tau = \omega_y t$. The heave and roll natural frequencies are defined as

$$\omega_y = (\rho g B/(M_b + \mu_{22}))^{1/2}, \quad (4)$$

$$\omega_\alpha = (M_b g\overline{GM}/(I_g + \mu_{33}))^{1/2}. \quad (5)$$

Equation (2) is known to be unstable at $\delta \approx 1/4$ even for a small value of ϵ, the nonlinear coupling term. This is equivalent to saying that the cylinder is unstable when $\omega_\alpha/\omega_y = 1/2$ even with only a small amount of forcing from heave. The stable and unstable regions were obtained by Stoker (1950) using perturbation methods. This is plotted in Fig. 2, which identifies that the Mathieu equation is highly unstable around $\delta = 1/4$. Beyond this critical value of δ, a finite amount of heave forcing is needed to induce roll instability.

In the figure, additional stable regions due to the presence of a linear damping term is also plotted. The damped Mathieu equation with linear coefficient μ, is given by:

$$\frac{d^2\alpha}{d\tau^2} + \mu\frac{d\alpha}{d\tau} + (\delta + \epsilon\cos\tau)\alpha = 0, \quad (6)$$

$$\mu \equiv \frac{\lambda_{33}}{\omega_y(I_g + \mu_{33})}. \quad (7)$$

The source of damping can result from both wave generation and viscous dissipation associated with the motion. The stability of Eqn. (6) is well studied especially for $\delta \approx 1/4$ (e.g., see Jordan and Smith, 1988). The Mathieu equation with damping is stable if the index

$$c_1 \equiv \left[(\delta - \frac{1}{4})^2 - \frac{1}{4}(\epsilon^2 - \mu^2)\right] > 0. \quad (8)$$

This means for δ=1/4 Eqn. (6) is unstable whenever $\epsilon > \mu$. Physically, this implies that a critical amount of damping is needed for a given heave response in order to suppress the instability. Investigation of this instability condition in the context of a cylinder in waves is therefore of fundamental and practical interest.

A "marginally stable" cylinder

In our laboratory tests and computer modeling, a marginally (dynamically) stable rectangular cylinder is designed so that its δ value is slightly larger than $1/4$. The unstable condition of Eqn. (8) can be acquired presumably by introducing bilge keels. The argument would be that the bilge keel would increase the added inertia μ_{33}, resulting in a δ very much closer to $1/4$. Thus the cylinder would easily fall into the unstable region of Fig. 2, All of these expectations are based on a damping estimate using inviscid theory alone. In physical reality, while the δ value moves closer to the critical value of $1/4$ because of the bilge keels, the viscous damping or its "linear equivalent " value will increase also. As a matter of fact, the damping would increase sufficiently that the cylinder could remain in the stable region. The laboratory experiments of Roddier et al (2000) indicate that the cylinder has no roll stability problem with or without bilge keels. This subtle behavior offers a challenging test for a time-domain computational model such as FSRVM, which can have viscosity turned on or off.

The geometrical properties of the cylinder are: beam to draft ratio $B/H = 2$, corner radius of bilges $R = 0.0205B$, center of gravity $y_g = -0.141B$, and the radius of gyration $R_g = 0.352B$. The depth of the bilge keels is 6% of the beam B. Details of the keels may be found in Roddier et al. (2000.) To calculate the resonant frequencies, ω_y and ω_α, the "FSRVM" of Yeung and Vaidhyanathan (1994) is applied to simulate *forced* heave and roll oscillations to obtain added mass and added moment of inertia coefficients. After μ_{22} and μ_{33} are obtained for both inviscid and viscous solutions over a range of frequency (Yeung et al., 1998), ω_y and ω_α are calculated through iteration using Eqns. (4) and (5). The damping or equivalent linear damping coefficients λ_{33} are also obtained through the simulations of forced oscillations.

The stability investigation is performed at an incident-wave frequency of $\tilde{\omega} \equiv \omega\sqrt{B/2g} = 0.7455$, and wave amplitude to wavelength ratio $A/\lambda = 2\%$. This frequency is very close to the resonant heave frequency of the model. There are four configurations of the cylinders considered in this study: inviscid and viscous fluid simulations for the cylinder, each for the case of with, or without bilge keels. Table 1 summarizes the estimated parameters in Eqn. (6) for these four scenarios based on frequency domain solutions. Case $I1$ & $I2$ represent inviscid fluid modeling, whereas Case $V1$ & $V2$ represent full Navier Stokes solutions of the problem. In the case of viscous flow, the equivalent linear damping coefficient μ is obtained by Fourier analysis of the time history of the applied moment.

In Table 1, the stability index c_1 of Eqn. (8) is also shown for the specific values of δ, ϵ, and μ. Thus, the cylinder is stable if $c_1 > 0$ and vice versa. It is seen that Case $I2$, an inviscid model with bilge keels, will have an unstable roll response, while the other cases are dynamically stable.

The boundaries of stability in Fig. 2 near $\delta = 1/4$ can be obtained by setting Eqn. (8) equal to 0. Figure 3 shows the "maximum" heave-motion parameter ϵ for stability as a function of δ. In each curve μ is taken as the minimum damping based on the specific ϵ and δ values for the case at issue. This plot shows that Case $I2$ is clearly unstable while Case $V2$ has the largest amount of stability margin.

Time-domain theoretical model

The computational model FSRVM used to obtain the motion of a freely-floating body in a viscous fluid is fully nonlinear. The boundary-value problem is defined in Figure 4, where a vorticity and stream-function formulation is used. The computational domain is bounded by the body ∂D_b, the free surface ∂D_f, and the open boundary ∂D_Σ. On the free surface, an oscillating pressure patch is used to generate waves. The vorticity equation is solved by a fractional-step of successive convection and diffusion. The convection calculations are carried out using a complex-variable integral-equation formulation. The details can be found in Yeung and Liao (1999) and Roddier et al. (2000). Applications of FSRVM to a fixed submerged body in large waves were considered in Yeung et al. (1999).

Since the body is freely floating, the boundary conditions on the body are coupled to the rigid-body dynamics equations. A methodology is established to couple the body accelerations to the boundary conditions of the fluid by using Newton's Second Law. The following linear system can be derived and solved explicitly for $(\ddot{x}_b, \ddot{y}_b, \ddot{\alpha})$ at any t.

$$\begin{bmatrix} (M_b + A_{11}) & A_{12} & (A_{13} - M_b y_{og}) \\ A_{21} & (M_b + A_{22}) & (A_{23} + M_b x_{og}) \\ (A_{31} - M_b y_{og}) & (A_{32} + M_b x_{og}) & (I_o + A_{33}) \end{bmatrix} \begin{bmatrix} \ddot{x}_b \\ \ddot{y}_b \\ \ddot{\alpha} \end{bmatrix} = \begin{bmatrix} W_{41} + M_b x_{og}\dot{\alpha}^2 \\ W_{42} + M_b y_{og}\dot{\alpha}^2 - M_b g \\ W_{43} - M_b g x_{og} \end{bmatrix}. \quad (9)$$

In Eqn. (9), $A_{ij}s$ depend only on the contour of ∂D. On the other hand, $W_{4i}s$ depend on solutions to the fluid velocity and vorticity field, which includes effects of wave excitation and hydrostatic terms.

Numerical results

To establish the validity of the computational model, results given in Roddier et al. (2000) are shown for assessment. Figure 5 shows a comparison between the calculated and measured free-surface elevation for a slightly different frequency, $\omega \hat{=} 0.6$. The results of 3 dof of motion response are shown in Fig. 6. Figures 5 and 6 show that the agreement is very good between calculated and measured results. In the experiments, the model slides unrestrained along a pair of horizontal guides. The friction of these guides need to be accounted for (see Case (c)).

If a cylinder is unstable, a valid numerical model should be able to capture the expected instability. Results of numerical simulations using the FSRVM model are presented for the four configurations discussed in the previous section (see Table 1). Since the instability is associated with excessive heave motion, the instability should disappear if the cylinder is restrained in heave. To verify this, inviscid results are also presented for the cylinder being restrained in heave and sway.

Figure 7 shows the roll displacements of the freely floating cylinder cylinder for the same four configurations mentioned. It can be seen that the response is bounded for all cases except for the inviscid case with keels (Case $I2$). This confirms that the time-domain modeling of FSRVM can predict the instability correctly. The roll response for the unstable case shows that the cylinder primarily rolls at the wave frequency for $\tilde{t} < 10$. For $\tilde{t} > 10$, the cylinder starts rolling at the roll natural frequency, which is one half of the wave frequency! Shortly after, the cylinder capsized. Figure 8 shows two sets of inviscid results of roll displacements for the cylinder restrained in heave and sway. The roll response is bounded if there is no heave motion, but grows without bound when there it is restrained from swaying. This also confirms the instability is related to the nonlinear coupling between heave and roll.

Conclusions

The nonlinear effects, associated with bilge keels and fluid viscosity, on the response of cylinders in waves were investigated.

Case		$\tilde{\omega}_y$	$\tilde{\omega}_\alpha$	δ	μ	ϵ	c_1
Inviscid fluid							
$I1$	No keel	0.7603	0.4194	0.3024	0.1680	0.1719	0.00168
$I2$	With keels	0.7455	0.3736	0.2511	0.1395	0.1545	-0.00110
Viscous fluid							
$V1$	No keel	0.7604	0.4131	0.2952	0.1791	0.1633	0.00169
$V2$	With keels	0.7455	0.3969	0.2834	0.3374	0.1604	0.02361

Table 1: Nondimensional parameters for various numerical cases.

It was shown that the response characteristics were very different depending on whether or not bilge keels and fluid viscosity was considered. For the cylinder with keels, the response showed that the proper modeling of fluid viscosity was critical in order to predict the motion correctly. On the other hand, inviscid-fluid models could predict an instability which is not always present in the physical world.

References

[1] Cointe, R., Geyer, P., King, B., Molin, B., and Tramoni, M. (1990). *Proc. 18th Symp. on Naval Hydrodyn.*, Ann Arbor, Michigan.

[2] Froude, W. (1966). *The Papers of William Froude*, INA, 1995. See also *Transactions*, INA, 1863.

[3] Himeno, Y. (1981). Dept. Naval Arch.& Mar. Engrg., University of Michigan, Rep. no 239.

[4] Jordan, D. W. and Smith, P. (1988). *Nonlinear Ordinary Differential Equatons*, Oxford University Press, Oxford, UK.

[5] Paulling, J. R. and Rosenberg, R. M. (1959). *J. Ship Res.*, **3**, pp. 36-46.

[6] Roddier, D., Liao, S.-W., and Yeung, R. W. (2000). *Int'l J. Offshore and Polar Engrg.*, **10**, No 4, pp. 241-248.

[7] Sen, D. (1993). *J. Ship Res.*, **37**, pp. 307-330.

[8] Tanizawa, K. and Naito, S. (1997). *Proc. 11th Int'l Offshore and Polar Engrg. Conf.*, Honolulu, Hawaii.

[9] Van Daalen, E. F. G. (1993). Ph.D. dissertation, University of Twente, The Netherlands.

[10] Vinje, T. and Brevig, P. (1980). Tech. Rept., The Norwegian Inst. of Tech., Trondheim.

[11] Wu, G. X. and Eatock-Taylor, R. (1996). *Proc. 11th Int'l Workshop on Water Waves and Floating Bodies*, Hamburg, German.

[12] Yeung, R. W. and Liao S.-W. (1999). *Proc. 9th Int'l Offshore and Polar Engrg. Conf.*, Brest, France.

[13] Yeung, R. W., Liao S.-W., and Roddier D. (1999). *Proc. 14th Int'l Workshop on Water Waves and Floating Bodies*, Port Huron, MI.

[14] Yeung, R. W. and Vaidhyanathan, M. (1994). *Proc. Int'l Conf. on Hydrodyn.*, Wuxi, China.

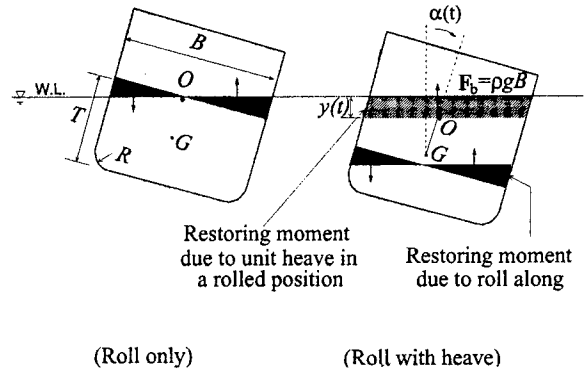

Figure 1: Roll restoring moment with and without heave displacement.

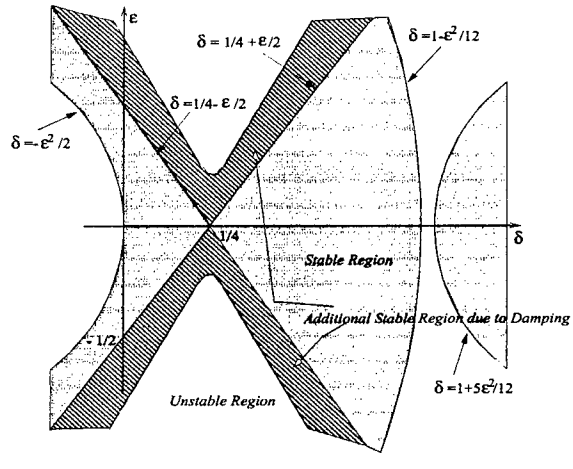

Figure 2: Stoker's approximation of stable and unstable regions for the Mathieu equation.

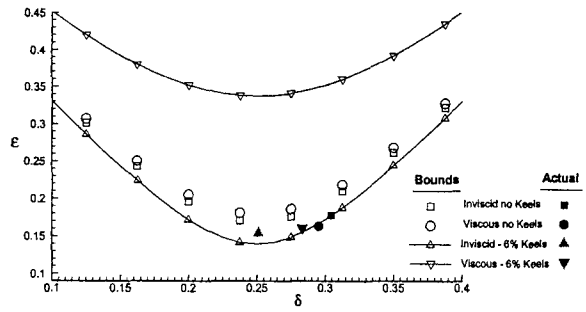

Figure 3: Values and upper bounds for ϵ (for stability) vs. δ.

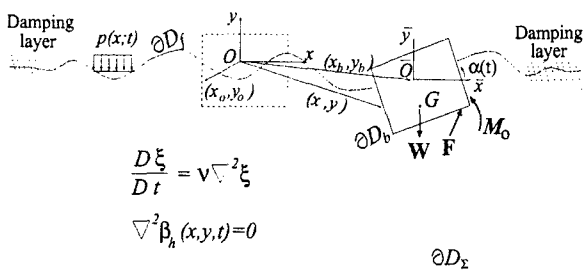

Figure 4: Definitions and the computational domain D.

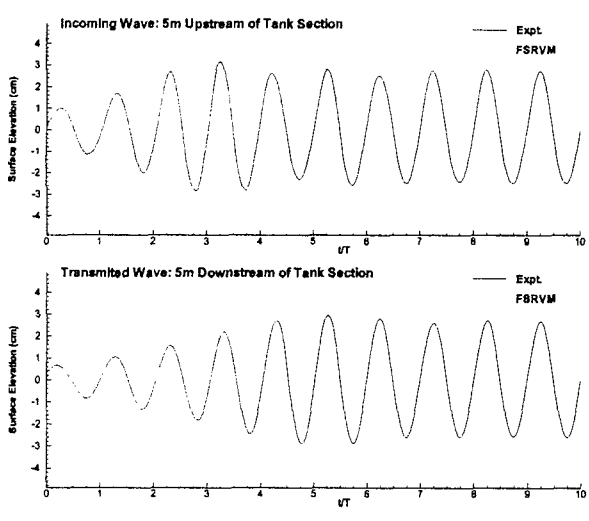

Figure 5: Incident and transmitted waves for $\tilde{\omega} = 0.6$

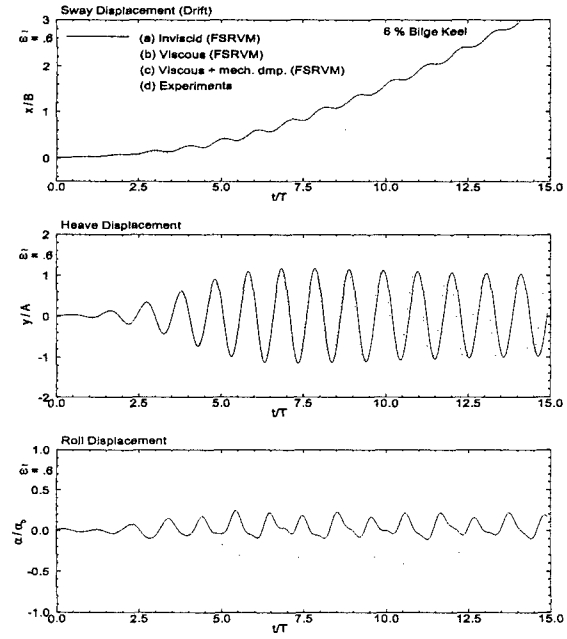

Figure 6: Motion response of freely-floating cylinder with 6% keels, $\tilde{\omega} = 0.6$

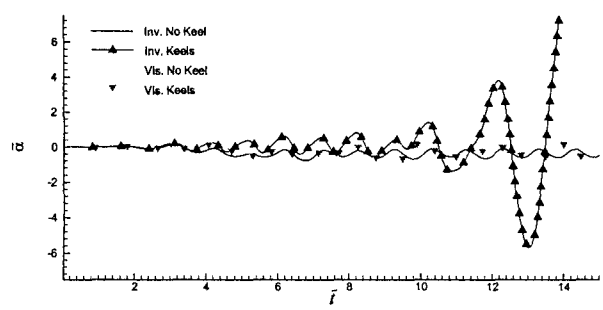

Figure 7: Numerical results of roll displacements for freely floating cylinders, $\tilde{\omega} = 0.746$

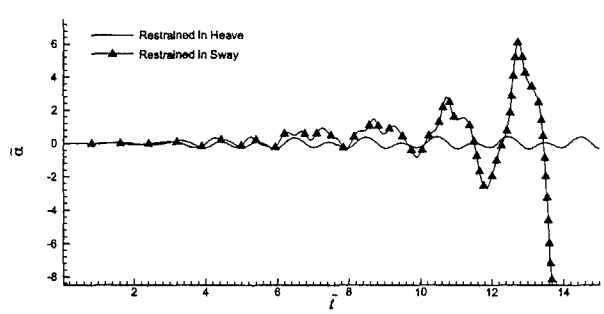

Figure 8: Inviscid results of roll displacements for restrained cylinder, $\tilde{\omega} = 0.746$

Resonances for cylinder arrays

by C M Linton & M McIver
Department of Mathematical Sciences, Loughborough University,
Leicestershire, LE11 3TU, UK

INTRODUCTION

The importance of trapped modes in the design of offshore structures which are supported by large arrays of vertical cylindrical structures was brought to prominence by Maniar and Newman (1997) who, in an investigation into the scattering of surface waves by a long but finite array of bottom-mounted vertical circular cylinders, discovered that at particular frequencies the hydrodynamic loads on the cylinders could become abnormally large. They identified this phenomenon with the existence of resonant trapped modes when cylinders are placed in channels on the walls of which either Neumann or Dirichlet boundary conditions are applied. For the Neumann case such modes were well known, but Maniar and Newman's observation that such modes could exist when the potential rather than its normal derivative was made to vanish on the walls, provided the cylinder radius was smaller than some critical value, was new. The trapped modes that can exist when N circular cylinders are placed across a channel in such a way that they form a section of an infinite array of equally-spaced cylinders were subsequently investigated by Utsunomiya and Eatock Taylor (1999). By representing the solution as a series of multipole potentials they were able to numerically compute N distinct trapped modes for any given cylinder radius when Neumann boundary conditions were applied on the tank walls, but for the case of Dirichlet boundary conditions they found $N-1$ or N modes depending on whether the cylinder radius was greater than or less than some critical value.

Porter and Evans (1999) used an integral equation technique to investigate the more general phenomenon of Rayleigh-Bloch surface waves (for which no general existence criteria are known) travelling along arbitrary periodic structures. Such waves are characterized by two parameters, k and β, the first being related to the frequency and the second corresponding to the dominant wavenumber in the direction along the structure. The parameter β provides a natural cut-off in that for values of k less than β energy cannot propagate away from the structure and so it is possible to look for specific values of $k < \beta$ at which pure Rayleigh-Bloch surface waves can occur. Porter and Evans showed that for certain discrete values of β these modes may correspond to trapped modes in the vicinity of a finite array of cylinders spanning a channel; precisely the situation studied by Utsunomiya and Eatock Taylor for an array of circular cylinders. If one assumes the existence of pure Rayleigh-Bloch surface waves for a particular periodic structure, then Porter and Evans' work explains the results of Utsunomiya and Eatock Taylor.

The purpose of this paper is to show that the channel modes found by Utsunomiya and Eatock Taylor and by Porter and Evans correspond to discrete eigenvalues below the continuous spectrum for certain differential operators and to show how standard variational arguments can be used to prove their existence. The key ingredient is a decomposition theorem which shows that functions $f(y)$ defined on domains which are both periodic and symmetric about zero and which also satisfy conditions equivalent to Neumann or Dirichlet boundary conditions on $y = 0$ and $2N$ can be decomposed into $N+1$ orthogonal functions. This is a direct extension of the decomposition of a function defined on a symmetric domain into its symmetric and antisymmetric parts (which corresponds to the case $N = 1$). This result can be applied to the scattering potentials for channels containing periodic structures and the class of all such potentials decomposed into $N+1$ subclasses. Green's theorem then shows that an incident wave in a particular class only scatters waves from the same class.

Spectral theory can be used to show that $N+1$ operators exist for each problem, all of whose continuous spectra are bounded away from zero in the Dirichlet case and N of which have this property in the Neumann case. The existence of trapped modes then follows from a standard variational argument.

DECOMPOSITION THEOREM

Assume that $D \subset \mathbb{R}$ is periodic with period 2 and also symmetric about zero, i.e. if $y \in D$ then $y+2 \in D$ and $-y \in D$ (from which it follows that $2n \pm y \in D$, $n \in \mathbb{Z}$). Let $f : D \cap [0, 2N] \to \mathbb{R}$, $N \in \mathbb{N}$, be given and extend it to a function on the whole of D by either

$$f(-y) = f(y), \qquad f(2N+y) = f(2N-y), \tag{1}$$

which will be referred to as the Neumann case, or

$$f(-y) = -f(y), \qquad f(2N+y) = -f(2N-y), \tag{2}$$

which will be referred to as the Dirichlet case. Under these conditions

$$f(y) = \sum_{m=0}^{N} f_m(y), \tag{3}$$

where

$$f_m(y) = \frac{\gamma_m^N}{2N} \sum_{n=1-N}^{N} c_{mn}^N f(y+2n), \tag{4}$$

$$c_{mn}^N = \cos\frac{mn\pi}{N}, \qquad \gamma_m^N = \frac{2}{1+\delta_{m0}+\delta_{mN}} \tag{5}$$

and δ_{mn} is the Kronecker delta.

Furthermore, suppose that two functions f and g, which are defined on the same domain D and which both satisfy either (1) or (2), are decomposed according to (3) and (4), then the following orthogonality result holds:

$$\int_0^{2N} f_m(y) g_\mu(y)\,\mathrm{d}y = \delta_{m\mu}\frac{\gamma_m^N}{2N} \sum_{s=-N}^{N-1}\sum_{\sigma=-N}^{N-1} c_{m,s-\sigma}^N \int_0^1 f(y+2s) g(y+2\sigma)\,\mathrm{d}y. \tag{6}$$

When $N = 1$ this decomposition theorem is nothing more than the splitting of a function defined on a symmetric domain into its symmetric and antisymmetric parts. For $N > 2$ the symmetry properties of the functions f_m are still of interest, but they are insufficient to completely characterize the decomposition.

As an example, consider the Green's function for the two-dimensional Helmholtz equation $(\nabla^2 + k^2)\phi = 0$ in a channel of width $2N$, satisfying Neumann boundary conditions on the guide walls. One way to represent this function is as an eigenfunction expansion and then from (3) we can obtain

$$G(x-\xi, y, \eta) = \sum_{m=0}^{N} G_m(x-\xi, y, \eta), \tag{7}$$

where

$$G_m(x-\xi, y, \eta) = -\frac{\gamma_m^N}{4N} \sum_{n=-\infty}^{\infty} \frac{\mathrm{e}^{-\alpha_{mn}|x-\xi|}}{\alpha_{mn}} \cos\beta_{mn} y \cos\beta_{mn}\eta \tag{8}$$

and

$$\alpha_{mn} = \left(\beta_{mn}^2 - k^2\right)^{1/2} = -\mathrm{i}\left(k^2 - \beta_{mn}^2\right)^{1/2}, \quad \beta_{mn} = \frac{(m+2nN)\pi}{2N}. \tag{9}$$

The function G_m represents a sum of unequal sources at $x = \xi$, $y = 2n \pm \eta$, $n \in \mathbb{Z}$ and thus has $2N$ singularities within the guide (at $y = \eta$, $y = 2n \pm \eta$, $n = 1, \ldots, N-1$, $y = 2N - \eta$) even though the combination of these functions given by (7) only has one such singularity.

Suppose now that we wish to solve a scattering problem in a channel spanned by an array of cylinders. The potential ϕ can be split up into $N+1$ orthogonal functions and if we apply Green's theorem to ϕ and G_m we obtain

$$\frac{1}{2}\phi_m(\xi, \eta) = \int_B \phi_m \frac{\partial G_m}{\partial n}\,\mathrm{d}s + \chi_m, \qquad (\xi, \eta) \in B, \tag{10}$$

where χ_m comes from the decomposition of the incident wave and B is the boundary of the cylinder array. Thus, for the special types of geometry under consideration, an arbitrary scattering problem can be decomposed into $N+1$ independent problems.

This result is of both practical and theoretical importance. From a practical point of view, the decomposition leads to a significant computational saving when calculating the effects of scattering by an array of cylinders spanning a channel, and from a theoretical viewpoint it enables us to prove the existence of trapped modes as described below.

RESONANCES

If we denote the fluid domain by Ω, then the solution to a scattering problem of the type described above will not be unique if a non-trivial solution to the homogeneous boundary-value problem

$$(\nabla^2 + k^2)\phi = 0 \quad \text{in} \quad \Omega, \tag{11}$$

$$\frac{\partial \phi}{\partial y} = 0 \quad \text{on} \quad y = 0, 2N, \tag{12}$$

$$\frac{\partial \phi}{\partial n} = 0 \quad \text{on} \quad B, \tag{13}$$

$$\phi \to 0 \quad \text{as} \quad |x| \to \infty, \tag{14}$$

exists. If such a solution exists for a given k^2 then k^2 is an eigenvalue of $-\nabla^2$ (with Neumann boundary conditions) on the domain Ω. The solution itself (which is known as a trapped mode or an acoustic resonance) is the corresponding eigenvector.

In terms of the spectral theory of operators we can think of (11)–(14) as being an eigenvalue problem for an operator A consisting of $-\nabla^2$ in Ω together with the various boundary conditions. The spectrum of A is a closed set containing all the values of k^2 for which the operator $A - k^2 I$ does not have a bounded inverse and for the above problem this set can be divided into two disjoint subsets. The values of k^2 for which the operator $A - k^2 I$ is not invertible are called eigenvalues of A and together they make up the point spectrum of A, denoted by $\sigma_p(A)$. It is well-known that for the problem specified in (11)–(14) any eigenvalues are real and non-negative. The remainder of the spectrum of A is called the continuous spectrum and denoted by $\sigma_c(A)$. We can also consider the set of values of k^2 for which we can set up a wave scattering problem. This set is the essential spectrum of A and is denoted by $\sigma_{\text{ess}}(A)$. The essential spectrum is the union of the continuous spectrum and any embedded eigenvalues.

It is well-known that $\sigma_{\text{ess}}(A) = [0, \infty)$ and so any eigenvalue of A is necessarily embedded in the continuous spectrum which makes analysis of these eigenvalues difficult. One way of overcoming the problem is to find a decomposition of the space of functions on which A operates, $S = S_0 \oplus S_1$ say ($\oplus$ denotes direct sum), such that when we consider the operator A restricted to one of these subspaces the continuous spectrum is moved away from the origin. An example is provided by Evans, Levitin, and Vassiliev (1994) who considered the case $N = 1$. Below we extend this decomposition to arbitrary $N \in \mathbb{N}$ which allows N eigenvalues to be found for each geometry.

Suppose then that we have a channel spanned by a periodic structure. The decomposition theorem shows that any function which is defined on Ω can be written as

$$\phi(x, y) = \sum_{m=0}^{N} \phi_m(x, y) \tag{15}$$

and we can thus decompose the space of square integrable functions in the fluid region Ω as

$$L^2(\Omega) = S_0 \oplus S_1 \oplus \cdots \oplus S_N, \tag{16}$$

where S_m is the space of functions of the form $\phi_m(x, y)$. It makes sense to restrict the operator A to one of the spaces S_m and this restricted operator will be labelled A_m. Within a given space

S_m, waves can only exist if $k^2 > m^2\pi^2/4N^2$. We write $\beta_m = m\pi/2N$ and then it follows that the essential spectrum for A_m is given by

$$\sigma_{\rm ess}(A_m) = [\beta_m^2, \infty) \tag{17}$$

and so there is a non-zero cut-off for each of the spaces except for S_0. Standard variational arguments can then be used to show that the operator A_m, $m \in \{1, \ldots, N\}$ has at least one eigenvalue less than β_m^2.

Different results apply to the Dirichlet case. Thus we consider the homogeneous boundary-value problem (11)–(14) with (12) replaced by

$$\phi = 0 \quad \text{on} \quad y = 0, 2N, \tag{18}$$

though we will still refer to the associated operator as A. The space $L^2(\Omega)$ can be decomposed exactly as before. The essential spectrum for A_m is now given by

$$\sigma_{\rm ess}(A_m) = \begin{cases} [\beta_m^2, \infty) & m = 1, \ldots, N, \\ [\pi^2, \infty) & m = 0 \end{cases} \tag{19}$$

and so there is a non-zero cut-off for all of the spaces. However, the case $m = N$ corresponds to a single body symmetrically placed about the centreline of a channel of width 2 with Dirichlet conditions on the walls and it has been proven (see McIver and Linton 1995, p548) that no trapped modes can exist in this case for $k < \pi/2 = \beta_N$. Hence we can only hope to prove the existence of trapped modes for $m = 0, \ldots, N-1$.

Variational arguments in fact show that the operator A_m, $m \in \{1, \ldots, N-1\}$ has at least one eigenvalue and that the operator A_0 has at least one eigenvalue if the body shape satisfies some geometric condition.

References

Evans, D. V., Levitin, M., & Vassiliev, D. (1994). Existence theorems for trapped modes. *J. Fluid Mech.*, **261**, 21–31.

Maniar, H. D., & Newman, J. N. (1997). Wave diffraction by a long array of cylinders. *J. Fluid Mech.*, **339**, 309–330.

McIver, M., & Linton, C. M. (1995). On the non-existence of trapped modes in acoustic waveguides. *Q. Jl Mech. Appl. Math.*, **48**(4), 543–555.

Porter, R., & Evans, D. V. (1999). Rayleigh-Bloch surface waves along periodic gratings and their connection with trapped modes in waveguides. *J. Fluid Mech.*, **386**, 233–258.

Utsunomiya, T., & Eatock Taylor, R. (1999). Trapped modes around a row of circular cylinders in a channel. *J. Fluid Mech.*, **386**, 259–279.

Semi analytical solution for heave radiation of the air cushion supported vertical circular cylinder in water of finite depth

Malenica Š & Zalar M.

BUREAU VERITAS - DTA, 17bis Place des Reflets, 92400 Courbevoie, France

Introduction

The hydrodynamic problem of air cushion supported floating bodies appears in several situations of marine hydrodynamics : the use of the air cushions was the only way to tow the Gravity Base Structures (GBS) from dry dock to the field of production, the surface effect ships (SES) use the advantages of the air cushions to increase their performances, the succion anchors in the phase of instalation, the projects of huge Mobile Off shore Units (MOB), the projects of the bottomless FPSO-s, ... From the hydrodynamic point of view all these situations are similar. The hydrodynamic behaviour of the structure change considerably, and the air cushion effects should be taken into account properly in the mathematical model. Several numerical methods were proposed [1, 2, 3, 4]. Even if these methods solves the same physical problem, the approaches are quite different. The motivation for this work comes from the necessity to have the analytical solution for one particular boundary value problem (BVP), which may be used for the benchmark purposes. For this objective, we chose the case where the air cushion effects are most pronounced which is the heaving motion of the body. In order to be able to produce semi-analytical solution the case of the vertical circular cylinder in water of finite depth is considered.

Theory

All definitions correspond to the figure 1. We skip the basic steps, and just recall the final (frequency domain) boundary value problem (BVP) which have to be solved [2]:

$$\left.\begin{array}{ll} \Delta\psi = 0 & in\ \ \Omega \\ -\nu\psi + \dfrac{\partial\psi}{\partial z} = 0 & z = 0,\ r > a \\ -\nu\psi + \dfrac{\partial\psi}{\partial z} + \dfrac{\alpha}{A_{c0}} \iint_{S_{I0}} \dfrac{\partial\psi}{\partial z} dS = \alpha & z = -d,\ r < a \\ \dfrac{\partial\psi}{\partial r} = 0 & -d < z < 0,\ r = a \\ \dfrac{\partial\psi}{\partial z} = 0 & z = -h \\ \lim[\sqrt{\nu r}(\dfrac{\partial\psi}{\partial r} - i\nu\psi)] = 0 & r \to \infty \end{array}\right\} \quad (1)$$

where $A_{c0} = 2a\pi$ and α is the nondimensional number accounting for the air cushion effects:

$$\alpha = \kappa \frac{p_{c0} A_{c0}}{\varrho g V_{c0}} \quad (2)$$

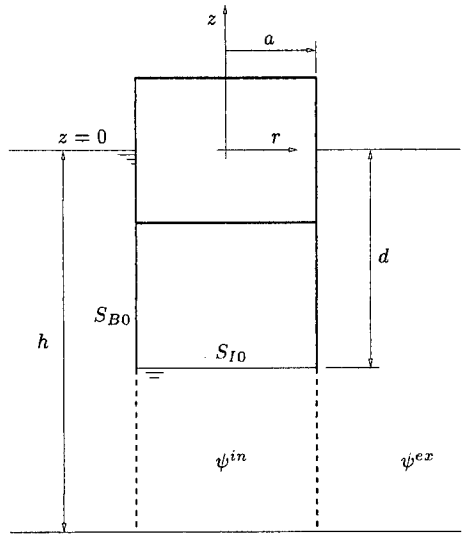

Figure 1: *Basic configuration and notations*

Potential decomposition

As usually, we make use of the eigenfunction expansions to represent the potential in the different domains (exterior and interior). We note that,due to the fact that only heave is considered, only the $0-th$ Fourier mode in the Fourier series expansion in circumferential direction, need to be considered.
In the exterior domain we write the well known representation:

$$\psi^{ex} = c_0 f_0(z) H_0(k_0 r) + \sum_{n=1}^{\infty} c_n f_n(z) K_0(k_n r) \tag{3}$$

where $\nu = k_0 \tanh k_0 h = -k_n \tan k_n h$, H_0 is the Hankel function, K_0 is the modified Bessel function of the second kind, and:

$$f_0(z) = \frac{\cosh k_0(z+h)}{\cosh k_0 h} \quad , \quad f_n(z) = \frac{\cos k_n(z+h)}{\cos k_n h} \tag{4}$$

Concerning the interior domain, the situation is little bit more complicated due to the presence of the air cushion interface i.e. the "unusual" boundary condition which should be applied on it. In order to find the correct eigenfunction expansion for the interior potential, first we assume the solution as a combination of one homogeneous and one particular part:

$$\psi^{in} = \psi_h^{in} + C\psi_p^{in} \tag{5}$$

where the associated free surface conditions at interface are:

$$-\nu\psi_h^{in} + \frac{\partial \psi_h^{in}}{\partial z} = 0 \quad , \quad -\nu\psi_p^{in} + \frac{\partial \psi_p^{in}}{\partial z} = 1 \tag{6}$$

For the homogeneous part ψ_h^{in} we can write the representation similar to ψ^{ex} :

$$\psi_h^{in} = b_0 g_0(z) J_0(k_0 r) + \sum_{n=1}^{\infty} b_n g_n(z) I_0(k_n r) \tag{7}$$

where J_0 stands for the Bessel function of the first kind, I_0 stands for the modified Bessel function of the first kind, and:

$$g_0(z) = \frac{\cosh \kappa_0(z+h)}{\cosh \kappa_0(h-d)} \quad , \quad g_n(z) = \frac{\cos \kappa_n(z+h)}{\cos \kappa_n(h-d)} \tag{8}$$

with $\nu = \kappa_0 \tanh \kappa_0(h-d) = -\kappa_n \tan \kappa_n(h-d)$.
The particular solution may be found, by inspection:

$$\psi_p^{in} = -\frac{1}{\nu} \tag{9}$$

From the boundary condition at the interface, we can now deduce the constant C:

$$C = \alpha[1 - \frac{\nu}{2a\pi}\int_0^{2\pi}\int_0^a \psi_h^{in} r dr d\theta] = \alpha\{1 - \nu[b_0 \frac{J_1(\kappa_0 a)}{\kappa_0} + \sum_{n=1}^{\infty} b_n \frac{I_0(\kappa_n r)}{\kappa_n}]\} \tag{10}$$

which gives the following final expression for ψ^{in}:

$$\psi^{in} = -\frac{\alpha}{\nu} + b_0[\frac{\alpha}{\kappa_0} J_1(\kappa_0 a) + g_0(z) J_0(\kappa_0 r)] + \sum_{n=1}^{\infty} b_n[\frac{\alpha}{\kappa_n} I_1(\kappa_n a)] + g_n(z) I_0(\kappa_n r)] \tag{11}$$

In order to obtain the unknown coefficients b_n and c_n we make use of the orthogonality of the eigenfunctions by applying the boundary condition on the cylinder and the continuity conditions (potential and radial velocity) at the intersection of the exterior and interior domains:

$$\left.\begin{aligned} \int_{-h}^{-d} \psi^{ex} g_n(z) dz &= \int_{-h}^{-d} \psi^{in} g_n(z) dz \quad ; \quad n = 0, \infty \\ \int_{-h}^{0} \frac{\partial \psi^{ex}}{\partial r} f_n(z) dz &= \int_{-h}^{-d} \frac{\partial \psi^{in}}{\partial r} f_n(z) dz \quad ; \quad n = 0, \infty \end{aligned}\right\} \tag{12}$$

This leads to the following type of the linear system of equations for b_n and c_n:

$$\left.\begin{aligned} b_l &= c_0 D_{l0} + \sum_{n=1}^{\infty} c_n D_{ln} + F_l \quad ; \quad l = 0, \infty \\ c_l &= b_0 E_{l0} + \sum_{n=1}^{\infty} b_n E_{ln} + G_l \quad ; \quad l = 0, \infty \end{aligned}\right\} \tag{13}$$

where the coefficients D_{ln}, E_{ln}, F_l and G_l follow from (12).

Forces

The forces are obtained by integrating the pressure over the body surface (hydrodynamic and air cushion pressure). It may be shown [2] that, in the case of radiation, the force can be written in the following form:

$$F_{ij} = -\omega^2 A_{ij} + i\omega B_{ij} = \varrho\omega^2[\iint_{S_{B0}} \varphi_{Rj} N_i dS + \frac{\alpha}{1+\alpha}\iint_{S_{I0}} \varphi_{Rj} N_i dS] \tag{14}$$

where A_{ij} and B_{ij} are the well known added mass and damping coefficients and φ_{Rj} is the radiation potential (in our case ψ).

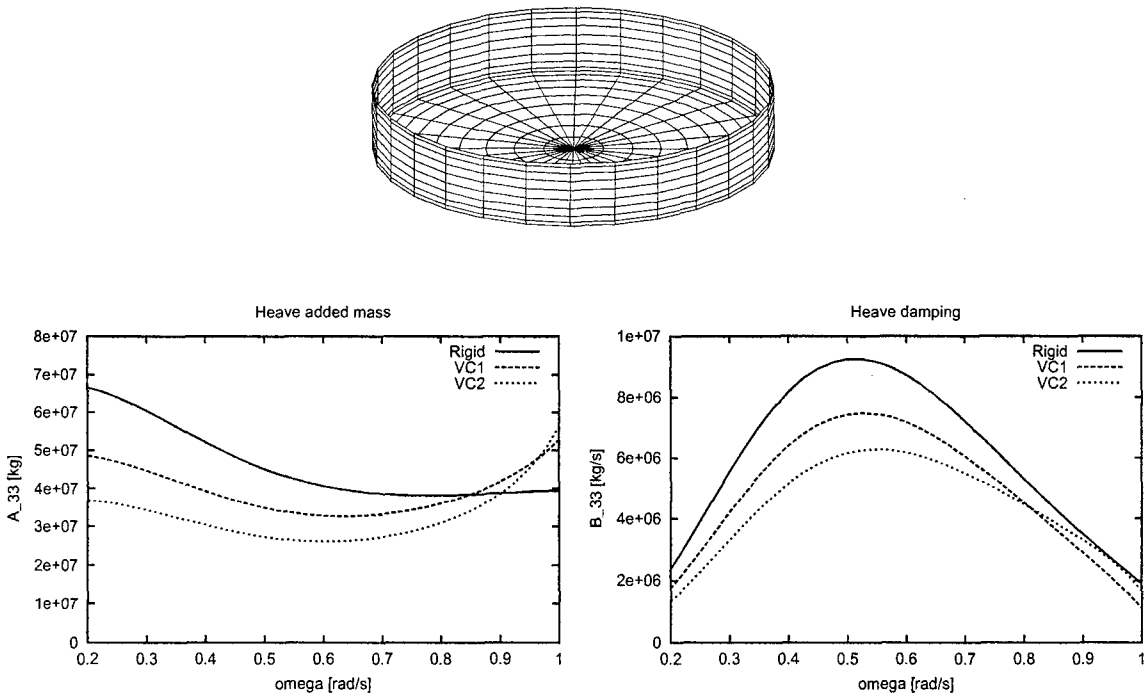

Figure 2: *Added mass and damping.*

Some results

On the figure 2 we present the numerical results for the heave added mass and damping for the cylinder with the radius of $30m$ and with the draught of $10m$. Static pressure in the air cushion is $p_{c0} = 2 \cdot 10^5 Pa$ and $\kappa = 1.4$. Two values of the static air cushion volume V_{c0} are considered so that the notation VC1 stands for $V_{c0} = 14137.2m^3$ and VC2 for $V_{c0} = 28174.3m^3$. We can clearly appreciate the influence of the air cushion on these coefficients.

References

[1] LEE C.H. & NEWMAN J.N., 1999. : "Wave effects on large floating structures with air cushions.", VLFS'99, Honolulu, USA.

[2] MALENICA Š., ESPANET A. & ZALAR M., 2001. : "Tenue à la mer des objets flottants supportés par des coussins d'air.", 8eme Journées de l'Hydrodynamique, Nantes, France.

[3] NAKOS D.E., NESTEGARD A., ULSTEIN T. & SCLAVOUNOS P.D., 1991. : "Seakeeping analysis of surface effect ships.", FAST'91, Trondheim, Norway.

[4] PINKSTER J.A., 1997. : "The effect of air cushions under floating offshore structures", BOSS'97, Delft, Netherlands.

Trapping of waves by a submerged elliptical torus

by M. McIver* & R. Porter†

* Department of Mathematical Sciences, Loughborough University, Loughborough, Leicestershire, LE11 3TU, UK

† School of Mathematics, University of Bristol, University Walk, Bristol, BS8 1TW, UK

Introduction

In linear water-wave theory a trapped mode is defined to be a non-zero solution of the homogeneous equations and boundary conditions, which doesn't radiate waves and has finite energy. The existence of such modes supported by three-dimensional, surface-piercing bodies in the open sea was first established by McIver & McIver[1]. They constructed an axisymmetric potential and defined the shape of the body to be one of the stream surfaces of the flow. In practice, however, it would be more useful to be able to specify the shape of the obstacle and determine whether there are any trapped modes for that geometry. The purpose of this work is to show how this may be done for certain classes of bodies by exploiting the link between three-dimensional trapped modes and zeros of transmission for two-dimensional obstacles. First a plane wave approximation to a trapped mode is derived, then a numerical technique for finding exact trapped mode wave numbers is described. Finally some results which show that modes may be trapped by a submerged elliptical torus are presented.

The plane wave approximation

A two-dimensional body which is totally submerged in deep water and which possesses a zero of transmission is rotated through 360^o about a vertical axis outside the body, to form a submerged torus. The axis of rotation is at a distance c from a reference axis through the body where $c/a \gg 1$ and a is a typical dimension of the original two-dimensional body. Rectangular Cartesian coordinates are chosen so that the origin is in the mean free surface above the centre of the torus and the z-axis points vertically upwards. An approximation to the trapped mode potential is sought which represents a standing wave in the region $r = \sqrt{x^2+y^2} \ll c$ and is zero for $r \gg c$. The two potentials are then matched across the torus using the plane wave approximation of Simon[2]. The axisymmetric standing wave is given by

$$Re[\phi\, \mathrm{e}^{-\mathrm{i}\omega t}] = Re[J_0(kr)\, \mathrm{e}^{kz-\mathrm{i}\omega t}] \tag{1}$$

where J_0 is the zero-order Bessel function of the first kind, ω is the angular frequency of oscillation, $k = \omega^2/g$ and g is the acceleration due to gravity. By writing $kr = k(r-c) + kc$ and using the addition theorem and the large argument expansion for Bessel functions, it may be shown that

$$\phi \sim \sqrt{\frac{1}{2\pi kc}}\, \mathrm{e}^{\mathrm{i}(kc-\pi/4)+kz} \left[\mathrm{e}^{\mathrm{i}k(r-c)} + \mathrm{i}\, \mathrm{e}^{-2\mathrm{i}kc}\, \mathrm{e}^{-\mathrm{i}k(r-c)}\right], \quad kc \gg 1, \quad k(r-c) = O(1). \tag{2}$$

Near the body of the torus this represents a plane wave which propagates outwards along a radial line and which is totally reflected by the two-dimensional body formed by the cross-section of the torus. Clearly this can only occur if the wave number corresponds to a point of zero transmission of the two-dimensional body and the reflection coefficient is given by

$$R = \mathrm{i}\, \mathrm{e}^{-2\mathrm{i}kc}. \tag{3}$$

This last equation gives possible values of kc in terms of the phase of the reflection coefficient. So, if $R = \mathrm{e}^{\mathrm{i}\delta}$ is known from the solution of the two-dimensional scattering problem, then

$$kc = \frac{\pi}{4} - \frac{\delta}{2} + n\pi, \tag{4}$$

where n is an arbitrary integer. (Newman[3] used matched asymptotic expansions to perform a similar but more rigorous analysis of a floating torus at small but non-zero values of R.) It is interesting to observe that the corresponding result for a wide-spacing approximation to two-dimensional modes trapped between two bodies is $kc = -\delta/2 + n\pi$, and so there is a difference of $\pi/4$ between the two and three dimensional approximate values of kc.

Numerical location of trapped modes

The analysis of the previous section is only approximate and so it is not obvious whether the torus can support trapped modes or whether it just has highly tuned resonances. In this section a method is described which both demonstrates that there is a perturbation of the torus which supports a trapped mode, and allows its accurate computation.

An exact axisymmetric trapped mode for a submerged torus is sought where, without loss of generality, the potential ϕ is assumed to be real. An application of Green's theorem to ϕ and the ring source gives ϕ at an arbitrary point in the fluid in terms of an integral of ϕ multiplied by the normal derivative of the ring source around the boundary of the torus. This is then differentiated, evaluated on the boundary of the torus and integrated by parts to give

$$\int_0^{2\pi} H(r(t),z(t);r(\tau),z(\tau))\,q(t)\,\mathrm{d}t = \psi_c, \quad 0 \le \tau < 2\pi, \tag{5}$$

where $q(t) = \partial\phi/\partial s\,\mathrm{d}s/\mathrm{d}t$. The function $\partial\phi/\partial s$ is the tangential derivative of ϕ on the boundary of the cross-section of the torus, $(r(t),z(t))$ are the radial and vertical coordinates of a point on the torus, ψ_c is the unknown, real, constant value of the Stokes' stream function on the torus and

$$\begin{aligned} H(r,z;r_0,z_0) &= \frac{2krkr_0}{\pi}\int_0^\infty \frac{(\nu\sin\nu kz - \cos\nu kz)(\nu\sin\nu kz_0 - \cos\nu kz_0)I_1(\nu kr_<)K_1(\nu kr_>)}{\nu^2+1}\,\mathrm{d}\nu \\ &\quad - \mathrm{i}\pi krkr_0\,\mathrm{e}^{k(z+z_0)}\,J_1(kr_<)H_1(kr_>), \end{aligned} \tag{6}$$

where J_1, H_1, I_1 and K_1 are the usual Bessel and modified Bessel functions, $r_< = \min(r_0,r)$ and $r_> = \max(r_0,r)$. In addition, to ensure zero circulation around the torus

$$\int_0^{2\pi} q(t)\,\mathrm{d}t = 0. \tag{7}$$

The boundary of the torus is assumed to be smooth and so $q(t)$ is approximated by a series of trigonometric functions

$$q(t) \approx \sum_{n=1}^{2N} a_n u_n(t), \quad \text{where} \quad u_{2n-1}(t) = \sin nt, \quad u_{2n}(t) = \cos nt. \tag{8}$$

(The omission of the constant term ensures that (7) is automatically satisfied.) An application of Galerkin's method yields a real homogeneous matrix equation for the coefficients $\{a_n\}$

$$\sum_{n=1}^{2N} K_{mn}a_n = 0, \quad \text{where} \quad K_{mn} = \int_0^{2\pi}\int_0^{2\pi} \mathrm{Re}[H(r(t),z(t);r(\tau),z(\tau)]u_m(\tau)u_n(t)\,\mathrm{d}\tau\,\mathrm{d}t, \quad m = 1,\ldots,2N. \tag{9}$$

In addition, in order to satisfy the imaginary part of (5)

$$S \equiv \sum_{n=1}^{2N} f_n a_n = 0, \quad \text{where} \quad f_n = \int_0^{2\pi} kr(t)\,\mathrm{e}^{kz(t)}\,J_1(kr(t))u_n(t)\,\mathrm{d}t. \tag{10}$$

Thus, a trapped mode wave number is a value of k for which $\det(K_{mn}) = 0$ and the resulting eigenfunction satisfies the side condition (10).

Results and discussion

Numerical calculations were performed for a submerged elliptical torus whose boundary is parameterised by

$$(r, z) = (c + a\cos t, -d + b\sin t), \quad 0 \leq t < 2\pi. \tag{11}$$

Computations for a submerged ellipse with $b/a = 0.16$ and $d/a = 0.25$ show that a zero of transmission exists at $ka = 0.525$ and the plane wave approximation predicts that a torus with $c/a = 3.600$ supports a trapped mode. Exact trapped modes are sought for an elliptical torus with the same values of b/a and d/a and neighbouring values of c/a and ka. Figure 1 illustrates the curves $\det(K_{mn}) = 0$ and $\tilde{S} \equiv \sum_{n=1}^{2N} f_n \tilde{a}_n = 0$ as functions of c/a and ka in the vicinity of $c/a = 3.600$ and $ka = 0.525$, where the coefficients $\{\tilde{a}_n\}$ are the coefficients in the eigenfunction for the eigenvalue of K_{mn} which has the smallest magnitude. At the point where the two curves cross $\tilde{S} = S$ and so

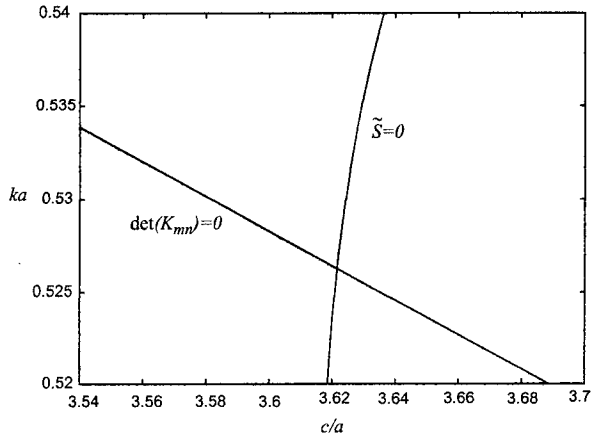

Figure 1: Crossing of the curves $\det(K_{mn}) = 0$ and $\tilde{S} = 0$ for an elliptical torus, $b/a = 0.16$, $d/a = 0.25$.

$\det(K_{mn}) = 0$ and $S = 0$ there. The two curves are generated by determining where real quantities change sign and the fact that the curves cross rather than touch gives confidence that a trapped mode exists, even though the values of ka and c/a may not be found exactly. Table 1 summarises the trapped mode parameters obtained by this method for different values of b/a and d/a.

	b/a					
d/a	0.04	0.08	0.12	0.16	0.2	0.24
0.3	-	-	-	-	4.22430 0.48159	3.98209 0.45113
0.25	-	3.96860 0.56043	3.71152 0.56145	3.62155 0.52627	3.66547 0.45148	4.21728 0.28664
0.2	3.25850 0.65717	3.26333 0.61093	3.33559 0.53944	3.57864 0.42465	-	-
0.15	3.03694 0.63019	3.23079 0.52534	3.75368 0.36853	-	-	-
0.1	3.31776 0.47983	4.43568 0.27962	-	-	-	-

Table 1: Summary of values of c/a (upper entry) and ka (lower entry) for trapping by an elliptical torus for selected values of aspect ratio, b/a, and submergence, d/a.

Figures 2 and 3 illustrate the non-dimensional heave added mass and damping for a torus with $b/a = 0.16$, $d/a = 0.25$ and $c/a = 3.62155$, calculated using WAMIT with a varying number of panels. The panels are distributed at equal azimuthal angles and at equal values of the arc length around the boundary of the torus. It is clear from the figures there is a large spike in the added mass and damping at $ka \approx 0.527$ which supports the existence of a trapped mode at that value.

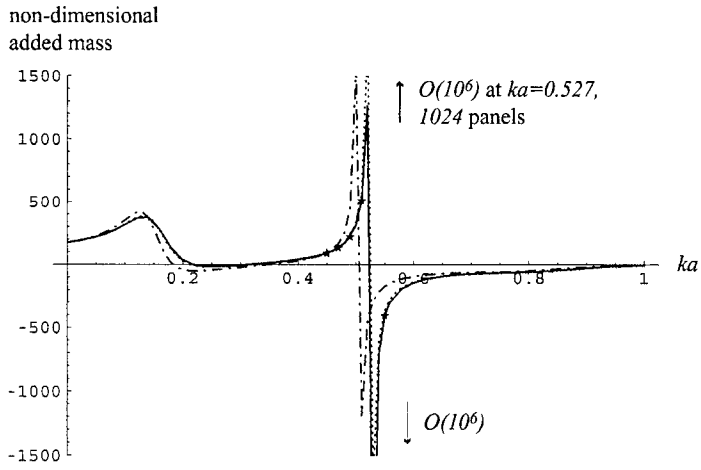

Figure 2: Heave added mass for a submerged elliptical torus, $b/a = 0.16$, $d/a = 0.25$, $c/a = 3.62155$. Number of panels on 1/4 torus, $\star$: 1920, —: 1024, $\cdots$: 512, $-\cdot-$:256

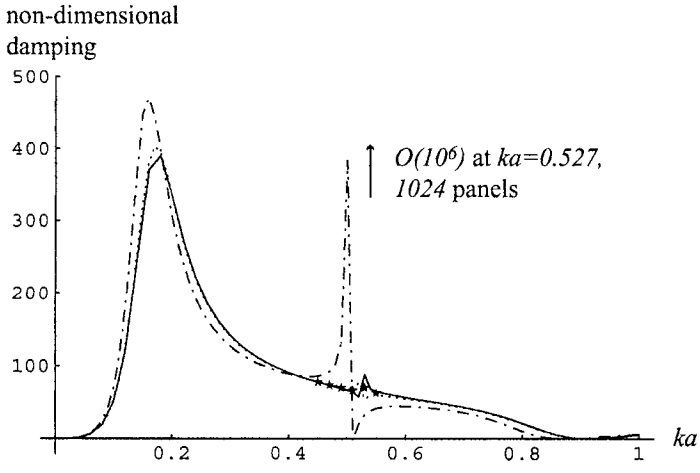

Figure 3: Heave damping for a submerged elliptical torus, $b/a = 0.16$, $d/a = 0.25$, $c/a = 3.62155$. Number of panels on 1/4 torus, $\star$: 1920, —: 1024, $\cdots$: 512, $-\cdot-$:256

References

[1] McIver, P. & McIver, M. 1997. Trapped modes in an axisymmetric water-wave problem *Quarterly Journal of Mechanics and Applied Mathematics* **50**, 165–178.

[2] Simon, M. J. 1982. Multiple scattering in arrays of axisymmetric wave-energy devices. Part 1. A matrix method using a plane-wave approximation *Journal of Fluid Mechanics* **120**, 1–25.

[3] Newman, J. N. 1977. The motion of a floating slender torus *Journal of Fluid Mechanics* **83**, 721–735.

Abstract submitted to 16th IWWWFB, Hiroshima, Japan, 22–25 April 2001

Non-axisymmetric trapping structures in the three-dimensional water-wave problem

P. McIver[1] and J. N. Newman[2]
[1]Loughborough University, UK (p.mciver@lboro.ac.uk)
[2]MIT, Cambridge, MA USA (jnn@mit.edu)

Introduction

Trapped modes are free oscillations with finite energy of an unbounded fluid for which the fluid motion is essentially confined to the vicinity of a fixed structure. In recent years it has been discovered that such modes exist in the three-dimensional linearized water-wave problem and may be supported at specific frequencies by certain 'trapping structures' [1,2]. The existence of a trapped mode at a particular frequency implies the non-uniqueness, or even non-existence, of the solution to the scattering or radiation problem at that frequency.

Axisymmetric trapped modes in the presence of axisymmetric structures may be constructed by an inverse procedure in which the main idea is to specify an axisymmetric velocity field that decays at large distances, and then to seek stream surfaces that correspond to rigid structures [1]. A time-harmonic circular ring source of radius c, and with a vertical axis of symmetry, is placed in the free surface. There is no wave propagation to infinity at the frequencies given by $Kc = j_{0,n}$, where $K = \omega^2/g$, ω is the radian frequency, g is the acceleration due to gravity, and $j_{0,n}$ is the nth zero of the Bessel function J_0. Axisymmetric stream surfaces of this flow correspond to particular toroidal structures intersecting the free surface which, by construction, are able to support free oscillations of the fluid; an example of such a structure is shown in figure 1. Subsequently, the construction was extended [2] to give non-axisymmetric trapped modes in the presence of axisymmetric toroidal structures by allowing the strength of the ring source, and hence the corresponding velocity field, to have a sinusoidal azimuthal variation. A hydrodynamic analysis has been performed for axisymmetric trapping structures [3] and singular behaviour of, for example, the added mass and damping is observed in the vicinity of the trapped-mode frequency.

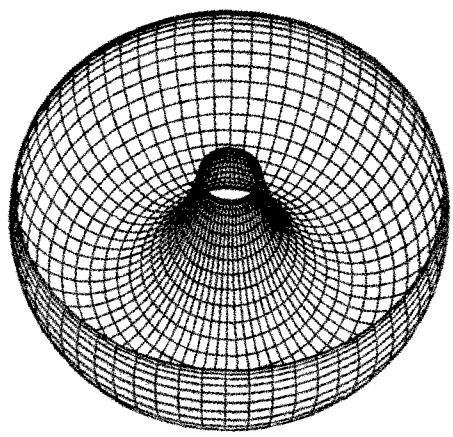

Figure 1: Perspective view of the submerged surface of an axisymmetric trapping structure.

The question arises 'Can non-axisymmetric trapping structures be found?'. The present work answers this question in the affirmative and, in particular, it is demonstrated that *non-axisymmetric* trapping structures can be constructed from an *axisymmetric* velocity field.

Construction of trapped modes

It is most convenient to work in terms of toroidal coordinates (r, θ, β) with $r > 0$, $0 \le \theta < \pi$, and $0 \le \beta < 2\pi$ [4], which are related to rectangular Cartesian coordinates (x, y, z) by

$$x = (c - r\cos\theta)\cos\beta, \quad y = (c - r\cos\theta)\sin\beta, \quad z = r\sin\theta, \tag{1}$$

where c is the radius of a circular ring in the free surface (perhaps coinciding with a ring source as described above), and z is directed vertically downwards with $z = 0$ corresponding to the mean free surface. Thus, β is an azimuthal angle measured around the z axis and, in any vertical plane through the z axis, (r, θ) are equivalent to plane polar coordinates with origin at $R = (x^2+y^2)^{1/2} = c$, $z = 0$.

As in previous work [1,2], a flow field is first specified in terms of a velocity potential

$$\Phi(r, \theta, \beta, t) = \phi(r, \theta, \beta) \cos \omega t, \tag{2}$$

where t is time and ω is the radian frequency of the fluid oscillations. Let $\mathbf{e}_r$, $\mathbf{e}_\theta$, and $\mathbf{e}_\beta$ be unit vectors in the r, θ and β directions respectively. With the time dependence removed, the velocity is

$$\nabla\phi = \frac{\partial\phi}{\partial r}\mathbf{e}_r + \frac{1}{r}\frac{\partial\phi}{\partial\theta}\mathbf{e}_\theta + \frac{1}{c - r\cos\theta}\frac{\partial\phi}{\partial\beta}\mathbf{e}_\beta \tag{3}$$

and it is required to determined a surface $r = r(\theta, \beta)$ such that

$$\nabla\phi.\boldsymbol{n} = 0, \tag{4}$$

for all normals

$$\boldsymbol{n} = -\mathbf{e}_r + \frac{1}{r}\frac{\partial r}{\partial\theta}\mathbf{e}_\theta + \frac{1}{c - r\cos\theta}\frac{\partial r}{\partial\beta}\mathbf{e}_\beta \tag{5}$$

to the surface. In other words, the kinematic condition to be satisfied on a structural surface is

$$q_\theta\frac{\partial r}{\partial\theta} + q_\beta\frac{\partial r}{\partial\beta} = q_r \tag{6}$$

where

$$q_r = \frac{\partial\phi}{\partial r}, \quad q_\theta = \frac{1}{r^2}\frac{\partial\phi}{\partial\theta}, \quad q_\beta = \frac{1}{(c - r\cos\theta)^2}\frac{\partial\phi}{\partial\beta}. \tag{7}$$

Now for $q_\theta \neq 0$ equation (6) can be rewritten as

$$\frac{\partial r}{\partial\theta} + \frac{q_\beta}{q_\theta}\frac{\partial r}{\partial\beta} = \frac{q_r}{q_\theta} \tag{8}$$

so that

$$\frac{\mathrm{d}r}{\mathrm{d}\theta} = \frac{q_r}{q_\theta} \tag{9}$$

on the curves

$$\frac{\mathrm{d}\beta}{\mathrm{d}\theta} = \frac{q_\beta}{q_\theta}. \tag{10}$$

The last two equations determine the so-called characteristic curves [5, Chapter II, §1]. Under certain not very restrictive conditions, given an initial curve Γ in the free surface defined by $r = r(0, \beta)$, equations (9)–(10) can be integrated from initial points $(r(0, \beta_0), 0, \beta_0)$ on Γ to determine curves that are everywhere parallel to the velocity field. Thus, given the velocity field and an appropriately chosen initial closed curve Γ in the free surface, a stream surface can be generated by simultaneous integration over $0 \leq \theta \leq \pi$ of the two first-order differential equations (9)–(10). For a velocity field generated from a ring source that is singular in the free surface at $R = c$, a sensible choice for Γ is a closed curve surrounding the origin and entirely within $R = c$.

For the special case in which the specified flow is axisymmetric, so that $q_\beta = 0$, equation (10) gives immediately that β is constant on any characteristic curve and it is sufficient to integrate (9) to determine the characteristics. Although the velocity field is axisymmetric there is no requirement that the initial curve Γ must also be axisymmetric. Thus, non-axisymmetric stream surfaces can be generated from axisymmetric velocity fields!

Stream-function approach

Another approach to the axisymmetric flow case is to express the given velocity field in terms of a function $\psi(r, \theta, \beta)$ so that

$$\nabla\phi = -\frac{1}{r(c - r\cos\theta)}\frac{\partial\psi}{\partial\theta}\mathbf{e}_r + \frac{1}{r(c - r\cos\theta)}\frac{\partial\psi}{\partial r}\mathbf{e}_\theta; \tag{11}$$

the particular form arises from the requirement that $\nabla^2\phi = 0$. For some constant C, a normal to a surface S defined by

$$\psi(r, \theta, \beta) = C \tag{12}$$

is

$$\nabla\psi = \frac{\partial\psi}{\partial r}\mathbf{e}_r + \frac{1}{r}\frac{\partial\psi}{\partial\theta}\mathbf{e}_\theta + \frac{1}{c - r\cos\theta}\frac{\partial\psi}{\partial\beta}\mathbf{e}_\beta \tag{13}$$

and the construction ensures that $\nabla\psi$ is perpendicular to $\nabla\phi$ everywhere on S, and hence S is a stream surface of the flow. Given an axisymmetric velocity field, (11) can be solved to determine ψ; this is probably best done in a different coordinate system. In most applications ψ is chosen to be axisymmetric (and often called the Stokes' stream function) so that ψ is independent of β and the surfaces S are also axisymmetric. This is the approach initially adopted in this problem in order to generate axisymmetric trapping structures from axisymmetric velocity fields [1]. However, if

$$\psi(r, \theta, \beta) = \Psi(r, \theta) \tag{14}$$

is a particular solution to (11) then

$$\psi(r, \theta, \beta) = \Psi(r, \theta) + \chi(\beta) \tag{15}$$

is also a solution for any reasonable $\chi(\beta)$. In general, the surfaces S generated from (12) using (15) are not axisymmetric.

An example of a non-axisymmetric trapping structure

Many types of non-axisymmetric trapping structures can be generated in the manner described above. For instance, the structure shown in figure 1 can be distorted so that the inner and outer radii are smoothly varying functions of the azimuthal angle β. Here we present another example in which sections of different radius are joined together.

The axisymmetric flow is specified in terms of the potential for a ring source of radius one. The geometry of the structure shown in figure 2 is defined explicitly, in a manner described elsewhere [6]. Three 'patches' are defined in one quadrant as follows. Patch 1 consists of a partial torus with inner waterline radius 0.2 restricted to the range $\beta \in (0, \pi/4)$, patch 2 consists of a partial torus with inner waterline radius 0.3 restricted to the range $\beta \in (\pi/4, \pi/2)$, and patch 3 is the portion of the azimuthal plane $\beta = \pi/4$ between the generating sections of the first two patches (planes of constant β are also stream surfaces of an axisymmetric flow). After reflection about the planes $x = 0$ and $y = 0$ a *non-axisymmetric* closed structure is formed, with the property that its surface coincides with the *axisymmetric* stream surfaces generated by the ring source. The toroidal radial coordinates of the generating sections for the first two patches are defined by economized polynomials of degree 10 in the angle θ. The maximum error in these polynomial approximations is 5×10^{-6}.

Figure 3 shows the heave added-mass coefficient for this structure, computed by the program WAMIT with quadratic B-spline representation of the potential and exact representation of the geometry as defined by the above polynomial approximations. Three different results are shown, with N=48, 108, and 300 unknowns in the linear system of equations, corresponding to subdivisions

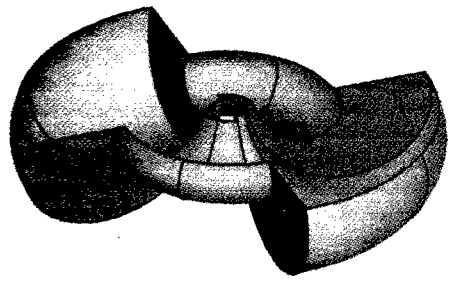

Figure 2: Perspective view of a non-axisymmetric trapping structure. The dark lines show the boundaries of each patch and its reflections about the planes of symmetry.

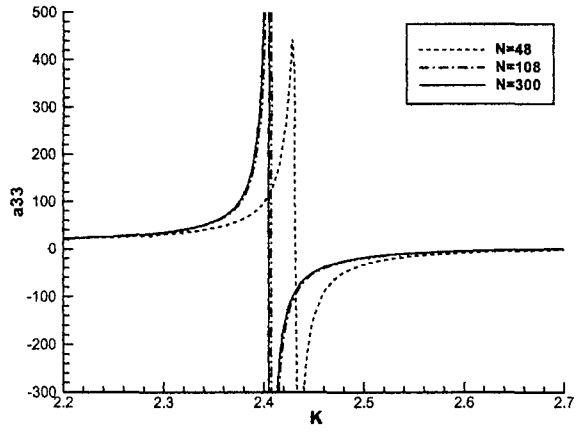

Figure 3: Heave added-mass coefficient a_{33}, normalized with respect to the radius of the ring source and fluid density vs. the wavenumber K.

N	panels	K_0	$\lvert a_{33}\rvert$
48	2×2	2.430	374
108	4×4	2.406	4,440
300	8×8	2.4048	69,000

Table 1: Singular wave number K_0 and added mass a_{33} as a function of the number of unknowns N.

of each patch into 2×2, 4×4, and 8×8 elements. These results are computed in the range shown using 102 closely spaced wavenumbers. In the vicinity of the singular wavenumber $K = j_{0,1} \approx 2.4048$ the increment is $\Delta K = 0.0001$. The value K_0 of the wavenumber where the added-mass coefficient changes sign and the maximum value of this coefficient are shown in table 1. These numerical results give strong supporting evidence for the existence of non-axisymmetric trapping structures.

References

1. McIver, P. and McIver, M. 1997 Trapped modes in an axisymmetric water-wave problem. *Quarterly Journal of Mechanics and Applied Mathematics*, **50**, 165–178.
2. Kuznetsov, N. and McIver, P. 1997 On uniqueness and trapped modes in the water-wave problem for a surface-piercing axisymmetric body. *Quarterly Journal of Mechanics and Applied Mathematics*, **50**, 565–580.
3. Newman, J. N. 1999 Radiation and diffraction analysis of the McIver toroid. *Journal of Engineering Mathematics*, **35**, 135–147.
4. Bourne, D. E. and Kendall, P. C. 1977 *Vector Analysis and Cartesian Tensors.* 2nd edition, Van Nostrand Reinhold.
5. Courant, R. and Hilbert, D. 1962 *Methods of Mathematical Physics: Volume II.* John Wiley & Sons.
6. Lee, C.-H. and Newman, J. N. 2001 Solution of radiation problems with exact geometry. (extended abstract submitted to this Workshop)

Spectral Solution of Time-Dependent Shallow Water Hydroelasticity

Michael H. Meylan

Institute of Information and Mathematical Sciences, Massey University New Zealand

1 Introduction

If a hydroelastic problem is linear the time-dependent motion can be found using spectral theory, at least theoretically. However the spectral theory for linear hydroelasticity has not been developed, even for the simplest cases. For example, the work of [1] which presented a method to determine the scattering frequencies for hydroelastic problems did not develop any spectral theory. This has meant that spectral methods to solve the time-dependent motion, such as [4], have only solved for the motion is restrictive cases.

In this paper the spectral theory for a simple hydroelastic problem, the two dimensional thin plate floating on shallow water, is developed. This work, while it has practical applications, primarily aims to motivate the development of a spectral theory for more complicated hydroelastic problems. Two separate methods are developed, both based on a special inner product which represents the energy of the plate-water system. The first method uses the single frequency solutions as the eigenfunctions and the problem is solved by a generalised Fourier transform. The second method is based on Lax-Philips scattering and calculates the solution by an expansion in modes. These modes represent the natural frequencies of the plate-water system and include the decay due to the radiation of energy into the surrounding water.

2 Formulation: A Thin Plate on Shallow Water

A thin plate of shallow draft covers the region $-b \leq x \leq b$ of shallow water of depth h. The mathematical description of the problem follows from [5]. The kinematic condition is

$$\partial_t \zeta = -h\partial_x^2 \phi \qquad [2.1]$$

where ϕ is the velocity potential of the water and ζ is the displacement of the water surface or the plate. The equation for the pressure is

$$-\rho g\zeta - \rho\partial_t\phi = \begin{cases} 0, & x \notin (-b,b), \\ D\partial_x^4\zeta + \rho' d\partial_t^2\zeta, & x \in (-b,b), \end{cases} \qquad [2.2]$$

where D is the bending rigidity of the plate per unit length, ρ is the density of water, ρ' is the density of the plate, g is the acceleration due to gravity, and d is the thickness of the plate. We also have the free edge boundary conditions

$$\lim_{x\downarrow -b}\partial_x^2\zeta = \lim_{x\uparrow b}\partial_x^2\zeta = \lim_{x\downarrow -b}\partial_x^3\zeta = \lim_{x\uparrow b}\partial_x^3\zeta = 0. \qquad [2.3]$$

Non-dimensional variables are now introduced. The space variables are non-dimensionalised using the water depth h, and the time variables are non dimensionalised using $\sqrt{\frac{h}{g}}$. The non-dimensionalised variables are

$$\bar{x} = \frac{x}{h},\ \bar{t} = t\sqrt{\frac{g}{h}},\ \bar{\zeta} = \frac{\zeta}{h},\ \text{and}\ \bar{\phi} = \frac{\phi}{h^2\sqrt{g/h}}.$$

In these new variables, ([2.1]) and ([2.2]) become

$$\partial_{\bar{t}}\bar{\zeta} = -\partial_{\bar{x}}^2\bar{\phi} \qquad [2.4]$$

and

$$-\bar{\zeta} - \partial_{\bar{t}}\bar{\phi} = \begin{cases} 0, & \bar{x} \notin (-\bar{b},\bar{b}), \\ \beta\partial_{\bar{x}}^4\bar{\zeta} + \gamma\partial_{\bar{t}}^2\bar{\zeta}, & x \in (-\bar{b},\bar{b}), \end{cases} \qquad [2.5]$$

subject to the boundary conditions

$$\lim_{\bar{x}\downarrow -\bar{b}}\partial_{\bar{x}}^2\bar{\zeta} = \lim_{\bar{x}\uparrow \bar{b}}\partial_{\bar{x}}^2\bar{\zeta} = \lim_{\bar{x}\downarrow -\bar{b}}\partial_{\bar{x}}^3\bar{\zeta} = \lim_{\bar{x}\uparrow \bar{b}}\partial_{\bar{x}}^3\bar{\zeta} = 0. \qquad [2.6]$$

The non-dimensional variables β and γ are given by

$$\beta = \frac{D}{\rho g h^4} \quad \text{and} \quad \gamma = \frac{\rho' d}{\rho h}.$$

For clarity the overbar is dropped from now on. Following [3] we set the inertia term, $\gamma\partial_t^2\zeta$ to zero since it is much

smaller than ζ. This follows from the fact that $d \ll h$ and, since the water is shallow, the wavelengths (and hence the frequencies) must be much greater than h so that $\partial_t^2 \zeta \ll \zeta$.

3 The self-adjoint solution method

In this section, a solution for the time dependent motion of the plate-water system is developed using the theory of self-adjoint operators. We define a two-component variable $U(x,t)$ by

$$U(x,t) = \begin{pmatrix} \phi(x,t) \\ i\zeta(x,t) \end{pmatrix}. \qquad [3.1]$$

Equations ([2.4]) and ([2.5]) are now converted to the following equation for U

$$\frac{1}{i}\partial_t U = \mathcal{P}U \qquad [3.2]$$

where

$$\mathcal{P} = \begin{pmatrix} 0 & 1+\beta\left(H(x-b)-H(x+b)\right)\partial_x^4 \\ -\partial_x^2 & 0 \end{pmatrix}$$

and H is the Heavyside function. Equation ([3.2]) is also subject to the boundary conditions at the end of the plate given by equation ([2.6]) and the initial condition

$$U(x,t)_{t=0} = U_0(x) = \begin{pmatrix} \phi_0(x) \\ i\zeta_0(x) \end{pmatrix}. \qquad [3.3]$$

The operator $\mathcal{P}$ is self adjoint in the Hilbert space $\mathcal{H}$ with inner product given by the energy. The energy inner product for the two vectors

$$U_1 = \begin{pmatrix} \phi_1 \\ i\zeta_1 \end{pmatrix} \text{ and } U_2 = \begin{pmatrix} \phi_2 \\ i\zeta_2 \end{pmatrix}$$

is

$$\langle U_1, U_2 \rangle_{\mathcal{H}} = \langle \partial_x\phi_1, \partial_x\phi_2 \rangle + \left\langle \left(1+\beta\left(H(x-b)-H(x+b)\right)\partial_x^4\right) i\zeta_1, i\zeta_2 \right\rangle. \qquad [3.4]$$

The subscript $\mathcal{H}$ is used to denote the special inner product and the angle brackets without the $\mathcal{H}$ denote the standard inner product

$$\langle f(x), g(x) \rangle = \int_{-\infty}^{\infty} f(x)\, g^*(x)\, dx.$$

Since $\mathcal{P}$ is self-adjoint the solution to ([3.2]) can be calculated using the eigenfunctions of $\mathcal{P}$. There are two eigenfunctions for each eigenvalue $\lambda \in \mathbb{R}$, a unit incoming wave from the left ($x = -\infty$) denoted by $\Phi^>$ and a unit wave incoming from the right ($x = \infty$) denoted by $\Phi^<$. The eigenfunctions $\Phi^>(\lambda, x)$ consist of the two components $\phi^>(\lambda, x)$ and $i\zeta^>(\lambda, x)$ given by

$$\phi^>(\lambda,x) = \begin{cases} e^{-i\lambda x} + S_{11}(\lambda)\, e^{i\lambda x}, & x < -b, \\ \sum_{j=1}^{6} \alpha_j e^{\mu_j(\lambda)x}, & -b < x < b \\ S_{12}(\lambda)\, e^{-i\lambda x}, & x > b, \end{cases} \qquad [3.5]$$

and

$$i\zeta^>(\lambda,x) = \begin{cases} \lambda e^{-i\lambda x} + \lambda S_{11}(\lambda)\, e^{i\lambda x}, & x < -b, \\ \frac{-1}{\lambda}\sum_{j=1}^{6} \mu_j(\lambda)^2 \alpha_j e^{\mu_j(\lambda)x}, & -b < x < b \\ \lambda S_{12}(\lambda)\, e^{-i\lambda x}, & x > b, \end{cases} \qquad [3.6]$$

where $\mu_j(\lambda)$ are the six roots of the equation

$$\beta\mu^6 + \mu^2 + \lambda^2 = 0 \qquad [3.7]$$

and the values of $S_{11}(\lambda)$, $S_{12}(\lambda)$, and α_j are chosen so that $\phi^>(\lambda,x)$ and $\zeta^>(\lambda,x)$ satisfy the boundary conditions ([2.3]) and the continuity of ϕ and $\partial_x\phi$ at $x = \pm b$. Also, since S_{11} represents the amplitude of the reflected wave and S_{12} represents the amplitude of the transmitted wave, conservation of energy requires that $|S_{11}|^2 + |S_{12}|^2 = 1$. The eigenfunctions for the wave propagating from the right $\Phi^<$ are found similarly.

Since the boundary conditions are symmetric we must have $S_{22}(\lambda) = S_{11}(\lambda)$ and $S_{12}(\lambda) = S_{21}(\lambda)$. Also, the scattering matrix

$$\mathbf{S}(\lambda) = \begin{pmatrix} S_{11}(\lambda) & S_{12}(\lambda) \\ S_{21}(\lambda) & S_{22}(\lambda) \end{pmatrix} \qquad [3.8]$$

is unitary as a consequence of the Lax-Philips scattering structure which will be discussed in section 4.

Equation ([3.2]) can be solved by a generalised Fourier transform based on the eigenfunctions of the operator $\mathcal{P}$. The eigenfunctions are orthogonal since $\mathcal{P}$ is self-adjoint and the normalising constant is determined by calculating the inner

product of these eigenfunctions with themselves. These inner products are given by

$$\left\langle \Phi^{>}(x,\lambda_1), \Phi^{>}(x,\lambda_2) \right\rangle_{\mathcal{H}} = 4\pi\delta(\lambda_1-\lambda_2)\lambda_1^2,$$
$$\left\langle \Phi^{<}(x,\lambda_1), \Phi^{<}(x,\lambda_2) \right\rangle_{\mathcal{H}} = 4\pi\delta(\lambda_1-\lambda_2)\lambda_1^2, \qquad [3.9]$$

and

$$\left\langle \Phi^{>}(x,\lambda_1), \Phi^{<}(x,\lambda_2) \right\rangle_{\mathcal{H}} = 0. \qquad [3.10]$$

Using these eigenfunctions the solution to ([3.2]) subject to ([3.3]) is

$$U(x,t) = \int_{-\infty}^{\infty} \left\langle U_0(x), \frac{\Phi^{>}(x,\lambda)}{4\pi\lambda^2} \right\rangle_{\mathcal{H}} \Phi^{>}(x,\lambda)\, e^{i\lambda t} d\lambda + \int_{-\infty}^{\infty} \left\langle U_0(x), \frac{\Phi^{<}(x,\lambda)}{4\pi\lambda^2} \right\rangle_{\mathcal{H}} \Phi^{<}(x,\lambda)\, e^{i\lambda t} d\lambda. \qquad [3.11]$$

4 The Lax-Philips Scattering Solution Method

In this section, a solution to the time-dependent motion of the plate-water system is developed using the Lax-Philips scattering theory ([2]). This solution method will only solve for an initial condition which is zero outside the region of water covered by the plate ($|x| > b$). The basic idea and consequences of the Lax-Philips scattering theory will be outlined here for our specific problem. The Hilbert space $\mathcal{H}$ is decomposed into three subspaces called the incoming, outgoing and scattering spaces. The incoming space, denoted by D_-, consists of all waves travelling towards the plate, either from the left or the right, as appropriate. The outgoing subspace, denoted by D_+, consists of all waves travelling away from the plate, either to the left or right, as appropriate. What remains is called the scattering region, and is denoted by K. In our problem, K is nothing more than the potential and displacement under the plate.

We introduce a new operator $\mathcal{B}$ which describes the evolution of the plate in the absence of wave forcing. If we again denote the motion of the plate by the two component vector $U(x,t)$ ([3.1]) then the equation for the motion of the plate in the absence of wave forcing is

$$\frac{1}{i}\frac{\partial}{\partial t}U = \mathcal{B}U.$$

This means that $\mathcal{B}$ is the infinitesimal generator of the semigroup (dissipative evolution operator) given by restricting the problem to K, i.e.,

$$e^{i\mathcal{B}t} = P_K\, e^{i\mathcal{P}t}\big|_K$$

where P_K is the projection onto the subspace K and the $|_K$ means that the input is restricted to K. Therefore $e^{i\mathcal{B}t}$ is the evolution of an initial condition which is zero outside K and which is subsequently restricted to K, i.e. the evolution of the plate motion in the absence of wave forcing.

The solution to the non self-adjoint problem requires the eigenvalues and eigenfunctions of $\mathcal{B}$, sometimes referred to as scattering frequencies or resonances. The eigenvalues of $\mathcal{B}$ are found using the analytic extension of the scattering matrix $\mathbf{S}(\lambda)$ ([3.8]) to $\mathbb{C}$ since the eigenvalues of $\mathcal{B}$ occur precisely at the singularities of $\mathbf{S}(\lambda)$. These singularities are found by a complex integration search method to give a rough estimate and Newton's method to determine their location accurately.

The eigenfunctions of $\mathcal{B}$ associated with the eigenvalue λ_n are denoted by $\Phi^{+}(\lambda_n, x)$, and those of $\mathcal{B}^*$ (the adjoint of $\mathcal{B}$) associated with the eigenvalue λ_n^* are denoted by $\hat{\Phi}^{+}(\lambda_n^*, x)$. That is,

$$\mathcal{B}\Phi^{+}(\lambda_n, x) = \lambda_n \Phi^{+}(\lambda_n, x)$$

and

$$\mathcal{B}^*\hat{\Phi}^{+}(\lambda_n^*, x) = \lambda_n^*\hat{\Phi}^{+}(\lambda_n^*, x).$$

The eigenfunction $\Phi^{+}(\lambda_n, x)$ is given by

$$\Phi^{+}(\lambda_n, x) = \begin{pmatrix} \phi^{+}(\lambda_n, x) \\ i\zeta^{+}(\lambda_n, x) \end{pmatrix} = \begin{pmatrix} \sum_{j=1}^{6} \alpha_j e^{\mu_j(\lambda_n)x} \\ \sum_{j=1}^{6} -\dfrac{\alpha_j \mu_j(\lambda_n)^2}{\lambda_n} e^{\mu_j(\lambda_n)x} \end{pmatrix} \qquad [4.1]$$

where $\mu_j(\lambda)$ are the six roots of equation ([3.7])

$$\beta\mu_j(\lambda)^6 + \mu_j(\lambda)^2 + \lambda^2 = 0.$$

The α_j are determined by the condition that the waves are of unit amplitude and are outgoing at $x = -b$,

$$\phi^{+}(\lambda_n, -b) = e^{i\lambda_n b}, \quad \partial_x\phi^{+}(\lambda_n, x)\big|_{x=-b} = i\lambda_n e^{i\lambda_n b},$$

and the boundary conditions at the end of the plate ([2.3]) are satisfied. The eigenfunctions of $\mathcal{B}^*$ are found similarly.

A biorthogonal system with respect to the energy inner product ([3.4]) is formed by the eigenfunctions of $\mathcal{B}$, $\Phi^+(\lambda_n, x)$, and the eigenfunctions of $\mathcal{B}^*$, $\hat{\Phi}^+(\lambda_n, x)$. To normalise the biorthogonal system, the inner product of $\Phi^+(\lambda_n, x)$ and $\hat{\Phi}^+(\lambda_n, x)$ must be found and this can be calculated analytically. Once this has been accomplished the evolution of the plate from some initial displacement $U_0(x)$ is given by

$$U(x,t) = \sum_{n=-\infty}^{\infty} e^{i\lambda_n t} \frac{\left\langle U_0(x), \hat{\Phi}(\lambda_n, x) \right\rangle_{\mathcal{H}}}{\left\langle \Phi(\lambda_n, x), \hat{\Phi}(\lambda_n, x) \right\rangle_{\mathcal{H}}} \Phi(\lambda_n, x) \qquad [4.2]$$

where $U_0(x)$ is the initial condition given by equation ([3.3]).

5 Summary

Two methods have been presented to solve the time dependent motion of a thin plate floating on shallow water. One method was based on self-adjoint operator theory, and the other on Lax-Philips scattering. The Lax-Philips method only solved the problem of a free plate and cannot be used to solve for wave forcing. The self-adjoint method solves both the wave forcing and free plate problem. The eigenfunctions for the self-adjoint method are orthogonal and the eigenvalues are continuous and consist of all $\mathbb{R}$, which makes the calculation of the eigenvalues trivial. The Lax-Philips method has discrete eigenvalues and the system of eigenfunctions is biorthogonal. The eigenvalues for the Lax-Philips method must be calculated numerically. however the Lax-Philips method has the significant advantage that the modes of vibration of the plate-water system and their frequency and rate of decay are found.

References

[1] C. Hazard and M. Lenoir. Determination of scattering frequencies for an elastic floating body. *SIAM J. Math. Anal.*, 24(4):1458–1514, 1993.

[2] P. D. Lax and R. S. Philips. *Scattering Theory*. Academic, 1989.

[3] Y. Namba and M. Ohkusu. Hydroelastic behaviour of floating artifical islands in waves. *Int. J. of Offshore and Polar Engineering*, 9(2):39–47, 1999.

[4] S. Ohmatsu. Numerical calculation of hydroelastic behavior of VLFS in time domain. In M. Kashiwagi, W. Koterayama, and M. Ohkusu, editors, *Hydroelasticity in Marine Technology*, pages 89–97. Yomei Printing Cooperative Society, Fukuoka, Japan, 1998.

[5] J. J. Stoker. *Water Waves: The Mathematical Theory with Applications*. Interscience, 1957.

Water entry of a perforated wedge

B. Molin*, A.A. Korobkin**
*ESIM, 13451 Marseille cedex 20, France, molin@esim.fr
**Lavrentyev Institute of Hydrodynamics, Novosibirsk 630090, Russia

1. Introduction

Since the pioneering works of von Karman and Wagner the water entry of solid bodies has received a considerable attention.

In this paper we apply Wagner's approach to two-dimensional bodies which are perforated. This problem has some relevance in coastal engineering, to study wave impact upon perforated breakwaters. One may also conceive of using perforated shrouds as outer protections for other bodies subjected to wave impacts, like the under-sides of the decks of offshore platforms, or for bodies entering the free surface at large speeds.

Another reason to get interested into water entry of perforated bodies is that the jets that occur through the openings directly reflect the extension of the wetted area, and that their velocities are in proportion with the ambient pressures. With high speed cameras of appropriate resolution it should be possible to quantify, in time, the locations and velocities of the jets. Comparisons between theoretical and experimental results could then be easier than with solid bodies.

2. Formulation of the problem

The boundary condition on the wetted part of the entering body is inspired by previous work carried out by the first author on the hydrodynamics of perforated bodies (Molin, 1992). It is assumed that the flow through the openings results into pressure drops, which are proportional to the square of the local traversing velocities (relative to the body surface). The relationship between pressure drops and traversing velocities is taken in an averaged sense (over a large number of perforations), yielding:

$$p^- - p^+ = \rho \, \frac{1-\tau}{2\,\mu\,\tau^2} \, v\,|v|, \tag{1}$$

where τ is the porosity ratio (area of the perforations divided by total area) and μ a discharge coefficient, usually close to 0.5.

Here we consider the initial stage of the water entry of a porous blunt shape into still water. Some fluid leaks through the porous surface (as small jets through the openings), but the upper side remains at atmospheric pressure. Equation (1) then reduces to the simple form (after linearization à la Wagner)

$$-\Phi_t(x,0,t) = \frac{1-\tau}{2\,\mu\,\tau^2} \, (U + \Phi_y(x,0,t))^2, \tag{2}$$

where $y = 0$ is the initial level of the free surface, U is the vertical velocity of the body and $\Phi(x,y,t)$ is the velocity potential.

If the body is solid, then $\tau = 0$ and the boundary condition (2) resumes to the usual one: $\Phi_y = -U$. If the body is porous, then $\tau \neq 0$ and (2) can be interpreted as an evolution equation for Φ.

In the case of symmetric body shape, $y = f(x) = f(-x)$, the boundary-value problem with respect to the velocity potential has the form

$$\begin{array}{lcll} \Delta\Phi & = & 0 & y < 0 \\ \Phi_t & = & -\alpha\,(U+\Phi_y)^2 & |x| < c(t) \qquad y = 0 \\ \Phi & = & 0 & |x| > c(t) \qquad y = 0 \\ \nabla\Phi & \to & 0 & x^2 + y^2 \to \infty \end{array} \tag{3}$$

where $\alpha = (1-\tau)\,/\,(2\,\mu\,\tau^2)$.
The wetted length $2\,c(t)$ of the body is obtained from the Wagner condition of continuous joining of the free surface and the surface of the entering body at $x = \pm c(t)$

$$f(c) = U\,t + \int_0^t \Phi_y(c,0,T)\;dT, \tag{4}$$

where $t = 0$ is the impact instant and $\Phi_y(c(t),0,T)$ is the vertical velocity of the free surface at the time instant T at the point $x = c(t)$.

3. Self-similar solution for a porous wedge

We consider the case of a wedge, with deadrise angle β, entering vertically the free surface with constant speed U. The self-similar problem is derived by introducing the non-dimensional variables:

$$x = \gamma\,U\,t\,X \qquad y = \gamma\,U\,t\,Y \qquad \Phi = \gamma\,U^2\,t\,\phi(X,Y) \qquad c = \gamma\,U\,t. \tag{5}$$

In the stretched variables the boundary condition on the wetted part of the wedge (2) and the Wagner condition (4) take, respectively, the forms

$$\phi - X\,\phi_X = -\frac{\alpha}{\gamma}\,(1+\phi_Y)^2 \qquad |X| \le 1 \qquad Y = 0, \tag{6}$$

$$\gamma\,\tan\beta = 1 + \int_1^\infty \frac{\phi_Y(u,0)}{u^2}\;du. \tag{7}$$

The numerical difficulties mostly reside with the nonlinearity of equation (6), and with the fact that γ is not known a priori. To overcome them, an iterative resolution method is used with equation (6) being presented as

$$\phi^{(n)} - X\,\phi_X^{(n)} + \frac{\alpha}{\gamma^{(n-1)}}\,(2+\phi_Y^{(n-1)})\,\phi_Y^{(n)} = -\frac{\alpha}{\gamma^{(n-1)}} \tag{8}$$

This means that an equation of the type

$$\phi - X\,\phi_X + f(X)\,\phi_Y = k \qquad |X| \le 1 \qquad Y = 0 \tag{9}$$

has to be solved at each iteration.

This scheme turned out to be efficient for small values of the parameter $\alpha\,\tan\beta$. At large values of the parameter it is more expedient to reverse equation (6), writing it under the form

$$\phi_Y = -1 + \sqrt{\frac{\gamma}{\alpha}\,(X\,\phi_X - \phi)} \tag{10}$$

and to solve it iteratively through the scheme

$$\phi_Y^{(n)} = -1 + \sqrt{\frac{\gamma^{(n-1)}}{\alpha}\,\left(X\,\phi_X^{(n-1)} - \phi^{(n-1)}\right)}. \tag{11}$$

The choice between either iterative scheme is decided upon the value of the product $\alpha\,\tan\beta$. When $\alpha\,\tan\beta$ is smaller than 1, the first scheme is used. When it is larger than 1, the second one is followed.

To present preliminary results, we use a very crude numerical method. That is, we bound the domain at some distance $X = \pm L$ and use eigenfunction expansion of the potential

$$\phi(X,Y) = \sum_{n=1}^{N} A_n\,\cos\lambda_n X\;e^{\lambda_n Y} \tag{12}$$

in the region $-L \le X \le L$ and $-\infty < Y \le 0$, where $\lambda_n = (2\,n-1)\,\pi/(2\,L)$ so that $\Phi(\pm L, Y) \equiv 0$.

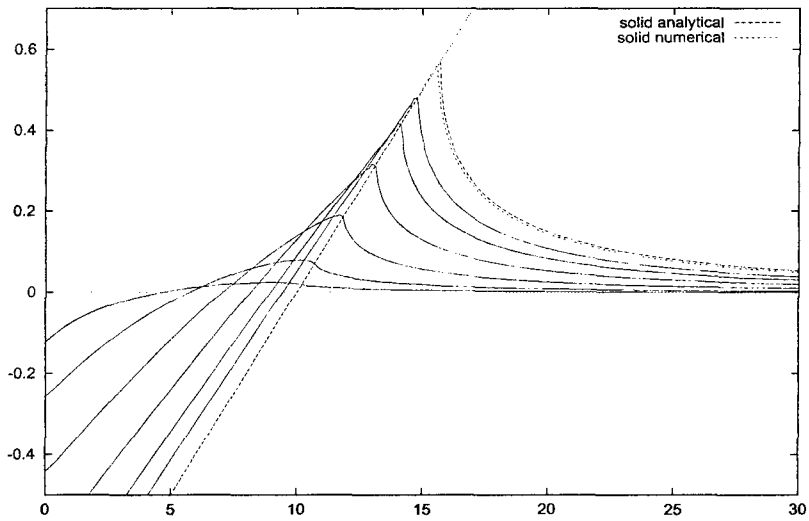

Figure 1: Porous wedge. $\cot\beta = 10$. Free surface elevation obtained from self-similar solution for $\alpha = 1$, 4, 16, 64, 256, 1024 and for a solid wedge.

A Galerkin procedure is then followed to build up a linear system which is solved by a standard Gauss routine to yield the A_n coefficients. This procedure is repeated until convergence, which is always attained within a few iterations.
When convergence has been reached the free surface position in the self-similar variables is given by

$$E(X) = \frac{1}{\gamma}\, X \int_X^\infty \frac{\phi_Y(u,0)}{u^2}\, du = \frac{1}{\gamma} \sum_{n=1}^{N} \lambda_n^2\, A_n\, X \int_{\lambda_n X}^\infty \frac{\cos v}{v^2}\, dv \qquad (X > 0). \tag{13}$$

The free surface elevation $\eta(x,t)$ is related to $E(X)$ through

$$\eta(x,t) = \gamma\, U\, t\, E\left(\frac{x}{\gamma\, U\, t}\right).$$

Finally the vertical force on the porous wedge is obtained as

$$f_y = -\rho\, \frac{d}{dt}\left\{\int_{-\infty}^{\infty} \Phi(x,0,t)\, dx\right\} = -2\,\rho\,\gamma^2\, U^3\, t \int_{-L}^{L} \phi(X,0)\, dX = 4\,\rho\,\gamma^2\, U^3\, t \sum_{n=1}^{N} \frac{(-1)^n\, A_n}{\lambda_n}. \tag{14}$$

In the case of small porosity, $\tau \ll 1$, the iterative scheme (11) can be followed to derive the asymptotic behaviour of the solution. Then it is found that the ratio $f_y(\tau)/f_y(0)$ (that is the force on the porous wedge divided by its value for the solid one) behaves as $1 - b\sqrt{\gamma/\alpha}$, where $b = 1.113$, and the quantity γ is $\pi^2\alpha[\sqrt{a^2 + 2\pi\alpha\tan\beta} + a]^{-2}$, where $a = 0.712$, for large values of the product $\alpha\tan\beta$.

We first present results for a wedge with a deadrise angle β such that $\cot\beta = 10$. The half-length L of the numerical domain is taken equal to 8 and the truncation order N of the series (12) is $N = 800$. Figure 1 shows the free surface elevation $\gamma\, E$ plotted versus $\gamma\, X$ (that is $\eta(x,t)/(U\,t)$ plotted against $x/(U\,t)$), for different α values: $\alpha = 1$, 4, 16, 64, 256 and 1024 (or, roughly, porosity ratios of 62, 39, 22, 12, 6 and 3 %). As the porosity increases, the profiles of the liquid surface (inside and outside of the wedge) are getting smoother and the points of maximum elevation move inside the wedge.
It should be noted that the profiles obtained inside the porous wedge reflect the (locally) averaged amount of water that has leaked through it. The actual elevations of the tips of the jets that have flowed through the openings are given by

$$\eta_j(x,t) = (\gamma\, \tan\beta - 1)\, \frac{x}{\gamma} + \frac{U\,t}{\tau}\, \left(1 - \frac{x}{\gamma\, U\, t}\right)\, \left[1 - \tau + E\left(\frac{x}{\gamma\, U\, t}\right)\right]$$

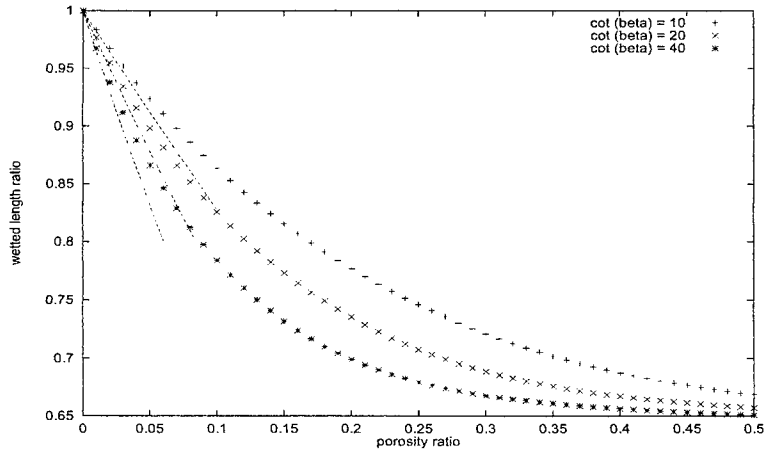

Figure 2: Porous wedge. Wetted length ratio $\gamma(\tau)/\gamma(0)$ as a function of the porosity ratio τ, for different deadrise angles.

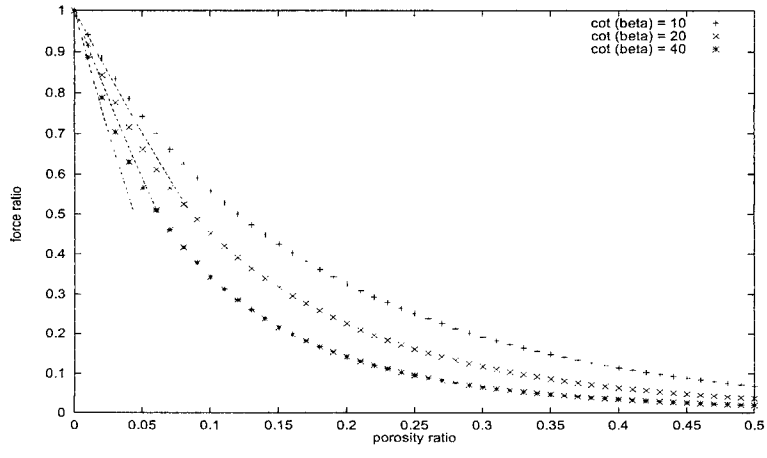

Figure 3: Porous wedge. Vertical force ratio $f_y(\tau)/f_y(0)$ as a function of the porosity ratio τ, for different deadrise angles.

The profiles related to a solid wedge ($\alpha = \infty$) are also shown, as obtained analytically and with the proposed numerical method; it can be seen that they are in fair agreement.

Then we give results relative to three deadrise angles β such that $\cot\beta$ takes the values 10, 20 and 40. The discharge coefficient μ is taken equal to 0.5. Figure 2 gives the wetted length ratio $\gamma(\tau)/\gamma(0)$ for porosity factors τ ranging from 0 (solid wedge) to 0.5. Figure 3 gives the vertical force ratio $f_y(\tau)/f_y(0)$. Also shown on these figures are the values provided by the asymptotic expressions given above, with a fair agreement at low porosity ratios. It can be observed that a porosity of 10 % reduces the force by a factor of 3 for the flattest wedge, as compared to the solid case. With 20 % porosity the reduction factor comes up to 7.

Reference

Molin B. 1992 Motion damping by slotted structures. In *Hydrodynamics: Computations, Model Tests and Reality, Developments in Marine Technology, 10.* Elsevier.

Waves Generated by Ship Motions

M. Ohkusu
Research Institute for Applied Mechanics, Kyushu University, Japan

1 Introduction

I am interested in seeing actual radiation waves or diffraction waves of ships at constant forward speed. One reason is that the wave pattern of those waves, let alone the quantitative information of the contour of the wave pattern, is not visible at usual tank test; the Kelvin wave pattern and the incident waves prevent us from seeing them. It is interesting not only for its own sake (for example Cao, Shultz and Beck (1994)) but practically; the damping of ship motions and added resistance in waves are direct results of those waves. My second interest is to know if our theoretical methods are capable of predicting accurately the contour of the wave pattern of radiation and diffraction waves. This will be a crucial issue in studies of ship motion theory.

Purpose of my study is to visualize instanteneous contour of the dynamic radiation wave pattern measured at tank test and to compare the measured contour with the one theretically predicted.

2 Computarized measurement of the wave contour

Our technique is able to visualiza the instanteneous contour of unsteady free surface elevation around a ship model moving at forward speed and oscillating at a frequency. Idea of this technique is briefly described below (see Ohkusu and Wen (1996) for the details). Wave is recorded with several wave probes continuously during a run of the experiment; their locations are fixed to the water tank and set on a line paralell to the ship model track with an equal distance between the neiboring probes. The wave probes move relatively in the reference frame fixed to the average position of the ship model (the ship reference frame) as it runs at a constant forward speed U. The wave probes reach an identical position P in the ship reference frame at different time instants. Adopt the wave record of each probe at the time instant when it reaches the location P, then we have wave records at a location P at sveral different time instants. Those wave records will determine $\zeta_0(x,y)$ (the Kelvin wave), $\zeta_1(x,y)$ (the fundamental harmonics of the radiation wave) and $\zeta_2(x,y)$ (the second harmonics) of the total wave elevation around the ship model $\zeta(x,y,t)$:

$$\zeta(x,y,t) = \zeta_0(x,y) + \zeta_1(x,y)e^{i\omega t} + \zeta_2(x,y)e^{i2\omega t} + \cdots \tag{1}$$

The wave probes record the wave elevation continuously and consequently the determination of $\zeta_{0,1,2}$ will be done at any location on the line i.e.we can determine the steady wave elevation and the amplitude and phase of the unsteady wave elevation everywhere on the line at a distance from the ship model's track. This process is feasible by the computer involvement.

The measurement is repeated at another line of the wave probes with different distance from the ship model's track. Repeatability of the measurement is confirmed and accurate contour of the waves $\zeta_1 e^{i\omega t}$ and $\zeta_2 e^{i\omega t}$ are constructed by the results obtained when we repeat this many times.

One example of snapshots of the contour of the first order wave elevation $\zeta_1 e^{i\omega t}$ and the second order's one $\zeta_2 e^{i2\omega t}$ (all are normalized by the amplitude of the vertical motion at FP)are shown on the last page of this report. They are for S175 model forced to pitch at $\tau = \omega U/g = 1.446$ and the amplitude of about 2.2° (the amplitude of the vertical motion at FP is about 30 percent of the draft) towed at the Froude number $F_n = 0.275$. It is concluded from the results of experiment at two different amplitude of pitch that ζ_1 is certainly the first order wave elevation and ζ_2 the secodn order wave (even if some other order effect is included, it will be very small). The upper part of the first order wave is the wave contour at $\omega t = 0$ and the lower part the wave contour at $\omega t = \pi/2$. For the second order wave, the upper is at $2\omega t = 0$ but the lower at $2\omega t = \pi/2$.

One wave system significant in the first order wave pattern: the wave peaks are on a diagonal line emanating from the ship; the diagonal line makes about 21° with the ship's track. This angle as well as the " wave lenght " of the peaks is in agreement with that of the asymptotic wave pattern of the longer wave component (k_2-wave). Two wave systems will be seen in the second order wave pattern. One is on a diagonal line of the angle 21° which is the same as in the first order k_2-wave. Other is on a digonal line of 13.5° which is the angle of the asymptotic k_2 wave pattern if we assume the frequency of the motion as 2ω and the linear dispersion relation.This is true in terms of the wave length of the peaks on the diagonal line. The former wave system is interpreted by an analogy of the Stokes waves as the bound wave component mainly resulting from the nonlinerity in the free ayrface condition and the latter the free wave component due to the body nonlinearity. It must be discussed in the comparison with the theoretical prediction.

Another significant result seen in the wave contours is that the second order wave elevation is as large as 25percent of the first order wave elevation. This will be discussed in terms of the theoretical prediction.

3 Theoretical prediction

We assume that the steady flow around the ship is uniform flow U into the x direction. Another assumption is that two small parameters, the slenderness parameters ε and the motion amplitude δ, are independent of each other; when we are concererned with, for example, δ^2 terms, we retain the terms of the lowest order with respect to ε .

We may assume the derivative of any flow quantity f in the x direction is higher order than the derivatives into the y and z in terms of ε. Yet we retain $U\partial f/\partial x$ in the free surface conditions because of high speed U of the ship. As a consequence we may employ $2.5D$ approach. One way is to analyze fully nonlinear flow and to take ω and 2ω components to compare with each component of the measured wave field presented in the previous section. However here our analysis is rather by classical perturbation expansion in terms of δ. It is for better understanding of the behavior of the second order wave elevation separately and the convenience of direct comprison with the measured wave pattern of the second order. Velocity potentilal ϕ and wave elevation ζ will be written in the form

$$\phi = \phi_1 + \phi_2, \qquad \zeta = \zeta_1 + \zeta_2$$

Here we consider that the terms ϕ_2 and ζ_2 are of higher order than the first terms with respect to δ.

From now on we are concerned only with the oscillatory part of the flow i.e. we understand hereafter that $\phi_{1,2}$ and $\zeta_{1,2}$ represent the oscillatory parts of the flow. Our analysis is in the frequency domain and everything of the first order is oscillating at the frequency ω. Then it is readily shown that we may put

$$\phi_j(x,y,z) = \psi_j(x,y,z)e^{-ij\omega x/U+ij\omega t}, \quad \zeta_j(x,y,z) = \eta_j(x,y,z)e^{-ij\omega x/U+ij\omega t} \qquad j = 1,2 \qquad (2)$$

Substitution of those expressions into the first and second order free surface conditions respectively will derive the conditons for $\psi_{1,2}$ and $\eta_{1,2}$ on $z = 0$

$$U\psi_{1x} = -g\eta_1, \quad U\eta_{1x} = \psi_{1z} \qquad (3)$$

$$U\psi_{2x} = -g\eta_2 - \frac{U}{2}\eta_1\psi_{1zx} - \frac{1}{4}(\psi_{1y}^2 + \psi_{1z}^2), \quad U\eta_{2x} = \psi_{2z} - \frac{1}{2}\psi_{1y}\eta_{1y} - \eta_1\psi_{1zz} \qquad (4)$$

Subscripts x,y and z denote the differentiation into the respective direction. In deriving (4) we have retained the lowest order terms of ε among the terms of δ^2. The same reasoning leads to the govering equation in fluid

$$\psi_{jyy} + \psi_{jzz} = 0 \quad j = 1,2 \qquad (5)$$

The body boundary conditions are derived in the same manner based on the same assumptions.

$$\psi_{1n} = -\delta[(x - x_0)i\omega + F_n]n_z e^{i\omega x/U} \tag{6}$$

$$\psi_{2n} = 0.5\delta^2(x - x_0)n_z\psi_{1zz}e^{i2\omega x/U} \tag{7}$$

The body conditions (6) and (7) are both imposed on the surface of the ship at the equilibrium position. n is the normal directed to the fluid on the ship's sectional contour and n_z is the z component of the normal. x_0 is the x coordinate of the longituidinal center of mass around which the pitch motion is defined. The formulation above is under the condition that the ship form is wall sided i.e. the hull surface intersects vertically the $z = 0$ plane.

Equations (4) and (7) suggest that ψ_2 and η_2 will be decomposed into two parts, one part satisfying the homogeneous free surface conditions corresponding to (3) and the body condition (7), and other part sastisfying the free surface condition (4) and the homogeneous body condition (7) with the right hand side replaced by 0. The former will be understood as the free wave part due to the body nonlinearity and the latter the bound part due to the free surface nonlinearity.

Numerical implementation of this approach for ϕ_1 is straightforward and well known. The 2nd order Runge-Kutta scheme was used to forward the solution from one section to next section; behavior of ψ_1 on $z = 0$ away from the body surface ($|y| > 0.5L$) is approximated by vertical dipole behavior; intial condition at the bow $x = 0$ for the marching is $\psi_1 = \eta_1 = 0$ (This must be improved in future while it doee not have a serious effect with a slender hull form of S175).

After ψ_1 and η_1 are obtained, we solve for ψ_2 and η_2 in almost similar manner. Equations (4) is integrated to forward ψ_2 and η_2. We need to evaluate the forcing terms due to ψ_1 and η_1 on the right hand side. We must rely on numerical differentiation for evaluating ψ_{1zx} for ψ_{1z} given on $z = 0$. We evaluated ψ_{1zz} by solving a new boundary value problem for ψ_{1z} when ψ_{1z} is prescribed on both the ship section and the free surface.

The condition imposed for ψ_2 at large $|y|$ is determined as follows. The forcing terms bahavior at large $|y|$ are known because ψ_1 bahves as a vertical dipole. For ψ_2 we assume the slowest attenuation expected from the forcing terms on the right hans side of (4) at large $|y|$ i.e. the same behavior as ψ_1.

Numerical treatment of the singularity of the velocity potential at the intersection of the body surface and $z = 0$ will be crucial for the computation of the second order component, which will be discussed at the Workshop.

Wave elevation computed by this approach is compared with the measured wave elevation presented in the previous section. The predicted of the first order wave contour is apprently in good agreement with the measured but not quantitatively with the second order wave contour. The details of the results will be presented at the Workshop

References

(1) Cao YS, Shultz W and Beck R (1994) Inner-angle Wavepackets in an Unsteady Wake, Proc.19th ONR Symposium, Seoul

(2) Ohkusu M and Wen G (1996) Radiation and Diffraction Waves of a Ship at Forward Speed, Proc.22nd ONR Symposium,Trondheim

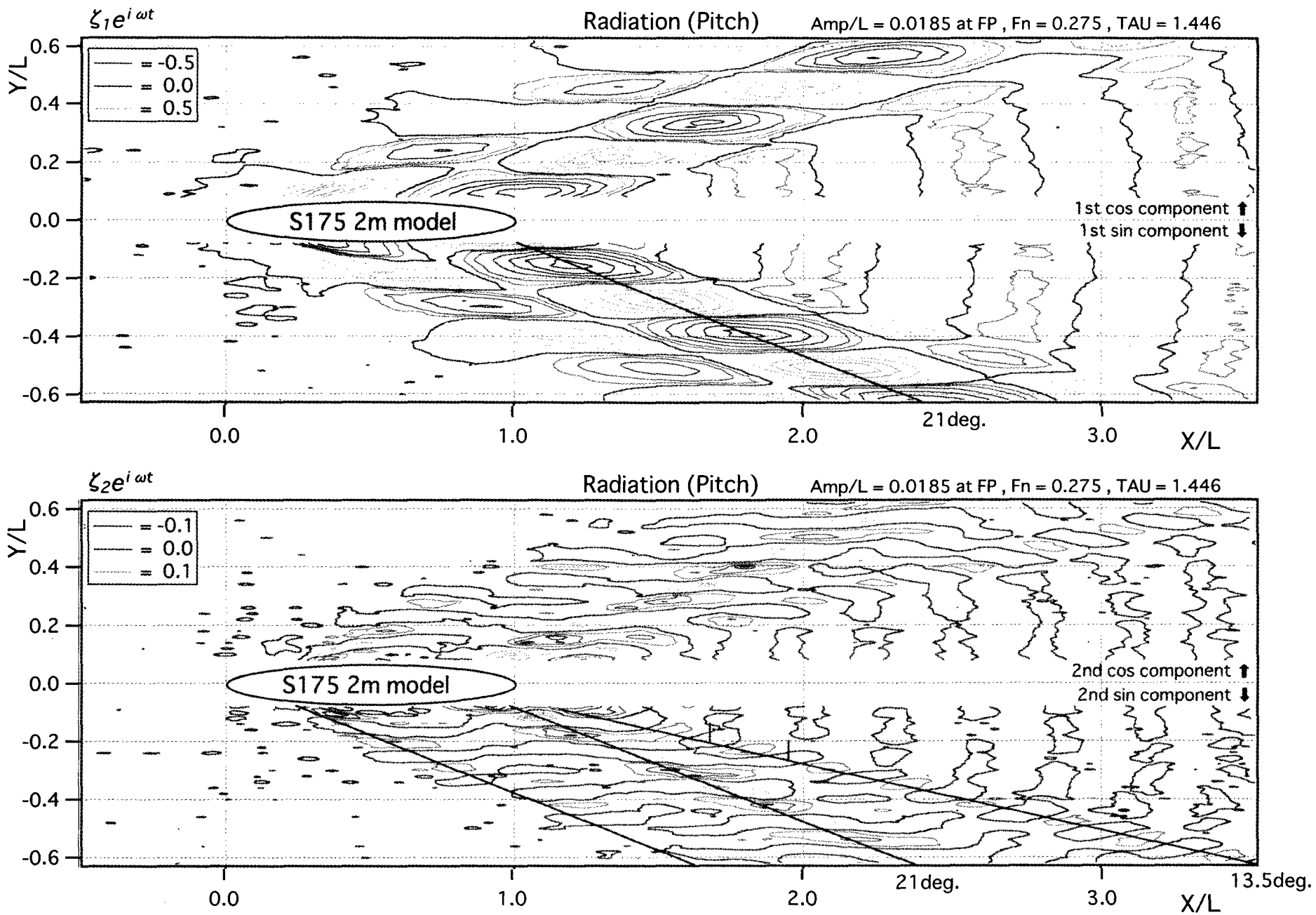

Figure Measured Wave Contour

A Panel-Free Method for the Time-Domain Radiation Problem

W. Qiu[1] and C.C. Hsiung[2]
[1] Martec Limited, CANADA
[2] Centre for Marine Vessel Development and Research, Dalhousie University, CANADA

1. INTRODUCTION

Based on the desingularized Green's formula of Landweber & Macagno (1969), a method has been developed to solve the radiation problem of a floating body in the time domain. In this method, the singularity in the Rankine source of the Green function is removed. The body surface is mathematically represented by Non-Uniform Rational B-Spline (NURBS) surfaces. Thus, the integral equation can be globally discretized over the body surface by Gaussian quadrature. We call this method as the panel-free method (PFM). The accuracy of PFM based on the NURBS surface representation was demonstrated by its application to a classical problem of uniform flow past a sphere. Computed impulse response function, added-mass and damping coefficients of a hemisphere at zero speed are compared with other published results.

2. MATHEMATICAL FORMULATION

For the radiation problem of a floating body with forward speed U_0 in the time domain, the potential function, $\phi(P;t)$ can be represented as a source distribution as follows:

$$\phi(P;t) = \int_0^t d\tau \int_{\bar{S}_b} G(P,Q;t-\tau)\sigma(Q;\tau)dS + \frac{U_0^2}{g}\int_0^t d\tau \oint_\Gamma n_1 G(P,Q;t-\tau)\sigma(Q;\tau)dl \tag{1}$$

where $\bar{S}_b$ is the mean wetted surface, Γ denotes the waterline, n_1 is the x-component of the inner unit normal vector $\mathbf{n}$ which points into the body surface, and the time-dependent Green function is given by (Wehausen & Laitone 1960, Eq. (13.49)):

$$G(P,Q;t-\tau) = -\frac{1}{4\pi}(\frac{1}{r}-\frac{1}{r_1})\delta(t-\tau) + F(P,Q;t-\tau)H(t-\tau) \tag{2}$$

with

$$F(P,Q;t-\tau) = -\frac{1}{2\pi}\int_0^\infty \sqrt{gk}\sin[\sqrt{gk}(t-\tau)]e^{k(z+z')}J_0(kR)dk \tag{3}$$

where r and r_1 are distances between $P(x,y,z)$ and $Q(x',y',z')$, and P and the image point Q' of Q, $R = \sqrt{(x-x')^2+(y-y')^2}$, J_0 is the Bessel function of the zeroth order, and $\delta(t-\tau)$ and $H(t-\tau)$ are the delta function and the Heaviside step function, respectively. The source strength, σ, can be solved from

$$V_n(P;t) = -\frac{1}{2}\sigma(P;t) + \int_0^t d\tau \int_{\bar{S}_b} \frac{\partial G(P,Q;t-\tau)}{\partial n(P)}\sigma(Q;\tau)dS + \frac{U_0^2}{g}\int_0^t d\tau \oint_\Gamma n_1 \frac{\partial G(P,Q;t-\tau)}{\partial n(P)}\sigma(Q;\tau)dl \tag{4}$$

For a floating body, if the waterline integral is omitted, Eq.(4) can be desingularized as follows:

$$V_n(P;t) = -\sigma(P;t) + \int_{\bar{S}_b}\left[\sigma(Q;t)\frac{\partial G_1(P,Q)}{\partial n(P)} - \sigma(P;t)\frac{\partial G_1(P,Q)}{\partial n(Q)}\right]dS \tag{5}$$
$$+2\int_{\bar{S}_b}\sigma(Q;t)\frac{\partial G_2(P,Q)}{\partial n(P)}dS + \int_0^t d\tau\int_{\bar{S}_b}\frac{\partial F(P,Q;t-\tau)}{\partial n(P)}\sigma(Q;\tau)dS$$

The LHS of Eq.(5) is known from the body boundary condition, and $G_1(P,Q) = -1/(4\pi)(1/r + 1/r_1)$ and $G_2(P,Q) = 1/(4\pi r_1)$. The source strength can be obtained by solving Eq.(5). Based on the work by Landweber and Macagno, the non-singular representation for the velocity potential can be derived as follows:

$$\phi(P;t) = \int_{\bar{S}_b} G_1(P,Q)\left[\sigma(Q;t) - \gamma(Q)\frac{\sigma(P;t)}{\gamma(P)}\right]dS + 2\int_{\bar{S}_b}\sigma(Q;t)G_2(P,Q)dS + \frac{1}{4\pi}\phi_0\frac{\sigma(P;t)}{\gamma(P)} \tag{6}$$

$$+\int_0^t d\tau \int_{\bar{S}_b} \sigma(Q;\tau)F(P,Q;t-\tau)dS$$

where $\gamma(P)$ is the source distribution on $\bar{S}_b$ which makes the body surface an equipotential surface of potential ϕ_0 and satisfies the homogeneous integral equation

$$\gamma(P) = \int_{\bar{S}_b} \gamma(Q)\frac{\partial K(P,Q)}{\partial n(P)}dS \tag{7}$$

Equation (7) can be desingularized in a similar way as Eq.(5), and $\gamma(P)$ can be solved by finding the eigenfunction of $\partial K(P,Q)/\partial n(P)$ with the eigenvalue equal to 1, where $K(P,Q) = 1/(2\pi)(1/r + 1/r_1)$. The potential, ϕ_0, is constant in the interior of the equipotential surface. It can be computed at the origin by $\phi_0 = -\int_{\bar{S}_b} \gamma(Q)(1/|Q| + 1/|Q'|)dS$, where $|Q|$ and $|Q'|$ denote distances between Q and the origin, and Q' and the origin, respectively.

3. NUMERICAL IMPLEMENTATION

It is assumed that N_p patches are used to describe a body surface. Each patch can be represented by a NURBS surface (Farin, 1991). Let $P(x(u,v), y(u,v), z(u,v))$ be a point on a patch; x, y and z denote the Cartesian coordinates; and u and v are two parameters for the surface definition. On a NURBS surface, $P(u,v)$ can be defined as follows:

$$P(u,v) = \frac{\sum_{i=0}^{n}\sum_{j=0}^{m} w_{ij}C_{i,j}N_{i,p}(u)N_{j,q}(v)}{\sum_{i=0}^{n}\sum_{j=0}^{m} w_{ij}N_{i,p}(u)N_{j,q}(v)} \tag{8}$$

where w_{ij} are the weights; $C_{i,j}$ form a network of control points; and $N_{i,p}(u)$ and $N_{j,q}(v)$ are the normalized B-splines basis functions of degrees p and q in the u and v directions, respectively.

Since Eq.(5) is singularity free, it can be discretized by directly applying the Gaussian quadrature and the trapezoidal time integration scheme. The Gaussian quadrature points are arranged in the computational space, rs, then their corresponding coordinates, normals, Jacobian in the physical space can be obtained based on Eq.(8). Therefore, the Eq.(5) can be written as

$$V_n(P_i;t) = -\sigma(P_i;t) + \sum_{j=1}^{N_p}\sum_{r=1}^{N_j}\sum_{s=1}^{M_j} w_r w_s \left[\sigma(Q_j^{rs};t)\nabla_P G_1(P_i,Q_j^{rs})\cdot\mathbf{n}_{p_i} + \sigma(P_i;t)\nabla_P G_1(P_i,Q_j^{rs})\cdot\mathbf{n}_{q_j^{rs}}\right] J_j^{rs} \tag{9}$$

$$+2\sum_{j=1}^{N_p}\sum_{r=1}^{N_j}\sum_{s=1}^{M_j} w_r w_s \sigma(Q_j^{rs};t)\nabla_P G_2(P_i,Q_j^{rs})\cdot\mathbf{n}_{p_i}J_j^{rs}$$

$$+\Delta t\left[\frac{1}{2}\sum_{j=1}^{N_p}\sum_{r=1}^{N_j}\sum_{s=1}^{M_j} w_r w_s \sigma(Q_j^{rs};0)\frac{\partial F(P_i,Q_j^{rs};t)}{\partial n}J_j^{rs} + \sum_{k=1}^{k_t-1}\sum_{j=1}^{N_p}\sum_{r=1}^{N_j}\sum_{s=1}^{M_j} w_r w_s \frac{\partial F(P_i,Q_j^{rs};t-t_k)}{\partial n}\sigma(Q_j^{rs};t_k)J_j^{rs}\right],$$

$$i = 1,2,...,N_p$$

where N_j and M_j are the number of Gaussian quadrature points in the u- and v-directions on the jth patch. $P_i = P_i(u_n, v_m), n = 1,...N_i, m = 1,...M_i$ and $Q_j^{rs} = Q_j(u_r, v_s)$ are the position vectors of Gaussian quadrature points on the ith and jth patches in the physical space, respectively; $\mathbf{n}_{p_i}$ and $\mathbf{n}_{q_j^{rs}}$ are the corresponding unit normals; w_r and w_s are the weighting coefficients in the u and v directions; J_j^{rs} is the Jacobian of Q_j^{rs}; t is the time; and Δt is the time step, $t_k = k\Delta t$ and $t = k_t\Delta t$, where k and k_t are the time constants at any instant and for the total time, respectively. It can be seen that the algorithm is only controlled by the number of Gaussian quadrature points.

4. NUMERICAL RESULTS

Since the singularity occurs only in the $1/r$ term, it is important to validate the desingularization of the integral equation with the $1/r$ term only before it is applied to the time-domain integration. The numerical scheme was

applied to the problem of uniform flow ($U = -1.0$) past a sphere surface ($R = 1.0$). Due to the symmetry, only one-half of the surface was considered. In Figure 1, the dashed lines represent the control net of NURBS with 5x5 control points on one of patches ($N_p = 2$). The solid meshes are the surface of one-quarter of the sphere generated by the control net. The disturbed velocity potentials at the Gaussian quadrature points were computed using both NURBS and analytical expressions of the surface. The numerical testing was also conducted to investigate the convergence of numerical solution to the number of Gaussian quadrature points (NxN) over the hemisphere. The root-mean-squared (RMS) errors of computed velocity potentials based on the analytical expression and the NURBS representation of the surface are shown in Figure 2. It is shown that the computed velocity potentials converge to the analytical solution as the number of Gaussian quadrature points increased. The RMS error of the solution based on the NURBS representation is less than 1% when 10x10 Gaussian quadrature points are applied.

The panel-free method was applied to compute the response function for a hemisphere (R=5.0m) in heave. Figure 3 shows the nondimensional response function, $K_{33}(t)/(\rho\nabla)\sqrt{R/g}$, versus nondimensional time, $t\sqrt{g/R}$, for different Gaussian quadrature points used on the hemisphere, where R is the radius of the sphere and ∇ is the volume displacement. The time step was chosen as 0.05 second. The circle points give the analytic solution of Barakat (1962) obtained by the Fourier transformation from his frequency-domain results.

The nondimensional response function for the heaving hemisphere was also computed using different time steps with 16x16 Gaussian quadrature points. As shown in Figure 4, PFM is insensitive to the size of time steps. Figure 5 and Figure 6 present the added-mass and damping coefficients versus the nondimensional frequency for the hemisphere in heave. The numerical results were obtained by Fourier transformation from the response function using 16x16 Gaussian points as shown in Figure 3, and the analytical results were from Barakat (1962). Also in these figures, the frequency, the added-mass and the damping coefficients are nondimensionalized as $\omega^2 R/g$, $A_{33}/(\rho\frac{2}{3}\pi R^3)$ and $B_{33}/(\omega\rho\frac{2}{3}\pi R^3)$, respectively.

5. CONCLUSIONS

The panel-free method has been developed to solve the radiation problem of a hemisphere at zero speed in the time domain. The boundary integral equation in terms of source strength distribution is desingularized so that the Gaussian Quadrature can be directly applied to the exact body surface. Compared with the panel method, the advantages of PFM are: a) less numerical manipulating, since panelization of a body surface is not needed; b) more accurate, since the assumption for the configuration of source strength distribution as in the panel method is not needed and no approximation of surface geometry is involved; c) the Gaussian quadrature points, and their respective Jacobian and normals on the surface can be accurately computed from the NURBS expression; and d) the accuracy of the solution is controlled only by the number of Gaussian quadrature points. This method is currently being applied to the computation of ship motions in the time domain. The wave diffraction effect is also considered.

ACKNOWLEDGMENTS

This work was supported by the Natural Science and Engineering Research Council, Canada. Useful discussions with Dr. J.M. Chuang are also appreciated.

REFERENCES

BARAKAT, R.: *Vertical Motion of a Floating Sphere in a Sinewave Sea*, Journal of Fluid Mechanics, Vol.13, pp.540-556 (1962).

FARIN, G. E.: *NURBS for Curve and Surface Design.* SIAM Activity Group on Geometric Design (1991).

LANDWEBER, L. and MACAGNO, M.: *Irrotational Flow about Ship Forms*, IIHR Report, No. 123, Iowa (1969).

WEHAUSEN, J.V. and LAITONE, E.V.: *Surface Waves* in *Handbuch der Physik* (ed. S. Flügge), Springer-Verlag, Vol. 9 (1960).

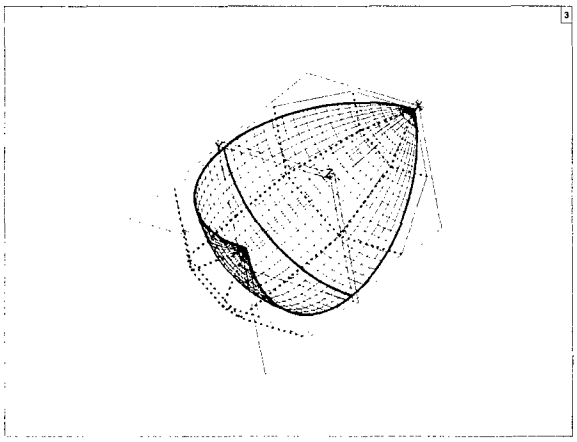

Figure 1: Sphere surface and control points

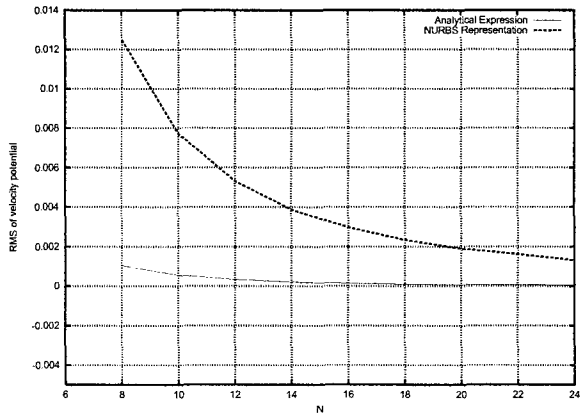

Figure 2: Convergence of numerical solution to the number of Gaussian quadrature points

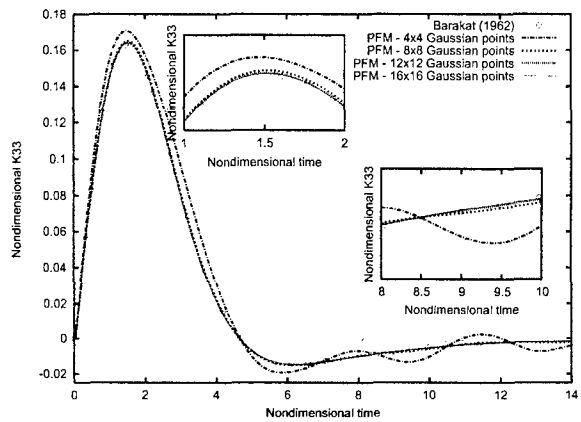

Figure 3: Nondimensional heave response function on a hemisphere versus nondimensional time ($\Delta t = 0.05s$)

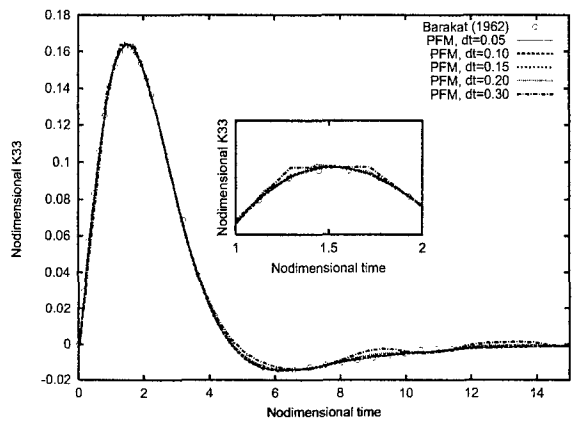

Figure 4: Nondimensional heave response function on a hemisphere versus nondimensional time (16x16 Gaussian points)

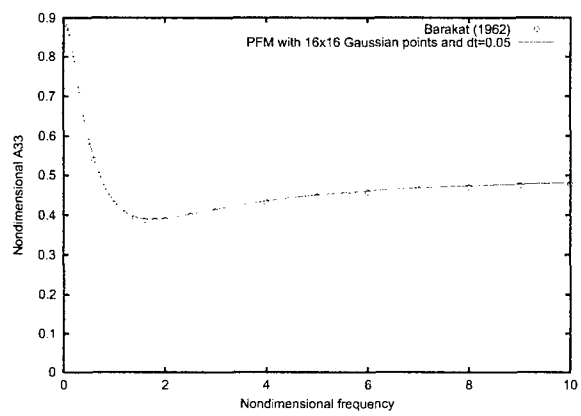

Figure 5: Nondimensional added-mass for a hemisphere in heave versus nondimensional frequency ($\Delta t = 0.05s$, 16x16 Gaussian points)

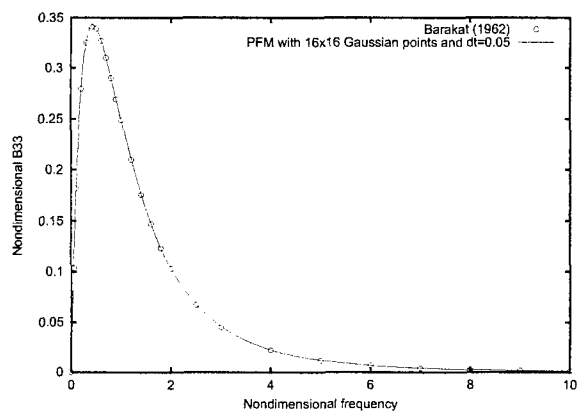

Figure 6: Nondimensional damping coefficient for a hemisphere in heave versus nondimensional frequency ($\Delta t = 0.05s$, 16x16 Gaussian points)

THE PELAMIS WAVE ENERGY CONVERTER: IT MAY BE JOLLY GOOD IN PRACTICE, BUT WILL IT WORK IN THEORY?

R.C.T.RAINEY WS Atkins Oil & Gas, Berkshire House, 171 High Holborn, London WC1V 7AA

1. Background

The design of wave energy converters (WECs) has hitherto concentrated primarily on hydrodynamic efficiency, see the 1985 review by David Evans [1] (1985). The Pelamis WEC is a promising new concept which is designed instead primarily for survival in extreme seas. This is accomplished by its end-on orientation to the waves, which enables the WEC negotiate breaking waves safely, and by its relatively small diameter (3.5m), which non-linearly limits power output in extreme conditions. See Figure 1 below – further details are on the website www.oceanpd.com.

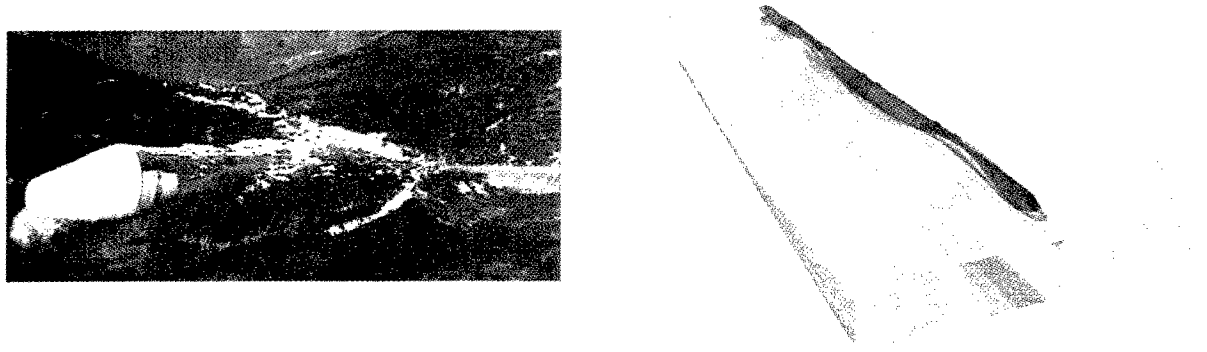

Figure 1. The Pelamis wave energy converter

The power take-off is from hydraulic jacks at the articulated joints - the hydrodynamic efficiency of the device has been optimised empirically, by extensive model testing and numerical modelling. It has been found that the efficiency is greatly improved by making the transverse motions resonant (by suitable choice of transverse stiffness at the joints), and coupling them to the vertical motions (by introducing suitable coupling terms in this stiffness). All this may be excellent in practice, but will it work in theory?

2. The waves generated by a single segment in isolation.

The theory of wave power absorption is concerned with the waves generated by the WEC. For a single segment of Pelamis in isolation, these may readily be found with a 3-D diffraction program. Figure 2 below shows a surface element mesh generated by the WS Atkins program AQWA-LINE (which gives substantially identical results to MIT's program WAMIT, see [2]). The segment is 3.5m diameter, 30m long with uniform density, and floating freely exactly half immersed in water of infinite depth (and density $\rho = 1.000$ tonne/m^3 with $g = 10.00$ m^2/s).

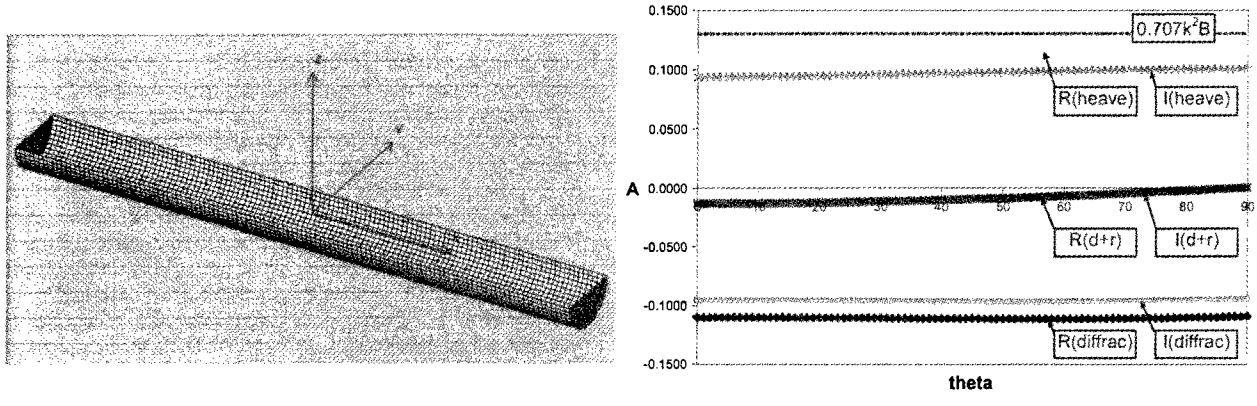

Figure 2. Analysis of a single segment with the diffraction program AQWA-LINE.

Figure 2 also shows the amplitude of the various waves produced by the segment. In this paper we characterise any waves propagating away to infinity by the complex function $A(\theta)$, from which the elevation of the waves at great distance is defined as:

$$\Re\left\{\frac{A(\theta)ae^{i(kR-\omega t)}}{\sqrt{2\pi kR}}\right\} \tag{1}$$

This is because in the polar coordinates (R, θ) these waves will ultimately decay inversely as the square root the distance R from the centre of the device, by energy conservation. The incident waves are assumed to travel in the direction $\theta = 0$ in the sense of increasing R, and to have angular frequency ω and wave number k. Finally a is the complex amplitude of the motion responsible for the waves of (1). Thus when we consider free-floating behaviour in incident waves, $\Re\{ae^{-i\omega t}\}$ is the elevation of the incident waves at the centre of the segment. And when we consider heave motion in still water $\Re\{ae^{-i\omega t}\}$ is the heave motion (positive upwards).

Figure 2 gives results (diffracted and diffracted+radiated waves) with the segment in incident waves 150m long (i.e. as long as all five segments of Pelamis combined) and also for heave motion in still water, at the same frequency. In the first case the diffracted+radiated waves are much smaller than the diffracted wave alone, so the segment is following the incident waves like a small raft, so as to be almost transparent to them. For the heave motion the waves are almost equal and opposite to the diffracted waves. Since the heave motion in waves is almost equal to the incident wave elevation (94% of its amplitude according to AQWA-LINE, and within 0.02 degrees of its phase), we may deduce that in the former case it is the waves radiated by the heave motion that are cancelling the diffracted waves.

Theoretically ([3] eqn 24b), $A(\theta)a$ for heave motion is equal to $-i\omega H(\theta)e^{i\pi/4}/g$, where $H(\theta)$ is the 'Kochin function' ([3] eqn 17). In our case of long waves $H(\theta)$ may be approximated without difficulty as $-k(-i\omega a)B$, where B is the waterplane area of the segment. This leads to a value of $A(\theta) = k^2Be^{i\pi/4}$, which is shown in Figure 2, and agrees correctly with the computations. See also [4] eqn 10 - the more sophisticated slender-body approximation there will in fact recover the θ-dependence seen in Figure 2. For present purposes it is sufficient to observe that this dependence is small, and that the amplitude of the waves radiated by heave motion is proportional to the waterplane area B.

3. Energy flux in the far field: single segment

Hitherto the segment has been floating freely; we are now in a position to assess the effect of incorporating a power take-off so as to extract some wave energy. We will depart from the earlier literature cited above by considering the energy flux in the far field directly. Since the freely-floating segment is practically transparent to the waves, and the only significant wave radiation is from heave motion, we will take the far field waves produced by the segment (the 'produced waves') as being simply those due to the *additional heave motion compared with the freely-floating segment.* Thus in (1) we will take $\Re\{ae^{-i\omega t}\}$ is this additional heave motion (positive upwards), and denote the incident wave elevation at the centre of the segment as $\Re\{be^{-i\omega t}\}$.

The mean energy flux in the far field is the product of the wave pressure and the wave velocity, integrated over a fixed cylindrical control surface where R has some large value R_c, say. The product of wave velocity and hydrostatic pressure does not count because it is purely oscillatory, and the flux of kinetic energy does not count because it is of higher order in wave height. The mean value of the product of any two complex oscillatory variables a and b is $\frac{1}{2}\Re(\bar{a}b)$, so if the incident and produced complex wave pressures are p_I and p_P, and their complex velocities into the control surface are v_I and v_P, the mean energy flux into the control surface is:

$$\int_{-\pi}^{\pi}\tfrac{1}{2}\Re\left\{\overline{(p_I+p_P)}(v_I+v_P)\right\}R_c\frac{d\theta}{2k} \tag{2}$$

Here the variables are taken at the still-water position, the depth integration having yielded the factor $1/(2k)$. We now observe that:

- The p_Iv_I term must integrate to zero because there is zero mean energy flux from the incident waves alone
- The p_Pv_P term must always give an energy loss because the produced waves are leaving the system
- The cross terms must therefore be the source of any energy input

Dealing with energy loss term first, and taking $A(\theta) = k^2 B e^{i\pi/4}$ as above, this is readily integrated as:

$$\int_{-\pi}^{\pi}\frac{1}{2}\Re\left\{\overline{\{(\rho g\frac{k^2 B a e^{i(kR_c+\pi/4)}}{\sqrt{2\pi kR_c}})(-\omega\frac{k^2 B a e^{i(kR_c+\pi/4)}}{\sqrt{2\pi kR_c}})\}}\right\}R_c\frac{d\theta}{2k}=-\int_{-\pi}^{\pi}\frac{\rho g\omega k^2 B^2|a|^2}{8\pi}d\theta=-\frac{\rho g\omega k^2 B^2|a|^2}{4} \qquad (3)$$

The energy input form the cross terms is:

$$\int_{-\pi}^{\pi}\frac{1}{2}\Re\left\{\overline{(\rho g b e^{ikR_c\cos\theta})}(-\omega\frac{k^2 B a e^{i(kR_c+\pi/4)}}{\sqrt{2\pi kR_c}})+(\rho g\frac{k^2 B a e^{i(kR_c+\pi/4)}}{\sqrt{2\pi kR_c}})\overline{(-\omega b e^{ikR_c\cos\theta}\cos\theta)}\right\}R_c\frac{d\theta}{2k}$$

$$=-\frac{\rho g\omega B}{2}\Re\left\{\bar{a}b\frac{\sqrt{kR_c/2}}{2\sqrt{\pi}}\int_{-\pi}^{\pi}(1+\cos\theta)e^{i(kR_c[1-\cos\theta]+\pi/4)}d\theta\right\} \qquad (4)$$

The integrand in (4) is plotted in Figure 3 below for kR_c=30.

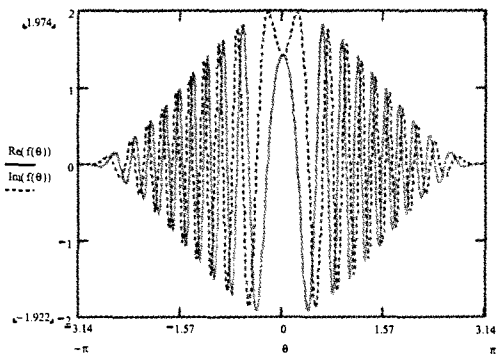

Figure 3. Angular dependence of input energy flux

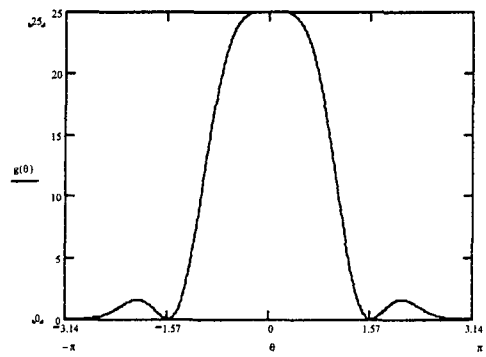

Figure 4. Angular dependence of energy loss, 5 segments

The mean energy flux evidently fluctuates rapidly around the control surface, with the significant peak being at θ = 0, i.e. downwave of the segment. This is because at that point the produced waves are travelling in the same direction as the incident waves, so that the total energy flux is proportional to the square of their combined amplitude. Depending on their relative phase, this is either greater or less than the sum of their individual amplitudes squared, so requiring a substantial cross term. At θ = ±π, on the other hand, the integrand is zero because the waves are travelling in opposite directions, and their total energy flux is thus equal to the sum of their individual fluxes (as is well-known, and can be seen from (2) given the opposite directions of the velocities under wave crests). The required integral can be found exactly by the method of stationary phase ([5] art 241). Only the energy flux around θ = 0 is significant to the integral, and (4) becomes:

$$-\frac{\rho g\omega B}{2}\Re\{a\bar{b}e^{i(\pi/4+\pi/4)}\}=\frac{\rho g\omega B}{2}\Re\{ib\bar{a}\} \qquad (5)$$

For any given $|a|$, the energy loss term (3) will be fixed, so we are at liberty to choose the phase of a as equal to that of ib, so as to maximise the energy input (5). The net energy input will then be:

$$\frac{\rho g\omega B}{2}|b||a|-\frac{\rho g\omega k^2 B^2|a|^2}{4}=\frac{\rho g\omega B}{4}(2|b||a|-k^2 B|a|^2) \qquad (6)$$

The energy input term is proportional to $|a|$ whereas the energy loss term is proportional to $|a|^2$, so the maximum net energy can easily be found to occur when $|a|=|b|/(k^2B)$ and to be:

$$\frac{\rho g\omega B}{4}\left(\frac{2|b|^2}{k^2 B}-\frac{|b|^2}{k^2 B}\right)=\left[\frac{\rho g\omega|b|^2}{4k}\right]k^{-1} \qquad (7)$$

Since the term in square brackets is the incident energy per unit length of wave crest, we have recovered the well-known result (e.g. [1] eqn 4.2) that the maximum crest 'capture width' is k^{-1} for a device radiating waves equally in all directions. However, this requires $|a|/|b| = (k^2B)^{-1} = 5.4$ in our case – since $|a|$ is limited to about 1m, this limits the wave amplitude at which this 'capture width' can be achieved, to about 20cm.

4. Energy flux in the far field: complete device

So far there is nothing new in these results. However, Figure 3 and the argument below it suggest that the design objective for the complete device should be to produce waves concentrated on a *downwave* direction ($\theta = 0$). This will maintain the energy input, which only depends on the waves produced in a downwave direction, while reducing the energy loss which depends on the waves produced in all directions. For example, an effective strategy would appear to be to arrange the additional heave motions of each segment considered above (i.e. the heave motions compared with freely floating segments – the segments will be transparent to the waves produced by other segments, just as they are to incident waves) to be phase lagged between each other in the same way as the incident wave itself. The waves produced by each segment will then interfere constructively in a downwave direction, but interfere destructively in the upwave direction. Given the five 30m segments exactly spanning a 150m wavelength, with the centre of the central one at $R=0$, the complex amplitude will in fact vary with θ as:

$$e^{-i0.8\pi(1-\cos\theta)} + e^{-i0.4\pi(1-\cos\theta)} + 1 + e^{i0.4\pi(1-\cos\theta)} + e^{i0.8\pi(1-\cos\theta)}$$

$$= 1 + 2\cos(0.4\pi[1-\cos\theta]) + 2\cos(0.8\pi[1-\cos\theta]) \qquad (8)$$

As far as the energy loss integral (3) is concerned, it is the variation of (amplitude)^2 with θ which counts; this is shown in Figure 4 above. For the same energy input, numerical integration shows that the energy loss is about one third of a single segment, which will increase the 'capture width' to about half a wavelength. Given the larger waterplane area of the complete device, moreover, the limiting wave amplitude is increased from 20cm above to 35cm. In waves of 3.5m amplitude, say (i.e. 7m height, which is quite steep for the given 150m wavelength), the capture width will reduce to about a tenth of a wavelength. This is consistent with the measured performance of the Pelamis WEC. The required large heave motions are achieved in practice by the coupling to a resonant sway mode, as described at the start of this paper. According to AQWA-LINE the sway damping force is less than 1% of the heave damping force (both per unit motion in still water), so the additional waves produced by this sway motion will be negligible.

In the earlier literature cited above, by contrast, the design aim of WECs appears to be to concentrate radiated waves (as opposed to the 'produced' waves considered above which are radiated+diffracted) in the *upwave* direction. See in particular [4] eqn (2), which applies to a device like the Pelamis WEC. The diffracted waves from the Pelamis WEC will clearly be in a downwave direction (by the argument of (8) above, in fact, which applies equally to the diffracted waves) - it is not clear how combing these with radiated waves in an upwave direction will make the Pelamis WEC produce waves downwave overall, as appears to be necessary from the arguments of this paper.

Indeed, it appears that the emphasis on radiating waves upwave has encouraged the development of WECs which are wave reflectors in the quiescent condition, like the Salter "duck". Here such a radiated wave is clearly required, to cancel the wave reflection, without introducing losses behind the WEC. From an engineering point of view, however, it is very difficult to make such a device which is also capable of surviving extreme storms.

Acknowledgement

This paper arose out of discussions with David Evans, whose help is gratefully acknowledged. I am also grateful to Drs David Pizer, Chris Retzler, and Richard Yemm of Ocean Power Delivery Ltd, for many helpful discussions.

References

[1] Evans, D.V. 1985 The hydrodynamic efficiency of wave-energy devices. Proc. IUTAM Symposium on Hydrodynamics of Ocean Wave-Energy Utilisation, ed D.V.Evans & A.F.deO.Falcao, pp1-34. Springer-Verlag.

[2] Newman, J.N. 1998 Hydrodynamic analysis of the McIver toroid. Proc. 13th International Workshop on Water Waves and Floating Bodies, Discussion p76

[3] Newman, J.N. 1976 The interaction of stationary vessels with regular waves. Proc. 11th Symposium on Naval Hydrodynamics, London pp 491-501

[4] Newman, J.N. 1980 Absorption of wave energy by elongated bodies. Applied Ocean Research

[5] Lamb, Sir H. 1932 Hydrodynamics. Cambridge University Press, 6th Ed.

EFFECT OF SLOSHING ON SHIP MOTIONS

Olav F. Rognebakke and Odd M. Faltinsen
Department of Marine Hydrodynamics
Norwegian University of Science and Technology
N-7491 Trondheim, Norway

When a ship carrying liquid cargo moves in waves, sloshing may occur. The ship motions excite sloshing which in return affects the ship motions. 2-D experiments on a box-shaped ship section excited by regular beam sea have been conducted to study this coupling effect. The section contains two tanks and can only move in sway. The external ship motion problem may be solved by using a standard linear strip theory program, while the sloshing must be described by a nonlinear method. The adaptive multimodal approach by Faltinsen and Timokha [1] has been used. This method has been extensively validated for forced tank motions. The present study represents a first validation for coupled internal and external flows.

The experiments were carried out in the wave flume of the Department of Marine Hydrodynamics at NTNU. The flume has an overall length of 13.5 m and is 0.6 m wide. It is equipped with an electronically operated, computer controlled, single flap wavemaker, calibrated for a water depth of 1.03 m. The side walls and the bottom of the flume are made of glass.

Fig. 1 shows model parameters. The ship section with an overall length of 596 mm has 2 mm clearance from the flume walls. The breadth is 400 mm and the draft 200 mm. The two identical tanks have breadth b of 376 mm, a length of 150 mm and a height of 288 or 388 mm depending on the position of the deck. The deck may be lowered when sloshing induced water impact on the tank roof is desirable. No tank roof impact occurred in the reported examples. Weights are added to the model so that the total weight equals the buoyancy for the fixed draft and different amounts of water in the tanks. The section slides along two rails where low friction bearings are used. It is restrained from drifting off by springs with a total stiffness of 30.9 N/m. The springs cause an eigenfrequency well below the studied wave frequencies. The steepness of the waves was kept below a certain threshold value to prevent breaking. Fig. 2 gives the chosen relation between frequency ω and amplitude ζ_a of the generated regular waves.

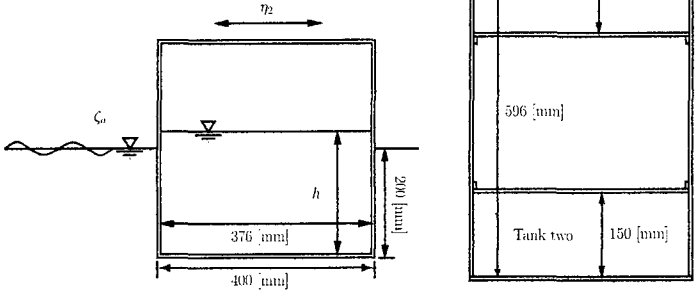

Figure 1: Box-shaped ship section, side and top view

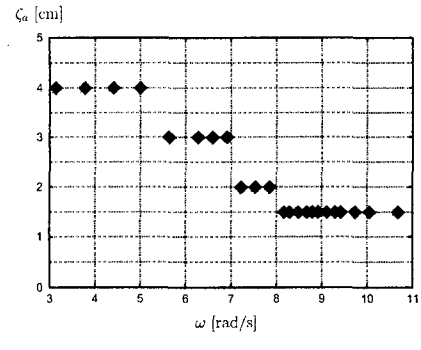

Figure 2: Relationship between wave amplitude and wave frequency

A typical time series for the sway motion of the section with water in one tank, is shown in Fig. 3. A transient phase precedes a steady state for the system. A beating period of ≈ 5 s is evident during the transient phase. This is the eigenperiod of the system consisting of the springs and the ship model. A shift in mean position of the section occurs due to 2nd order drift force. The steady state motions show almost no higher order harmonics. This indicates that the higher order part of the sloshing force is filtered out by the system. The steady state phase is short for long waves and consequently the uncertainties in measured sway amplitude increase. For wave periods very close to the first natural period of the fluid in the tanks an unstable situation may occur. The sway amplitude shifts and thus two steady state responses take place during one run. In the experimental data presented later where one tank is filled with $h = 0.184$ m, this can be seen as two very different measured sway amplitudes for a wave frequency $\omega = 8.65$ rad/s. This is associated with jumps between different branches of the steady-state sloshing solution [2]. The steady state ends when waves reflected from the wavemaker and the beach reach the model.

Measured and calculated sway amplitudes for empty tanks have been compared to validate the accuracy of the measurements, (see Fig. 4). A standard linear seakeeping program was used in the calculations. The

experimental results for rigid mass agree well with the computed values.

Fig. 4 illustrates the large effect of the fluid motion inside the tanks. When ω is smaller or slightly higher than the lowest linear eigenfrequency σ_n of the fluid motion in the tanks, a sway response lower than for a rigid fluid mass is observed for half-filled tanks. The force resulting from the fluid motion in the tanks acts against the sway excitation force in this case. When $\omega \approx \sigma_n$ the sway motion is almost zero. For ω slightly above σ_n the sway motion increases due to the fluid in the tanks. This behaviour can be qualitatively explained by using a linear model for the sloshing. The phase of the sloshing force shifts 180° when the excitation frequency moves from below to above the first natural frequency.

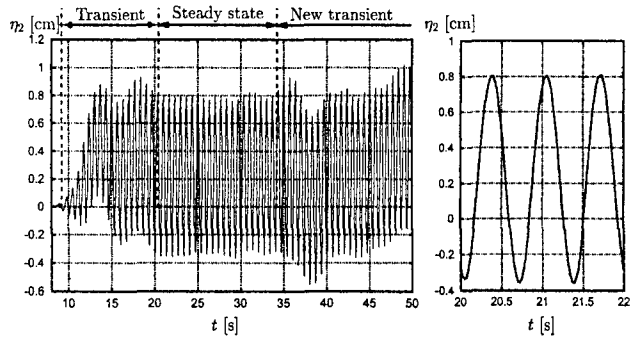

Figure 3: Example of time history of the sway motion of the ship section. $\omega = 9.42$ rad/s and $\zeta_a = 0.015$m

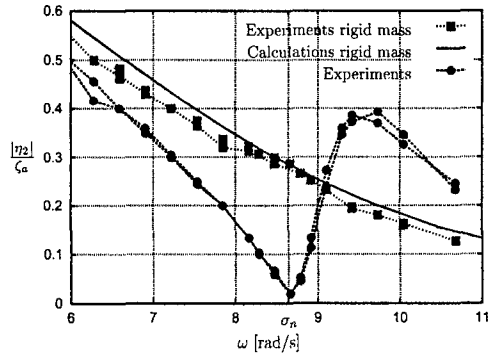

Figure 4: Sway amplitude for rigid mass and for two tanks filled with $h = 0.184$ m

The change with wave frequency of the phasing between the forces acting on the model is visually apparent from Fig. 5. The right plot in this figure gives the experimental values for sway motion when one of the tanks is filled with $h = 0.184$ m. Snapshots show the instantaneous position of the free surface both inside the tank and outside the ship section, for three different wave frequencies. The phasing between the internal and external fluid motion permits to qualitatively understand why the internal fluid motion can either amplify or reduce the ship motion. The phasing is evident from the relative vertical motion of the free surfaces inside and outside the model.

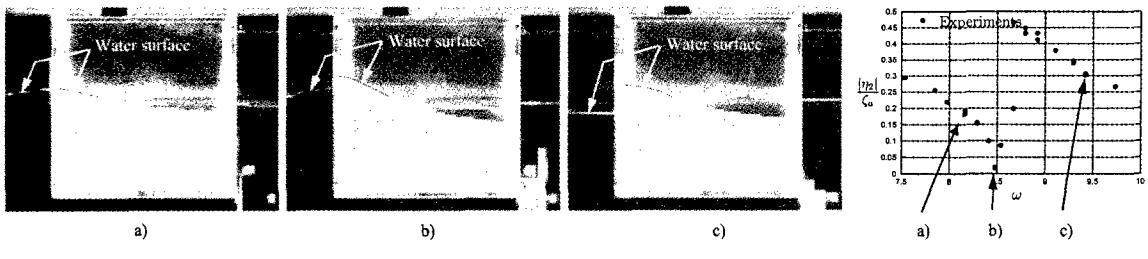

Figure 5: Motion of fluid inside and outside the tank. $h = 0.184$ m. One tank is filled

An interesting phenomenon is observed for wave frequencies close to the resonance for the fluid motion in the tanks. When the wave front hits the model, a significant sway motion is initiated. This in turn excites sloshing in the tanks, and thus a sloshing force starts to counteract the excitation force from the waves. The sway motion decreases until an equilibrium is reached. At this stage the sway induced sloshing force almost balances the excitation force from the waves. However, since $\omega \approx \sigma_n$ a very small sway motion causes a violent sloshing response.

Fig. 6 shows experimental and computed values of the sway motion of the model for different filling levels of one or two tanks. The first linear eigenfrequency σ_n is indicated in the plots. Calculated values found by using an analytical linear and nonlinear sloshing solution and a standard linear seakeeping program for the external flow are presented for all cases. The calculations based on the linear sloshing model follow the general trend of the experiments. However, the sway amplitude is consistently over-predicted for frequencies right above σ_n. The reason is that the linear sloshing force is either in phase or exactly 180° out of phase with the position of the model. Actually, the phase transition occurs over a certain range of frequencies. Furthermore, when a large percentage of the sloshing force acts in phase with the mass and added mass forces and works against them, the increased motion results in an increased sloshing force amplitude. When the frequency is equal to σ_n

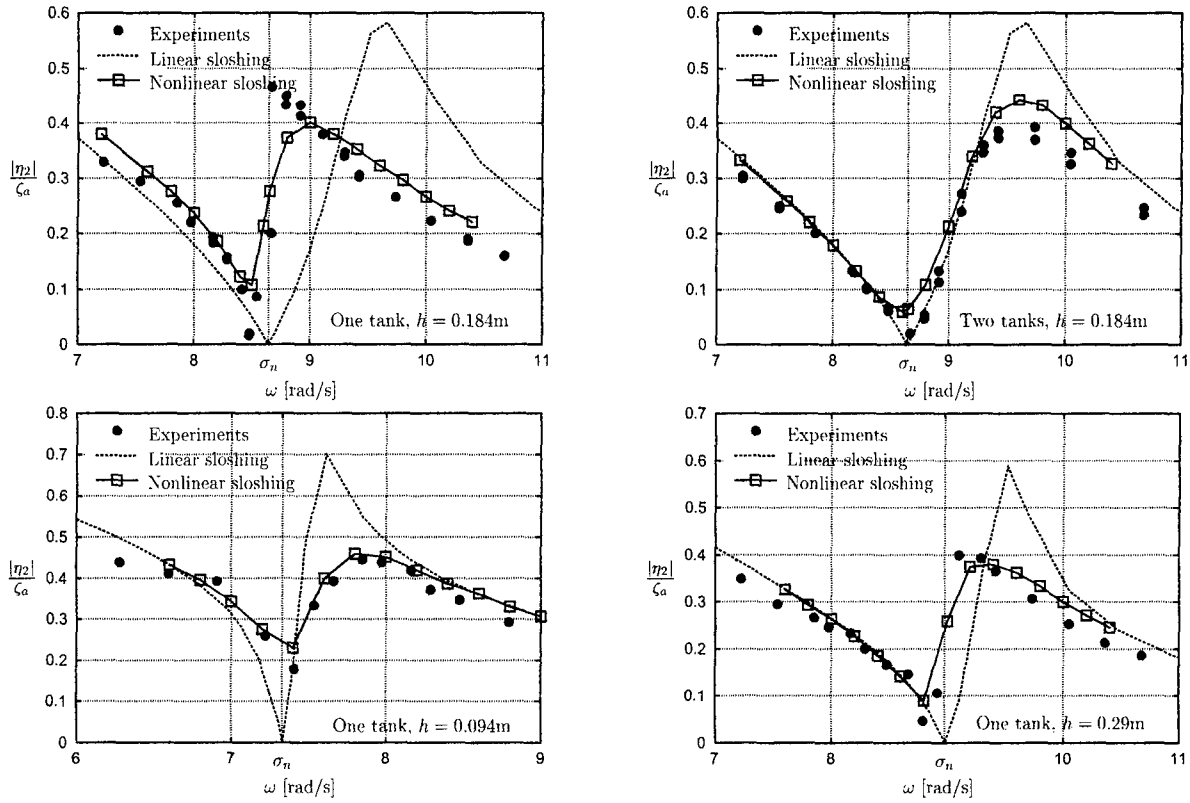

Figure 6: Comparisons between experiments and calculations

in the linear sloshing model the resulting sloshing force is infinite for finite sway motion. The combination of the linear sloshing force with the dynamics of the model cause zero sway for $\omega = \sigma_n$, while in reality the sway motion will have a minimum different from zero in the vicinity of σ_n.

The linear sloshing model fails in predicting the frequency of minimum sway motion for the three cases when only one tank is filled, since the large amplitude sloshing at resonance invalidates the assumption of a constant natural frequency for the internal fluid motion. In [2] it is shown how the first natural frequency varies as a function of the sloshing amplitude. When the filling height h is below the critical value $h/b = 0.3374$, σ_n increases as the amplitude increases. This explains the discrepancy in minimum sway by the linear sloshing model for $h = 0.094$ m. For $h = 0.29$ m and 0.184 m, the water level is above the critical depth and consequently the experiments show a minimum below σ_n. When $h = 0.184$ m and two tanks are filled, the amplitude of the sloshing motion at $\omega \approx \sigma_n$ is rather small. Hence the linear sloshing model gives an acceptable result.

In the computational results where the nonlinear model is included, the equation of motion Eq. (1) is solved in time and coupled with the nonlinear sloshing model.

$$(M + A_{22})\,\ddot{\eta}_2 + B_{22}\dot{\eta}_2 + C_{22}\eta_2 - F_{\text{exc}}(\zeta_a) - F_{\text{slosh}}(\eta_2) = 0 \tag{1}$$

In (1) M is structural mass excluding internal fluid mass, A_{22} and B_{22} are the frequency dependent added mass and damping due to the external linear flow, C_{22} is the linear spring coefficient, F_{exc} is the horizontal linear wave excitation force and F_{slosh} is the horizontal force caused by sloshing. The simulations are prolonged until steady state sway motion is achieved. The external flow model needs justification. A proper linear external model should be based on the methodology presented by Cummins [3] which implies that the radiation force is a function of convolution integrals. This would be needed in order to calculate the transient phase of the external flow and sloshing induced higher order harmonic motions. But several authors, e.g. Adegeest [4], report difficulties in applying such a formulation in practice. Actually the influence of higher harmonics in the sloshing force is negligible. This can be seen from spectral analysis of the sway motion time history. In our case, since we focus on the steady-state motions, the present external force model represents a satisfactory approximation.

By including a nonlinear sloshing model a better agreement between the calculations and the experiments is obtained. For instance a much improved prediction of the minimum sway motion is achieved.

The computed sway amplitudes for two tanks and $h = 0.184$ m were found to be sensitive to the level of damping chosen for the sloshing motion. Fig. 7 shows how the damping of the internal flow affects the results

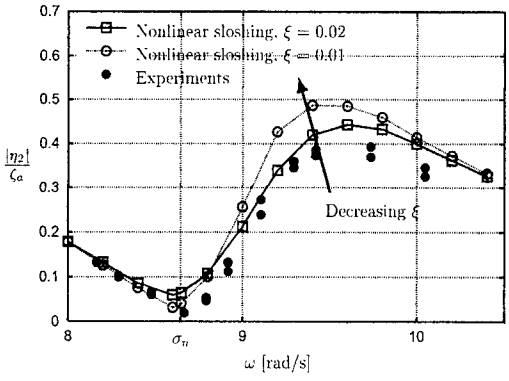

Figure 7: Experimental and computed sway amplitudes for two tanks, $h = 0.184$ m. Effect of sloshing damping ξ

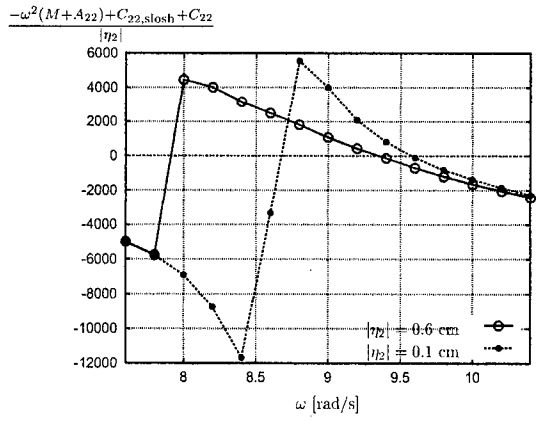

Figure 8: Mass terms - in phase with sway acceleration $\ddot{\eta}_2$

when a variation from 2% to 1% of the critical damping is considered. A description of how damping is included in the sloshing model can be found in [2]. This damping may represent e.g. viscous effects or local breaking and is not rationally predicted. The effect of external vortex shedding at the sharp corners was studied and found to be small. For $\omega > \approx \sigma_n$ the sway amplitudes increase with a decreasing damping, while around sloshing resonance the motion becomes smaller. In order to explain this phenomenon, the balance between the different terms in the equation of motion was studied. A quasi-linear approach was applied. The sum of the terms in or 180° out of phase with the sway accelerations are presented in Fig. 8. The contribution from the sloshing force is expressed as a frequency dependent restoring term $C_{22,\text{slosh}}$. By making an analogy with a linear system the zero of this sum corresponds to an eigenfrequency for the sway motion. The sum is close to zero just above or below $\omega = 9.5$ rad/s for the two amplitudes of steady state sway motion presented. Further, the sloshing force is large and nearly 180° out of phase with the acceleration in the vicinity of this frequency. Thus a small change in the phasing will lead to an important alteration of the part of the sloshing force which can be considered as a damping term for the coupled system. The damping terms are in this case all that balances the external force. For the example presented in Fig. 7 a phase change of 5° for F_{slosh} at $\omega = 9.4$ rad/s leads to a change of 10% in the sway motion. The phase is a function of the damping of the fluid motion inside the tanks. This explains the observed theoretical behaviour. If heavy tank roof impact had occurred, the damping of the internal fluid motion would be dominated by tank roof impact damping, [5]. Since the latter damping component can be rationally calculated, the ambiguity in selecting ξ demonstrated in Fig. 7 would be unimportant.

Further work will include the effect of tank roof impact. A natural next step is to include the roll and heave motion in the 2-D model before starting on a 3-D analysis to avoid that too many physical effects are included simultaneously in a complicated dynamic system.

Acknowledgements

This work is part of a Ph. D. thesis sponsored by the Research Council of Norway.

References

[1] Faltinsen, O. M. and Timokha, A. N. (2001) Adaptive multimodal approach to nonlinear sloshing in a rectangular tank., *J. Fluid Mech.*

[2] Faltinsen, O. M., Rognebakke, O. F., Lukovsky, I. A., Timokha, A. N. (2000) Multidimensional modal analysis of nonlinear sloshing in a rectangular tank with finite water depth., *J. Fluid Mech.*. **407**, 201-234

[3] Cummins, W. E. (1962), The impulse-response function and ship motions. *Schiffstechnik 9*(47), 101-109

[4] Adegeest, L. J. M. (1995), Nonlinear hull girder loads, Ph.D. thesis, Delft University of Technology, Faculty of Mechanical Engineering and Marine Technology

[5] Rognebakke, O. F. and Faltinsen, O. M (2000), Damping of sloshing due to tank roof impact, *15th International Workshop on Water Waves and Floating Bodies*, Caesarea, Israel

Abstract submitted to the 16th International Workshop on Water Waves and Floating Bodies (Hiroshima, 22–25 April 2001).

The energy distribution from impact of a three-dimensional body onto a liquid free surface

Y.-M. Scolan*, A.A. Korobkin**
*ESIM, 13451 Marseille cedex 20, France, scolan@esim.fr
**Lavrentyev Institute of Hydrodynamics, Novosibirsk 630090, Russia

1. Introduction

The three-dimensional (3D) problem of blunt-body impact onto a free surface of an ideal and incompressible liquid is considered. During the initial stage of impact the flow region is divided into three parts: (i) outer region, (ii) jet root region and (iii) jet region. In the outer region, the flow is three-dimensional. It is described within Wagner approach. Under the classical assumptions of linearization, this approach leads to a mixed boundary-value problem for the velocity potential in the lower half-space. The boundary of the half-space consists of two parts: the liquid free surface and the wetted surface of the body. These parts are separated by the contact line which varies in time. Position of the contact line is obtained from the so called Wagner condition, which implies continuous joining of the free surface and the surface of the entering body.

Wagner theory is formally valid during initial stage, when the penetration depth of the entering body is much smaller than the dimension of its wetted part. Close to the contact line, the theory fails since both the liquid velocity and the hydrodynamic pressure have singularities along this line. The singularity is yet integrable and the force can hence be calculated. However, in order to get uniformly valid pressure distribution and to improve prediction of the hydrodynamic force on the entering body, a solution which describes details of the flow close to the contact line, must be introduced.

Such a solution was derived by Wagner (1932) in two-dimensional case. The solution was matched with that in the outer flow region. An infinite length of jet was theoretically predicted. For 3D bodies we must even deal with a jet sheet. In order to obtain shape of this jet sheet and the flow inside it, the jet region has to be also considered. The jet solution has then to be matched with that for the jet root region. In the 2D wedge entry problem the jet solution was derived by Howison *et al.* (1991). It was shown that the flow in the jet region is governed by the shallow-water equations and the jet is wedge-shaped. This technique was extended by Korobkin (1994, 1997) to the case of a parabolic contour entering a compressible liquid. Using both the known liquid flow in the jet region and the geometry of this region, the energy of the jet was evaluated in both plane and axisymmetric cases. It was shown that during the impact of two-dimensional or axisymmetric blunt bodies onto a compressible liquid free surface at a constant velocity, half of the work done to move the body goes to the main flow kinetic energy and the other half is taken away with spray jets. The jets are very thin at the initial stage but the jet velocity far exceeds the velocity of the entering body.

This result was confirmed by Molin *et al.* (1996) using another method for 2D problem of impact onto an incompressible liquid surface. This method is based on the concept of energy flux evaluated through the jet root region. The main advantage of this approach is that the flux can be directly determined from the solution in the jet root region and there is no need to deal with the flow in the jet region and its geometry. This approach is used in the present paper to evaluate a part of the energy taken away with the jet in three-dimensional impact problem. It will be shown that, in order to evaluate the jet energy, we need only to know the asymptotic behaviour of the outer solution close to the contact line.

The outer solution for an arbitrary shape of three-dimensional entering body is still not available even within Wagner theory. We restrict the study to elliptic contact line, for which the velocity potential is known and the so called inverse Wagner problem has solutions (see Scolan & Korobkin 2001a). In this frame, shapes of practical interest can be generated (see Scolan & Korobkin 2000).

It is shown that the outer flow – even singular – is approximately two-dimensional close to elliptic contact lines. Therefore it makes it possible to use the planar nonlinear solution by Wagner (1932) for the jet root region. By matching locally the three-dimensional outer solution with the two-dimensional jet root solution, we arrive at a uniformly valid asymptotic description of the pressure distribution. In the case of elliptic contact region this combined solution is used to evaluate the energy distribution throughout the flow domain and to prove that the energy is equally transmitted to the bulk of the fluid and to the spray jet in the case of constant velocity of the entering body.

2. Asymptotics of the outer solution close to the contact line

Within Wagner theory the wetted part of the entering body is approximated by an equivalent expanding flat disc $D(t)$, the boundary conditions are linearised and imposed on the initially undisturbed liquid level

$z = 0$, the liquid flow caused by the impact is assumed irrotational and is described by the velocity potential $\phi_{out}(x, y, z, t)$, where $z < 0$. It is important to notice that the liquid flow in the Wagner approximation depends on both the shape of the contact region $\mathrm{D}(t)$ and the body velocity but not directly on the body shape. We assume that the Wagner problem has been solved already so that the region $\mathrm{D}(t)$ and the body velocity $U(t)$ are prescribed. Moreover, we restrict ourselves to the case of elliptic contact regions, $\mathrm{D}(t) = \{x, y \mid x^2/a^2(t) + y^2/b^2(t) < 1\}$, with the planar and axisymmetric problems representing the limiting cases. Here $a(t)$, $b(t)$ and $U(t)$ are arbitrary positive functions, which satisfy the following inequalities $a(t) \le b(t)$, $U(t) \ll \dot{a}(t)$ and $b(0) = 0$ according to the basic assumptions of Wagner theory. Dot stands for the time derivative.

The velocity potential of the flow initiated by impact of an expanding elliptic disc is given as

$$\phi_{out} = -\frac{Ua^2b}{E(e)\sqrt{(a^2+\lambda)(b^2+\lambda)}}\sqrt{1 - \frac{x^2}{a^2+\lambda} - \frac{y^2}{b^2+\lambda}} - \frac{Ua^2bz}{2E(e)}\int_\lambda^\infty \frac{(a^2+b^2+2\sigma)d\sigma}{\sigma^{\frac{1}{2}}(a^2+\sigma)^{\frac{3}{2}}(b^2+\sigma)^{\frac{3}{2}}}, \tag{1}$$

where $e(t) = \sqrt{1 - a^2/b^2}$ and $\lambda(x, y, z, t)$ is the non-negative root of the cubic equation

$$a^{-2}b^{-2}\lambda^3 + L_2\lambda^2 + L_1\lambda - z^2 = 0, \tag{2}$$

$$L_1(x, y, z, t) = 1 - \frac{x^2}{a^2} - \frac{y^2}{b^2} - \frac{a^2+b^2}{a^2b^2}z^2, \qquad L_2(x, y, z, t) = \frac{1}{a^2} + \frac{1}{b^2} - \frac{x^2+y^2+z^2}{a^2b^2}.$$

This form of the velocity potential is suitable for analysis of the behaviour of the outer solution near the contact line $\Gamma(t) = \{x, y \mid x = a(t)\cos\alpha,\ y = b(t)\sin\alpha,\ 0 \le \alpha < 2\pi\}$.

It is convenient to introduce the local coordinate system (P, x_1, y_1, z_1), where $x = a\cos\alpha + x_1$, $y = b\sin\alpha + y_1$, $z = z_1$ and $(x_1^2 + y_1^2 + z_1^2)/a^2 = O(\varepsilon)$, $\varepsilon \ll 1$. Within the new coordinate system we find

$$L_1 = -2s(x_1, y_1, \alpha, t)[1 + O(\varepsilon)], \qquad s(x_1, y_1, \alpha, t) = x_1a^{-1}\cos\alpha + y_1b^{-1}\sin\alpha,$$

$$L_2 = \mu(\alpha, t)[1 + O(\varepsilon)], \qquad \mu(\alpha, t) = a^2(t)\sin^2\alpha + b^2(t)\cos^2\alpha,$$

where $\mu = O(1)$ and $s = O(\varepsilon)$ in the leading order as $\varepsilon \to 0$. Equation (2) provides $\lambda = O(\varepsilon)$ and

$$1 - \frac{x^2}{a^2+\lambda} - \frac{y^2}{b^2+\lambda} = -2s + \frac{\lambda\mu}{a^2b^2} + O(\varepsilon), \qquad \frac{\lambda\mu}{a^2b^2} = s + \sqrt{s^2 + \frac{\mu z_1^2}{a^2b^2}} + O(\varepsilon^2).$$

Therefore,

$$\phi_{out} = -\frac{Ua}{E(e)}\left(\sqrt{s^2(x_1, y_1, \alpha, t) + \frac{\mu z_1^2}{a^2b^2}} - s(x_1, y_1, \alpha, t)\right)^{\frac{1}{2}}[1 + O(\varepsilon^{\frac{1}{2}})]$$

in a small vicinity of the contact line. It is seen that within the coordinate system (P, ξ, η, ζ), which is obtained by rotation of the system (P, x_1, y_1, z_1) counterclockwise at the angle $\theta = \tan^{-1}[(a/b)\tan\alpha]$ so that $x_1 = \xi\cos\theta - \eta\sin\theta$, $y_1 = \xi\sin\theta + \eta\cos\theta$ and $z_1 = \zeta$, the flow is approximately two-dimensional, $s = \xi\sqrt{\mu}/(ab)$, and near the contact line, $\sqrt{\xi^2 + \zeta^2}/a \ll 1$, the velocity potential of the outer flow behaves as

$$\phi_{out} = -UE^{-1}(e)\mu^{\frac{1}{4}}(a/b)^{\frac{1}{2}}(\sqrt{\xi^2+\zeta^2} - \xi)^{\frac{1}{2}}[1 + O(\varepsilon^{\frac{1}{2}})]. \tag{3}$$

It can be verified that the axes $P\xi$ and $P\eta$ are in normal and tangential directions to the contact line, respectively. Therefore, near the contact line the flow in the tangential direction is negligible compared to the flow in the normal direction. The local flow pattern is given by (3) and is similar to that in the planar case. This two-dimensional flow can be matched to the solution in the jet root region established by Wagner (1932) for the planar impact problem.

3. Parameters of the jet in 3D impact problem

The flow in the jet root region is considered within the moving coordinate system (P, ξ, η, ζ), where $\sqrt{\xi^2 + \eta^2 + \zeta^2}/a \ll 1$ and the local velocity potential ϕ_{root} does not depend on the tangential coordinate η. The flow is approximately quasi-stationary in the leading order as the size of the jet root region tends to zero, and is characterized by the jet thickness $\delta(\alpha, t)$ and the velocity $V(\alpha, t)$ of the fluid in the jet. The dynamic boundary condition shows that the jet velocity $V(\alpha, t)$ is equal to the normal velocity of the point P, which is the origin of the moving system. The 2D jet root solution by Wagner (1932) provides, in particular, the asymptotics of both the velocity potential and the pressure

$$\phi_{root} \approx -4V\sqrt{\frac{\delta|\xi|}{\pi}}, \qquad p_{root} \approx 2\rho V^2\sqrt{\frac{\delta}{\pi|\xi|}}, \tag{4}$$

in the far field, where $|\xi|/\delta \gg 1$, $|\xi|/a \ll 1$ and $\zeta = 0$. Expressions (4) have to be considered as the "outer" asimptotics of the "inner" solution and matched to the "inner" asymptotics (3) of the "outer" solution. Comparing asymptotic formulae (3) and (4), we obtain the jet thickness as

$$\delta(\alpha,t) = \frac{\pi}{8}\frac{U^2(t)(a/b)\mu^{\frac{1}{2}}(\alpha,t)}{E^2(e)V^2(\alpha,t)}. \tag{5}$$

The jet velocity $V(\alpha,t)$ is equal to the normal velocity of the moving contact line, position of which is described by the equation $G(x,y,t)=0$, where $G(x,y,t) = 1 - x^2/a^2(t) - y^2/b^2(t)$. We obtain

$$V(\alpha,t) = \frac{\dot{G}}{|\nabla G|}, \qquad \dot{G}(\alpha,t) = 2\frac{\dot{a}}{a}\cos^2\alpha + 2\frac{\dot{b}}{b}\sin^2\alpha, \qquad |\nabla G|(\alpha,t) = \frac{2\mu^{\frac{1}{2}}(\alpha,t)}{a(t)b(t)}, \tag{6}$$

where the upper dot denotes the time derivative and ∇ is the gradient operator. Equations (5) and (6) lead to the equality

$$\delta(\alpha,t)V^3(\alpha,t) = \frac{\pi}{16}\frac{U^2a^2}{E^2(e)}\dot{G}(\alpha,t) \tag{7}$$

used below to evaluate the flux of kinetic energy through the jet.

4. Repartition of kinetic energy

It is well-known that the energy conservation law is not satisfied within classical Wagner theory. In general case (see Scolan & Korobkin 2001a),

$$\frac{d}{dt}[A(t) - T(t)] = \frac{1}{2}U^2(t)\frac{dM_a}{dt}, \tag{8}$$

where $T(t)$ is the kinetic energy of the liquid flow in the outer region, $T(t) = \frac{1}{2}M_a(t)U^2(t)$, $A(t)$ is the work done to oppose the hydrodynamic force on the entering blunt body, and $M_a(t)$ is the added mass of the flat disk $\mathrm{D}(t)$. During the initial stage of the water impact, the added mass of the expanding flat disk $\mathrm{D}(t)$ increases, $dM_a/dt > 0$. Therefore, $T(t) < A(t)$, which is usually considered as an indication that a part of the energy is "lost" during the impact. It is proved below that the flux of energy in the right-hand side of equation (8) is equal to the flux of kinetic energy through the jet in the case of elliptic contact lines.

The total velocity of fluid in the jet $V_f(\alpha,t)$ is equal to the jet velocity $V(\alpha,t)$ plus the normal velocity of the moving contact line, which is $V_f(\alpha,t) = 2V(\alpha,t)$. The part of the kinetic energy $\Delta E_j(\alpha,t)$, which leaves the main flow region through the jet root region of small length $\Delta\ell$ during small time interval Δt, is given as

$$\Delta E_j(\alpha,t) = \frac{1}{2}\Delta m(\alpha,t)V_f^2(\alpha,t), \qquad \Delta m(\alpha,t) = \rho\cdot\delta(\alpha,t)\Delta\ell\cdot V(\alpha,t)\Delta t, \tag{9}$$

where ρ is the liquid density and $\Delta\ell = \mu^{\frac{1}{2}}(\alpha,t)\Delta\alpha$. Equations (7) and (9) provide the total flux of the kinetic energy through the 3D jet in the form

$$\frac{dE_j^{tot}(t)}{dt} = 2\rho\int_0^{2\pi}\delta(\alpha,t)V^3(\alpha,t)\mu^{\frac{1}{2}}(\alpha,t)d\alpha = \frac{\pi}{8}\frac{\rho U^2a^2}{E^2(e)}\int_0^{2\pi}\dot{G}(\alpha,t)\mu^{\frac{1}{2}}(\alpha,t)d\alpha. \tag{10}$$

The integral in (10) is equal to

$$\int_0^{2\pi}\dot{G}(\alpha,t)\mu^{\frac{1}{2}}(\alpha,t)d\alpha = \frac{8}{3ae^2}[(\dot{a}b(1+e^2) + a\dot{b}(2e^2-1))E(e) + (1-e^2)(a\dot{b} - \dot{a}b)K(e)], \tag{11}$$

where $K(e)$ and $E(e)$ are the complete elliptic integrals of first and second kind, respectively.

The added mass $M_a(t)$ of the elliptic disk $\mathrm{D}(t)$ is given as $M_a(t) = 2\pi\rho a^2 b/(3E(e))$, with its time derivative being

$$\frac{dM_a}{dt}(t) = \frac{2\pi\rho a}{3e^2E^2(e)}[(\dot{a}b(1+e^2) + a\dot{b}(2e^2-1))E(e) + (1-e^2)(a\dot{b} - \dot{a}b)K(e)]. \tag{12}$$

In order to derive equation (12), the following formulae were used

$$\frac{dE}{de} = \frac{E(e)-K(e)}{e}, \qquad \frac{de}{dt} = \frac{a(a\dot{b} - \dot{a}b)}{b^3e}.$$

Substituting (11) into (10) and comparing the result with (12), we obtain

$$\frac{dE_j^{tot}}{dt} = \frac{1}{2}U^2(t)\frac{dM_a}{dt},$$

where the right-hand side is the same as in (8). Equation (8) provides after its integration with respect to time

$$A(t) = T(t) + E_j^{tot}(t).$$

Therefore, the energy conservation law is hold within the 3D Wagner theory if the jet energy is taken into account. It should be noted that this result has been proved only for the case of elliptic contact lines.

It is seen that the energy is equally transmitted to the bulk of the fluid and to the spray jet, $T(t) = E_j^{tot}(t)$, if and only if the velocity of the entering body is constant. If the body velocity is not constant, we find

$$E_j^{tot}(t) = T(t) - \int_0^t M_a(\tau)U(\tau)\dot{U}(\tau)d\tau,$$

where $M_a(\tau) \geq 0$ and $U(\tau) > 0$. Therefore, main part of the energy is transmitted to the bulk of the fluid, $T(t) > E_j^{tot}(t)$, if the body velocity increases, $\dot{U}(t) > 0$, after the impact instant. Correspondingly, the main part of the energy is transmitted to the jet , $E_j^{tot}(t) > T(t)$, if the body velocity decreases, $\dot{U}(t) < 0$, after the impact. The velocity of the entering body decreases, in particular, in the case of free fall of the body onto the liquid free surface.

5. Conclusion

As soon as the matching of the jet root and main flow solutions is performed along the contact line, we know all necessary quantities to evaluate the pressure field. This is done in Scolan and Korobkin (2001b). Two pressure field formulations are considered. Either the composite solution by Zhao and Faltinsen (1992) or the "second order" solution by Cointe (1987) can be used. The force is calculated from the numerical pressure integration all over the wetted area. For the sake of brevity the formulations and results are not presented here. Comparisons are made with results by Zhao and Faltinsen (1997, 1998) which are considered as more exact. For cone and circular paraboloids (as a sphere), it is shown that the "second order" formulation of the pressure provides a force in good agreement for cone aperture less 20^o and before the maximum of force is reached for the sphere. Experimental data concerning the pressure field acting on an elliptic paraboloid should be also obtained soon.

A.A.K. acknowledges the support from RFBR (projects No. 00-01-00839 and No. 00-15-96162) and SB RAS (integrated grant No. 1).

6. References

Cointe R., 1987, "Two dimensional fluid-solid impact.", J. Offshore Mech. and Artic Engng., 111, pp 109–114.

Faltinsen, O. & Zhao, R., 1997 Water entry of ship sections and axisymmetric bodies., Proc. of AGARD FDP and Ukraine Inst. Hydromechanics Workshop on "High speed body motion in water".

Howison, S.D., Ockendon, J.R. & Wilson, S.K. 1991 Incompressible water-entry problems at small deadrise angles. *J. Fluid Mech.* **222**, 215-230.

Korobkin, A.A. 1994 Blunt-body penetration into a slightly compressible liquid. In *Proc. 20th Symposium on Naval Hydrodynamics* Santa Barbara **3**, 179-186.

Korobkin, A.A. 1997 *Liquid-Solid Impact* Novosibirsk, Siberian Branch of the Russian Academy. 200pp.

Molin, B., Cointe, R. & Fontaine, E. 1996 On energy arguments applied to the slamming force. In *Proc. 11th Workshop on Water Waves and Floating Bodies, Hamburg, 17 - 20 March 1996*, 4pp.

Scolan, Y.-M. & Korobkin, A.A. 2000 Design of three-dimensional bodies subject to water impact. In *Proc. 15th Workshop on Water Waves and Floating Bodies, Dan Caesarea, Israel*, 4pp.

Scolan, Y.-M. & Korobkin, A.A. 2001a Three-dimensional theory of water impact. Part 1. Inverse Wagner problem. (submitted to publication)

Scolan, Y.-M. & Korobkin, A.A. 2001b On the pressure distribution and energy transfer for three-dimensional bodies subject to water impact. In preparation.

Wagner, H. 1932 Über Stoss- und Gleitvorgänge an der Oberfläche von Flüssigkeiten. *ZAMM* **12**, 193-215.

Zhao, R. & Faltinsen, O., 1992 Water entry of two-dimensional bodies. J. Fluid Mech., 246, pp 593–612.

Zhao, R. & Faltinsen, O., 1998 Water entry of arbitrary axisymmetric bodies with and without flow separation., Proc. of ONR, pp 290–301.

Extension of the Havelock/Dawson Method to Include Nonlinear Free-Surface Boundary Conditions

Carl A. Scragg
Science Applications International Corporation
San Diego, California

The Havelock/Dawson method of solving linearized free-surface problems was discussed by the author in 1999 [1]. A combination of Rankine singularities distributed on the surface of the ship hull and Havelock singularity distributions placed over the undisturbed free surface can be used to impose either the classic Kelvin linearized free-surface condition or Dawson's linearized boundary condition. With this approach we have been able to generate numerical solutions that combine the near-field accuracy of Rankine codes with the far-field accuracy of Havelock codes. We have found this method to be both robust and computationally efficient. An extension of the basic Havelock/Dawson approach to include fully nonlinear free-surface boundary conditions is discussed here.

The Kelvin and the Dawson linearized free-surface boundary conditions are special cases of the general expansion of the nonlinear free-surface conditions about an arbitrary basis function. Taking the velocity potential Φ as the sum of a known basis function ϕ_0 and an unknown perturbation potential ϕ_1, we can write the free-surface boundary condition in the following form:

$$\tfrac{1}{2}\nabla\phi_1 \cdot \nabla(\nabla\phi_0 \cdot \nabla\phi_0) \;+\; \nabla\phi_0 \cdot \nabla(\nabla\phi_0 \cdot \nabla\phi_1) \;+\; g\,\tfrac{\partial}{\partial z}\phi_1 \;=$$

$$-\tfrac{1}{2}\nabla\phi_0 \cdot \nabla(\nabla\phi_0 \cdot \nabla\phi_0) \;-\; g\,\tfrac{\partial}{\partial z}\phi_0 \;+\; \mathrm{O}(\nabla\phi_1)^2 \,.$$

Assuming that the perturbation potential is "small", $\nabla\phi_1 \ll \nabla\phi_0$, we hope to be able to neglect the higher order terms in $\nabla\phi_1$. Of course, the nonlinear boundary condition should be satisfied on the exact position of free surface, $z = \zeta$. However, consistent with our intent to retain only the first order terms in the perturbation potential, we can expand this boundary condition in a Taylor series about the position of the free surface corresponding to the basis flow, $z = \zeta_0$. Such an expansion leads to first order terms in $\Delta\zeta = \zeta_1 - \zeta_0$, that should properly be retained under the assumption that they can be of the same order as the first order terms in ϕ_1; see Nakos and Sclavounos, 1991 [2], for details. However, Raven, 1996 [3], pointed out that the $\Delta\zeta$ terms can be quite irregular and suggested that the convergence of an iterative scheme may actually be improved by leaving these terms out. We decided to follow Raven's approach in order to take advantage of the numerical simplification, and we apply the boundary condition directly on $z = \zeta_0$.

In our iterative scheme, we use the Havelock/Dawson solution as the initial basis flow (or zeroth iteration). We then attempt to solve for the perturbation potential by applying

the linearized expansion about the basis flow using

$$\tfrac{1}{2}\nabla\phi_{i+1}\cdot\nabla(\nabla\phi_i\cdot\nabla\phi_i) \;+\; \nabla\phi_i\cdot\nabla(\nabla\phi_i\cdot\nabla\phi_{i+1}) \;+\; g\,\tfrac{\partial}{\partial z}\phi_{i+1} \;\approx$$

$$-\tfrac{1}{2}\nabla\phi_i\cdot\nabla(\nabla\phi_i\cdot\nabla\phi_i) \;-\; g\,\tfrac{\partial}{\partial z}\phi_i\;, \quad \text{on } z=\zeta_i\,.$$

The new free-surface elevation ζ_{i+1} is calculated by applying the Bernoulli equation on $z=\zeta_i$. It was not obvious that such an iterative scheme would necessarily be convergent. However, by first extending our existing Havelock/Dawson code to include the perturbation expansion about an arbitrary basis flow, and then nesting the code within an iterative loop, we are able to investigate the convergence numerically.

With the basic Havelock/Dawson method, Rankine source panels are distributed over the surface of the hull $S(x,z)$, and Havelock source panels are distributed over a local region of the undisturbed free surface $Z(x,y)=0$. It has been found that the Havelock singularity density necessary to satisfy the free-surface boundary condition tends to zero rapidly as the distance from the hull increases, and therefore the number of free-surface panels required can be quite small relative to other methods. For the nonlinear problem, we wish to distribute the free-surface panels on $\zeta_i(x,y)\neq 0$, and the accuracy achieved by panelizing a small near-field region of the free surface needs to be demonstrated. Furthermore, positioning Havelock singularities at locations above the mean free surface presents mathematical difficulties that will be addressed in the following section. For the moment, imagine that we distribute N Rankine panels over the surface of the hull $S(x,z)$, and M Havelock panels over the near-field region of the free surface $\zeta_i(x,y)$, to solve for ϕ_{i+1}. The determination of the source strengths σ^S and σ^Z necessary to satisfy the boundary conditions will involve solving a matrix equation of the form

$$\begin{bmatrix}\mathbf{A}_{11} & \mathbf{A}_{12}\\ \mathbf{A}_{21} & \mathbf{A}_{22}\end{bmatrix}\begin{bmatrix}\sigma^S\\ \sigma^Z\end{bmatrix}=\begin{bmatrix}\mathbf{B}^S\\ \mathbf{B}^Z\end{bmatrix}\,, \quad \text{where}$$

$\mathbf{A}_{11}$ contains the influence of the Rankine hull panels on the hull collocation points,

$\mathbf{A}_{12}$ contains the influence of the Havelock free-surface panels on hull collocation points,

$\mathbf{A}_{21}$ contains the influence of the Rankine panels on free-surface collocation points, and

$\mathbf{A}_{22}$ contains the influence of the Havelock panels on the free-surface collocation points.

The vectors $\mathbf{B}^S$ and $\mathbf{B}^Z$ contain the boundary conditions to be satisfied on the hull and free surface respectively.

There is no difficulty calculating the $\mathbf{A}_{11}$ and $\mathbf{A}_{21}$ sub-matrices since the influence of Rankine panels is well defined for arbitrary field points. However, evaluation of the $\mathbf{A}_{12}$ and $\mathbf{A}_{22}$ sub-matrices can be problematic since either the source point, the field point, or both, might occur at positions above the level of the undisturbed free surface, $z=0$. The $e^{k(z+z')}$ term in the Havelock Green function represents the attenuation of free-surface waves due to either the depth of the source point z or the field point z', and generally both z and z' are ≤ 0. With positive values of the source and field points, the influence of the

Havelock wave potential will grow exponentially. One method of avoiding this problem is to use a coordinate system fixed relative to the local free surface. Then the position of both the field point and the source point can be taken as the local depth and the $e^{k(z+z')}$ term will always be ≤ 1.

In the calculation of the $\mathbf{A}_{22}$ sub-matrix, we have employed an *ad hoc* assumption that since both the source point and the field point are located on the free surface at zero depth, the depth attenuation term is equal to unity. In the calculation of the $\mathbf{A}_{12}$ sub-matrix, the Havelock source point is always located at zero depth and the depth of the field point on the hull is calculated relative to the local dynamic waterline. Otherwise, the subroutines that we use to calculate the influence of Havelock singularity distributions are similar to those used in the linear Havelock/Dawson code.

As always, the Wigley hull was the initial geometry used to investigate the convergence of the iterative scheme. Since the wetted area of the hull will change with each iteration, one should repanelize at every step. However, for this investigation, the hull was assumed to be fixed in sinkage and trim and we could then simply panelize the hull to some distance above the design waterline, and assign a source strength of zero to each panel that is not submerged at any particular iteration. We allowed the iterative scheme to proceed until the Rankine and Havelock singularity strengths associated with the perturbation potential were two orders of magnitude less than the singularity strengths calculated for the basis

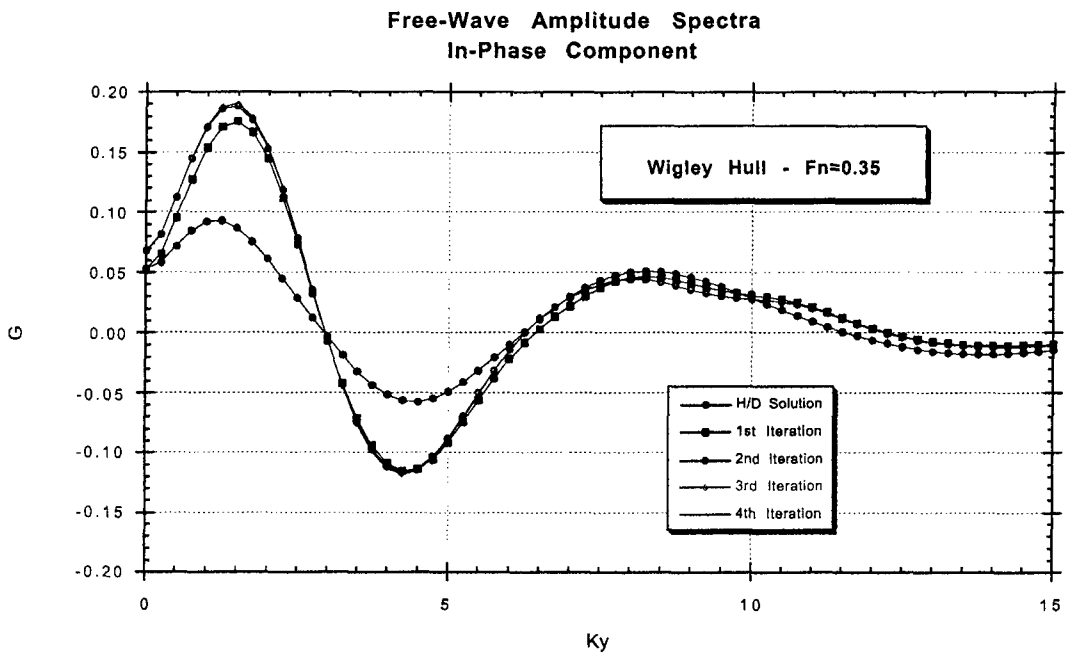

Figure 1 – Free-Wave Spectra Calculated for First 4 Iterations

flow (Havelock/Dawson solution). We found that this convergence criterion was satisfied in just 4 iterations for the Wigley hull test case at Fn = 0.35. Moreover, the radiating waves had converged after only 2 iterations, as can be seen from the plots of the free-wave spectra. The hull was panelized with 604 Rankine panels and a similar number of Havelock panels were distributed on the free surface. These computations required about 22 minutes to run on a 400 MHz Macintosh G3.

We ran a second test case using a more complex hull geometry – a high-speed naval combatant hull form. This geometry required 890 Rankine panels to define the hull shape. The local free-surface domain was panelized with 975 Havelock panels. For an 18-knot case (Fn = 0.23), the convergence criterion was met in 7 iterations. However, as was observed with the Wigley hull test case, the calculated free-wave spectra are quite close to the final nonlinear results even after the first two iterations. In the near-field, the dominant effects of the nonlinear free-surface conditions appear as a deepening of the wave troughs, an increase in the wave slopes, and a minor phase shift in the bow wave. This computation took about 100 minutes on the same Macintosh G3 computer.

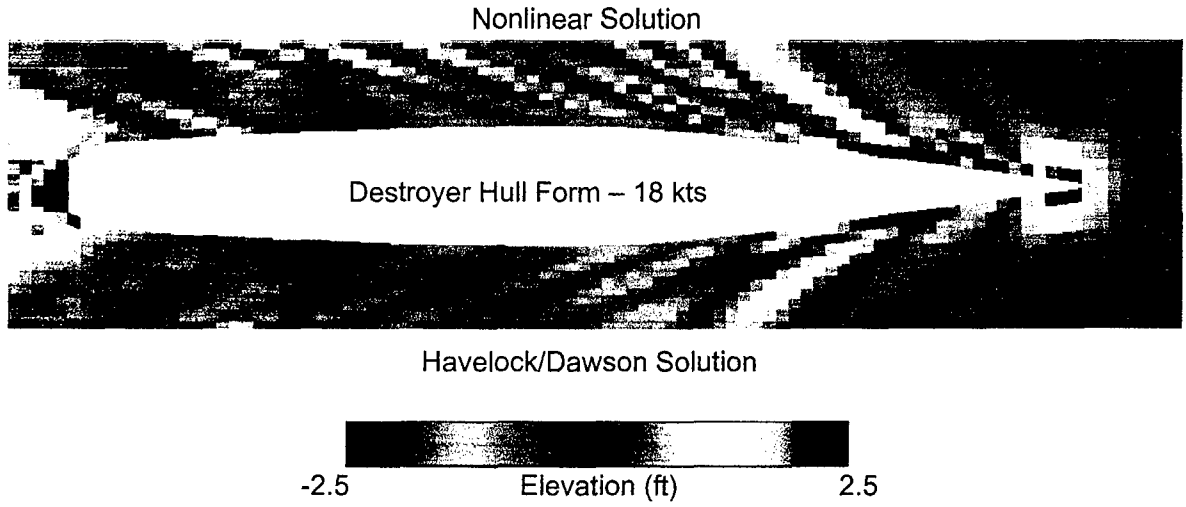

Figure 2 – Nonlinear vs. Linearized Free-Surface Waves

[1] Scragg, C.A. "On the Use of Free-Surface Distributions of Havelock Singularities," 14th International Workshop on Water Waves and Floating Bodies, Port Huron, Michigan, 1999, pp 133-37.

[2] Nakos,D. and P.Sclavounos "Ship Motions by a Three-Dimensional Rankine Panel Method," 18th Sym. on Naval Hydrodynamics, Ann Arbor, 1991. pp 21-40

[3] Raven, H. "A Solution Method for the Nonlinear Ship Wave Resistance Problem," Thesis, Technische Universiteit Delft, 1996, 220 pages.

A new type of trapped mode and its relevance to the forces on parallel arrays of breakwaters

B.J. Shipway & D.V. Evans

School of Mathematics, University of Bristol, University Walk, Bristol BS8 1TW

The classical linearised equations and boundary conditions governing water waves and their interaction with obstacles permit few explicit analytical solutions. The exceptions include Havelock's 1929[5] solution for a vertical wavemaker and the solution derived from this by Ursell in 1947[17] for the scattering of two-dimensional water waves by a thin partly-immersed barrier in deep water. Susequently a number of authors, including Mei[12] and Porter D.[15] showed that an explicit analytical solution was possible for the scattering by or radiation from, any number of thin vertical barriers positioned on the same vertical line.

Later Levine & Rodemich[8] showed that the scattering by a pair of identical parallel partly-immersed vertical barriers could also be solved explicitly but the usefulness of their solution was restricted by its complexity. In contrast the simpler case of a pair of identical parallel vertical barriers extending indefinitely into the fluid from a point beneath the free surface was solved by Jarvis[6] and useful results on the transmission and reflection coefficients obtained.

In 1972 Evans & Morris[3] revisited the case of the surface-piercing pair of barriers and utilising a powerful variational method were able to get accurate results for the scattering coefficients. In particular they were able to prove that for certain spacings, depths of immersion and incident wave frequency, a wave could be completely reflected by the pair of barriers, the first time this had been observed in classical water wave theory. The same phenomenon did not hold true for the submerged pair of barriers although in both cases the more common phenomenon of complete transmission did occur.

The result of zero transmission was subsequently confirmed by Newman[13] using matched asymptotics for closely-spaced barriers and by McIver[11] for finite water depth using matched eigenfunction expansions. Finally Porter R. & Evans[16] confirmed McIver's results using an accurate complementary variational approach.

The importance of the zero transmission result to Evans & Morris lay in the possibility of designing efficient breakwaters although the closeness in frequency of complete transmission for the same barrier configuration ruled this out as a practical breakwater in mixed seas. Further examples showed that zero transmission does not require a pair of separated surface-piercing bodies for it to occur. Thus a careful scrutiny of the curves of transmission published by Haren & Mei in 1979[4] in their paper on the scattering by a Salter duck wave-energy device shows that it occurs here also whilst more recently Parsons & Martin[14] have shown numerically that it occurs in the scattering of waves by an inclined partly-immersed thin plate provided the plate is not vertical.

Speculation over the question of the uniqueness or otherwise of the two-dimensional water wave problem led to a revival in interest in zero transmission configurations. Thus Evans argued that at that frequency and configuration an identical pair of barriers positioned at an appropriate and sufficiently large distance from the first pair would totally reflect a wave incident upon them from the direction of the other pair and that the reflected wave would itself be totally reflected on reaching that pair and so on so that the net effect would be a standing wave between two identical widely-spaced pairs of barriers and only a local evanescent field outside each pair. Such a motion would provide an example of a non-uniqueness as any multiple of this solution could be added to the solution to the scattering of a wave incident on the two pairs of barriers from the region exterior to both pairs.

The uniqueness question was put to rest in 1996 on the publication by McIver M.[10] of an explicit example of non-uniqueness obtained by superposing two identical line sources in the free

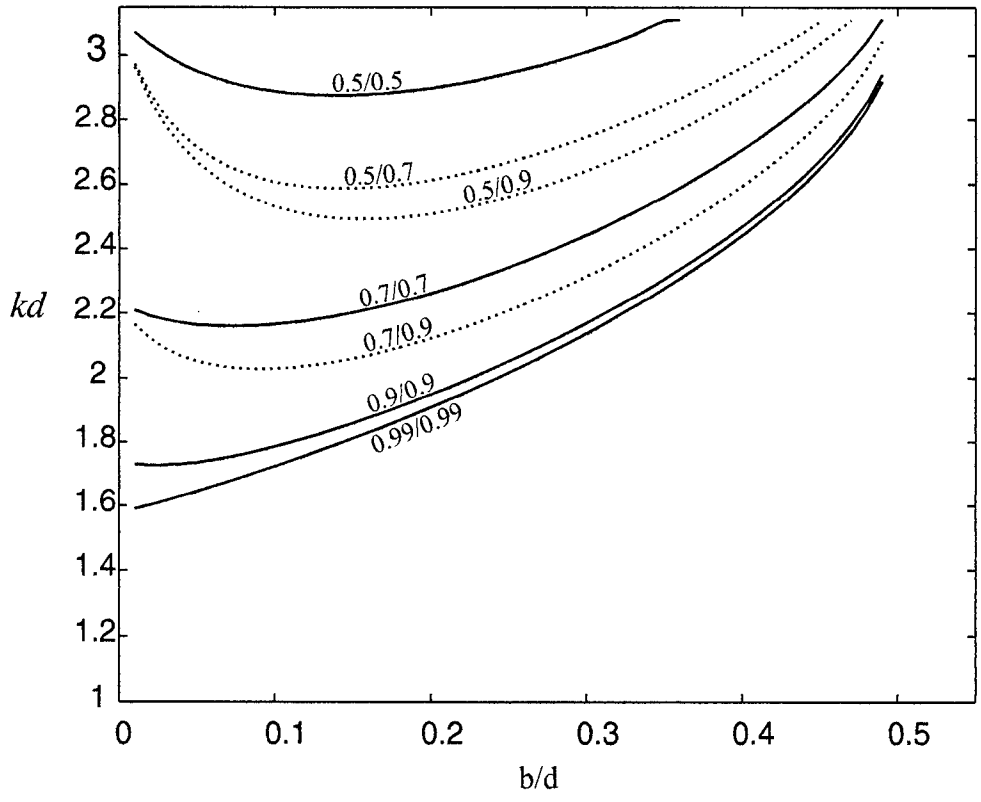

Figure 1: Curves of zero transmission past 2 barriers. Pairs of numbers next to curves indicate ratios of barrier widths to channel width d. b is the barrier spacing and k is the wave number related to the radian frequency through the relation $\omega^2 = gk \tanh kH$ where H is the depth of water in the channel.

surface at a spacing which cancelled their net far field. She showed that certain streamlines of the resulting field entered the sources from above the free surface and could be replaced by pairs of rigid bodies entirely enclosing the singularities with an open free surface between them. The rigid bodies all have the property that they intersect the free surface non-vertically a property shared also by the Salter duck thus adding weight to the Evans argument but the authors are not aware as to whether a single McIver body is capable of demonstrating zero transmission.

Recently Kuznetsov et al[7] have solved the four-barrier problem numerically using the variational approximations described by Porter & Evans and have confirmed that there are solutions describing standing waves or trapped modes between the pairs of barriers with just a local decaying field outside the pairs and that these solutions do indeed occur close to the spacings and frequencies predicted by the wide-spacing arguments of Evans.

The existence of trapped modes in an infinite wave channel containing a vertical bottom-mounted surface-piercing circular cylinder was first proved by Callan et al[1] and their relevance to the large forces on large finite arrays of identical cylinders was pointed out by Maniar & Newman[9] at a previous Workshop. The existence of trapped modes about an arbitrary cross-sectional cylinder in a channel was proved by Evans et al[2]. In all cases the condition satisfied on the centre-line was the Dirichlet condition of the vanishing of the potential, corresponding to a fundamental sloshing motion.

In the present work we obtain for the first time solutions describing trapped modes for bodies on the centre-line of an infinite channel which satisfy a Neuman condition on the centre-line and which can therefore be accessed by an incident plane wave from infinity. The method is a direct extension of the ideas on zero transmission described above.

Thus we first show that two identical vertical thin plates with axes perpendicular to the walls of the channel can if suitably spaced, when partly spanning the channel, exhibit zeros of transmission at certain frequencies. Figure 1 gives an example of how these frequencies depend upon spacing and span.
Armed with this information it will be shown that trapped modes exist in the interior fluid region between this pair of plates and its mirror image at suitable spacings and frequencies which approach the values corresponding to zero transmission as the spacing between the two pairs increases. The relevance of the results to large double arrays of breakwaters and the forces they might experience will be discussed. Curves showing the variation of the trapped mode frequencies with the geometry of the configuration will be presented. An extension to the case of Rayleigh-Bloch waves between a double row of identical parallel plates with gaps will be discussed showing for the first time the existence of such waves at wave numbers above the fundamental wavenumber associated with Rayleigh-Bloch waves.

References

[1] Callan, M., Linton, C.M. & Evans, D.V. 1991 *J. Fluid Mech.* **229**, 51-64.

[2] Evans, D.V., Levitin, M. & Vassiliev, D. 1994 *J. Fluid Mech.* **261**, 21-31.

[3] Evans, D.V. & Morris, C.A.N. 1972 *J. Inst. Appl. Maths. Applics.* **10**, 1-9.

[4] Haren & Mei C.C. 1979 *App. Ocean Res.* vol.**1**, No. 3, 147-157.

[5] Havelock, T.H. 1929 *Phil. Mag.* **8**, 569-576.

[6] Jarvis, R.J. 1971 *J. Inst. Maths. Applic.* **7**, 207-215.

[7] Kuznetsov, N., McIver, P. & Linton, C.M. 2001 *Wave Motion* **33**, 283-307.

[8] Levine, H. & Rodemich, E. 1958 *Tech. Rep. No. 78. Applied Maths & Statistics Lab.* Stanford University.

[9] Maniar & Newman, J.N. 1997 *J. Fluid Mech.* **339**, 309-330.

[10] McIver, M. 1996 *J. Fluid Mech.* **315**, 257-266.

[11] McIver, P. 1985 *IMA J. Appl. Math.* **35**, 339-355.

[12] Mei, C.C. 1966 *Quart. J. Mech. Appl. Math* **19**, 417-440.

[13] Newman, J.N. 1974 *J. Fluid Mech.* **66**, 97-106.

[14] Parsons, N.F. & Martin, P.M. 1993 *Appl. Ocean Res.* **16**, 129-139

[15] Porter, D. 1974 *J. Fluid Mech.* **63**, 625-634

[16] Porter, R. & Evans, D.V. *J. Fluid Mech.* **294**, 155-180

[17] Ursell, F. 1947 *Proc. Camb. Phil. Soc.* **43**, 374-382

Parabolic Approximation of the Hydro-elastic Behavior of a Very Large Floating Structure in Oblique Waves

Ken TAKAGI

Department of Naval Architecture and Ocean Engineering, Osaka University, Suita, JAPAN

1.INTRODUCTION

Recently the estimation of elastic motion of a very large floating structure (VLFS) has been carried out for the Mega-Float project in Japan. The latest version of the computer code is based on the Finite Element Method. This code can deal with arbitrary shape of the structure and the topology of the sea bottom, however the code is time consuming and is not useful for the conceptual design. Actuary, the committee of the project regards this code as a program for the detail design.

It is obvious that we need a method to estimate the effects from all environments, for example the bottom topology, break water, geometry of the structure and so on, in the conceptual design. The method should be easy to handle and should not be time consuming. In this aspect, Takagi and Kohara[2000] proposed an application of the ray-theory to hydro-elastic behavior of VLFS. The theory itself is based on the classical ray theory. The hydro-elastic behavior of VLFS is treated as wave propagation in the platform. The wave field around the platform and in the platform is represented as a summation of wave rays.

The shortcoming of the ray theory is that corners of the platform are singular point. Takagi [1999] solved the corner problem that is the wave propagation from the water region to the semi-infinite quarter plane covered with the elastic platform and it is found that the corner effects is inversely proportional to the square root of the distance from the corner. Therefore, the corner effect is limited around the corners. Another shortcoming is that the wave amplitude is suddenly changed along a ray that passes through a corner. This shortcoming is overcome by applying the parabolic approximation in this paper.

2.FORMULATION OF THE RAY THEORY

It is well known that the water wave problem is greatly simplified by the shallow water approximation, since all evanescent terms are vanished. Although extension of the ray theory to the finite depth problem or the varying depth problem has no essential problem, the shallow water approximation is employed in this paper for the simplification of the problem. The velocity potential satisfies the modified continuity equation

$$\frac{K}{h}\phi + [1 + M\nabla^4]\nabla^2\phi = 0, \tag{1}$$

where $K = \frac{\omega^2}{g}$, $M = D/\rho g$ and h is the water depth. D is the flexural rigidity of the platform, g is the gravitational acceleration and ρ is the density of the water. (1) gives the dispersion relation in the platform.

$$K = (1 + M\alpha^4)\alpha^2 h \tag{2}$$

It is well known that (2) has six roots, and three of them are suitable for present problem. We call these roots as α_n $(n = 0, 1, 2)$ herein after.

The ray tracing is performed, according to the characteristic form of the conservation of the wave number

$$\frac{d\boldsymbol{\alpha_0}}{ds} = -\frac{\partial\Omega}{\partial \boldsymbol{r}} \quad \text{on} \quad \frac{d\boldsymbol{r}}{ds} = \frac{\partial\Omega}{\partial\boldsymbol{\alpha_0}}. \tag{3}$$

where $\Omega(\alpha_0) = \sqrt{g\alpha_0(1 + M\alpha_0^4)\alpha_0^2 h}$.

If the water depth and the flexural rigidity were constant, the problem would be very simple. We just take the refraction of the ray into account at the edge of the platform. The difficulty is that the displacement of the platform is suddenly changed along a ray that passes through a corner as stated previously. In order to overcome this difficulty, we discuss the asymptotic form of the exact representation of the wave propagation in the platform.

3.ASYMPTOTIC FORM IN THE PLATFORM

According to the boundary integral formulation derived by Takagi [1999], the hydro-elastic behavior of the platform is represented by the sinusoidal distribution of the Green function.

$$\begin{aligned} I &= \lim_{\epsilon\to 0}\int_0^\infty e^{-i(k_y - i\epsilon)\eta} G(x, 0, y, \eta)d\eta \\ &= \lim_{\epsilon,\iota\to 0}\frac{1}{2\pi}\int_0^\infty e^{-i(k_y - i\epsilon)\eta}\int_0^\infty \frac{1}{k}\left(\frac{K}{(K - i\iota) - (1 + Mk^4)k\ 2h} - 1\right) J_0(kR')dkd\eta, \end{aligned} \tag{4}$$

where ϵ and ι ensure the radiation condition.

Applying a contour integral to (4), a component of plane waves can be derived. The detail of the derivation is found in Takagi[1999].

$$I = -\frac{i}{2\pi}\frac{K}{\alpha_0\Lambda'(\alpha_0)}\int_{-\infty}^{\infty}\frac{e^{-i\alpha_0 R\cosh\theta}}{k_y-\alpha_0\sin(\beta+i\theta)}d\theta - \frac{i}{2\pi}\frac{K}{\alpha_1\Lambda'(\alpha_1)}\int_{-\infty}^{\infty}\frac{e^{i\alpha_1 R\cosh\theta}}{k_y+\alpha_1\sin(\beta+i\theta)}d\theta$$
$$- \frac{i}{2\pi}\frac{K}{\alpha_4\Lambda'(\alpha_4)}\int_{-\infty}^{\infty}\frac{e^{-i\alpha_4 R\cosh\theta}}{k_y-\alpha_4\sin(\beta+i\theta)}d\theta + C_{I1}+C_{I2}+C_{I3}, \tag{5}$$

where,

$$C_{I1} = \begin{cases} 0 & \text{when } 0>\beta>\mu_0 \\ -i\dfrac{Ke^{-iR\alpha_0\cos(\mu_0-\beta)}}{\alpha_0^2\Lambda'(\alpha_0)\cos\mu_0} & \text{when } \frac{\pi}{2}<\beta<\mu_0 \end{cases}, \tag{6}$$

$$C_{I2} = -i\frac{Ke^{-iR\alpha_1\cos(\mu_1-\beta)}}{\alpha_1^2\Lambda'(\alpha_1)\cos\mu_1} \tag{7}$$

$$C_{I3} = \begin{cases} 0 & \text{when } \beta<\Re[\mu_4] \\ -i\dfrac{Ke^{-iR\alpha_4\cos(\mu_4-\beta)}}{\alpha_4^2\Lambda'(\alpha_4)\cos\mu_4} & \text{when } \beta>\Re[\mu_4] \end{cases}, \tag{8}$$

$$\frac{k_y}{\sqrt{\alpha_n^2-k_y^2}} = \tan\mu_n, \qquad \left.\begin{matrix} x \\ y \end{matrix}\right\} = R\left\{\begin{matrix} \cos\beta \\ \sin\beta \end{matrix}\right. \tag{9}$$

and $\Lambda(\alpha)=(1+M\alpha^4)\alpha^2 h$. It is noted that C_{I1} denotes plane progressive waves and it does not affect the other edge i.e. on the line $y=0$. C_{I2} and C_{I3} are also plane progressive waves, however their wave number is a complex number and these waves decay quickly as the coordinate x becomes large. The first three terms in (5) represent the end effect and the first term is asymptotically proportional to $1/\sqrt{\alpha_0 R}$. When the observation point is far from the corner, the end effect vanishes and the solution coincides with the solution of the semi-infinite half platform problem.

A difficulty is expected when θ equals to β, because the stationary phase method can not be applied to the first term of (5). Therefore, the asymptotic form along this line is discussed. The following coordinate is defined

$$\left.\begin{matrix} x' \\ y' \end{matrix}\right\} = R\left\{\begin{matrix} \cos(\beta-\mu_0) \\ \sin(\beta-\mu_0) \end{matrix}\right., \tag{10}$$

and the order of y' is assumed to be $O(\alpha_0^{-1/2})$. It is also noted that the we are considering the region $R=O(1)$.

After some manipulations we obtain

$$\frac{\alpha_0\cos\mu_0}{2\pi}\int_{-\infty}^{\infty}\frac{e^{-i\alpha_0 R\cosh\theta}}{k_y-\alpha_0\sin(\beta+i\theta)}d\theta + i\frac{\alpha_0^2\Lambda'(\alpha_0)}{K}C_{I1}$$
$$= e^{-i\alpha_0 x'}\frac{1+i}{2}\left[\frac{1}{2}+C(\sigma)-i\left(\frac{1}{2}+S(\sigma)\right)\right]+O(\alpha_0^{-1}), \tag{11}$$

where $\sigma=\alpha_0 y'/(\pi\alpha_0 x')^{1/2}$. It is obvious that the right hand side of (11) is the anti-symmetric solution of the parabolic approximation that is found in May[1989].

4.PARABOLIC APPROXIMATION

According to the previous analysis, it is reasonable to assume the velocity potential of the form

$$\phi(x,y)=\psi(x,y)e^{-i\alpha_0(x\cos\mu_0+y\sin\mu_0)}. \tag{12}$$

If the angle of wave propagation μ_0 is large enough, ψ would be the anti-symmetric type solution of the parabolic approximation as stated previously. On the contrary, when $\mu_0=0$ (head sea case), Ohkus[1999] showed that ψ is the symmetric solution of the parabolic approximation. A difficulty may be expected, when $\mu_0=O(\alpha_0^{-1/2})$. In this case, the parabolic approximation leads

$$-2i\alpha_0\left(\frac{\partial\psi}{\partial x}-\mu_0\frac{\partial\psi}{\partial y}\right)+\frac{\partial^2\psi}{\partial y^2}=0, \tag{13}$$

in which the all terms are equal in order of magnitude when $x = O(1)$ and $y = O(\alpha_0^{-1/2})$. In such a order-assumption, the relative error of (13) is $O(\alpha_0^{-1})$.

To solve this equation, we require the conditions,

$$\psi(x,y) \to 1, \qquad \text{when} \quad y \to +\infty, \tag{14}$$

$$\psi(x,y) = 0, \qquad x < 0. \tag{15}$$

It is noted that these boundary conditions are not enough to solve (13). Another boundary condition is required along the line $y = 0$. This boundary condition is given from the matching condition that will be discussed later. Only the following condition is necessary here that guarantees the radiation condition of the solution in the water region.

$$\psi(1 + iT\alpha_0\mu_0) = T\frac{\partial \psi}{\partial y}, \qquad \text{on} \quad y = 0, \tag{16}$$

where T is a constant value.

The Fourier transformation technique is convenient to solve (13). The solution is represented in the Fourier transformation space,

$$\mathcal{F}[\psi(x,y) - H(x)] = A(l)e^{(i\alpha_0\mu_0 - \sqrt{2\alpha_0}\sqrt{l-\alpha_0\mu_0^2/2})y}. \tag{17}$$

To satisfy the boundary conditions, $A(l)$ shoul have the form

$$A(l) = -i\frac{1 + iT\alpha_0\mu_0}{l\left(1 + T\sqrt{2\alpha_0}\sqrt{l - \alpha_0\mu_0^2/2}\right)}. \tag{18}$$

The inverse Fourier transformation gives the solution

$$\begin{aligned}\psi(x,y) = {} & \frac{1+i}{2}\left[\frac{1}{2} + C(\sigma) - i\left(\frac{1}{2} + S(\sigma)\right)\right] \\ & -\frac{1-i}{4\sqrt{\pi}}\int_0^x \left(\frac{\sqrt{x-\xi}}{T\sqrt{\alpha_0}} - i\frac{\sqrt{\alpha_0}y}{\sqrt{x-\xi}}\right)\frac{[V_1(\xi) + V_2(\xi)]}{x-\xi}e^{-i\alpha_0\{y-(x-\xi)\mu_0\}^2/2(x-\xi)}d\xi,\end{aligned} \tag{19}$$

where

$$\begin{aligned}V_1(x) &= \frac{T\alpha_0\mu_0}{i + T\alpha_0\mu_0}erfc\left[\frac{(1+i)\sqrt{\alpha_0\mu_0^2}}{2\sqrt{2}}\sqrt{x}\right], \\ V_2(x) &= \frac{i}{i + T\alpha_0\mu_0}e^{-i(1+T^2\alpha_0^2\mu_0^2)x/2T^2\alpha_0}erfc\left[\frac{1-i}{2\sqrt{\alpha_0 T}}\sqrt{x}\right],\end{aligned} \tag{20}$$

and $erfc(x)$ is the complementary error function.

It is obvious that the first term of (19) remains when θ approaches to infinity. This is the anti-symmetry solution of the parabolic approximation that obtained in the previous section.

We also have the alternative form of (19),

$$\psi(x,y) = 1 - \frac{1-i}{2\sqrt{\pi}}\int_0^x \left(\frac{1}{T\sqrt{\alpha_0}}[V_1(\xi) + V_2(\xi)] + i\sqrt{\alpha_0}\mu_0\right)\frac{e^{-i\alpha_0\{y-(x-\xi)\mu_0\}^2/2(x-\xi)}}{x-\xi}d\xi. \tag{21}$$

This form shows that the solution approaches to the symmetric solution of the parabolic approximation when θ is very small.

In order to achieve the matching with the inner solution that will be discussed in the next section, a function $U(x)$ is defined as

$$U(x) = 1 - \frac{1-i}{2\sqrt{\pi}}\int_0^x \left(\frac{1}{T\sqrt{\alpha_0}}[V_1(\xi) + V_2(\xi)] + i\sqrt{\alpha_0}\mu_0\right)\frac{e^{-i\alpha_0(x-\xi)\mu_0/2}}{x-\xi}d\xi. \tag{22}$$

It is apparent that ψ approach to $U(x)$ when y approaches to zero.

5.INNER SOLUTION

It is noted that (19) does not satisfies the edge conditions, and the parabolic approximation ignores the exponentially-decay term that is one of fundamental solutions in the platform region. This fact implies the necessity of the inner solution, and the inner solution is valid in the region of $y = O(\alpha_0^{-1})$.

It is easily obtained that *psi* should satisfy the following equation in this region.

$$\frac{K}{h}\psi + \left[1 + M\left(-\alpha_0^2 - 2i\alpha_0\mu_0\frac{\partial}{\partial y} + \frac{\partial^2}{\partial y^2}\right)^2\right]\left(-\alpha_0^2 - 2i\alpha_0\mu_0\frac{\partial}{\partial y} + \frac{\partial^2}{\partial y^2}\right)\psi = 0. \tag{23}$$

The solution of (23) in the platform region is supposed to have the form

$$\psi_I(x,y) = U(x)\sum_{n=1}^{2} B_n e^{\left(\alpha_0 \sin\mu_0 - \sqrt{\alpha_n^2 - \alpha_0^2\cos\mu_0{}^2}\right)y} + B_0\psi(x,y). \tag{24}$$

It is obvious that the matching condition requests

$$B_0 = 1 \tag{25}$$

On the other hand the inner solution in the water region should satisfy (23) of the case $M = 0$. Therefore, the inner solution in the water region has the form

$$\phi_I = U(x)\sum_{n=1}^{2} B_n e^{-ik(x\cos\chi_R - y\sin\chi_R)}, \tag{26}$$

where k is the solution of dispersion relation in the water region $K/h = k^2$ and $\chi_R = Cos^{-1}\alpha_0\cos\mu_0/k$.

The continuity of the flux along the line $y = 0$ requires

$$\frac{1}{T} - i\alpha_0\mu_0 + i\sum_{n=1}^{2} B_n\sqrt{\alpha_n^2 - \alpha_0^2\cos^2\mu_0} = ik\sin\chi_R\sum_{n=0}^{2} B_n. \tag{27}$$

The so-called free-free boundary condition at the edge of platform requires two conditions

$$\sum_{n=1}^{2}\left[\alpha_n^4 + \alpha_0^2\cos^2\mu_0(1-\nu)\alpha_n^2\right]\sqrt{\alpha_n^2 - \alpha_0^2\cos^2\mu_0}B_n + \left(\frac{1}{T} - i\alpha_0\mu_0\right)\alpha_0^4[1+\cos^2\mu_0] = 0 \tag{28}$$

$$\sum_{n=0}^{2}\left[\alpha_n^4 - \alpha_0^2\cos^2\mu_0(1-\nu)\alpha_n^2\right]B_n = 0. \tag{29}$$

Now we have three equations and three unknowns, thus the inner solution is completely determined with a simple linear algebra.

6.CONCLUDING REMARKS

It was found that the hydro-elastic behavior of a very large floating structure is represented with a simple equation by applying the parabolic approximation. It seems that this result is also extended to the case $\mu_0 < 0$ and to the improvement of the sudden change of wave elevation that appears in the water region. These will be the future works. Finally, it should be noted that the corner effect is still the problem, and further study is necessary since the magnitude of motion at corners of the platform is usually big.

REFERENCES

OHKUS, M. :*Hydroclastic Interaction of a Large Floating Platform with Head Seas*, Proc. of 14th Int. WWWFB, 1999, pp.119-122.

MAY, C.C. :*Applied Ocean Waves*, World Science Publishing, 1989

TAKAGI, K. :*Hydroelastic Behavior of a Very Large Floating Structure*, Proc. of 14th Int. WWWFB, Port Huron, 1999, pp.137-140.

TAKAGI, K. and KOHARA, K. :*Application of the Ray Theory to Hydroelastic Behavior of VLFS*, Proc. of 10th ISOPE, Seattle, Vol.1, 2000, pp.72-77.

(16th International Workshop on Water Waves and Floating Bodies, 22-25 April, 2001)

Development of a 3D-NWT for simulation of running ship motions in waves

Katsuji Tanizawa and Makiko Minami

Ship Research Institute,
6-38-1 Shinkawa, Mitaka, Tokyo, Japan

1 Introduction

Numerical Wave Tank (NWT) is a generic name of numerical simulators for nonlinear free surface waves, hydrodynamic forces and floating body motions. In the past two decades, a lot of efforts have been made to develop theories and numerical techniques for NWT.

The first pioneer work was the development of well known mixed Eulerian and Lagrangian method (MEL) by Longuet-Higgins and Cokelet (1976). In MEL method, as its name shows, Eulerian field equations are solved to obtain fluid velocity, and obtained velocity is used to track fluid particles on the free surface in Lagrangian way. The development of MEL enabled us to compute fully nonlinear free surface motions in time domain.

The second pioneer work was the development of modal decomposition method by Vinje and Brevig (1981). They introduced acceleration field and showed how to determine pressure distribution and resulting floating body acceleration simultaneously. This was the first consistent method to simulate nonlinear floating body motions in time domain. Cointe et al.(1990) used this method in their NWT. Following these works, other three consistent methods were developed in rapid succession. Tanizawa (1995) developed implicit boundary condition method. Berkvens (1998) developed 3D-NWT based on this method. Recently, Ikeno (2000) and Shirakura (2000) also developed 3D-NWT based on implicit boundary condition method. Cao et al.(1994) developed iterative method. Wu and Eatock-Taylor (1996) extended the modal decomposition method and proposed a new indirect method. Kashiwagi (1998) used this method as faster solver of floating body motions.

By these research efforts, theories and numerical techniques were developed and prepared as necessary parts of NWT. Nowadays, using these parts, we can develop practical 2D-NWT as we wish. On the other hand, development of practical 3D-NWT is still tough work. We have to develop additional theories and various numerical techniques for 3D-NWT. Desktop computers are still not powerful enough to run 3D simulations. However, development of 3D-NWT is present hot topic. Many challenging works are on going and overcoming the difficulties.

The authors are also developing 3D-NWT. The target of our 3D-NWT is simulation of running ship motions in waves. In this abstract, the basic formulations of our 3D-NWT and simulated results of running modified Wigley hull motions are presented.

2 Formulation

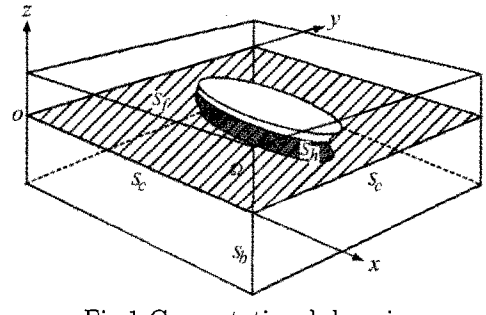

Fig.1 Computational domain

Fig.1 shows the computational domain bounded by free surface S_f, four vertical control surface S_c, a bottom S_b and hull surface S_h. Reference frame $o-xyz$ is a inertial system advancing with ship in constant velocity. The fluid is assumed to be homogeneous, incompressible, inviscid and its motion irrotational. All variables are nondimensionalized using fluid density ρ, gravitational acceleration g and hull length L. Velocity potential ϕ is used to describe the ideal fluid motion. In the fluid domain, the velocity potential satisfies Laplace's equation $\nabla^2\phi = 0$. Applying Green's theorem, boundary integral equation (BIE)

$$c(Q)\phi(Q) = \int_S \phi(P)u_n(P,Q) - u(P,Q)\phi_n(P)ds \quad (1)$$

is obtained, where P and Q are points on the boundary S, $c(Q)$ is solid angle of the boundary at point Q, $u(P,Q) = 1/||P-Q||$ is kernel function. Subscript n denotes the operation $\boldsymbol{n}\cdot\nabla$ in

E-mail tanizawa@srimot.go.jp URL http://www.srimot.go.jp/dyn/waveload.html

which $\boldsymbol{n}$ is the unit surface normal vector. This BIE is valid also for $\partial\phi/\partial t \equiv \phi_t$.

Originally, NWT is developed for nonlinear time domain simulation. However, 3D-NWT requires large amount of computation. Capacity and speed of desktop computers are still not enough to simulate practical problems. Therefore, as the first step, the authors developed a linearized 3D-NWT to test various ideas by trial and error. In the linear NWT, the boundary shape is fixed to the mean position of oscillation and following boundary conditions (BC) for velocity field and accceleration field are imposed on it.

- Free surface

$$\frac{\partial\zeta}{\partial t} = \phi_z - \frac{\partial\phi}{\partial x}\frac{\partial\zeta}{\partial x} - \frac{\partial\phi}{\partial y}\frac{\partial\zeta}{\partial y} , \tag{2}$$

$$\frac{\partial\phi}{\partial t} = -\zeta - \frac{1}{2}(\nabla\phi\cdot\nabla\phi) , \tag{3}$$

where ζ is wave elevation. Value of ϕ on $z=0$ is given by time integral of eq.(3). The second order term $(\nabla\phi\cdot\nabla\phi)/2$ is left to consider the steady wave field by running ship.

- Hull surface

$$\frac{\partial\phi}{\partial n} = \boldsymbol{n}\cdot(\boldsymbol{V}+\boldsymbol{\omega}\times\boldsymbol{r}) \tag{4}$$

$$\frac{\partial\phi_t}{\partial n} = \boldsymbol{n}\cdot(\dot{\boldsymbol{V}}+\dot{\boldsymbol{\omega}}\times\boldsymbol{r}) \tag{5}$$

where $\boldsymbol{V}$, $\boldsymbol{\omega}$ are velocity and angular velocity of the hull respectively, $\boldsymbol{r}$ is position vector of hull surface from the center of gravity.

- Bottom

$$\frac{\partial\phi}{\partial n} = \frac{\partial\phi_t}{\partial n} = 0 \tag{6}$$

- Vertical control surface

$$\frac{\partial\phi}{\partial n} = \frac{\partial\phi_o}{\partial n}, \quad \frac{\partial\phi_t}{\partial n} = \frac{\partial\phi_{ot}}{\partial n} \tag{7}$$

where ϕ_o is velocity potential of linear propagating waves observed from $o-xyz$ system.

To determine the acceleration of the hull $\dot{\boldsymbol{V}},\dot{\boldsymbol{\omega}}$, we need pressure distribution $p=-\phi_t-(\nabla\phi)^2/2-z$ on the hull. Therefore, the acceleration is unknown before we solve BIE of ϕ_t . This means we can not use BC(5) explicitly and some implicit methods are indispensable to solve the acceleration field. As explained in the introduction, implicit methods were studied in the past two decades and following four methods were available now.

(1) Iterative method
(2) Modal decomposition method
(3) Indirect method
(4) Implicit boundary condition method

In the present linear 3D-NWT code, the authors use modal decomposition method to save memory and CPU time. Above four methods are reviewed by Tanizawa(2000).

3 Simulation

3.1 Target of the simulation

For test trials of the newly developed 3D-NWT, motions of a modified Wigley hull were simulated. The modified Wigley hull form is defined as

$$\eta = (1-\xi^2)(1-\zeta^2)(1+0.2\xi^2) + \zeta^2(1-\zeta^8)(1-\xi^2)^4 , \tag{8}$$

where $\xi = 2x/L$, $\eta = 2y/B$, $\zeta = z/d$. The principle dimensions are shown in Table 1.

Table 1 Principle dimensions of ship

Length: L	$1L$
Breadth: B	$0.15L$
Draft: d	$0.0625L$
Displacement: ∇	$0.56LBd$
Water-Plane Area: A_w	$0.693LB$
Center of Gravity: OG	$0.012L$
Gyrational Radius: k_{yy}	$0.2325L$

The 3D-NWT is bounded by $4L\times 4L$ square free surface area, four vertical control surfaces and a bottom at the depth L . Wave damping zone, used by Cointe(1990), is allocated at the border of the free surface. Since the breadth of the damping zone is L , the effective free surface is $2L\times 2L$ square area. Boundary panels of the hull and NWT are shown in Fig.3 and Fig.4. On the damping zone, larger panels are used. At the location where flux is discontinuous such as intersection lines of free surface and hull, corner points on NWT and etc., double nodes and triple nodes are collocated. For this NWT, a higher order BEM (HOBEM) is newly developed. This HOBEM supports mixed use of triangular element (linear and quadratic) and rectangular element (linear, quadratic and Lagrangian). For the following simulation, linear triangular and linear rectangular elements are used. Total number of elements and collocation points are 4560 and 4827, respectively.

3.2 Simulated results

Using the 3D-NWT, motions of the running modified Wigley hull were simulated in regular waves. Parameters of simulations were 1) $\chi = 180deg.$ (head sea), 2) $Fn = 0.2$ and 3) $\lambda/L = 0.5 \sim 3.0$. Fig.5 shows simulated wave field around the hull at an instant of the periodical motion. Diffraction and radiation wave by hull is significant for shorter waves. We can observe small amplitude Kelvin wave pattern, too. However, the present code is still unstable for high speed simulation and convergence of Kelvin wave may be insufficient. The results presented in this paper is obtained by short simulation of about 10 wave encounter periods.

Next, simulated heave and pitch responses are shown in Fig.6. The thick solid line with black circle shows the result of simulation by 3D-NWT. The

thin solid line, broken line and white circle shows the result of enhanced unified theory (EUT), NSM and experiment by Kashiwagi et al.(2000). In comparison with heave responses, you see a gap in resonant frequency between NWT and others. The reason of this gap is under investigation and not clear now. In comparison with pitch responses, agreement between NWT and others are good. NWT gives a little larger response which looks nearer to experiment than EUT and NSM. Looking at phase, agreement between NWT and others is good in longer wave range. However in short wave range, $\lambda/L < 1.0$, the agreement is not enough. Since the panel size is fixed for entire wave range, lack of resolution may be the reason of this disagreement in shorter wave range.

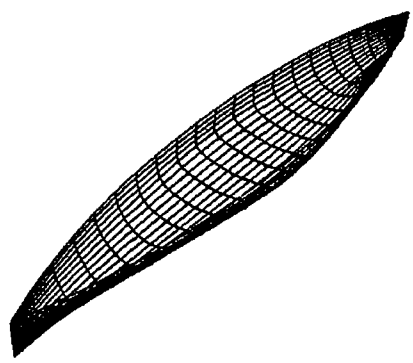

Fig.3 Boundary panels on the ship hull

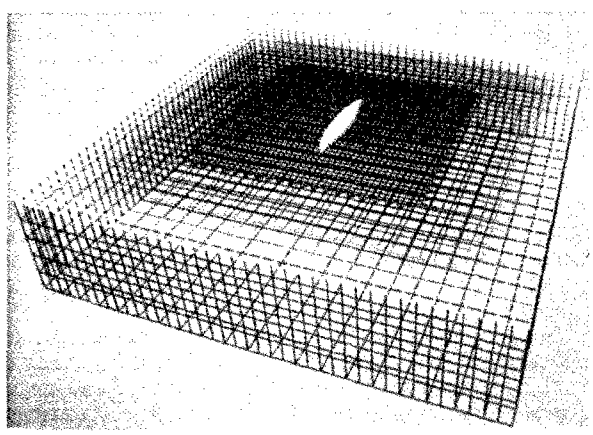

Fig.4 Boundary panels on NWT

4 Conclusion

In this short paper, a newly developed 3D-NWT is introduced and simulated running modified Wigley hull motions are reported promptly. The results qualitatively agree with EUT, NSM and experimental data of Kashiwagi. However, the accuracy and numerical stability are still insufficient. To make this 3D-NWT practicable, we have to stabilize the free surface simulation around hull and check the accuracy of hydrodynamic force and motions precisely. Diffraction problem, radiation problem and radiation-diffraction problem should be simulated step by step for systematic accuracy check. Result of these systematic accuracy check will be reported at the workshop.

Our final goal is development of fully nonlinear 3D-NWT for simulation of running ship motions in waves. After we complete linear 3D-NWT, we intend to extend it to body surface nonlinear code and fully nonlinear code step by step.

References

1) Longuet-Higgins,M.S. and Cokelet,E., (1976), "The deformation of steep surface waves on water I. A numerical method of computation", *Proc. Roy. Soc.* ser.A350, pp.1-26

2) Vinje, T. and Brevig, P. (1981), "Nonlinear Ship Motions", *Proc. 3rd. Int. Conf. on Num. Ship Hydro.*, pp.IV3-1-IV3-10

3) Cointe,R.,Geyer,P.,King,B.,Molin,B. and Tramoni,M. (1990), "Nonlinear and linear motions of a rectangular barge in perfect fluid", *Proc. 18th Symp. on Naval Hydro.*, AnnArbor, Michigan, pp.85-98

4) Tanizawa,K., (1995), "A Nonlinear Simulation Method of 3-D body Motions in Waves", *J. Soc. Nav. Arch. Japan*, vol.178, pp.179-191

5) Van Daalen, E.F.G. (1993), "Numerical and Theoretical Studies of Water Waves and Floating Bodies", *Ph.D. thesis*, University of Twente, The Netherlands, pp.1-285

6) Berkvens,P.J.F. (1998), "Floating bodies interacting with water waves", *Ph.D. thesis*, University of Twente, The Netherlands, pp.1-161

7) Ikeno,M., (2000), "A numerical model for 3-D floating body motion in nonlinear waves using the BEM", *Proc. 10th ISOPE Conf.*, Vol.3, pp.201-213

8) Shirakura,Y., Tanizawa,K. and Naito,S. (2000), "Development of 3-D fully nonlinear numerical wave tank to simulate floating bodies interacting with water waves", *Proc. 10th ISOPE Conf.*, Seattle, Vol.3, pp.253-262

9) Wu, G.X. and Eatock Taylor, R. (1996), "Transient motion of a floating body in steep water waves", *Proc. of 11th Int. Workshop on Water Waves and Floating Bodies*, Hamburg

10) Kashiwagi, M. (1998), "Nonlinear simulations of wave-induced motions of a floating body by means of MEL method", *Proc. of 3rd Int. Conf. on Hydrodynamics*, Seoul.

11) Cao, Y., Beck, R. and Schultz, W.W. (1994), "Nonlinear motions of floating bodies in incident waves", *9th Workshop on Water Waves and Floating Bodies*, Kuju,Oita, pp.33-37

12) Kashiwagi,M., Kawasoe,K. and Inada,M. (2000), "A study on ship motion and added resistance in waves", *J.Kansai Soc. N. A. Japan*, Vol.234, pp.85-94

13) Tanizawa,K., (2000),", The state of the art on numerical wave tank", *Proc. 4th Osaka colloquium on seakeeping performance of ships*, pp.95-114

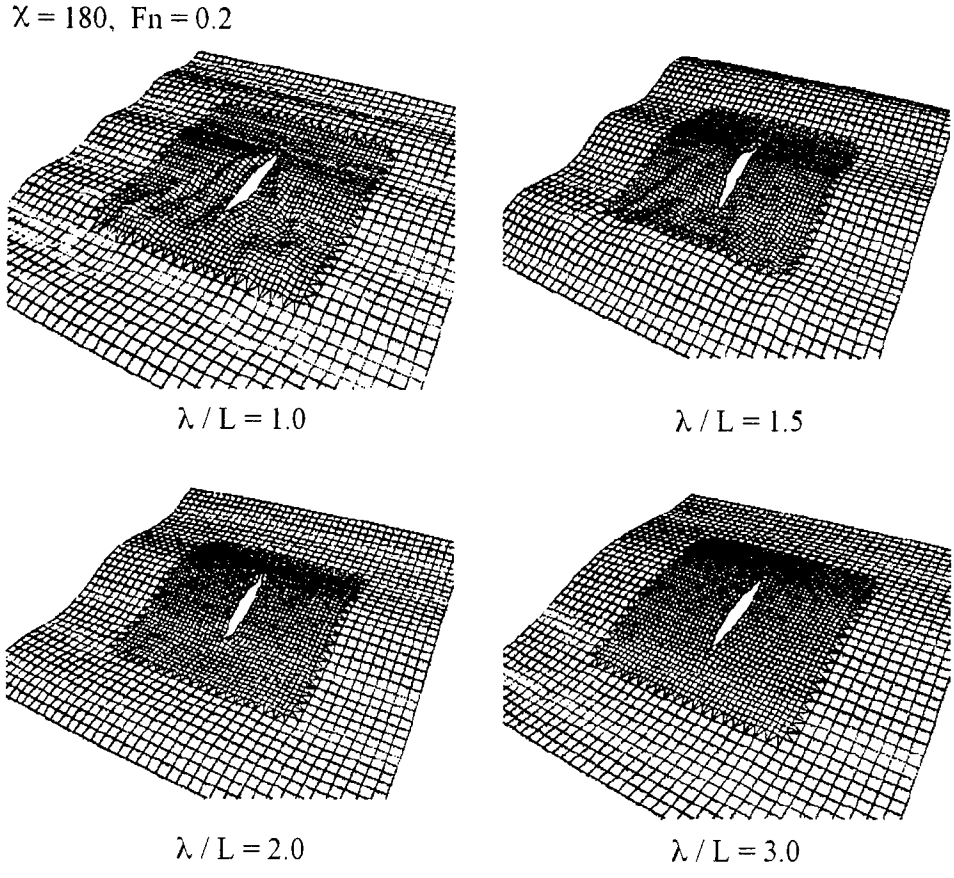

Fig.5 Wave Field around running ship hull

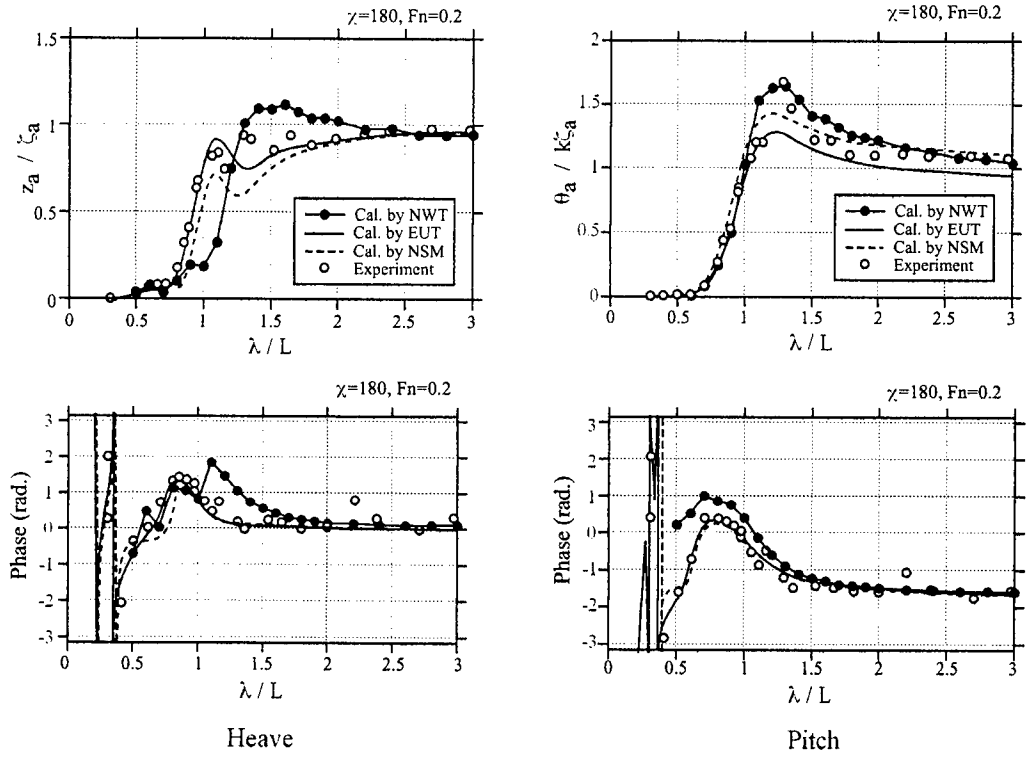

Fig.6 Simulated heave and pitch responses

Fast Multipole Method for Hydrodynamic Analysis of Very Large Floating Structures *

Tomoaki Utsunomiya & Eiichi Watanabe
Department of Civil Engineering, Kyoto University, Kyoto, Japan
Naoshi Nishimura
Department of Global Environmental Engineering, Kyoto University, Kyoto, Japan

1 Introduction

For linear hydrodynamic analysis of floating structures, boundary element methods (BEM) employing the free-surface Green function are frequently used as basic design tools. However, when the methods are applied for the analysis of Very Large Floating Structures (VLFS), the number of unknowns ($= N$) reaches the order of 10^4–10^5 and thus large storage requirement ($O(N^2)$) and the excessive computation time ($O(N^3)$ for factorization solvers or $O(N^2)$ for iterative solvers) make the application of conventional BEM impractical. The precorrected-FFT method [1, 2] has been successfully applied to such a large scale analysis, but not yet for a VLFS in shallow water. We hereby present an alternative approach using fast multipole methods [3, 4, 5], which have been more commonly used in many fields that would require excessive computation resources.

It is known that a fast multipole method for Helmholtz' equation in 2D is possible with the help of Graf's addition theorem for the Hankel function (see Fukui & Katsumoto [6], for example). Because the free surface Green function in shallow water is represented by series of Bessel and Hankel functions, the fast multipole method for linear wave diffraction/radiation problems can be formulated as a straight forward extention of the method applied to 2D Helmholtz' equation. Because the Green function in the series form converges rapidly when horizontal distance between source and field points relative to the water depth is large, the method will be most efficient when the horizontal dimensions of the analyzed area are large compared with the water depth. This is just the case for a VLFS in shallow water. We have implemented the multipole acceleration algorithm to our higher-order boundary element program [7] (which is based on the integral equation proposed in [8]), and examined its efficiency by benchmark calculations including VLFS response analysis in variable water depth environment of a real sea.

2 Formulations

The Green function in finite depth water of h can be represented by

$$G = \sum_{m=0}^{\infty} \frac{2K_0(k_m R)}{N_m} \cos k_m(z+h) \cos k_m(\zeta+h) \tag{1}$$

where $N_m = \frac{h}{2}(1 + \sin 2k_m h / 2k_m h)$, $k_m \tan k_m h = -\omega^2/g$, k_m $(m \geq 1)$ is positive real and $k_0 = \mathrm{i}k$, k: the wave number, g: gravitational acceleration, and time variance of $\mathrm{e}^{\mathrm{i}\omega t}$ is assumed for all first order quantities, R denotes the horizontal distance between the reference and the source points, and z and ζ are their vertical coordinates, respectively.

Graf's addition theorem for Bessel functions yields:

$$K_0(k_m R) = \sum_{n=-\infty}^{\infty} K_n(k_m r)\mathrm{e}^{\mathrm{i}n\theta} I_n(k_m \rho)\mathrm{e}^{-\mathrm{i}n\Phi} \tag{2}$$

*This study was supported by the Program for Promoting Fundamental Transport Technology Research from the Corporation for Advanced Transport & Technology (CATT).

where (r, θ) and (ρ, Φ) represent the horizontal coordinates of the reference and the source points, respectively, measured from the origin O which can be arbitrarily (but $r > \rho$) chosen. Substitution of Eq.(2) into Eq.(1) yields:

$$G = \sum_{m=0}^{\infty} \frac{2}{N_m} \sum_{n=-\infty}^{\infty} M_{mn} K_n(k_m r) \mathrm{e}^{\mathrm{i}n\theta} \cos k_m(z+h) \tag{3}$$

$$M_{mn} = I_n(k_m \rho) \mathrm{e}^{-\mathrm{i}n\Phi} \cos k_m(\zeta + h) \tag{4}$$

Note that the Green function is now represented in the form of multipole expansion around O. Therefore, we are now ready to apply the fast multipole algorithm. The normal derivative at the source point, $\partial G/\partial n$, can also be represented by the same form, with just replacing M_{mn} by $\partial M_{mn}/\partial n$. The origin of the multipole expansion can be moved arbitrarily (under $r > \rho$), and the coefficient $\tilde{M}_{m\nu}$ for the new origin O' can be calculated from M_{mn} at O by

$$\tilde{M}_{m\nu} = \sum_{n=-\infty}^{\infty} M_{mn} I_{\nu-n}(k_m \xi) \mathrm{e}^{-\mathrm{i}(\nu-n)\psi} \tag{5}$$

where (ξ, ψ) is the polar coordinate of O measured from O'. This can also be obtained from Graf's addition theorem.

In the evaluation of the integral $\int GV\mathrm{d}S$ (same procedure can be applied to $\int G_n \phi \mathrm{d}S$ in the followings), the influences from near panels are evaluated directly in a conventional manner; however, the influences from far panels can be evaluated using Eq.(3) where the M_{mn} is replaced by

$$M_{mn}^B = \int_{S_{far}} M_{mn} V \mathrm{d}S \tag{6}$$

where S_{far} represents the surface at the far distance from the collocation point. Firstly, we calculate M_{mn}^B for each panel locating the multipole expansion point at the horizontal coordinates of the panel center, then gather them at the center of 'leaf-cell' as a group of several panels, where Eq.(5) can be utilized. Further, a group of four cells form an upper level cell, and M_{mn}^B is also calculated at the center of the upper cell. Note that at this stage, we need not specify the reference (or collocation) points. We may define the level 0 cell as a square cell including all panels, and then level 1 cell as a quater portion of the level 0 cell, level n cell as a quarter of level $n-1$ cell, *etc.* [5]. After setting up the multipole coefficients M_{mn}^B for all cells at each level, we calculate $\int GV\mathrm{d}S$ utilizing Eqs.(3) and (6) for each collocation point, where larger cells are selected as far as possible. This hierarchical algorithm is known to be $O(N \log N)$ for the computation time [4]. Although the $O(N)$ algorithm [3, 5] is also possible as has been made by Fukui & Katsumoto [6] we hereby implemented the $O(N \log N)$ algorithm because of its simplicity and easiness for developing parallelized program. Because the integrals can be evaluated very fast using these algorithms, we can solve the integral equation with an iterative solver without holding large part of coeffieient matrices. The requirement of only $O(N)$ storage may be the most attractive feature of the method.

When a factorization solver is used, we usually use modal expansion approach to VLFS hydroelastic analysis, where a number of radiation problems are solved separately for each mode, and then generalized added-mass and radiation damping are calculated for modal coordinates [7]. However, it is not the case when an iterative solver is used; we would like to have the final solution from only one iterative procedure without solving a number of separate radiation problems. This can be done by solving the structural problem in each step of the iterative procedure and finding the relationships between ϕ_n and ϕ on the wetted-surface of the structure. If the modal method is applied, this may be represented schematically for a flat-bottom VLFS by

$$\{\phi_n\} = \rho\omega^2 [f][K - \omega^2 M]^{-1}[L]\{\phi\} \tag{7}$$

where $[f]$, $[K - \omega^2 M]$, and $[L]$ are $8N_E \times P$, $P \times P$, and $P \times N$ matrices, respectively, where N_E and N are the numbers of panels and nodes on the bottom surface of the VLFS, and P is the number

of deflection modes as an elastic plate. It should be noted that a large part of memory allocation is consumed for storing these matrices for the Fast Multipole Method in Table 1; the memory allocations only for hydrodynamic part are less than half of the indicated values.

A box-like VLFS, either in constant depth sea $h = 8$m or in variable depth sea (Fig.1), has been analyzed for the oblique wave of $\beta = \pi/4$ ($\beta = 0$ corresponds to the head wave from positive x direction and $\beta = \pi/2$ to the beam wave from positive y direction). The specifications of the VLFS are: the length $L = 1,500$m, the beam $B = 150$m, the draft $d = 1$m, the rigidity as an elastic plate $D = 3.88 \times 10^7$ kNm, and the Poisson's ratio $\nu = 0.3$. Number of modal functions employed are 160 (20 in longitudinal & 8 in beam). Results are shown in Tables 1 and 2, and Figs.2-5.

Table 1: Performance of the fast multipole method and the direct method using LU factorization on an EWS node (IBM RS/6000SP; POWER3 375MHz). The residual tolerance in GMRES $\epsilon = 10^{-4}$, $L/\lambda = 9.57$ ($T = 18$sec), $h = 8$m (constant). Values in parentheses are estimates.

Model	Typical panel size, Δ	Number of nodes	Fast Multipole Method				Direct Method	
			Number of iter.	CPU time per iter.	CPU time	Memory allocation	CPU time	Memory allocation
A	25m	1,609	31	3 sec	1.80 min	27 MB	1.55 min	54 MB
B	12.5m	5,377	32	15 sec	10.4 min	89 MB	28.5 min	489 MB
C	6.25m	19,393	32	86 sec	77.4 min	315 MB	(907 min)	(6 GB)
D	3.125m	73,345	32	570 sec	775 min	1.15 GB	(708 hr)	(85 GB)

Table 2: Numbers of iterations of GMRES and computation times for various L/λ. $h = 8$m (constant).

Model	L/λ	Wave period	Number of iterations		CPU time	
			$\epsilon = 10^{-3}$	$\epsilon = 10^{-4}$	$\epsilon = 10^{-3}$	$\epsilon = 10^{-4}$
C	9.57	18 sec	25	32	1.15 hr	1.29 hr
C	17.9	10 sec	112	148	3.46 hr	4.40 hr
C	33.2	6 sec	252	497	8.23 hr	15.7 hr
D	62.0	4 sec	287	—	63.8 hr	—
D	62.0	4 sec	287	—	14.5 hr*	—

*Parallel computation using 5 CPUs.

References

[1] T. Korsmeyer, J. Phillips and J. White, A precorrected-FFT algorithm for accelerating surface wave problems, *Proc. 11th IWWWFB*, Hamburg (1996).

[2] T. Korsmeyer, T. Klemas, J. White and J. Phillips, Fast hydrodynamic analysis of large offshore structures, *Proc. 9th Int. Offshore & Polar Eng. Conf.* (1999) 27–34.

[3] V. Rokhlin, Rapid solution of integral equations of classical potential theory, *J. Comput. Phys.* **60** (1983) 187–207.

[4] J. Barnes and P. Hut, A hierarchical $O(N \log N)$ force-calculation algorithm, *Nature* **324** (1986) 446–449.

[5] L. Greengard, *The Rapid Evaluation of Potential Fields in Particle Systems*, (1988) MIT Press.

[6] T. Fukui and J. Katsumoto, Fast multipole algorithm for two dimensional Helmholz equation and its application to boundary element method, *Proc. of 14th Japan National Symp. on Boundary Element Methods*, (1997) 81–86 (in Japanese).

[7] T. Utsunomiya, E. Watanabe and R. Eatock Taylor, Wave response analysis of a box-like VLFS close to a breakwater, *Proc. 17th Int. Conf. on Offshore Mech. & Arctic Eng.* (1998) OMAE98-4331.

[8] B. Teng and R. Eatock Taylor, New higher-order boundary element methods for wave diffraction/radiation, *Appl. Ocean Res.* **17** (1995) 71–77.

[9] R. Barrett, *et al.*, *Templates for the Solution of Linear Systems: Building Blocks for Iterative Methods*, (1994) SIAM.

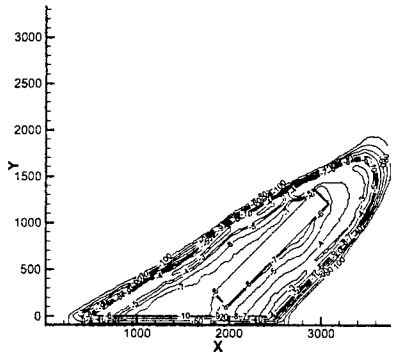

Figure 1: Contour plot of the variable depth configuration.

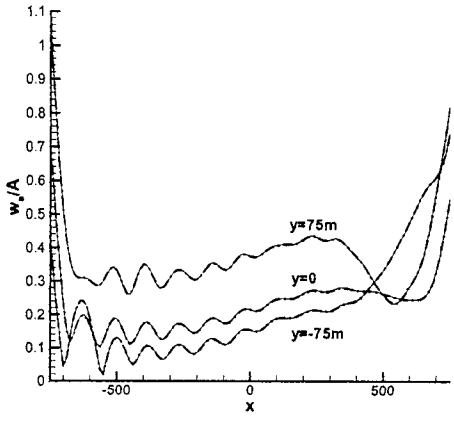

Figure 2: Deflection amplitudes of VLFS in costant depth sea (model B) at $T = 18$sec. — : direct method, - - -: fast multipole method ($\epsilon = 10^{-3}$).

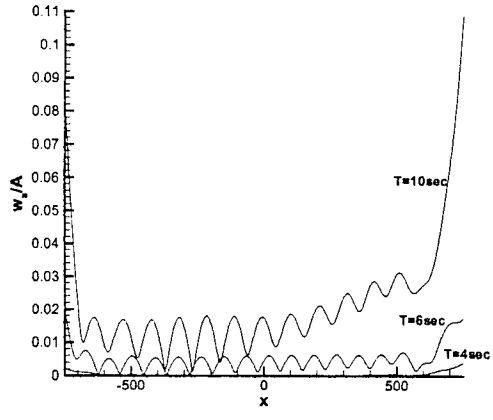

Figure 3: Deflection amplitudes of VLFS in costant depth sea for various T along $y = 0$.

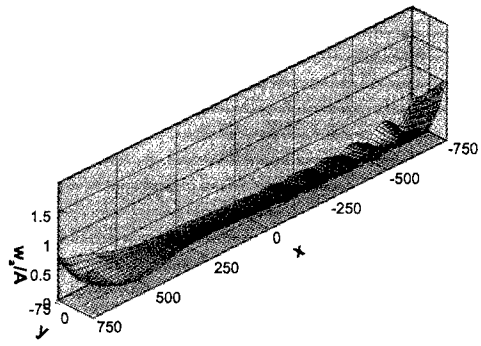

(a) in constant depth sea ($h = 8$m).

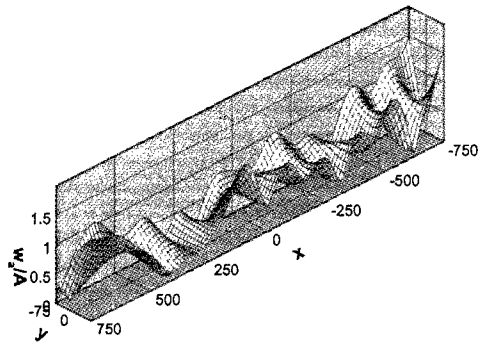

(b) in variable depth sea.

Figure 4: Deflection amplitudes at $T = 18$sec.

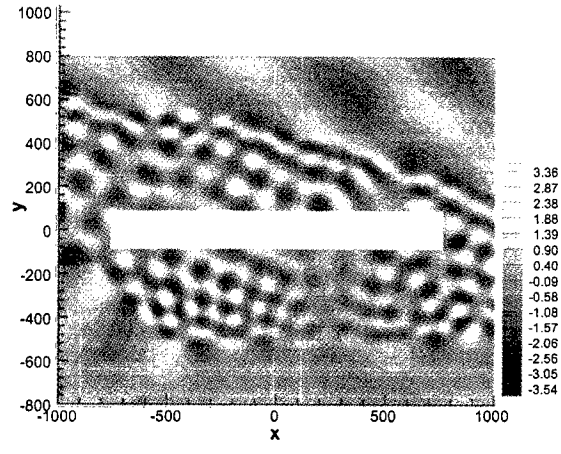

Figure 5: Snapshot of the surface elevation around the floating body in the variable depth sea. $T = 18$sec, total nodes: 67,098 (61,721 for the sea-bottom surface, 5377 for the VLFS).

The Coupled Finite Element and Boundary Element Analysis of Nonlinear Interactions Between Waves and Bodies

G.X. Wu+ and R. Eatock Taylor*

+ Department of Mechanical Engineering, University College London, Torrington Place, London WC1E 7JE, UK
* Department of Engineering Science, University of Oxford, Parks Road, Oxford OX1 3PJ, UK

1. INTRODUCTION

The fully nonlinear wave/body interaction problem is usually solved through a time stepping technique based on the potential flow theory. At each time step, the potential is commonly found by using the boundary element method (BEM) or the finite element method (FEM). The BEM divides only the boundary of the fluid domain into small panels. Early examples of the BEM for two dimensional (2D) flow include the work by Longuet-Higgins & Cokelet (1976), Faltinsen (1977), Vinje & Brevig (1981) and Lin et al (1984). More recent applications of the BEM to three dimensional (3D) flow include those published by Ferrant (1994) and Celebi et al (1998). The FEM, on the other hand, divides the entire fluid domain into small elements. Typical applications for 2D flow include those by Wu & Eatock Taylor (1994, 1995), Clauss & Steinhagen (1999), Robertson & Sherwin (1999); and for 3D flow include Wu et al (1998) and Ma et al (2001a, 2001b).

As argued by Wu & Eatock Taylor (1995, 1996) and Ma et al (2001a, 2001b), although the BEM has far fewer unknowns when applied to the wave/body interaction problem, it usually requires considerably more memory for "large" meshes because it leads to fully populated matrices. (An exception is when a multi-subdomain BEM approach is used, as for example by Wang et al 1995; and there may be other ways of improving the efficiency of the BEM). By contrast, direct application of the FEM needs significantly less memory and it is computationally more efficient. A drawback of the FEM, however, is the mesh generation. For a body having a complicated geometry, a sophisticated mesh generator is usually required to follow the motion of the body and the wave. Greaves et al (1997), for example, adopted a quadtree-based mesh generation scheme for the 2D problem. The scheme was found to be efficient when the horizontal and vertical dimensions of the fluid domain are comparable. For an extremely long or thin domain, the CPU requirement for the mesh generator increases rapidly. As remeshing is needed at every time step or after every few time steps, excessive CPU consumed by the mesh generator at each time step will make the overall computation very inefficient.

The present work therefore explores the use of a coupled BEM and FEM approach. Near the body, the BEM is used, as a boundary element mesh is easier to create in that region. Also, when the BEM is confined to a small domain, its memory requirement is limited. Away from the body, the fluid domain will be regular if the wave does not overturn or break. This allows some simple mesh generator to be used, which can deal efficiently with a large (including extremely long or thin) fluid domain. The adopted BEM and FEM are based on the approach described in Wu & Eatock Taylor (1995). The additional work required is to ensure that the potential and velocity are continuous at the interface of the BEM and FEM domain. This is achieved through iteration, in a similar manner to the approach used in that paper where we implemented the domain decomposition method for the FEM.

2. COUPLED FINITE AND BOUNDARY ELEMENT METHOD

We consider the interaction of a wave generated by a piston-like wavemaker with a two dimensional body. A Cartesian coordinate system Oxy is defined in which y coincides with the initial position of the wavemaker and points vertically upwards, and the origin of the system is on the mean free surface. All the physical parameters are nondimensionalized by the density of the fluid ρ, a typical dimension of the body L and the time $\sqrt{L/g}$, where g is the acceleration due to the gravity. The fluid is assumed to be incompressible and inviscid, and the flow is assumed to be irrotational. A velocity potential ϕ can then be introduced, which satisfies the Laplace equation and the usual non-linear boundary conditions on the body surface, free surface and wavemaker .

As shown in Figure 1, the fluid domain is divided into three regions. R_1 and R_3 are away from the body, where the finite element method can be adopted as the mesh can be generated easily. R_2 encloses the body,

where the boundary element method can be used. The continuity of the potential and velocity is enforced on the two interfaces Γ_{12} and Γ_{23}.

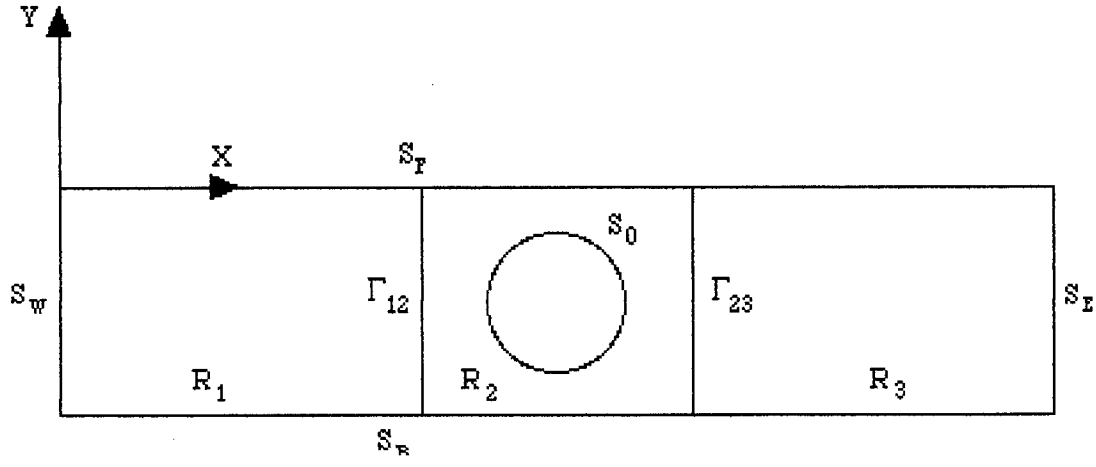

Figure 1 The coupled FEM and BEM computational domain

Based on the finite element method, the potential in R_1 can be written as

$$\phi^{(1)} = \sum_{j=1}^{n_1} \phi_j^{(1)} N_j(x,y) \tag{1}$$

where ϕ_j are the nodal values of the potential, n_1 is the number of the nodes in R_1 and $N_j(x,y)$ are the shape functions, which have been chosen to vary linearly over triangular elements in the present analysis. Application of the Galerkin method within R_1 leads to

$$\int_{R_1} \nabla N_i \sum_{j=1}^{n_1} \phi_j^{(1)} \nabla N_j dR|_{j\notin S_{F_1}} = -\int_{R_1} \nabla N_i \sum_{j=1}^{n_1} \phi_j^{(1)} \nabla N_j dR|_{j\in S_{F_1}} - U_0 \int_{S_w} N_i dS - \int_{\Gamma_{12}} \frac{\partial \phi^{(2)}}{\partial n} N_i dS\,. \tag{2}$$

It should be noted that the direction of the normal of Γ_{12} changes sign from R_1 to R_2.

Within R_2, the complex potential $\beta = \phi^{(2)} + i\psi^{(2)}$ is defined, where $\psi^{(2)}$ is the stream function. Along the boundary we can write

$$\beta = \sum_{j=1}^{n_2} \beta_j N_j(z)\,. \tag{3}$$

β_j are the nodal values of the complex potential and the interpolation function is chosen as

$$N_j(z) = \begin{cases} (z - z_{j+1})/(z_j - z_{j+1}) & z \in (z_j, z_{j+1}) \\ (z - z_{j-1})/(z_j - z_{j-1}) & z \in (z_{j-1}, z_j) \\ 0 \qquad z \notin (z_{j-1}, z_{j+1}) \end{cases}\,. \tag{4}$$

Application of Cauchy's theorem gives

$$\sum_{j=1}^{n_2} A_{kj}\phi_j^{(2)}\,|_{j\in S_0+S_{B_2}} + i\sum_{j=1}^{n_2} A_{kj}\psi_j^{(2)}\,|_{j\in S_{F_2}+\Gamma_{12}+\Gamma_{23}} = -\sum_{j=1}^{n_2} A_{kj}\phi_j^{(2)}\,|_{j\in S_{F_2}} - \sum_{j=1}^{n_2} A_{kj}\phi_j^{(2)}\,|_{j\in\Gamma_{12}} - \sum_{j=1}^{n_2} A_{kj}\phi_j^{(2)}\,|_{j\in\Gamma_{23}} - i\sum_{j=1}^{n_2} A_{kj}\psi_j^{(2)}\,|_{j\in S_0+S_{B_2}}, \tag{5}$$

where

$$A_{kj} = \frac{z_k - z_{j-1}}{z_j - z_{j-1}}\ln\frac{z_j - z_k}{z_{j-1} - z_k} + \frac{z_k - z_{j+1}}{z_j - z_{j+1}}\ln\frac{z_{j+1} - z_k}{z_j - z_k}. \tag{6}$$

In R_3, we can write

$$\int_{R_{31}} \nabla N_i \sum_{j=1}^{n_3} \phi_j^{(3)} \nabla N_j dR\,|_{j\in S_{F_3}+S_E} = -\int_{R_1} \nabla N_i \sum_{j=1}^{n_3} \phi_j^{(3)} \nabla N_j dR\,|_{j\in S_{F_3}+S_E} - \int_{\Gamma_{23}} \frac{\partial\phi^{(2)}}{\partial n} N_i dS \tag{7}$$

similar to equation (2). Here the potential on the boundary at the far end S_E is treated as known, because it can be obtained through the solution at the previous time step using the radiation condition (Ma et al 2001a, 2001b).

Equations (2), (5) and (7) can be solved iteratively. When $\partial\phi^{(2)}/\partial n$ in (2) is assumed, the equation becomes complete and can be solved. From the solution of $\phi^{(1)}$ we replace $\phi^{(2)}$ on Γ_{12} in (5) by $\phi^{(2)} + \gamma(\phi^{(1)} - \phi^{(2)})$, where γ is the relaxation coefficient. When $\phi^{(2)}$ on Γ_{23} is assumed in (5), the equation can be solved to give $\partial\phi^{(2)}/\partial n$ on Γ_{23} through the derivative of the stream function along the boundary. Subsequently, equation (5) can be solved to give the new value of the potential on Γ_{23} through $\phi^{(2)} + \gamma(\phi^{(3)} - \phi^{(2)})$. The solution procedure then returns to R_1 and is repeated until the desired accuracy has been achieved.

3. NUMERICAL RESULTS

The results given in Figure 2 are for a cylinder of radius r_0 with submergence $1.5r_0$ in water of depth $4r_0$. The cylinder is placed at a distance equal to $65r_0$ from both the wavemaker and the far end. The length of the BEM is equal to $4r_0$ with the cylinder being in the middle. The wavemaker is stationary and the cylinder moves with horizontal velocity $U = \omega a \sin\omega t$ (a = 0.1 and ω = 1.0, using the non-dimensional parameters previously specified). Based on the linear solution in the frequency domain, the vertical force is zero because of anti-symmetry. The result in Figure 2b, which has been divided by a, is therefore due to the nonlinear effect. In particular, it has been shown by Wu (1993, 2000) that when the motion becomes periodic, the nonlinear vertical force has only components of $2n\omega$ while the horizontal force has only components of $(2n+1)\omega$, $n = 0, 1, 2, \ldots$, which can be seen to be consistent with the results in Figure 2. More results and discussion will be given at the workshop.

ACKNOWLEDGEMENT

This work is supported by EPSRC through a joint project between UCL (GR/M57910) and Oxford University (GR/M56401), for which the authors are most grateful.

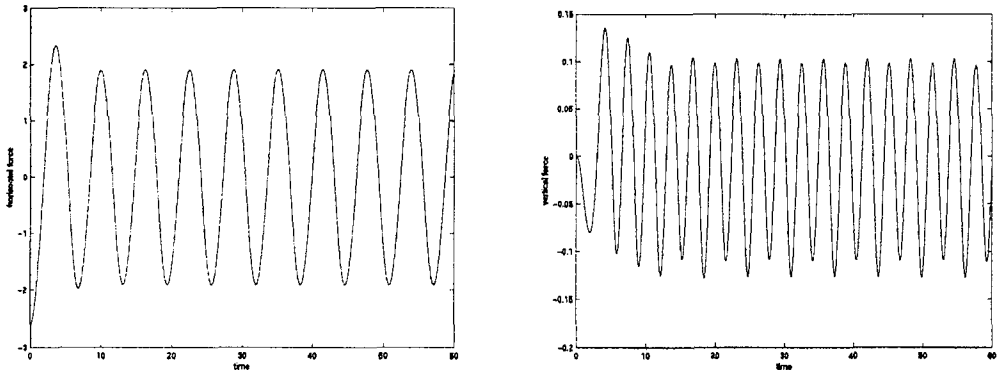

(a) horizontal force (b) vertical force

Figure 2 Time history of forces on a submerged circular cylinder in forced sinusoidal horizontal motion

References

Celebi, M.S., Kim, M.H. and Beck, R.F. (1998) "Fully nonlinear 3_D numerical wave tank simulation", *J. Ship Res.*, Vol. 42, No. 1, 33-45.

Clauss, G.F. & Steinhagen, U. (1999) "Numerical simulation of nonlinear transient waves and its validation by laboratory data", *Proc. 9th Int. Offshore and Polar Eng. Conf.*, Brest, France, Vol. 3, 368-375.

Faltinsen, O.M. (1977) "Numerical solution of transient nonlinear free surface motion outside or inside moving bodies", *Proc. 2nd Int. Conf. On Num. Ship Hydrodynamics,* Berkeley, California, USA, 347-357.

Ferrant , P. (1994) "Radiation and diffraction of nonlinear waves in three dimensions", *Proc. Int. Conf. on Behaviour of Offshore Structures*, MIT, USA, 507-524.

Greaves, D.M., Borthwick, A.G.L., Wu, G.X. and Eatock Taylor, R. (1997) "A moving boundary finite element method for fully nonlinear wave simulation", *J. Ship Res.*, Vol. 41, 181-194.

Lin, W,M., Newman, J.N. and Yue, D. K. (1984) "Nonlinear forced motion of floating bodies", *Prof. 15th Symp. Naval hydrodynamics*, Hamburg, Germany, 33-49.

Longuet-Higgins, M.S. & Cokelet, E.D. (1976) "The deformation of steep waves on water: I. A numerical method of computation", *Proc. Roy. Soc. London*, Vol. A350, 1-26.

Ma, Q.W., Wu, G.X. and Eatock Taylor, R. (2001a) "Finite element simulation of fully nonlinear interaction between vertical cylinders and steep waves-part 1: Methodology and Numerical procedure", *Int. J. for Nume. Meth. in Fluids (accepted).*

Ma, Q.W., Wu, G.X. and Eatock Taylor, R. (2001b) "Finite element simulation of fully nonlinear interaction between vertical cylinders and steep waves-part 2: Numerical results and validation", *Int. J. for Nume. Meth. in Fluids (accepted)*

Robertson, I. & Sherwin, S. (1999) "Free-surface flow simulation using hp/spectral elements" *J. Computational Physics*, Vol. 155, 26-53.

Vinje, T. & Brevig, P. (1981) "Nonlinear ship motions", *Proc. 3rd Int. Conf. On Numerical Ship Hydrodynamics*, Paris, France, 257-268.

Wang, P., Yao, Y. and Tulin, M.P. (1995) "An efficient numerical tank for non-linear water waves, based on the multi-subdomain approach with BEM". *Int. J. for Nume. Meth. in Fluids,* Vol. 20, 1315-1336.

Wu, G.X. (1993) "A note on hydrodynamic forces on body submerged below a free surface". *Appl. Ocean Res.*, Vol. 15, 371-372.

Wu, G.X. (1998) "Hydrodynamic force on a rigid body during impact with liquid", *J. Fluids and Structures*, Vol. 12, 549-559.

Wu, G. X. (2000) "A note on non-linear hydrodynamic force on a floating body" *Appl. Ocean Res.*, Vol. 22, 315-316.

Wu, G.X. & Eatock Taylor, R. (1994) "Finite element analysis of two dimensional non-linear transient water waves", *Appl. Ocean Res.*, Vol. 16, 363-372.

Wu, G.X. & Eatock Taylor, R. (1995) "Time stepping solution of the two dimensional non-linear wave radiation problem", *Ocean Eng*, Vol. 22, 785-798.

Wu, G.X. & Eatock Taylor, R. (1996) "Transient motion of a floating body in steep waves", *11th Int. Workshop on Water Waves and Floating Bodies,* Hamburg.

Wu, G.X., Ma.Q.W. and Eatock Taylor (1998) "Numerical simulation of sloshing waves in a 3D tank based on a finite element method", *Appl. Ocean Res.*, Vol. 20, 337-355.

CFD Simulation of Flow-Induced Floating-Body Motions

Y. Xing, I. Hadzic, S. Muzaferija [a] and M. Peric

Fluid Dynamics and Ship Theory Section, Technical University of Hamburg-Harburg,

Laemmersieth 90, 22305 Hamburg, Germany

[a] ICCM, Bramfelder Strasse 164, 22305 Hamburg, Germany

Abstract

The techniques of Computational Fluid Dynamics (CFD) are applied to simulate floating-body motions in free-surface flow (e.g. waves). It is demonstrated that a wide variety of problems associated with the coupled analysis of flow and flow-induced body motions can be dealt with by a single computer code, which solves the Navier-Stokes equations and the equations of motion for a floating body in a coupled manner. The method is relevant to a wide range of applications in ship and ocean engineering, such as ship seakeeping and maneuvering etc. In this paper, a series of predictions of floating-body motions in waves and in other flows is discussed and comparisons between calculations and measurements are also presented.

I Introduction

Ship motions and associated loads on a ship hull can only be predicted fairly accurately using methods based on potential flow assumptions. Large errors can be introduced by these assumptions for a few practically important cases like ships' motions in large amplitude waves, ships' responses under a wave impact load (slamming), or ship capsizing etc. The need for a numerical tool that can predict the motions and loads in large waves, taking into account viscous effects, turbulence, flow separation and wave-breaking phenomena is obvious.

The objective of this research is to develop and validate a computational technique for the coupled analysis of viscous flow and flow-induced body movements in large/irregular waves. In the present study, a finite volume method has been used, which can accommodate any type of grid, and is therefore applicable to complex geometry problems. SIMPLE algorithm [1] has been taken to couple the pressure field properly to the velocity field. HRIC (High-Resolution Interface Capturing) scheme [2] has been used to simulate the free surface and to achieve the sharpness of the interface between water and air.

For predicting the body movements, floating-body dynamics has been implemented into the program "Comet" [3] via user-coding; a fully-implicit predictor-corrector procedure has been employed, taking advantage of the iterative nature of the fluid-flow solver. By the use of moving grid strategies, the motions of the bodies are presented by the displaced and adapted grid system fitted to the bodies' surfaces. The body movements are calculated according to the forces obtained by integrating pressure and shear stress over body surface.

II Computation Procedure

1. Numerical Tank

Our numerical tank consists of a fluid domain with two phases (water and air) bounded by a layer of air on top, a bottom surface in water and four vertical boundaries. All boundaries can be physical ones if the fluid is really bounded, but otherwise they are imaginary ones. At one vertical boundary, the movement of a flapping wave-maker can be simulated by moving grid, or waves can be generated by giving inlet velocity at the corresponding section. Numerical beaches are incorporated near other imaginary boundaries so that no waves are reflected. At solid walls, no-slip conditions are applied.

Regular waves are generated by imposing appropriate inlet velocities at the wave-maker boundary. For testing the performance of the present numerical tank, the small amplitude waves with amplitude A = 0.001m, radian frequency ω = 17.73 (1/s) have been generated first. The numerical tank was set 10 wave-lengths long plus a double-sized damping zone. The results are presented below, as well as the comparisons with the analytical results according to potential theory [4].

Figure 1 shows the instantaneous displacement of the free surface at t = 8.0 s, the implicit three-time-

level scheme has been used for time integration. The sinusoidal wave profile is compared with the analytical solution in Fig. 2 at $t = 6.0$ s.

Furthermore, Fig. 3 compares the vertical distribution of the horizontal velocity amplitude and that of the vertical velocity amplitude at about 1.5 m away from the wave–maker obtained by the present calculation with the corresponding values given by the linear water–wave theory [4]. The agreements are very good.

Figure 4 shows an example wave profile of large amplitude, generated in the present numerical tank by prescribing a large inlet velocity. As it can be observed, the wave profile is unsymmetric about $y = 0$, the crests are steeper and the troughs flatter, as a result of the nonlinear effects. For comparison, the nonlinear 2nd–order Stokes waves [4] are plotted together with the computed surface elevation. The agreement is not as good as for small–amplitude waves as the viscous effects become more important.

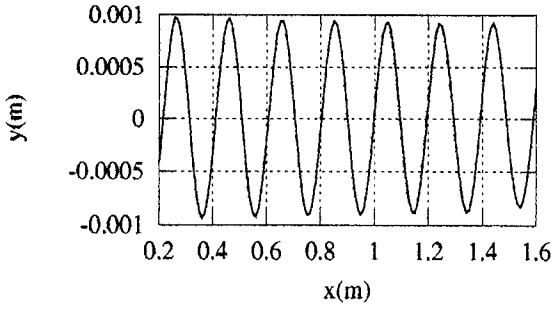

Fig. 1. Free surface profile at t = 8.0 s

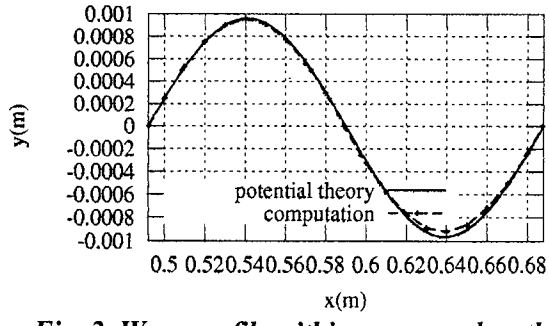

Fig. 2. Wave profile within one wave length

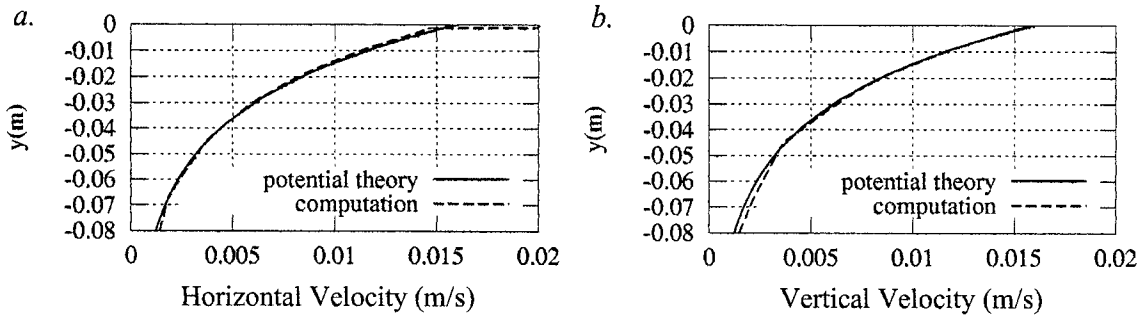

Fig. 3. The vertical distribution of velocity components at x = 1.5 m

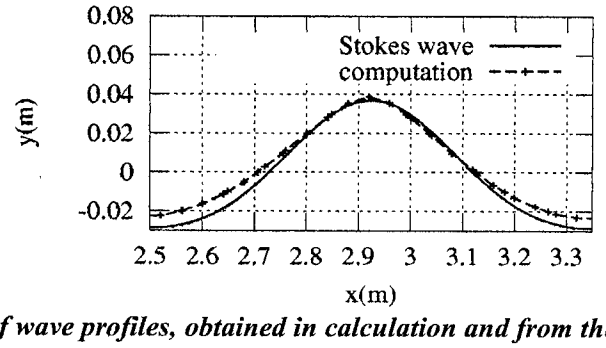

Fig. 4. Comparison of wave profiles, obtained in calculation and from the 2nd–order Stokes theory

2. Floating bodies

For testing the reliability of the method for predicting the flow–induced body motions, a number of simple 2D–cases, with translation or rotation only, was analyzed first to verify the procedure and estimate the accuracy. Figure 5 shows one example of the test cases. The center of square cylinder is initially located at a distance of 1.25 D (D is cylinder width) below the free surface and is at rest as well as the fluid itself. The cylinder is free to move only in the vertical direction as it should be. After being released, due to the buoyancy force (density of the body is half of the water density), the cylinder first moves upwards and oscillates towards its equilibrium position. Figure 5.a shows the free–surface and the body position at time $t = 0.6$ s and Fig. 5.b shows the integral vertical force Fy, velocity Vc and position Yc of

the body center as a function of time.

The horizontal lines in Fig. 5.b indicate the equilibrium states. Until at about 2 seconds, the strong damping of body movement due to viscous forces and generation of waves is present and then large oscillations of body are caused by the reflected waves from the vertical side walls of the channel (where no numerical beach is employed for this test case). A very complex situation is generated while the body breaks the free surface moving upwards and downwards with rapid change of force *Fy*, as shown in Fig. 5.b, representing the impingement of water at the body.

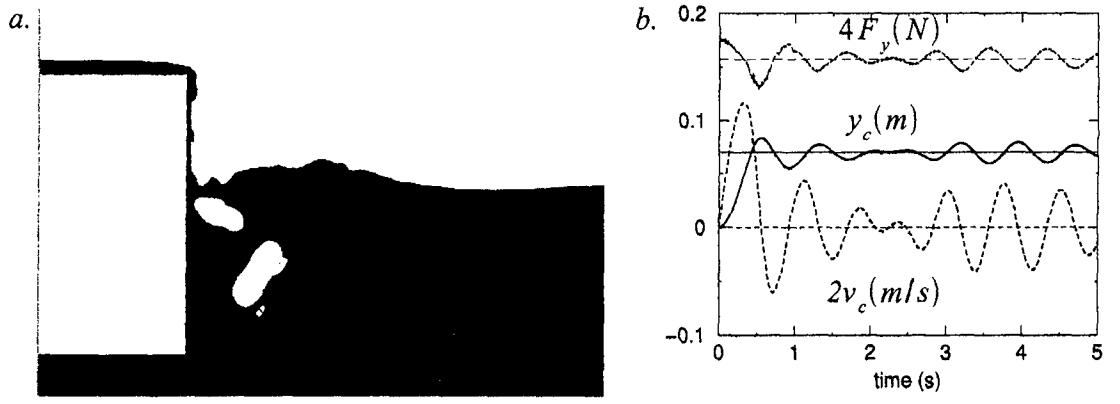

Fig. 5.a. The free–surface and the body position at time t = 0.6 s; b. The integral vertical force Fy, velocity Vc and position Yc of the body center as a function of time

3. Comparisons with experimental results

Since it has been confirmed that the basic performance of the present numerical tank is adequate for practical calculations associated with the wave–induced body motions, a series of computations is carried out, for which experiments can be executed for comparing the results.

a. Axis–fixed cylinder in waves

An experiment was set up for studying the axis–fixed cylinder motions in waves. The model has the dimensions of 12 cm width, 8 cm height and 20 cm length with the density of 665 kg/m ^{3} , initially 3 cm submerged under the still water surface. The fixed–axis is set at 5.5 cm above the bottom edge of the cross section of the model. Waves are generated by simulating the flapping movements of the wave–maker in our towing tank. The wave–maker moves sinusoidally with the period of movement 0.7 s. Water depth of towing tank is 1.0 m. The waves have been reproduced and tested in our present numerical tank. Figure 6.a shows the free surface deformation and the body position at t = 6.82 s. Slamming occurs in such a situation: waves are broken in the vicinity of the body and an amount of water has been splashed on the top of body, as it can also be observed from the experiment. Figure 6.b shows the angular movements obtained from 2D calculation compared with experimental results. Since the 3D effect is significant in the experiment, the difference in the amplitude of the angular movement is reasonable. For further steps, 3D calculations are about to be set up by the authors.

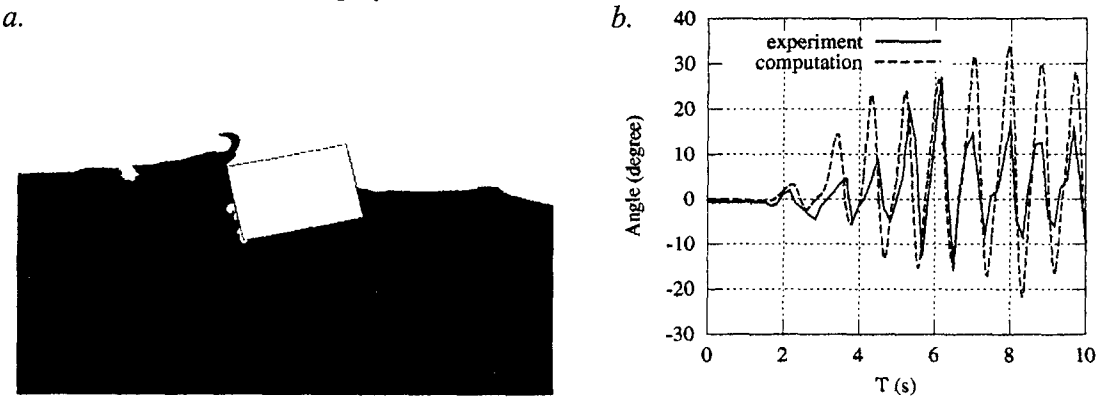

Fig. 6.a. The free surface deformation and the body position at t = 6.82 s; b. Comparison of the angular motion in experiment and calculation

b. Free–floating body in waves

The experiment of free–floating cylinder in waves was also set up in our towing tank. The body is made with 10 cm width, 5 cm height and 29 cm length, and with the density of 680 kg/m ^{3} . Both waves and body motions are compared with the experiment, as shown in Fig. 7. The agreement is rather good except at the initial stage, where the noise in the experiment is rather large. The fluid velocity vector profile at t = 4 s as well as the grid in the vicinity of the body are shown in Fig. 8, which gives some insight into the flow around the body and flow–body interaction.

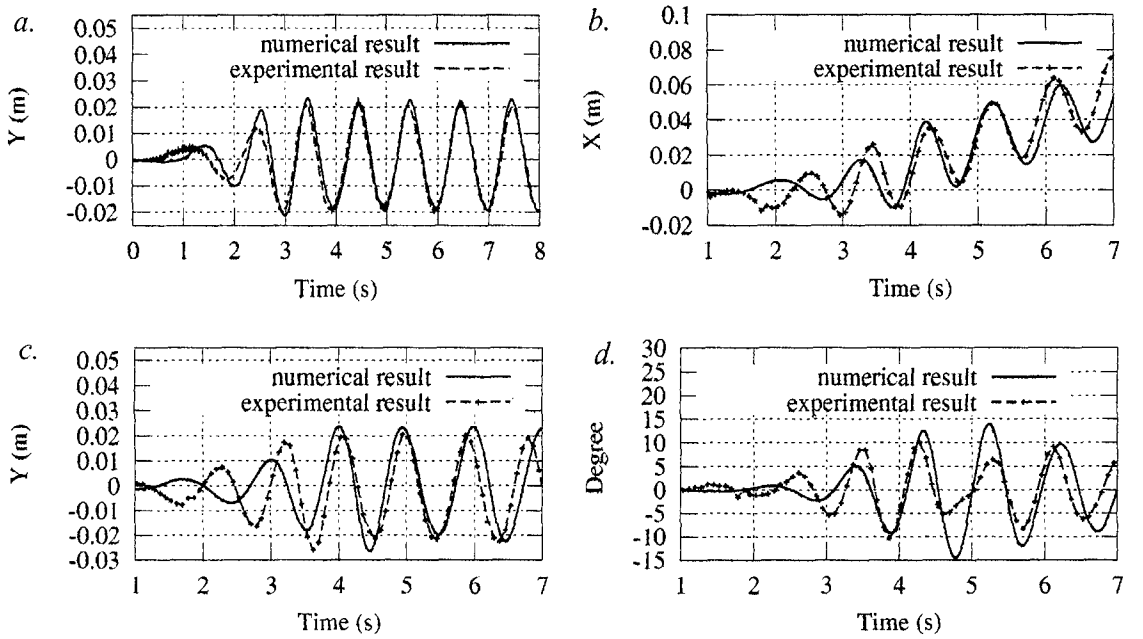

Fig. 7 a. The wave surface elevation at x = 1.5 m as a function of time; b., c., d. Comparison of free–floating body movements as a function of time in our computation and in the experimental results.

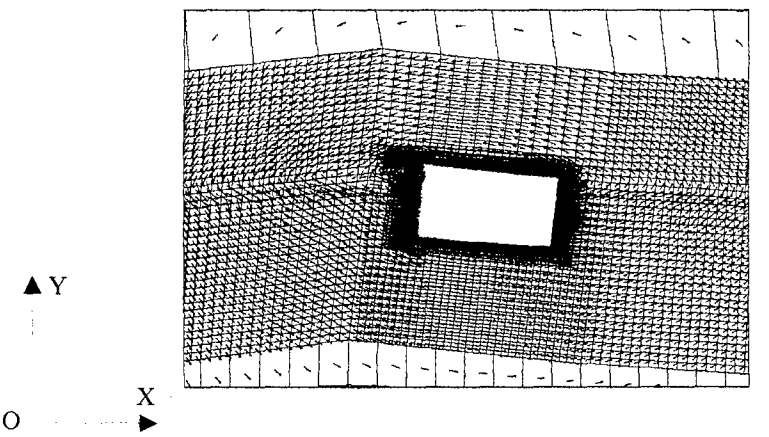

Fig. 8. The locally refined grid, fluid velocity vectors, and the body position at t = 4 s

References:

1. S. V. Patankar and D. B. Spalding: A calculation procedure for heat, mass and momentum transfer in three–dimensional parabolic flows, Int. J. Heat and Mass Transfer, 15:1787–1806, 1972.
2. S. Muzaferija and M. Peric: Computation of free–surface flows using interface–tracking and interface–capturing methods, chap. 2 in O. Mahrenholtz and M. Markiewicz (eds.), Nonlinear Water Wave Interaction, pp. 59–100, WIT Press, Southampton, 1999.
3. Comet user manual, ICCM (Institute of Computational Continuum Mechanics GmbH), Hamburg, 2000.
4. J. N. Newman: Marine Hydrodynamics, MIT Press, England, 1978.

Verification of Fourier-Kochin representation of waves

C. Yang*, F. Noblesse**, R. Löhner*
** School of Computational Sciences, George Mason University, USA
* David Taylor Model Basin, NSWC-CD, USA

The purpose of this study is to present a verification of the Fourier-Kochin representation of waves given in [1,2]. This representation expresses the waves generated by a given flow at a boundary surface in terms of single Fourier integrals and spectrum functions that are defined by distributions of elementary waves over the boundary surface. The Fourier-Kochin representation of waves is given in [1,2] for three classes of free-surface flows: (i) diffraction-radiation of time-harmonic waves without forward speed, (ii) steady ship waves, and (iii) time-harmonic ship waves (diffraction-radiation with forward speed).

The Fourier-Kochin representation of waves is considered here for steady flows associated with the linearized free-surface boundary condition $w + F^2 \partial u/\partial x = 0$ where $F = \mathcal{U}/\sqrt{gL}$ is the Froude number, and $(u, v, w) = \vec{u} = \vec{U}/\mathcal{U} = \nabla\phi$ is the disturbance-flow velocity; here, $\phi = \Phi/(\mathcal{U}L)$ is the velocity potential associated with the velocity $\vec{u}$. The Fourier-Kochin representation of waves defines the potential ϕ^W and the velocity $\vec{u}^W$ associated with the waves that are generated by a given velocity distribution $\vec{u}$ at a boundary surface Σ, which may intersect the mean free-surface plane $z=0$ along the boundary curve Γ. The boundary surface $\Sigma \cup \Gamma$ is divided into patches, i.e. $\Sigma \cup \Gamma = \sum_{p=1}^{p=N} \Sigma_p \cup \Gamma_p$, associated with reference points (x_p, y_p, z_p), with $\vec{x} = \vec{X}/L$, located near the centroids of the patches.

The wave potential ϕ^W and velocity $\vec{u}^W$ at a field point (ξ, η, ζ) of the flow domain outside a boundary surface $\Sigma \cup \Gamma$ are given by the single Fourier integrals

$$4\pi \begin{Bmatrix} \phi^W \\ u^W \\ v^W \\ w^W \end{Bmatrix} = \Re\mathrm{e} \int_{-\infty}^{\infty} \frac{d\beta\, \alpha^d}{k^d - \nu} \begin{Bmatrix} i \\ \alpha^d \\ \beta \\ i\,k^d \end{Bmatrix} \sum_{p=1}^{p=N} [\,1 + \mathrm{erf}(\frac{x_p - \xi}{\sigma F^2 C})\,]\, S_p^W\, e^{(z_p+\zeta)k^d + i[(x_p-\xi)\alpha^d + (y_p-\eta)\beta]}$$

where $\Re\mathrm{e}$ stands for the real part. The functions $\alpha^d(\beta)$ and $k^d(\beta)$ are defined as

$$\alpha^d = \sqrt{k^d}/F \qquad k^d = \nu + \sqrt{\nu^2 + \beta^2} \qquad \text{with} \quad \nu = 1/(2F^2)$$

Here, $k^d(\beta)$ stands for the value of the wavenumber k at the dispersion curves $\alpha = \pm\alpha^d(\beta)$, with $-\infty \le \beta \le \infty$, associated with the dispersion relation $F^2\alpha^2 - k = 0$. The function C in the error function erf is related to the curvature of the dispersion curves and is given by

$$C = 1 + |\,3/(F^2 k^d) - 2\,|\,/\,(\,4\,F^2 k^d - 3\,)^{3/2}$$

We have $C=2$ for $\beta=0$, where $\alpha^d = k^d = 1/F^2$, $C \to 1$ as $\beta \to \pm\infty$, and $C=1$ at the inflexion points defined by $F^2 k^d = 3/2$ and $F^2\beta = \pm\sqrt{3}/2$. The positive real constant σ may be chosen as in [2].

The contribution S_p^W of patch p to the wave-spectrum function $S^W(\beta)$ is given by

$$S_p^W = S_p^\Sigma + F^2 S_p^\Gamma \qquad \text{with}$$

$$S_p^\Sigma = \int_{\Sigma_p} d\mathcal{A}\, [\,\vec{u}\cdot\vec{n} + i\,\frac{\alpha^d}{k^d}\,(\vec{u}\times\vec{n})^y - i\,\frac{\beta}{k^d}\,(\vec{u}\times\vec{n})^x\,]\, e^{k^d(z+z_p) + i[\alpha^d(x-x_p) + \beta(y-y_p)]}$$

$$S_p^\Gamma = \int_{\Gamma_p} d\mathcal{L}\, [\,(t^x t^y + \frac{\alpha^d\beta}{(k^d)^2})\,\vec{u}\cdot\vec{t} - (t^y)^2\,\vec{u}\cdot\vec{\nu}\,]\, e^{i[\alpha^d(x-x_p) + \beta(y-y_p)]}$$

Here, the unit vector $\vec{n} = (n^x, n^y, n^z)$ is normal to the boundary surface Σ and points into the flow region outside Σ, and the unit vectors $\vec{t} = (t^x, t^y, 0)$ and $\vec{\nu} = (-t^y, t^x, 0)$ are tangent and normal to the boundary curve Γ in the mean free-surface plane $z=0$. The normal vector $\vec{\nu}$ points into the flow region outside Γ, like the normal vector $\vec{n}$, and the tangent vector $\vec{t}$ is oriented clockwise (looking down). The spectrum functions $S^\Sigma(\beta)$ and $S^\Gamma(\beta)$ are defined by distributions of elementary waves over the boundary surface Σ and the boundary curve Γ, respectively, with amplitudes given by the normal components $\vec{u}\cdot\vec{n}$, $\vec{u}\cdot\vec{\nu}$ and the tangential components $\vec{u}\times\vec{n}$, $\vec{u}\cdot\vec{t}$ of the velocity $\vec{u}$ at Σ and Γ.

Thus, the Fourier-Kochin wave representation defines the wave potential $\phi^W(\vec{\xi})$ and velocity $\vec{u}^W(\vec{\xi})$ at a field point $\vec{\xi}$ of the flow region outside a boundary surface $\Sigma \cup \Gamma$ in terms of the velocity distribution $\vec{u}(\vec{x})$ at the boundary surface Σ and the boundary curve Γ. This representation of the waves generated by a flow at a boundary surface only involves the boundary velocity $\vec{u}(\vec{x})$; i.e. the Fourier-Kochin wave representation does not involve the potential $\phi(\vec{x})$ at the boundary surface $\Sigma \cup \Gamma$, unlike the classical boundary-integral representation that defines the potential in a potential-flow region in terms of boundary-values of the potential ϕ and its normal derivative $\partial\phi/\partial n = \vec{u} \cdot \vec{n}$. The Fourier-Kochin wave representation is based on several recent new fundamental results obtained within the framework of the Fourier-Kochin theory [3,2] : (i) the boundary-integral representation, called velocity representation, given in [1,2], (ii) the representation of the generic super Green function defined in [4,5,2], and (iii) the transformations of spectrum functions given in [3,1,2]. The flow generated by a given flow at a boundary surface can be expressed as

$$\phi = \phi^W + \phi^L \qquad \vec{u} = \vec{u}^W + \vec{u}^L$$

where ϕ^W, $\vec{u}^W$ is the wave component defined by the Fourier-Kochin wave representation, and ϕ^L, $\vec{u}^L$ is a local-flow component. The Rankine and Fourier-Kochin nearfield flow representation given in [6] expresses the local component ϕ^L, $\vec{u}^L$ in terms of distributions of elementary Rankine singularities and Fourier-Kochin distributions of elementary waves over the boundary surface Σ and the boundary curve Γ. The local component ϕ^L, $\vec{u}^L$ is not considered here.

For the purpose of verifying the foregoing Fourier-Kochin wave representation, the flow due to a source-sink pair is considered here. Fig.1 shows the disturbance velocity $(u\,,v\,,w)$ generated by a point source and a point sink, of strength $q = Q/(\mathcal{U}L^2) = 0.001$, located at $(x\,,y\,,z) = (\pm 0.5\,,0\,,-0.02)$ over the lower half $z \leq 0$ of the ellipsoid $x^2/a^2 + y^2/b^2 + z^2/c^2$ with $(a\,,b\,,c) = (0.55\,,0.05\,,0.1)$. The velocity distribution $(u\,,v\,,w)$ generated by the point source-sink pair is evaluated, for a Froude number $F = 0.316$, using integral representations of the Green function given in [7]. The upper half of Fig.2 depicts the free-surface elevation, computed using integral representations of the Green function, due to the source-sink pair. The lower half of Fig.2 depicts the free-surface elevation obtained using the Fourier-Kochin wave representation and the velocity distribution generated by the source-sink pair at the ellipsoidal boundary surface depicted in Fig.1. The free-surface elevations computed using expressions for the Green function (upper half) and reconstructed using the Fourier-Kochin wave representation (lower half) are not identical in the vicinity of the ellipsoidal boundary surface because the local-flow component u^L is ignored in the Fourier-Kochin wave representation. The wave elevations shown in Fig.3 along the four longitudinal cuts $y = 0$, $y = 0.06$, $y = 0.1$, $y = 0.5$ show that the local component u^L in fact is only significant in the vicinity of the elliptical boundary curve.

The results depicted in Figs 1-3 provide a verification of the Fourier-Kochin representation of waves. Furthermore, Fig.3 shows that the wave component is dominant even in the nearfield. Illustrative practical applications of the Fourier-Kochin representation of waves are given in [8,9]. Specifically, the Fourier-Kochin representation of steady ship waves is coupled with nearfield calculations based on the Euler equations in [8] and is applied to the design of a wave cancellation multihull ship in [9].

References

[1] F. Noblesse (2001) *Velocity representation of free-surface flows and Fourier-Kochin representation of waves*, Appl. Ocean Res. (in press)

[2] F. Noblesse (2001) *Analytical representation of ship waves*, Ship Techn. Res. (in press)

[3] F. Noblesse, C. Yang (1995) *Fourier-Kochin formulation of wave diffraction-radiation by ships or offshore structures*, Ship Techn. Res. 42:115-139

[4] F. Noblesse, X.B. Chen (1995) *Decomposition of free-surface effects into wave and near-field components*, Ship Techn. Res. 42:167-185

[5] F. Noblesse, X.B. Chen, C. Yang (1999) *Generic super Green functions*, Ship Techn. Res. 46:81-92

[6] F. Noblesse (2001b) *Rankine and Fourier-Kochin Representation of Near-Field Ship Waves*, submitted

[7] F. Noblesse (1981) *Alternative integral representations for the Green function of the theory of ship wave resistance*, J. Eng. Math. 15:241-265

[8] C. Yang, R. Löhner, F. Noblesse (2000a) *Farfield extension of nearfield steady ship waves*, Ship Techn. Res. 47:22-34

[9] C. Yang, F. Noblesse, R. Löhner, D. Hendrix (2000b) *Practical CFD applications to design of a wave cancellation multihull ship*, 23rd Symp. on Naval Hydrodyn., Val de Reuil, France

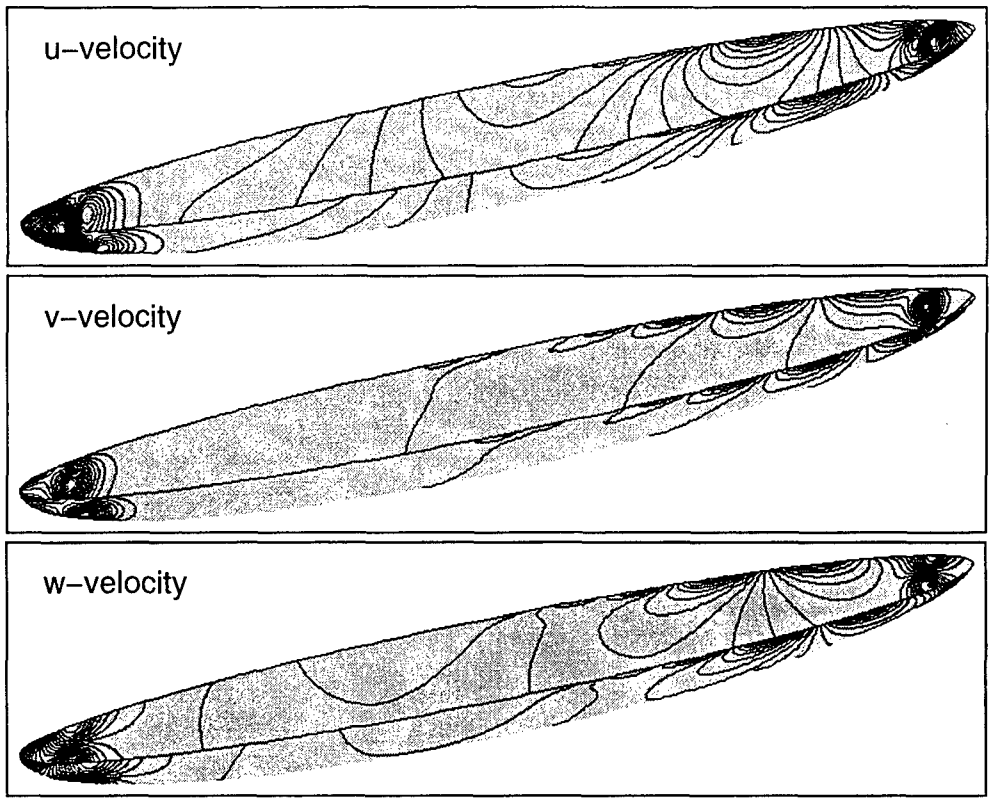

Fig. 1. Velocity distribution generated by souce-sink pair at boundary surface

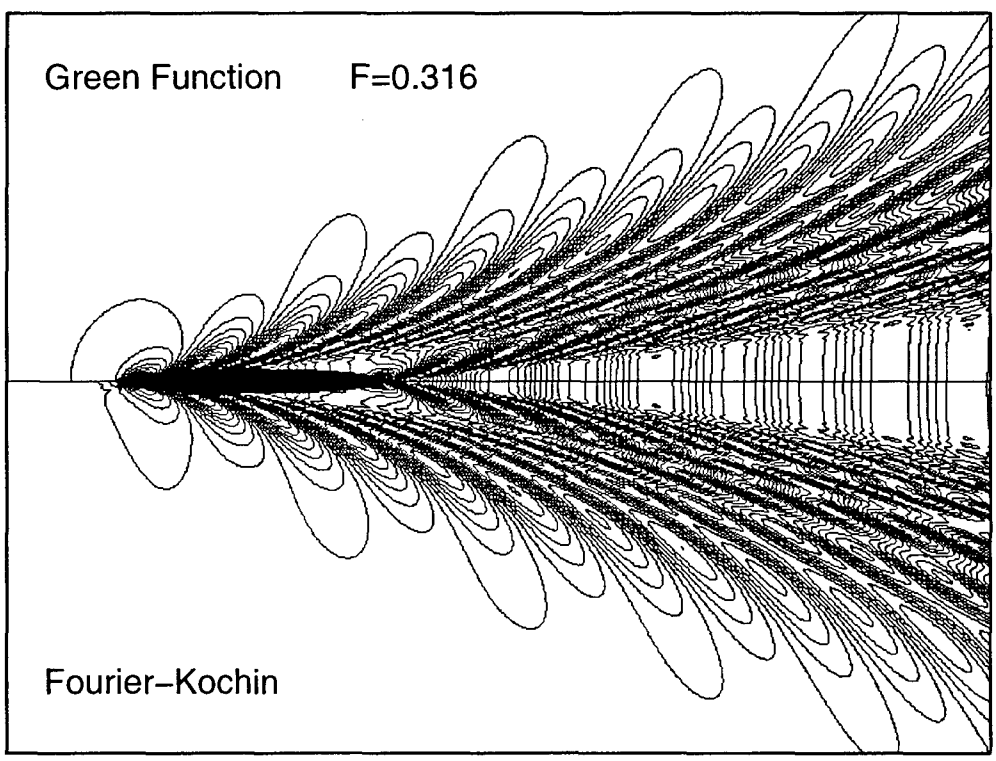

Fig. 2. Wave patterns due to souce-sink pair
top: wave pattern computed using Green function
bottom: wave pattern reconstructed using Fourier-Kochin wave representation

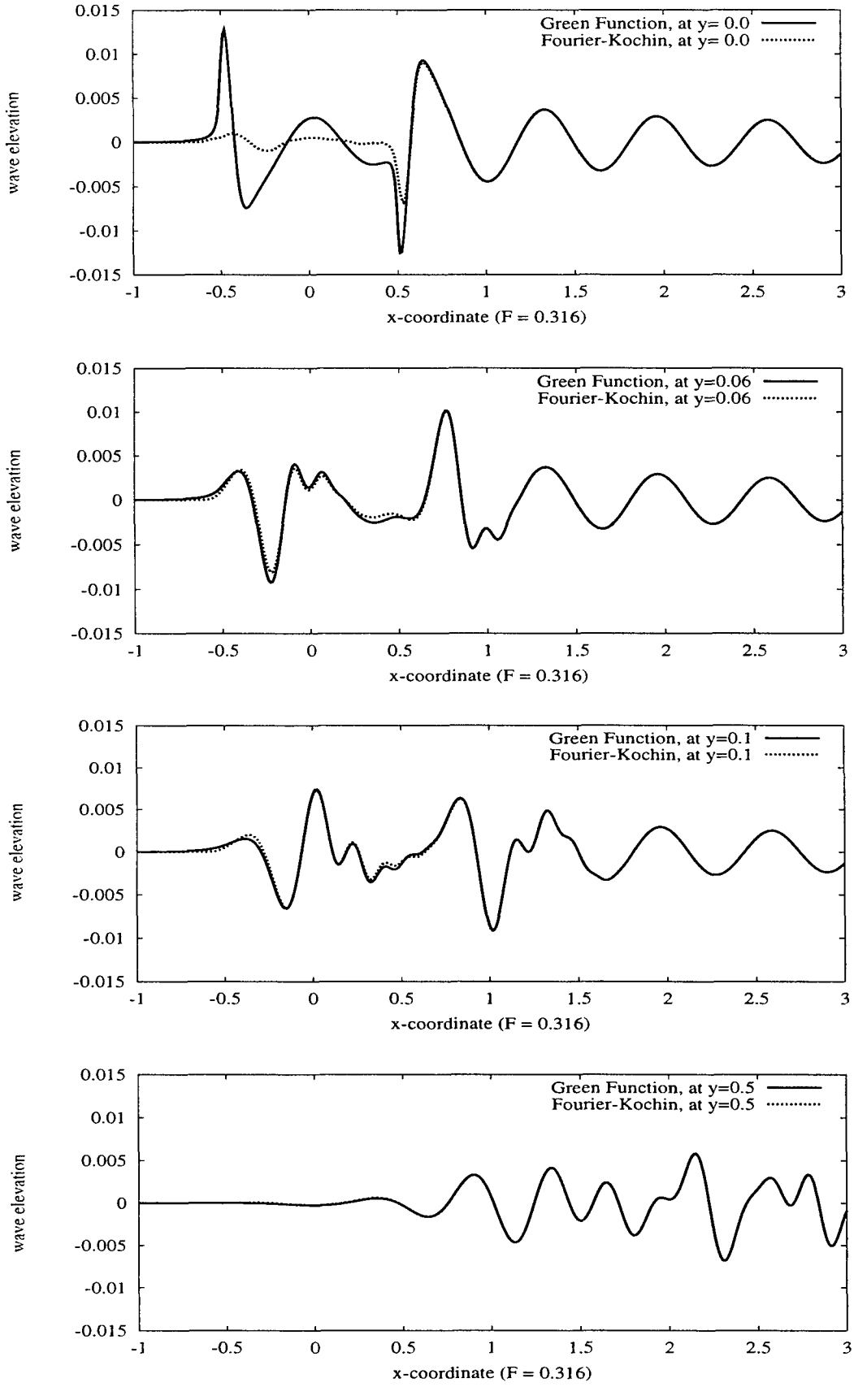

Fig. 3. Wave elevations along four cuts at y=0, 0.06, 0.1, 0.5 for F=0.316

Unsteady Wash Generated by a High Speed Vessel

Hironori YASUKAWA, *Nagasaki Experimental Tank, Mitsubishi Heavy Industries**

Introduction

The unsteady wash generated by a high speed vessel with decelerated motion in a channel is numerically investigated. This situation may be similar to that the vessel reduces the speed in the channel. Then, the Kelvin waves generated by the vessel progress straight and propagate in the channel. We carried out computations of the wash using a time domain panel method including the attitude change of the vessel. Several studies with respect to the time domain method have been carried out, for instance, by Maskew (1991), Beck et al.(1993), Li and Chwang(1997) and Yasukawa(1999, 2000). However, there is no analysis of the unsteady wash including the effect of the attitude change so far as we know. The time domain method and the computed results for the unsteady wash will be introduced.

Basic Equations

Let us consider the shallow channel of the water depth h. The vessel is assumed to move in center of the channel with the speed $U(t)$ which varies as the function of time t. The coordinate system fixed in the space is employed. The x-axis is defined as direction from the ship stern to the bow, y-axis to port and z-axis vertically upward. The $x-y$ plane is the still water surface.

The perturbation velocity potential due to the vessel moving in the channel is defined as $\phi(x,y,z,t)$. Then, ϕ has to fulfill the following boundary conditions as:

$$\frac{\partial \phi}{\partial t} = -g\zeta - \frac{\partial^2 \phi}{\partial t \partial z}\zeta - \frac{1}{2}\left\{\left(\frac{\partial \phi}{\partial x}\right)^2 + \left(\frac{\partial \phi}{\partial y}\right)^2 + \left(\frac{\partial \phi}{\partial z}\right)^2\right\} \quad \text{on } z = 0 \tag{1}$$

$$\frac{\partial \zeta}{\partial t} = \frac{\partial \phi}{\partial z} + \frac{\partial^2 \phi}{\partial z^2}\zeta - \frac{\partial \phi}{\partial x}\frac{\partial \zeta}{\partial x} - \frac{\partial \phi}{\partial y}\frac{\partial \zeta}{\partial y} \quad \text{on } z = 0 \tag{2}$$

$$\frac{\partial \phi}{\partial n} = \left(U(t)\cos\theta - \dot{\xi}_3 \sin\theta + \dot{\theta} z_H\right) n_x + \left(U(t)\sin\theta + \dot{\xi}_3 \cos\theta - \dot{\theta} x_H\right) n_z \quad \text{on } S_H \tag{3}$$

$$\frac{\partial \phi}{\partial n} = 0 \quad \text{on } S_W, \qquad \frac{\partial \phi}{\partial z} = 0 \quad \text{on } z = -h \tag{4}$$

The 2nd order non-linear free surface conditions expanded with respect to ζ, which means the wave height, around $z = 0$ are employed, eqs.(1) and (2). Eq.(3) is hull surface condition, and has to be satisfied on actual wetted surface S_H. In eq.(3), ξ_3 and θ denote dynamic sinkage and trim respectively, x_H and z_H the coordinate of hull surface, and n_x and n_z the component of outward normal vector. Eq.(4) is the boundary conditions on the channel wall S_W and the sea bottom $z = -h$.

Velocity potential ϕ is represented using source strength σ as follows:

$$\phi(P) = \iint_{S_H + S_F + S_W} \sigma(Q) G(P;Q) dS \tag{5}$$

where

$$G(P;Q) = \frac{1}{\sqrt{(x-x_1)^2 + (y-y_1)^2 + (z-z_1)^2}} + \frac{1}{\sqrt{(x-x_1)^2 + (y-y_1)^2 + (z+z_1+h)^2}} \tag{6}$$

*5-717-1 Fukahori-Machi, Nagasaki 851-0392, JAPAN, email: yasukawa@ngsrdc.mhi.co.jp

Here, $P = (x, y, z)$ is a field point and $Q = (x_1, y_1, z_1)$ the source point. S_F denotes the still water surface ($z = 0$). The 2nd term of the right hand side of eq.(6) is the additional term to fulfill the bottom surface condition.

Numerical Scheme

Numerical scheme to solve the boundary value problem is as follows:

1. Accelerations of dynamic sinkage and trim $(\ddot{\xi}_3^{k+1}, \ddot{\theta}^{k+1})$, and time derivatives of wave height and velocity potential on free-surface $(\zeta_t^{k+1}, \phi_t^{k+1})$ respectively at $(k+1)$-th time step are assumed using values at k-th step. Here suffix t represents time derivation.

2. According to Newmark's β method, the velocities and displacements of the sinkage and trim at $(k+1)$-th step are estimated as (herein, only $\dot{\xi}_3^{k+1}$ and ξ_3^{k+1} are written.):

$$\dot{\xi}_3^{k+1} = \dot{\xi}_3^k + \Delta t \left(\ddot{\xi}_3^k + \ddot{\xi}_3^{k+1} \right) / 2 \tag{7}$$

$$\xi_3^{k+1} = \xi_3^k + \Delta t \, \dot{\xi}_3^k + \frac{(\Delta t)^2}{2} \ddot{\xi}_3^k + \beta (\Delta t)^2 (\ddot{\xi}_3^{k+1} - \ddot{\xi}_3^k) \tag{8}$$

   where Δt is time increment, and β the acceleration factor.

3. Based on the given ship speed and the sinkage and trim estimated in Step 2, ship hull and free-surface panels are arranged.

4. According to Newmark's β method, wave height and velocity potential on free-surface at $(k+1)$-th step are estimated as:

$$\zeta^{k+1} = \zeta^k + \Delta t \left(\zeta_t^k + \zeta_t^{k+1} \right) / 2, \quad \phi^{k+1} = \phi^k + \Delta t \left(\phi_t^k + \phi_t^{k+1} \right) / 2 \tag{9}$$

5. Influence functions are calculated with respect to free-surface, ship hull and channel wall surfaces to make a matrix for determining all source strengths. Basic equations for the sources are discretized using constant panels.

6. Solving the base matrix by SOR method, source strengths on free-surface, hull and tank wall surfaces are obtained.

7. ϕ_t^{k+1} and ζ_t^{k+1} are calculated using eqs.(1) and (2). Then, velocity components on free-surface are analytically calculated. The derivatives of ζ with respect to x and y are obtained numerically using finite different technique.

8. Hydrodynamic forces acting on hull are calculated by Bernoulli's equation. Obtaining the hydrodynamic forces, $\ddot{\xi}_3$ and $\ddot{\theta}$ are calculated from the motion equations of the ship.

9. The $\ddot{\xi}_3, \ddot{\theta}$, ζ_t and ϕ_t obtained in step 7 and 8 are compared with those assumed in step 1. When the difference between both is sufficiently small, $\ddot{\xi}_3, \ddot{\theta}$, ζ_t and ϕ_t are regarded as reaching to the convergence. Otherwise, returning to step 2, calculations are continued using $\ddot{\xi}_3, \ddot{\theta}$, ζ_t and ϕ_t obtained in step 7 and 8 until obtaining converged solution through this iteration.

10. k is set one time step ahead and return to step 1.

Computed Results

Computations of the wash are carried out for a high speed vessel with L/B=7.50, B/d=4.58 and C_b=0.45, where L, B, d and C_b are ship length, breadth, draft and block coefficient respectively. L is assumed to be 1.0m in the computations. This vessel has a transom stern. In actual computations, we put round stern panels to the stern end to avoid the unexpected higher stern waves. The additional panels are dealt with as inexistent panels for calculation of the forces acting on the hull.

Fig.1 shows the propagation of the waves generated by the vessel in the channel from -2.35 to 4.35 for non-dimensional time T. $T = 0$ is corresponding to the stop time of the vessel after the deceleration. The assumed speed change is shown in Fig.2. Froude number based on the constant speed U_0 before the deceleration and the ship length F_n is 0.519. As the region of the channel, $24.5L$ for the length, $2.2L$ for the half breadth and $2.2L$ for water depth are assumed in this case. Then, Froude number based on the water depth F_h becomes 0.350. The breadth and the depth are the same size as the towing tank of Nagasaki R & D center, MHI. In the computation, 4,000 panels for free surface, 480 panels for the vessel and 2,400 panels for the channel walls are used. Time interval 0.02s is in the computation.

Typical Kelvin wave pattern is observed at T=-2.35. At T=0.35, we can see that shifting of the waves generated by the vessel strats just after the vessel stopped. Further, the waves reflected by the channel walls are remarkably observed at the rear region of the vessel. At T=2.35 and 4.35, the bow-shape waves observed in front of the vessel propagate up stream. Thus, propagation process of the unsteady wash generated by the high speed vessel in the channel is realistically demonstrated.

To obtain the verification data, the model test was carried out in the towing tank. Fig.2 shows the comparison of time histories of the ship motions (sinkage and trim) and wave heights at 3 positions fixed at the tank. The positions are $(x/L, y/L)$= (1.79, 0.5), (1.79, 0.643) and (1.79, 0.786) where x is longitudinal distance between fore peak of the stationary vessel and the wave height sensor and y the lateral distance from the tank center line. Behavior of the motions which occur due to the passage of the waves, arrival time of the wash and the wave period in the computation agree well those in the experiment.

In the workshop, we will present further results computed in shallow waters.

References

Beck, R.F., Cao, Y., and Lee, T.-H. (1993): *Fully Nonlinear Water Wave Computations using the the Desingularized Method*, 6th International Conference on Numerical Ship Hydrodynamics, Iowa City.

Li, D. and Chwang, T. (1997): *Time Domain Analysis of Ship-Generated Waves in Harbour using a Fast Hierarchical Method*, 7th International Offshore and Polar Engineering Conference, Honolulu.

Maskew, B. (1991): *A Nonliner Numerical Method for Transient Wave/Hull Problems on Arbitrary Vessel*, SNAME Trans., Vol.99.

Yasukawa, H. (1999): *Unsteady Wash Computation for a High Speed Vessel*, Numerical Towing Tank Symp.(NuTTS'99), Rome.

Yasukawa, H. (2000): *Nonlinear Time Domain Analysis of Ship Motions in Regular Head Waves*, Numerical Towing Tank Symp.(NuTTS'00), Tjärnö.

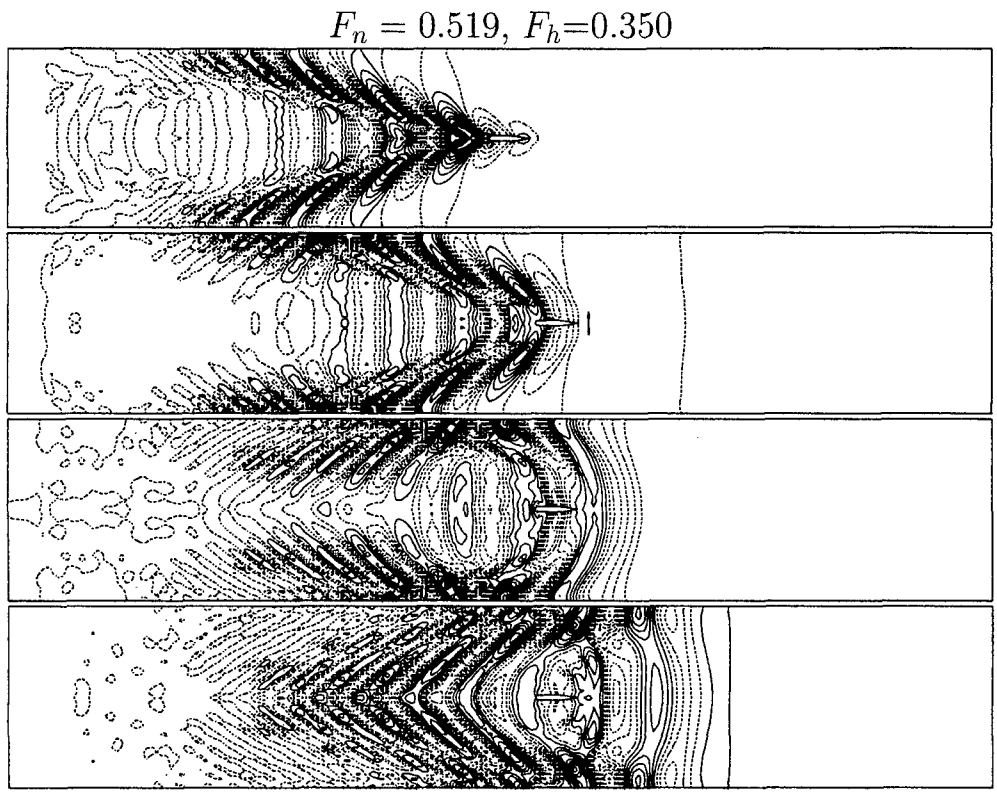

Fig.1: Propagation of the unsteady wash generated by a high speed vessel. The results are of T = -2.35, 0.35, 2.35 and 4.35 from the top.

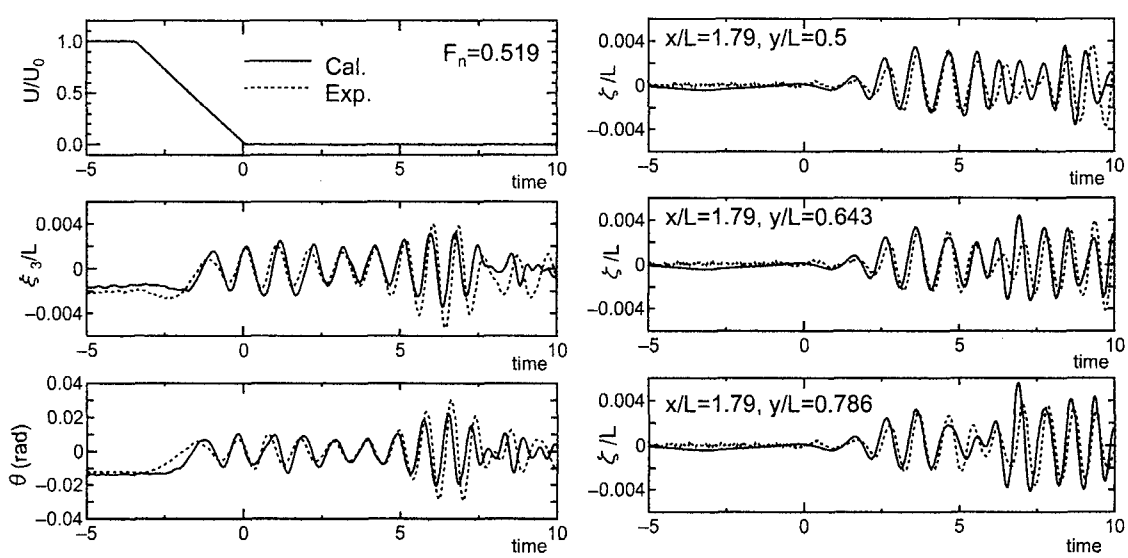

Fig.2: Change of ship speed and comparison of time histories of the motions (sinkage and trim) and wave heights at 3 positions fixed at the tank

Computation of Waves Generated by a Ship Using an NS Solver Based on B-Spline Solid

Chengbi Zhao and Zaojian Zou

Department of Naval Architecture and Ocean Engineering
Wuhan University of Technology,
Wuhan City, P.R.China,430063

ABSTRACT: A method has been discussed for obtaining the free surface turbulent flow solutions around an advancing ship, in which the pseudo-compressibility is used. The geometry grid systems are generated by the B-spline solid. The velocity and pressure are also represented by B-spline solid. The wave surface is shown for Wigley hull at Froude number $F_r = 0.348$ and Reynolds number $R_e = 3.21\times10^6$ in the paper.

1. INTRODUCTION

Some methods have been developed for wavemaking and seakeeping problem based on B-spline and NURBS surface[2][3][4][8][9][13], and some good results have been obtained. It is worth to noted that many efforts have been made in the simulation of the flow around a ship with free surface by resolving the NS equations[1][5][7][11][12]. The finite volume method and pseudo-compressibility method are adopted for solving NS equation, and the k ε, one equation and BL turbulence model are used respectively in their works. The above numerical methods are based on the difference formulation.

The objective of this work is to develop a discreting method based a B-spline solid. The pseudo-compressibility and BL turbulence model are adopted for present work, and the free surface turbulence flows around a Wigley hull is computed

2. FORMULATION

The governing equations with pseudo-compressibility form in the non-dimensional form can be written as

$$\frac{\partial u}{\partial t}+\nabla\bullet\vec{\phi}_x=0 \qquad \frac{\partial v}{\partial t}+\nabla\bullet\vec{\phi}_y=0 \qquad \frac{\partial w}{\partial t}+\nabla\bullet\vec{\phi}_z=0 \qquad \frac{\partial p}{\partial t}+\nabla\bullet\vec{\phi}_p=0 \tag{1}$$

where

$$\vec{\phi}_x=\begin{bmatrix} u^2+p-2\nu u_x \\ uv-\nu(u_y+v_x) \\ uw-\nu(u_z+w_x)\end{bmatrix} \quad \vec{\phi}_y=\begin{bmatrix} uv-\nu(v_x+u_y) \\ v^2+p-2\nu v_y \\ vw-\nu(v_z+w_y)\end{bmatrix} \quad \vec{\phi}_z=\begin{bmatrix} wu-\nu(u_z+w_x \\ wv-\nu(v_z+w_y) \\ w^2+p-2\nu w_z\end{bmatrix} \quad \vec{\phi}_p=\Gamma\begin{bmatrix} u \\ v \\ w\end{bmatrix} \quad p=p_{real}+\frac{z}{F_r^2}$$

$$\Gamma=\beta(u^2+v^2+w^2) \qquad \nu=1/R_e+\nu_t$$

The parameter β is a positive constant , and $\beta=0.25$. F_r is the Froude number. R_e is the Reynolds number. ν_t is the eddy viscosity.

The governing equations are integrated in the control volume moving with time, and the Reynolds transport theorem and the Gauss integral theorem are adopted. The governing equation in each

control volume become the following formulations

$$\frac{d}{dt}\int_{v(t)} u\,dV + \int_{s(t)} (\vec{\phi}_x - u\vec{u})\bullet \vec{n}dS = 0 \qquad \frac{d}{dt}\int_{v(t)} v\,dV + \int_{s(t)} (\vec{\phi}_y - v\vec{u})\bullet \vec{n}dS = 0$$

$$\frac{d}{dt}\int_{v(t)} w\,dV + \int_{s(t)} (\vec{\phi}_z - w\vec{u})\bullet \vec{n}dS = 0 \qquad \frac{d}{dt}\int_{v(t)} p\,dV + \int_{s(t)} (\vec{\phi}_p - p\vec{u})\bullet \vec{n}dS = 0 \tag{2}$$

where $\vec{u}$ is velocity vector,and $\vec{u} = (u,v,w)^T$. $\vec{n} = (n_x,n_y,n_z)^T$ is a unit outward normal of the control volume.The geometry shape can be represented by B-spline solid. The expression formulation is

$$\vec{x}(\xi,\eta,\zeta) = \sum_{i=0}^{L_G}\sum_{j=0}^{M_G}\sum_{k=0}^{N_G} \vec{X}_{ijk} N_{i,l}(\xi) N_{j,m}(\eta) N_{k,n}(\zeta) \tag{3}$$

where $\vec{x}$ is the locate vector, and $\vec{x} = (x,y,z)^T$. $\vec{X}_{ijk} = (X_{ijk},Y_{ijk},Z_{ijk})^T$ are the B-spline control nets representing the geometry shape. $N_{i,l}, N_{j,m}$ and $N_{k,n}$ are the B-spline basis function of order l,m and n, defined by the Cox-de Boor recursive expressions.
The velocity and pressure can also be expressed by B-spline solid in follow formulation.

$$\vec{u}(\xi,\eta,\zeta) = \sum_{i=0}^{L_S}\sum_{j=0}^{M_S}\sum_{k=0}^{N_S} \vec{U}_{ijk} N_{i,p}(\xi) N_{j,q}(\eta) N_{k,r}(\zeta) \tag{4}$$

$$p(\xi,\eta,\zeta) = \sum_{i=0}^{L_S}\sum_{j=0}^{M_S}\sum_{k=0}^{N_S} P_{ijk} N_{i,p}(\xi) N_{j,q}(\eta) N_{k,r}(\zeta) \tag{5}$$

where $\vec{U}_{ijk} = (U_{ijk},V_{ijk},W_{ijk})^T$ and P_{ijk} are the B-spline control nets representing the velocity and pressure. The integral equation(2) transformed to the parameter coordinate system can be written as

$$\frac{d}{dt}\int_{v(t)} uJd\xi d\eta d\zeta + \int_{s1+s2} (\vec{\phi}_x - u\vec{u})\bullet \vec{n}_1 H_1 d\eta d\zeta + \int_{s3+s4} (\vec{\phi}_x - u\vec{u})\bullet \vec{n}_2 H_2 d\xi d\zeta + \int_{s5+s6} (\vec{\phi}_x - u\vec{u})\bullet \vec{n}_3 H_3 d\xi d\eta = 0 \tag{6}$$

$$\frac{d}{dt}\int_{v(t)} vJd\xi d\eta d\zeta + \int_{s1+s2} (\vec{\phi}_y - v\vec{u})\bullet \vec{n}_1 H_1 d\eta d\zeta + \int_{s3+s4} (\vec{\phi}_y - v\vec{u})\bullet \vec{n}_2 H_2 d\xi d\zeta + \int_{s5+s6} (\vec{\phi}_y - v\vec{u})\bullet \vec{n}_3 H_3 d\xi d\eta = 0 \tag{7}$$

$$\frac{d}{dt}\int_{v(t)} wJd\xi d\eta d\zeta + \int_{s1+s2} (\vec{\phi}_z - w\vec{u})\bullet \vec{n}_1 H_1 d\eta d\zeta + \int_{s3+s4} (\vec{\phi}_z - w\vec{u})\bullet \vec{n}_2 H_2 d\xi d\zeta + \int_{s5+s6} (\vec{\phi}_z - w\vec{u})\bullet \vec{n}_3 H_3 d\xi d\eta = 0 \tag{8}$$

$$\frac{d}{dt}\int_{v(t)} pJd\xi d\eta d\zeta + \int_{s1+s2} (\vec{\phi}_p - p\vec{u})\bullet \vec{n}_1 H_1 d\eta d\zeta + \int_{s3+s4} (\vec{\phi}_p - p\vec{u})\bullet \vec{n}_2 H_2 d\xi d\zeta + \int_{s5+s6} (\vec{\phi}_p - p\vec{u})\bullet \vec{n}_3 H_3 d\xi d\eta = 0 \tag{9}$$

where

$$J = \left|\frac{\partial(x,y,z)}{\partial(\xi,\eta,\zeta)}\right| \quad \vec{n}_1 = \frac{\vec{x}_\eta \times \vec{x}_\zeta}{|\vec{x}_\eta \times \vec{x}_\zeta|} \quad \vec{n}_2 = \frac{\vec{x}_\zeta \times \vec{x}_\xi}{|\vec{x}_\zeta \times \vec{x}_\xi|} \quad \vec{n}_3 = \frac{\vec{x}_\xi \times \vec{x}_\eta}{|\vec{x}_\xi \times \vec{x}_\eta|} \quad H_i = \sqrt{E_i G_i - F_i^2}, i = 1,2,3$$

$$E_1 = \vec{x}_\eta \bullet \vec{x}_\eta \qquad G_1 = \vec{x}_\zeta \bullet \vec{x}_\zeta \qquad F_1 = \vec{x}_\eta \bullet \vec{x}_\zeta$$

The similar formulation can be obtained for E_2,F_2,G_2 and E_3,F_3,G_3. $\vec{x}_\xi$, $\vec{u}_\xi$ can be calculated by following formulation

$$\vec{x}_\xi = \sum_{i=0}^{L_G}\sum_{j=0}^{M_G}\sum_{k=0}^{N_G}\vec{X}_{ijk}\frac{dN_{i,l}(\xi)}{d\xi}N_{j,m}(\eta)N_{k,n}(\zeta) \tag{10}$$

$$\vec{u}_\xi = \sum_{i=0}^{L_S}\sum_{j=0}^{M_S}\sum_{k=0}^{N_S}\vec{U}_{ijk}\frac{\partial N_{i,p}(\xi)}{\partial\xi}N_{j,q}(\eta)N_{k,r}(\zeta) \tag{11}$$

The similar formulation can be obtained for $\vec{x}_\eta, \vec{x}_\zeta$ and $\vec{u}_\eta, \vec{u}_\zeta$. $\vec{u}_x, \vec{u}_y, \vec{u}_z$ can be represented in following

$$\begin{bmatrix}\vec{u}_x\\ \vec{u}_y\\ \vec{u}_z\end{bmatrix} = \frac{1}{J}\begin{bmatrix} y_\eta z_\zeta - z_\eta y_\zeta & y_\zeta z_\xi - z_\zeta y_\xi & y_\xi z_\eta - z_\xi y_\eta \\ z_\eta x_\zeta - z_\zeta x_\eta & z_\zeta x_\xi - z_\xi x_\zeta & z_\xi x_\eta - z_\eta x_\xi \\ x_\eta y_\zeta - x_\zeta y_\eta & x_\zeta y_\xi - x_\xi y_\zeta & x_\xi y_\eta - x_\eta y_\xi \end{bmatrix}\begin{bmatrix}\vec{u}_\xi\\ \vec{u}_\eta\\ \vec{u}_\zeta\end{bmatrix} \tag{12}$$

The formulation (6) is calculated by adopting the iteration formulaton(13).

$$\sum_{i=0}^{L_S}\sum_{j=0}^{M_S}\sum_{k=0}^{N_S}U_{ijk}^{n+1}\left(\int_{v(t)}N_{i,p}(\xi)N_{j,q}(\eta)N_{k,r}(\zeta)Jd\xi d\eta d\zeta\right)^n = \left(\int_{v(t)}uJd\xi d\eta d\zeta\right)^n$$
$$-\Delta t\left(\int_{s1+s2}(\vec{\phi}_x - u\vec{u})\bullet\vec{n}_1H_1d\eta d\zeta + \int_{s3+s4}(\vec{\phi}_x - u\vec{u})\bullet\vec{n}_2H_2d\xi d\zeta + \int_{s5+s6}(\vec{\phi}_x - u\vec{u})\bullet\vec{n}_3H_3d\xi d\eta\right)^n \tag{13}$$

The similar formulation can be obtained for formulation(7),(8),(9). The integrations items in the above formulation are calculated by applying Gaussian quadrature. The linear equation systems can be constructed by satisfing the integral equation in each control volume and the boundary conditions, thus $\vec{U}_{ijk} = (U_{ijk}, V_{ijk}, W_{ijk})^T$ and P_{ijk} can be obtained by solving the linear equation systems. The velocity $\vec{u}$ and pressure p can be obtained by appling the De Boor algorithm. The stress condition is adopted for the free surface boundary condition. It can be see in ref.[7]. The other boundary conditions are listed in Table 1.

Table 1 Boundary Condition

Boundary	u, v, w	p
Upstream	$u = 1, v = 0, w = 0$	$p = 0$
Downstream	$\partial u/\partial\vec{n} = 0, \partial v/\partial\vec{n} = 0, \partial w/\partial\vec{n} = 0$	$\partial p/\partial\vec{n} = 0$
Center	$\partial u/\partial\vec{n} = 0, v = 0, \partial w/\partial\vec{n} = 0$	$\partial p/\partial\vec{n} = 0$
Free Surface	Stresses	Stresses
Body	$u = 0, v = 0, w = 0$	$\partial p/\partial\vec{n} = 0$
Bottom	$u = 0, v = 0, w = 0$	$\partial p/\partial\vec{n} = 0$
Side	$\partial u/\partial\vec{n} = 0, \partial v/\partial\vec{n} = 0, \partial w/\partial\vec{n} = 0$	$\partial p/\partial\vec{n} = 0$

The new grid systems can be reconstructed by the following formulation approximately, and

$$\vec{X}_{ijk}^{n+1} = \vec{X}_{ijk}^{n} + \Delta t\cdot\vec{u} \tag{14}$$

the new velocity and pressure are smoothed by B-spline solid for next time calculation. It will take wave filter effect. The goal is for the numerical stability.

3. RESULT OF WIGLEY HULL

The Wigley hull is selected for turbulent flow computation. The Froude number and Reynolds number are $Fr = 0.348, R_e = 3.21\times10^6$. The grid system is shown in Fig.1. The wave surface is shown

in Fig.2 . The range of grid system is $-1.5 \le x \le 1{,}0 \le y \le 1.5, -1.5 \le z \le wave\ \ height$.

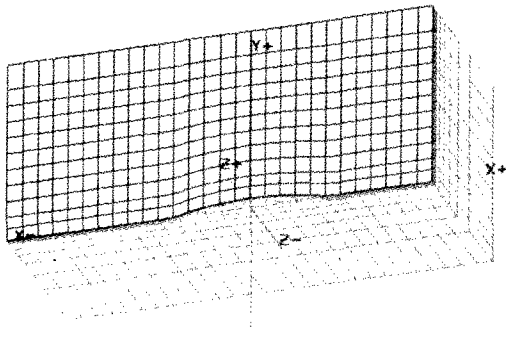

Fig.1.Grid System

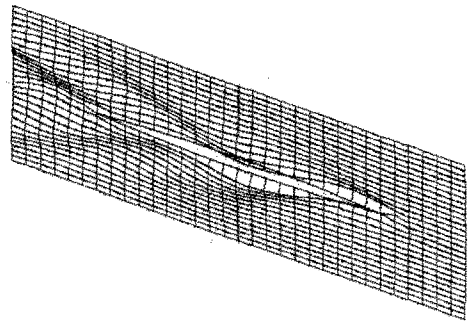

Fig.2. Wave Surface

4. CONCLUSION

Although this is a initial and incomplete work, it is feasible that the turbulence flow is calculated by adopting B-spline solid. The detail work need to do in the following several monthes.

REFERENCES

[1] Alessandrini,B. and Delhommeau,G. " A Multigrid Velovity-Pressure-Free Surface Elevation Fully Coupled Solver for Calculation of Turbulent Incompressible Flow around a Hull",21st Symp. Naval Hydrodynamics,1977

[2]Chengbi Zhao, Zaojian Zhu,"A 3D Potential Flow Computing Method Based On NURBS", Proc. Of the 14th international workshop on water waves and floating bodies, 11-14 April ,1999, Michigan USA.

[3]Chengbi Zhao,"Study on Modern Method and Software System for Ship Surface Design",Ph.D.thesis,Wuhan Transportation University,1999.

[4]Danmeier D. G.,"A Higher-Order Panel Method for Large-Amplitude Simulations of Bodies in Waves", Ph.D. dissertation, Massachusetts Institute of Technology, USA, 1999.

[5]F.Bet, D.Hänel and S.Sharma, "Nurmerical Simulation of Ship Flow by a Method of Artificial Compressibility",ONR, 2000

[6]Hsin C.Y., Kerwin J.E., and Nerman. J.N. "A Higher-Order Panel Method for Ship Motions Based on B-Spline", 6th International Conference on Numerical Hydrodynamics, Iowa, 1993

[7]Hao Liu, and Yoshiaki Kodama, "Computation of Waves Generated by a Ship Using an NS Solver with Global Conservation", Journal of The Society of Naval Architects of Japan,Vol.173.

[8]Nakos D.E., "Ship Wave Patterns and Motions by a Three Dimensional Rankine Panel Method",Ph.D. dissertation, Massachusetts Institute of Technology, USA, 1990.

[9]Maniar H.D., "A Three Dimensional Higher Order Panel Method Based on B-Splines", Ph.D. dissertation, Massachusetts Institute of Technology, USA, 1995.

[10]Nobuyuki Hirata and Takanori Hino, "An Efficient Algorithm for Simulating Free Surface Turbulent Flows around an Advancing Ship" , Journal of The Society of Naval Architects of Japan,Vol.185.

[11] Shiotani, S. and Hodama , Y.," Numerical Computation of Viscous Flows with Free Surface Flow around a series 60 Model", Journal of The Society of Naval Architects of Japan,Vol.180.

[12]Takanori Hino,"A 3D Unstructured Grid Method for Incompressible Viscous Flows", Journal of The Society of Naval Architects of Japan,Vol.182.

[13]"A 3D Method for the Motion and Force of a Ship with Advance Speed in Wave based on NURBS Surface", Research Report, Wuhan University of Technology, 2000.

Fluid Motions in a Tank with Internal Structure

Renchuan Zhu and Kimio Saito
Div. of Development Science, Hiroshima University, JAPAN

1. INTRODUCTION

The linear and nonlinear fluid motions has been widely studied by using Boundary Element Method (BEM)*(Brebbia (1978))*, which has a merit of reducing the dimensions by one and it is applicable even for the infinite domain problem. When BEM is used for the calculations of the velocity potential and the hydrodynamic forces, it is important to get a precise value in the boundary integral of the functions of $1/r$, in which r is the distance between elements. It is difficult to get the analytical solution for the three-dimensional (3D) problem and the numerical method such as Gaussian integration will be applied to the integral of the function $1/r$, in which the singular integration on the boundary should be paid attention. In a tank with the internal structure, the distance r between elements on both sides of the internal structure will tend to 0, when the thickness of the plate t tends to 0. So it is very difficult to avoid the numerical error in the integral of the function $1/r$. It has shown the errors between the analytical solution and the numerical integral in the paper of Nishino et al.*(1999)*.

In this paper, the sloshing in 3D tank with the internal structure and the vibration of the internal structure in 3D tank are discussed by extending the basic BEM to the multiple domain problems. The fluid motions in a tank with the internal structure that is subjected to the forced oscillations and the dynamic pressure distributions on the thin vibrating internal structure are shown. Some of the computed results are compared with the ones in the published paper. It indicates that they agree well each other and the present method is effective.

2. MULTIPLE DOMAIN "BEM"

As shown in Fig.1, we assume that the whole domain composes of the two connected domains, I and II with the imaginary boundary Γ_i. When the outside boundaries of the domain I and II are expressed by Γ_1 and Γ_2 respectively, the domain I is surrounded by Γ_1 and Γ_i, and the domain II by Γ_2 and Γ_i.

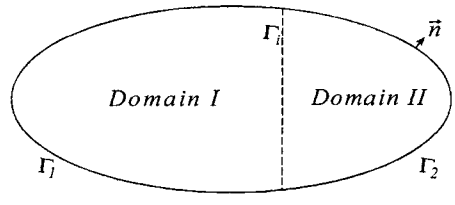

Fig.1 Multiple domain system

We assume the fluid is incompressible and the flow irrotational so that there exists a velocity potential ϕ that satisfies the Laplace equation, in the whole fluid domain, and the velocity potential is defined as $\nabla\phi = \vec{q}$ ($\vec{q}$ is the fluid velocity).

On the outside boundaries there are two kinds of conditions. One is expressed by the value of the velocity potential on the part of the outside boundary, i.e. ϕ=*known*. Another is the value of the normal differentiation of the velocity potential on the remaining outside boundary, $\partial\phi/\partial n$=*known*.

On the imaginary boundary, the flow velocity and its potential at any point is the same as the one in the adjacent domain, so that we obtain the following conditions on the imaginary boundary,

$$\phi\big|^{II} = \phi\big|^{I}, \qquad \frac{\partial\phi}{\partial n}\bigg|^{II} = -\frac{\partial\phi}{\partial n}\bigg|^{I}, \qquad on\ \ \Gamma_i \tag{1}$$

According to the Green's formula, the velocity potential ϕ can be written as,

$$c_P\phi_P = \oint_S \frac{\partial \phi}{\partial n} ln\frac{1}{r} ds - \oint_S \phi \frac{\partial}{\partial n}\left(ln\frac{1}{r}\right) dS \tag{2}$$

where r is the distance between the source and field point, c_p and ϕ_p is the radian measure and the velocity potential at the node P on the boundaries, S is the whole boundaries in the domain.

By using the expression of vector and matrix, it can be written as:

$$[H]\{\phi\} = [G]\left\{\frac{\partial \phi}{\partial n}\right\} \qquad \text{in domain I, II} \tag{3}$$

where matrices [H] and [G] consist of constants determined by Green's function and the mesh system of the boundary discretization method, vectors $\{\phi\}$ and $\{\partial\phi/\partial n\}$ are the values at the nodes on the boundaries.

By using the domain name for the superscript and the variables on the boundary for the subscript, the following matrix equation will be obtained,

$$\begin{Bmatrix} H_o^I & H_i^I & -G_i^I & 0 \\ 0 & H_i^{II} & G_i^{II} & H_o^{II} \end{Bmatrix} \Phi = \begin{Bmatrix} G_o^I & 0 \\ 0 & G_o^{II} \end{Bmatrix} V \tag{4}$$

where the subscript "i" means the variable of the nodes on the imaginary boundary Γ_i, and "o" denotes the variable of the nodes on the outside boundaries Γ_1 and Γ_2 and

$\Phi = \left\{\phi_o^I, \phi_i^I, \partial\phi/\partial n|_i^I, \phi_o^{II}\right\}^T$, $V = \left\{\partial\phi/\partial n|_o^I, \partial\phi/\partial n|_o^{II}\right\}^T$.

It is obvious that the velocity potential can be obtained by solving Eq. (4).

3. SLOSHING IN 3D TANK WITH INTERNAL STRUCTURE

We consider a 3D tank that is subjected to forced oscillations and assume that the fluid in a tank is inviscid and incompressible and the flow is irrotational in the whole domain.

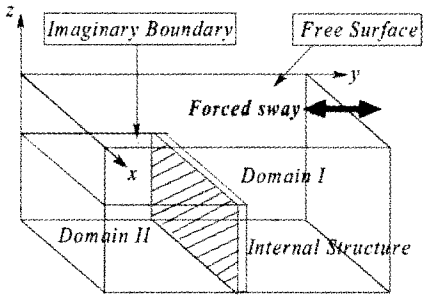

Fig.2 3D sloshing model and fluid domains

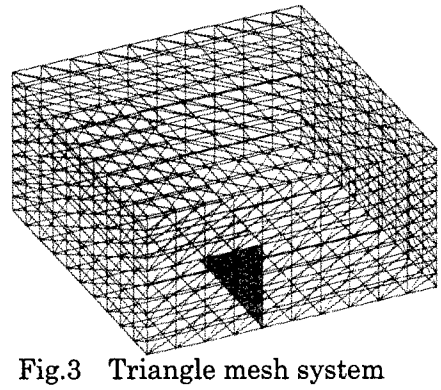

Fig.3 Triangle mesh system

As shown in Fig.2, for simplicity, we assume the tank is only a forced sway in y direction. The governing equation satisfies the 3D Lapalace equation. On the free surface, the dynamic and kinematic boundary conditions can be described by Eqs. (5) and (6),

$$\frac{\partial \phi}{\partial t} = -\frac{1}{2}\left\{\left(\frac{\partial \phi}{\partial x}\right)^2 + \left(\frac{\partial \phi}{\partial y}\right)^2 + \left(\frac{\partial \phi}{\partial z}\right)^2\right\} + a_y y + gz + \mu\phi \tag{5}$$

$$n_y \frac{\partial \varsigma}{\partial t} = \frac{\partial \phi}{\partial n} \tag{6}$$

where μ is the viscosity coefficient. On the rigid boundaries in the whole domain are all zero. The time-stepping technique and the center finite difference schemes with respect to time are used to

obtain the velocity potential at the node on the nonlinear free surface:

$$\phi|_{t+\Delta t} = \phi|_{t-\Delta t} + \left.\frac{d\phi}{dt}\right|_t \cdot 2\Delta t, \qquad \varsigma|_{t+\Delta t} = \varsigma|_{t-\Delta t} + \left.\frac{d\varsigma}{dt}\right|_t \cdot 2\Delta t \tag{7}$$

where $d\phi/dt = \partial\phi/\partial t + |\nabla\phi|^2$ and $d\varsigma/dt$ is substituted by $\partial\varsigma/\partial t$. From Eq. (7), the free surface profile and its cooresponding velocity potential at every time step will be obtained.

In order to verify the numerical method and the program of this study, the numerical calculations for the sloshing problem have been carried out and the results are compared with the one of Shinkai et al.*(1987)* which was computed by MAC (Mark and Cell) method. We used the same tank as Shinkai's having the breadth and length: a=40cm, the water depth of 14cm fitting with the 4cm internal structure on the centerline of the bottom. The tank is subjected to the forced sway oscillations in which the period is 1.0 second and the amplitude is 1.0cm. For the start of the computation, it is assumed that the tank is set to be horizontal and the water is at rest. The computed free surface elevations are shown in Fig. 4 and Fig. 5. The former gives the free surface profile in the tank at time t=2.40 second and the latter illustrates the time histories of the free surface elevation at the tank side on the centerline ($x=a/2$). In Fig. 5 the solid line denotes the result of present method, symbol is Shinkai's which is compared by using two dimensional method *(Shinkai et al.(1987))*. The periodic line is close to the symbols and it indicates the present method is effective.

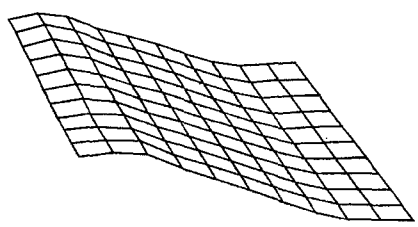

Fig. 4 Free surface profile in the tank at t=2.40

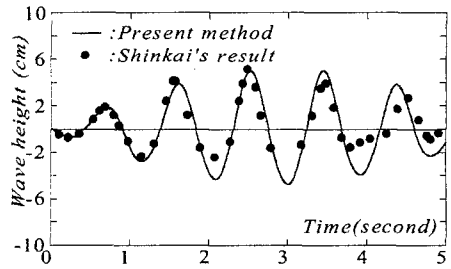

Fig. 5 Comparison of the free surface elevations at the tank side on the centerline ($x=a/2$)

4. VIBRATION OF INTERNAL STRUCTURE IN 3D TANK

We consider a 3D tank with an internal structure that is subjected to a periodical forced oscillation with an infinitely high frequency. It is assumed that the fluid is incompressible and the flow irrotational so that there exists a velocity potential ϕ that satisfies the Laplace equation. Since the frequency $\omega \to \infty$,

$$\phi = 0 \quad \text{on the free surface.} \tag{8}$$

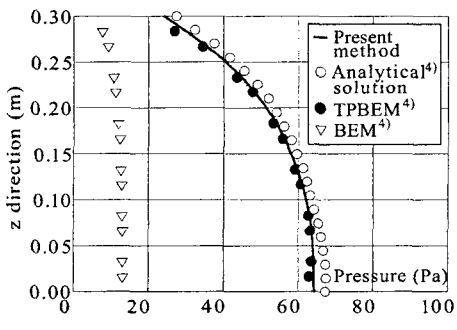

(a) Pressure gap distribution on thin plate

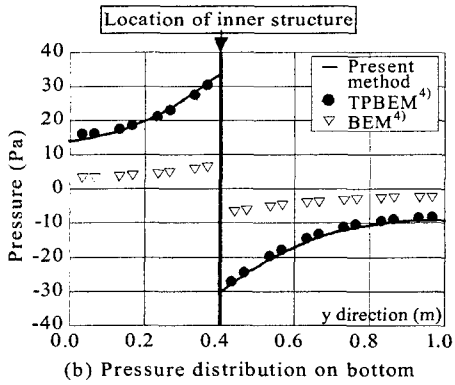

(b) Pressure distribution on bottom

Fig. 6 Pressure distribution due to a unit acceleration of the internal structure

On the tank wall and internal structure, $\partial\phi/\partial n=-V_y$ and on the tank bottom $\partial\phi/\partial n=0$ (n is the normal to the boundaries).From the Bernoulli's equation, the pressure can be expressed as,

$$p=-\rho\frac{\partial\phi}{\partial t} \quad (\rho\text{: fluid density}) \tag{9}$$

By the integration of Eq. (9) on the rigid boundaries, the hydrodynamic forces acting on the boundaries can be obtained.

For the numerical calculations, we choose the case of Nishino et al. *(1999)*, in which the dimensions of the tank and the internal structure are as shown in Fig. 2. Both the breadth and length of the tank: a=1.0m and the fluid depth is 0.50m. The internal structure locates at y=0.40m and it has a height of 0.30m. Here we also used the method of the triangle element mesh system to discretize two domains of the tank, which is similar to section 3. It is assumed that the internal structure oscillates in the fluid with unit acceleration in its normal direction. Fig. 6 shows the pressure distributions on the centerline ($x=a/2$) due to unit acceleration computed by using the triangle element with linear shape function. It also gives the pressure gap distribution on the thin internal structure and the pressure on the bottom of the tank. In the figure, the analytical solution, the results of the basic BEM and TPBEM (Thin Plate BEM by Nishino et al. *(1999)*) are shown by the symbols of circle and triangle respectively. The result of the present method is very close to the analytical solution and the one of TPBEM.

5. DISCUSSIONS

Nonlinear simulations have been carried out for the fluid motions in a tank with internal structure that is subjected to the forced sway oscillation. In order to avoid the numerical error which will be appeared in the integral on the internal structure, the basic BEM has been extended to the multiple domain problems. The computer program has been developed and applied to the simulation of the sloshing phenomena. Some of the computational results are compared with the ones in the published paper and it indicates that they agree well each other and the present method is effective.

The multiple domain BEM has been also applied to the vibration of the internal structure in contact with the water. From the comparison of the solutions among the basic BEM, TPBEM and the analytical ones, the present method agrees well with TPBEM and analytical solutions. It is also expected that the present method is a useful tool for the evaluation of the added mass in the fluid-structure interactive vibration.

REFERENCES

Brebbia, C. A.: *The Boundary Element Method for Engineers*, Pentech Press, London(1978).

Nishino, H., Ohta, K. and Fujita, K.: *Vibration Analysis of the Structure in Contact with Fluid by use of the Thin Plate Boundary Element Method* (in Japanese), J. Soc. of Nav. Arch. of Japan, Vol. 184 (1999), pp. 401-408.

Shinkai, A., Yamaguchi, S., Shintaku, E. and Iwamoto, S.: *Numerical Analysis of Liquid Sloshing in a Rectangular Tank with Baffle Plates* (in Japanese), the Soc. of Nav. Arch. of West Japan, Vol. 78 (1987) pp. 173-187 and Vol.79 (1987), pp.141-154.